Ultrafast Dynamics of Molecular Liquids Investigated by Femtosecond Light Scattering

by

Bern Kohler
B.S., Stanford University
1985

Submitted to the Department of Chemistry
in partial fulfillment of the requirements for the degree of

Doctor of Philosophy

at the

Massachusetts Institute of Technology
September, 1990

Signature of Author _____
Department of Chemistry
6 August 1990

Certified by _____
Keith A. Nelson
Associate Professor of Chemistry
Thesis Supervisor

Accepted by _____
Glenn A. Berchtold
Chairman, Departmental Committee on Graduate Students

This doctoral thesis has been examined by a committee of the Department of Chemistry as follows:

Professor Irwin Oppenheim _____
Chairman

Professor Keith A. Nelson _____
Thesis Supervisor

Professor Robert J. Silbey _____

Ultrafast Dynamics of Molecular Liquids Investigated by Femtosecond Light Scattering

by
Bern Kohler

Submitted to the Department of Chemistry on 6 August 1990 in partial fulfillment of the requirements for the degree of Doctor of Philosophy in Chemistry

Abstract

Sub-100 femtosecond optical pulses are used to study a variety of fast dynamical processes in nonassociated molecular liquids. These short optical pulses coherently drive low frequency (< 300 cm-1) modes by impulsive stimulated light scattering (ISS). By measuring the time-dependent nonlinear optical susceptibility of a liquid, it is possible to study intra- and intermolecular vibrations in liquids, as well as reorientational motions. This technique represents an important new kind of time-resolved intermolecular vibrational spectroscopy which provides new information about the dynamics of intermolecular encounters in liquids.

Results are presented for dibromomethane and several tetrahalide liquids which demonstrate the coherent excitation of intramolecular vibrations by femtosecond ISS. By time-resolving individual oscillation cycles, it is possible to characterize vibrational dephasing. A comparison with Raman spectroscopy is presented which demonstrates the equivalent information content of ISS and spontaneous light scattering.

A study of carbon disulfide is presented in which the ultrafast response of the liquid was recorded as a function of temperature. A weakly oscillatory signal is observed at temperatures < 240 K, indicating intermolecular motion which is vibrational in character. Although a variety of molecular motions can contribute to a time-dependent polarization, the signal is interpreted in terms of molecular orientational motion which is vibrational (i.e., librational) in character due to intermolecular interactions. Simple modelling of the signal suggests that the librations are predominantly inhomogeneously broadened. Temperature-dependent values of the configuration-averaged librational frequency and the extent of inhomogeneity in the neat liquid are estimated.

Femtosecond scattering data from benzene and related compounds are discussed which illustrate the general importance of intermolecular vibration in liquids of anisotropic molecules.

Combining femtosecond time-resolution with diamond anvil cell high pressure technology, the ultrafast response of liquid carbon disulfide was measured at room temperature as a function of pressure. The response of the liquid is again oscillatory, indicating that the dynamics are strongly affected by density.

A molecular dynamics simulation study of carbon disulfide over the entire liquid range is presented. Structural and dynamic properties are discussed. Particular attention is paid to the reorientation of molecules in the first several picoseconds. The simulations show that there is a component to the single molecule reorientation which relaxes on the subpicosecond time scale. Yet even at the highest densities simulated, structure arising from molecular libration is never observed in the correlation functions describing the reorientation of single molecules, and the simulated ISS signal is never oscillatory. Either dynamics involving pairs or higher configurations of molecules are responsible for the ultrafast transient, or the pairwise interaction potential used in the simulations is inadequate for describing short-time dynamical processes of single molecules in the dense liquid.

Thesis Supervisor: Dr. Keith A. Nelson
Title: Associate Professor of Chemistry

Acknowledgements

It is a pleasure to thank my advisor, Professor Keith Nelson, for his scientific enthusiasm and good humor. He constantly showed great interest in my work and was always available for discussions. Thanks are due, as well, to the entire Nelson family for providing welcome breaks from M.I.T., usually featuring delicious Mexican food and the refreshing company of those under 7 years of age.

I would like to thank Professor Mike Brown from the U. of Washington for providing us with a diamond anvil cell and much useful advice on high pressure techniques during his stay in our lab. Thanks are due Professor Steve Goates of Brigham Young University, who bravely lived with us in room 2-069 for a year. I enjoyed your company and your interest in running.

I am grateful for the companionship and scientific efforts of the early Nelson Group students, Leah Williams, Margaret Farrar, Lap-Tak Cheng and Yong-Xin Yan and post-doc Sandy Ruhman. They are proof that success lies beyond the portals of building two. Thanks, Leah and Sandy, for your considerable contributions to the femtosecond laser system.

Thanks to Tom Dougherty and Alan Joly for signing up with me for the Nelson group in the fall of 1985. Our three-way addition to the group made for enjoyable basketball games and championship volleyball seasons. May future group historians remember us kindly. Congratulations, Alan on the Ph.D. Without your company at the adjacent computer, and on treks to LaVerde's, I never would have survived these punishing thesis weeks.

Most of my adult life has been spent in the basement of building two. An experience made infinitely more pleasurable by the company of many friendly coworkers. Thanks to Scott Silence, Ion Halalay, Anil Duggal, Gary Wiederrecht, Matt Banet, Andy Cook, Lisa Dhar, Ivan Lorkovic and Weining Wang for many memorable adventures. Your company made for wonderful ski trips to New Hampshire, December trips to Talbot house and evenings at the Muddy Charles Pub. Thanks to venerable post-doc Mark Trulson for round-the-clock shift-work on the laser with me one summer, infamous Home Farms barbeques, and for introducing new vocabulary into

my speech. I am grateful to Matt Banet for recording Raman spectra and for providing a new home for the b-mobile.

Thanks to Peter and Linda Saeta for wonderful friendship outside the institute and late night dinners.

I thank my family for their love from distant California. Special thanks to my father who, by shining example, started me down this path.

Finally, to those who continue to toil in the basement: Be heartened and *Just keep going...*

Dedication

To my parents who encourage this sort of behavior.

Table of Contents

Chapter 1

Introduction

Frequency-domain light scattering has been used successfully for many years to study dynamical motions of molecules in simple molecular liquids. Translations, rotations and intramolecular vibrations modulate the collective polarizability of the liquid and scatter light [1]. The time scales of these motions (see table 1.1) give rise to the frequency-dependence or band shapes of the measured spectra. With the recent advent of lasers capable of generating optical pulses shorter than 100 femtoseconds, it has become possible to initiate and probe many of these fast, dynamical processes directly in the time domain [2,3]. This thesis describes the initial application of a femtosecond time-domain light scattering technique known as impulsive stimulated light scattering (ISS) to gain new information about the short-time behavior of intermolecular interactions in molecular liquids.

The dynamical behavior of molecular liquids has been the subject of extensive theoretical and experimental study [4-6]. Despite considerable progress, there are still many unresolved issues. Much of the difficulty has to do with the complexity of this state of matter. In the study of gases and solids considerable simplifying assumptions can be made which, at the very least, simplify the starting point for theoretical treatments. In a dilute gas, the low number density and the relatively infrequent interactions between molecules give rise to essentially free translation and rotation of individual molecules, periodically interrupted by collisions with others. In the

crystalline solid, the symmetries of the lattice and the strong interactions between molecules greatly simplify the description of dynamical properties. The motions of nuclei can be calculated about sites which are fixed in space.

In dense fluids, or liquids, the molecular dynamics lie somewhere in between those of solids and gases, and the history of theoretical models of the liquid state reflects a certain amount of uncertainty over whether the dynamical properties of the solid or gaseous phase present the more appropriate starting point. Molecules in the liquid phase experience frequent, strong interactions with neighboring molecules, yet they retain much of the independence, and disorder of the gas phase. This latter characteristic is indicated by the ability of liquids to flow and by the familiar process of molecular diffusion.

The reorientation and translation of molecules are sensitive probes to the balance between strong interactions and disorder in the liquid state. Intramolecular vibrations are also strongly affected by liquid phase interactions and these will be discussed briefly in chapter 4. The main focus here is on reorientation and translation. Because these processes are strongly affected by interactions between molecules, their study provides insight into intermolecular forces in the liquid state. For many molecular liquids these processes can be treated at an approximate level independently of intramolecular vibrations. This is a consequence of the strong bonding between atoms in molecules and the comparatively weak interactions between atoms on different molecules. A classical mechanics description in which molecules are treated as rigid bodies has been effective at understanding reorientation and translation in liquids. This is the approach adopted here.

Table 1.1 Elementary dynamical processes and their approximate time scales in simple liquids.

Process	Time scale
period of free translation	100 fs
period of free rotation	100 fs
collective structural rearrangements	100 fs - 10 ps
intramolecular vibration	50 fs - 500 fs
intermolecular vibration	100 - 500 fs
diffusive reorientation	1 - 10 ps

The solid-like and gas-like characteristics of the liquid phase are manifested in these dynamical processes. They appear dramatically different when viewed for different periods of times (i.e. different numbers of interactions). For example, the motions of molecules in the liquid state are gas-like for very short time intervals. During these short times the force field about a molecule is approximately constant. The inertia of molecules leads to brief periods of free translation and rotation. Considered over long time intervals, during which many intermolecular interactions occur, the trajectories of molecules are diffusional in character, showing little or no correlation with positions or orientations at earlier times.

At intermediate times, however, the dynamics are more complex. This is the timescale of correlated collisions, when molecules interact with

only a few near neighbors. As in solids, the forces between molecules due to specific interaction potentials give rise to local, preferred arrangements of molecules. While the molecules are constantly in flux, such local arrangements or structures persist for short time intervals. The ansatz that transient liquid structures determine short-time dynamics is incorporated in the so-called cage models of liquid dynamics [7-12]. In these models each molecule moves in a short-lived potential well or "cage" created by neighboring molecules. If the local liquid structure does not have sufficient time to relax, the motions of molecules may take on a vibrational character. In this thesis, the first direct, time-domain evidence for vibrational intermolecular motions is presented for several liquids of highly anisotropic molecules.

Even with optical pulses of shorter duration than the elementary dynamical steps we wish to study, our goal of understanding molecular dynamics in liquids is a difficult one. A fundamental challenge is the description of the scattered light in terms of microscopic variables. The frequent interactions between molecules affect not only the dynamics of individual molecules, but they also result in contributions to the light scattering which are difficult to model. For example, anisotropic fluctuations in the relative positions of molecules also contribute to depolarized light scattering. These are many-body effects involving relative motions of molecules. Such motions relax quickly, and, for this reason, the femtosecond time-resolved light scattering technique described in this thesis offers promise for the elucidation of the importance of such "interaction-induced" contributions to light scattering.

This thesis proceeds as follows. In chapter 2, the considerable laser technology necessary for the production of subpicosecond pulses is

described in some detail. The data collection method used in these experiments is described here as well. The theory of ISS as it applies to the study of liquid dynamics is the subject of chapter 3. This chapter contains the important result that ultrashort laser pulses can coherently excite elementary molecular motion through the nonlinear coupling of light with resonant material excitations. In chapter 4, ISS data from a variety of molecular liquids are presented which illustrate the excitation and dephasing of low-frequency intramolecular vibrations. The remainder of the thesis focuses on the short-time aspects of the dynamics of anisotropic molecules. In chapters 5 and 6, a temperature- and pressure-dependent study of liquid carbon disulfide is discussed. Experimental evidence is presented of the vibrational character of intermolecular motions in this liquid at short times. The data from carbon disulfide will be described in terms of simple models of molecular libration, assuming the signal reflects predominantly reorientational dynamics. Such an interpretation is supported by ISS data from benzene and related molecular liquids presented in chapter 7. In chapter 8, molecular dynamics simulations are described which provide information about the short time behavior of reorientation in a computer model of liquid carbon disulfide. Chapter 9 summarizes the new information obtained by femtosecond light scattering and two appendices provide technical information about aspects of the molecular dynamics simulations.

Chapter 2

The Generation of Amplified, Femtosecond Optical Pulses and Data Collection Method

2.1 Background and system overview

The most common method for generating subpicosecond optical pulses is by modelocking a dye laser. Passive modelocking induced by a thin jet of a saturable absorber dye in a dye laser pumped by a continuous wave (cw) argon ion laser forms the basis of the colliding pulse modelocked (CPM) laser system, the first laser to achieve sub-100 femtosecond (fs) duration pulses [13]. In 1984, G. Mourou et al. produced 80 fs pulses by synchronously pumping an antiresonant ring (ARR) dye laser through hybrid modelocking [14]. Work began in the Nelson group in 1985 on the construction of a similar system.† We chose to construct the synchronously pumped ARR dye laser for several reasons. First, the use of solid state Nd:YAG lasers as pump lasers gives the system greater reliability. Secondly, synchronous pumping provides a route to low-cost, highly efficient synchronous amplification at a high pulse repetition rate (PRR).

The femtosecond laser system is shown schematically in figure 2.1. The femtosecond dye laser (DYE) is synchronously pumped by the cw-modelocked Nd:YAG laser (YAG 1). Amplification to single pulse

† Laser system construction was done by Leah Williams, Sandy Ruhman, Alan Joly and Bern Kohler.

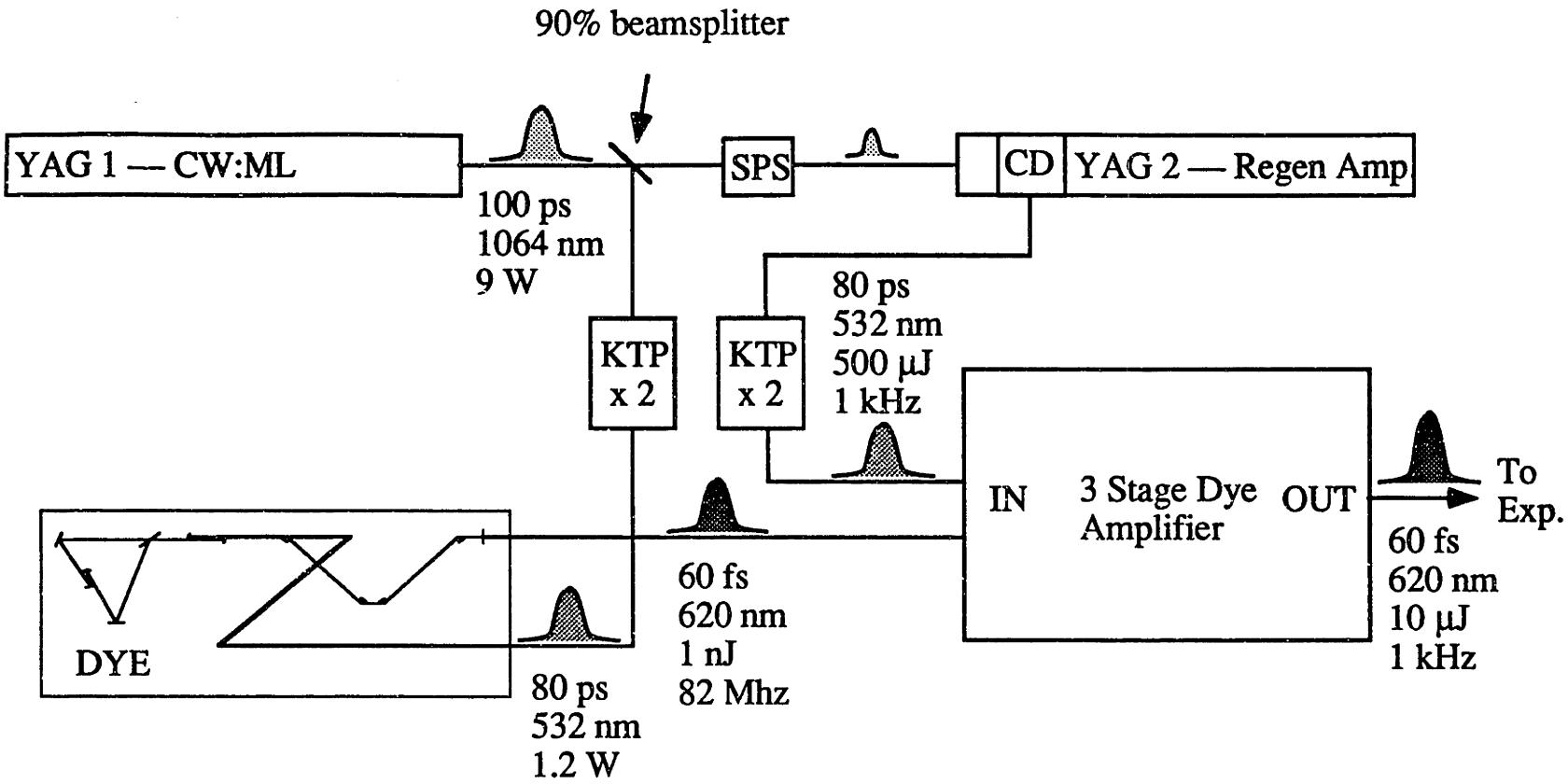

KEY SPS single pulse selector
CD cavity dumper
KTP Potassium titanyl phosphate laser doubling crystal

Figure 2.1 Overview of the femtosecond laser system showing the generation and amplification of 60 fs pulses with single-pulse energies of 10 μJ.

energies of several microjoules is achieved in the three stage flowing dye cell amplifier which is pumped by the doubled output of a second Nd:YAG laser (YAG 2) optically coupled to YAG 1. YAG 2 is operated as a regenerative amplifier optically seeded by a pulse synchronously selected from the pulse train of YAG 1. Each of these subsystems is described in greater detail in the following sections.

2.2 Synchronously pumped antiresonant ring dye laser

All dye laser components are mounted on a super invar optical breadboard for high resonator stability. Figure 2.2 shows the component layout. Sub-picosecond pulses are achieved through hybrid modelocking, resulting from the combination of synchronous pumping of the gain medium and passive modelocking action in the antiresonant ring (ARR) [14]. Two liquid dye jets are used: One for gain and the other for saturable absorption. The gain dye jet (G) uses Rhodamine 6G (Rh6G) dye dissolved in ethylene glycol (5×10^{-3} M), while the saturable absorber jet (SA) uses the saturable absorber dye DODCI dissolved in ethylene glycol (5×10^{-4} M). The entire dye laser is enclosed in a plexiglass box which greatly improves the long-term stability by reducing air currents.

A Nd:YAG laser (Spectra Physics series 3000) is acoustooptically modelocked (IntraAction Corp. modelocker model no. ML-41D) to produce 100 ps pulses (FWHM) at a wavelength of 1.06 microns at a pulse repetition rate of 82 MHz. These pulses are frequency-doubled in an 8 mm long single crystal of potassium titanyl phosphate (KTP) purchased from Airtron, and are used to synchronously pump the dye laser. The rms

Femtosecond Antiresonant Ring Dye Laser

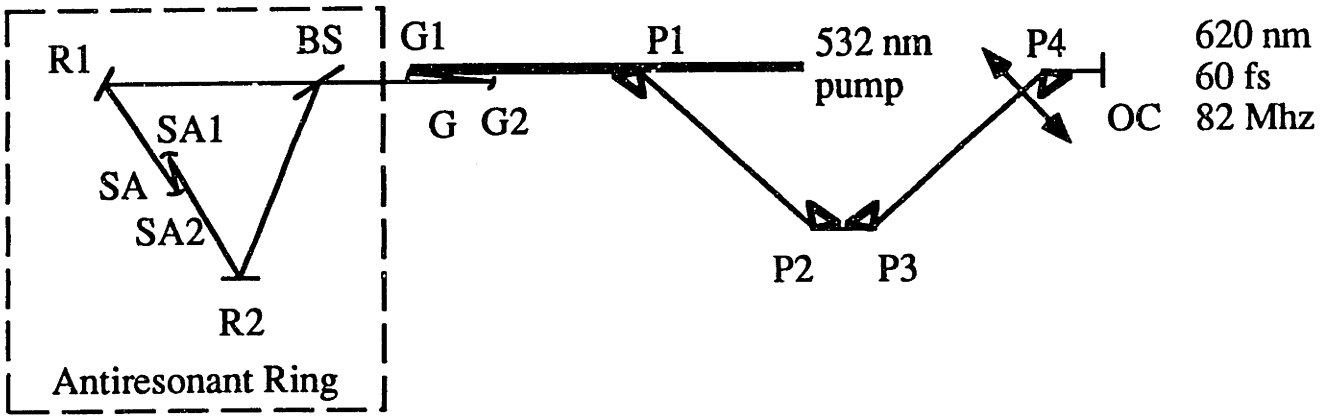

KEY

R1,R2	Ring mirrors, high reflector (HR) @ 620 nm, 28 degrees, P polarization
P1-P2	Isosceles Brewster prisms, fused silica
OC	Output coupler, 90 % reflector @ 620 nm, AR coated other surface
BS	50 % beamsplitter @ 620 nm, θ = 56 degrees, P polarization
G	gain jet, rhodamine 6G dye in ethylene glycol (EG) (5 x 10-3 M)
G1,G2	Gain jet fold mirrors, HR @ 532-620 nm, 10 cm radius of curvature (r.c.)
SA	Saturable absorber jet, DODCI in EG
SA1,SA2	Saturable absorber jet fold mirrors, HR @ 620 nm, 5 cm r.c.

Figure 2.2 Schematic of femtosecond antiresonant ring dye laser.

stability of the frequency-doubled green pulses is approximately 2-3%. A stable pump source with excellent single transverse mode quality is crucial to stable femtosecond pulse generation. Due to the synchronous pumping design, it is necessary to match the two laser cavity lengths as closely as possible [14].

The liquid in each dye jet is circulated by a pump (Micropump) connected in series to a 1 micron particle filter (Balston Filter Products) and a hydraulic accumulator (Hughes Corp.) before the jet nozzle. The accumulator reduces pressure fluctuations in the circulated dye. The jet nozzle for the gain jet is a 200 micron nozzle manufactured by Coherent. We did not find it necessary to control the temperature of the dye or to purge the air from the dye reservoir, although these measures can reduce noise and prolong the lifetime of the saturable absorber dye. The DODCI in the saturable absorber jet was replaced on average every two weeks due to oxidation and photochemical degradation. Degenerated saturable absorber dye results in a yellow-shifting of the lasing from the normal region of operation near 615 nm. In this condition the saturable absorber provides too little loss—we say the lasing "burns through" the saturable absorber—and competing lasing occurs near 580 nm (see figure 2.5).

Short pulses are obtained only when the saturable absorber (SA) jet is positioned in the center of the ARR. In this position the two pulses formed by the beamsplitter travel equal optical distances around the ring, recombining simultaneously in the SA jet. This sets up an intensity interference pattern which promotes short pulse generation [15]. In practice, the jet is centered in the ring of our laser by translating it together with the associated fold mirrors as a unit with all components mounted atop a large translation stage. When the dye laser is properly

aligned, it is possible to translate the entire assembly as far as 5 mm in each direction from ring center without adversely affecting the cavity alignment.

A 60 fs pulse has a spatial length of only 20 microns. In order to attain reliable short pulse operation the saturable absorber jet thickness must be kept on this order [15]. This requires a special jet nozzle capable of producing an extremely thin laminar dye stream. Such nozzles were carefully turned on a lathe from 1/4" stainless steel bar stock to the dimensions given in figure 2.3. The tip of the nozzle is shaped into its final form by gently squeezing it in a small, precision vise with flat jaws. Care must be taken not to pinch the end of the nozzle shut. The resulting dye jet thickness is determined from the attenuation of a He:Ne laser beam passing through a jet formed with an absorbing dye of known concentration. During several years of dye laser operation a variety of jet nozzles were used which produced dye jets 20-30 microns thick. All such jets consistently produced pulses of duration $\leq$ 80 fs.

The optics in the dye laser cavity all have single-stack dielectric coatings at 620 nm optimized for P polarized light. The ring mirrors are optimized for an angle of incidence of 28 degrees. The beamsplitter used in the ring is a 50 $\pm$ 1 % beamsplitter at 620 nm for P polarized light at an angle of incidence of 56 degrees. As described below, it is critical that the beamsplitter be as optically flat as possible. The beamsplitter used in our laser is supported by a 1 mm thick substrate with no back surface coating and was manufactured by CVI. The prisms used to control the cavity dispersion (P1-P4 in figure 2.2) are made of fused silica (Newport Optics). The output coupler used has a reflectivity of 90 %. The lens used to recollimate the green light after doubling is mounted on a translation stage,

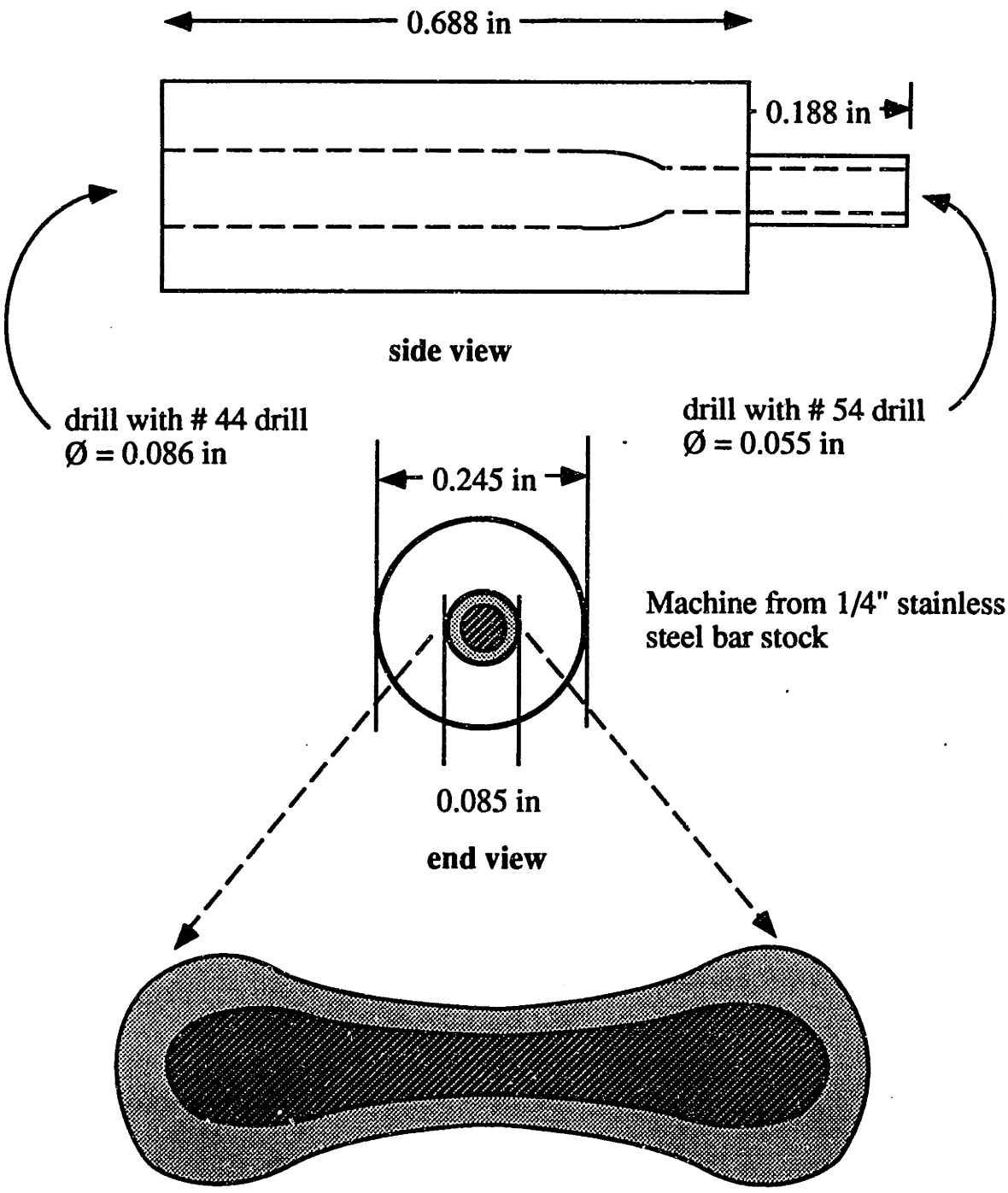

Optimal jet nozzle shape after squeezing (end view)

Figure 2.3 Machining plan for custom-made saturable absorber jet nozzles for producing a laminar jet approximately 20 microns thick..

enabling precise spatial mode matching. The power of green pump light incident on the gain jet can be variably attenuated using a half-wave plate and polarizer combination in the IR beam before the doubling crystal.

2.3 Dye laser alignment

Due to the large number of components the procedure for aligning the femtosecond dye laser to produce short pulses is complex. To help dispel the insidious reputation of this trade, the next two sections summarize some of the tricks (charms, secret rituals, and obscene incantations have been omitted in the interest of brevity) which we found useful for obtaining stable, short pulse operation. In section 2.3.1, the procedure for major realignment or initial setup is described. The steps necessary for optimizing operation each day are described in section 2.3.2.

2.3.1 Initial Setup

It is simplest to set up the laser in a progressive fashion, proceeding from simpler laser cavities to the final, complex one. At first the laser is run with the Rh6G gain jet only in a linear cavity configuration (figure 2.4a). The concentration of the gain dye is adjusted to absorb about 95 % of the incident pump energy. It is important at this step to adjust the focussing of the green pump beam to obtain optimal transverse mode operation, and to maximize output power. The energy conversion efficiency (ratio of average dye laser power measured outside the output

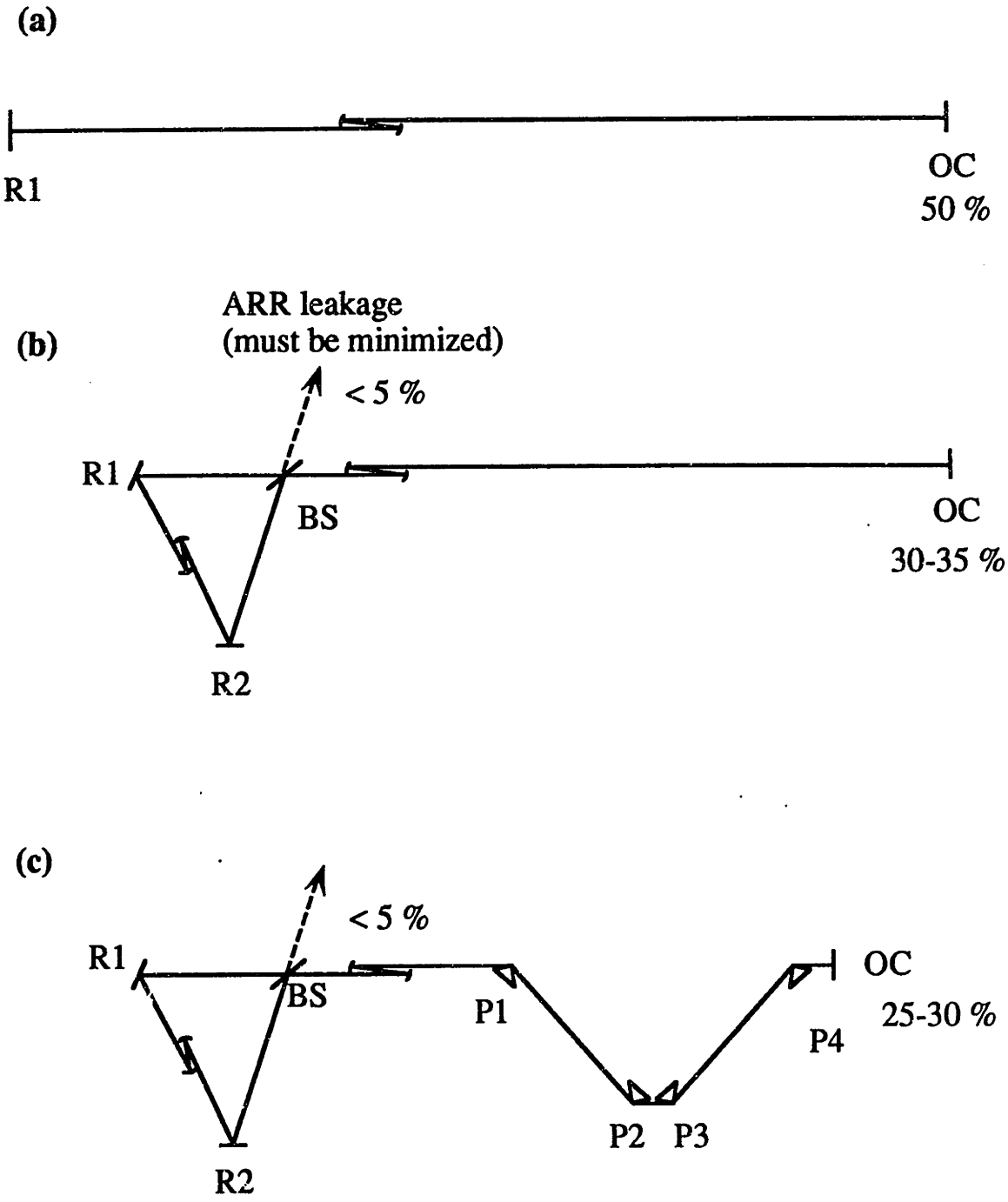

Figure 2.4 a-c Sequence of steps for setting up the femtosecond dye laser. First a straight cavity laser is set up (a). Next, the antiresonant ring is added (b). Finally, the 4 prisms for dispersion compensation are added (c). For each cavity, the expected energy conversion (ratio of output power with saturable absorber jet off to 532 nm pump power) is given as a percentage next to the 90 % output coupler, OC.

coupler to the average pump power) should be about 50%. Next the antiresonant ring is setup as shown in figure 2.4b. Again, an effort is made to extract as much energy as possible from a TEM_{00} mode. The loss out the ARR (dotted arrow in figure 2.4b,c) should be minimized. The biggest source of ARR energy loss is a bent or distorted beam splitter. Our beam splitter is only 1 mm thick and it is very important to avoid distorting its surface by clamping it too tightly to its mount. When properly aligned the energy conversion of the dye laser with the ARR is 35% with the leakage out the ARR amounting to no more than 5% of the total power out the output coupler.

Next, the sequence of 4 prisms is aligned and inserted into the cavity (figure 2.4c). This arrangement of prisms provides overall negative group-velocity dispersion which is used to cancel the positive dispersion arising from the saturable absorber jet and other components in the laser cavity [16]. Each prism is mounted on a rotation stage atop a translation stage. The rotation stages allow each prism to be set at Brewsters angle with respect to the lasing axis. With the translation stages it is possible to translate each prism along a direction normal to the prism base, permitting fine tuning of the cavity dispersion. By partially withdrawing prisms P2 and P3 the losses in the orange part of the spectrum can be increased. This is often necessary to maintain a short pulse in the red.

With the laser configured as illustrated in figure 2.4b, just the tip of prism P4 is inserted into the optical path sending a portion of the laser light around the bent path of the prism sequence while maintaining lasing down the straight axis. This beam is used to align the remaining prisms. Due to the many surfaces, a frequent cause of energy loss is dirty prism faces. With practice it is possible to align all four prisms so that the laser will

switch from lasing down the straight axis to around the four prism sequence just by inserting and removing prisms P1 and P4. With the prisms inserted the optical path length in the cavity increases by about 20 centimeters. It is therefore necessary to move the output coupler forward by this amount to once again match cavity lengths. Note that there is sufficient gain for lasing to occur with the prisms in and the output coupler in the back position, but the energy conversion is low, since the cavity lengths are mismatched. When the proper cavity length is reached, the energy output increases sharply. If there is any doubt, the cavity length of the dye laser should be measured and compared with that of the pump laser. There are many cavity lengths of the dye laser whose ratio to that of the pump laser is a rational number m/n (m, n integers) which result in an increase in power indicative of periodicity multiplication [17]. Such "false" cavity lengths must be avoided. Note that the prisms are aligned with the SA jet off. The SA jet is turned on only as a very last step.

2.3.2 Daily dye laser operation and alignment.

At this point the initial setup of the dye laser has been completed. In this section, daily maintenance and operation are described. A useful diagnostic is the spectrum of the laser light from the dye laser. An 1800 lines / mm grating disperses the leakage radiation from the ARR. By viewing the spectrum approximately one meter away from the grating much useful information is instantly visible about the current laser operation. In the paragraphs below I refer frequently to changes in the appearance of this spectrum with changes in the laser operation.

After warmup, the laser alignment is adjusted with the saturable absorber jet off. Generally, it is only necessary to adjust the beamsplitter slightly and the steering optics for the green pump beam. Adjustment of the ring mirrors (R1 and R2 in figure 2.2) should be avoided. With the SA jet turned off, the lasing is centered at a wavelength of about 580 nm at the peak of the Rh6G gain curve. The spectrum broadens appreciably when the laser cavity length is correctly matched to that of the pump laser, indicating maximum power output over a broad range of frequencies. When the SA jet is turned on the lasing shifts dramatically to the red and the power drops. On cavity length, the spectrum again broadens albeit less so than when the laser is run only with the gain jet on. When the SA jet is turned on the beam splitter must be adjusted slightly to compensate for the slight deviation of the beam through the jet.

To achieve the shortest pulses possible it is necessary to carefully center the SA jet in the ring. First the cavity length is detuned to be slightly short by roughly 100 microns. In this position the spectrum is narrow and red. Next, the SA jet is slowly translated through the approximate ring center while observing the dispersed spectrum of the laser mode. When the SA jet is translated through the optical center of the ring the spectrum shifts slightly to the orange. By eye the spectrum blue-shifts slightly, becoming slightly more orange. The shift is subtle and requires slowly translating the SA jet, being careful not to change the alignment of the laser. Qualitatively this blue shift of the spectrum when the SA jet is properly centered can be understood by considering the spectra in fig 2.5. The optical absorption spectrum of DODCI partially overlaps the fluorescence spectrum of Rh6G, causing the lasing to shift from 580 nm without the SA jet to 620 or so nm when the SA jet is

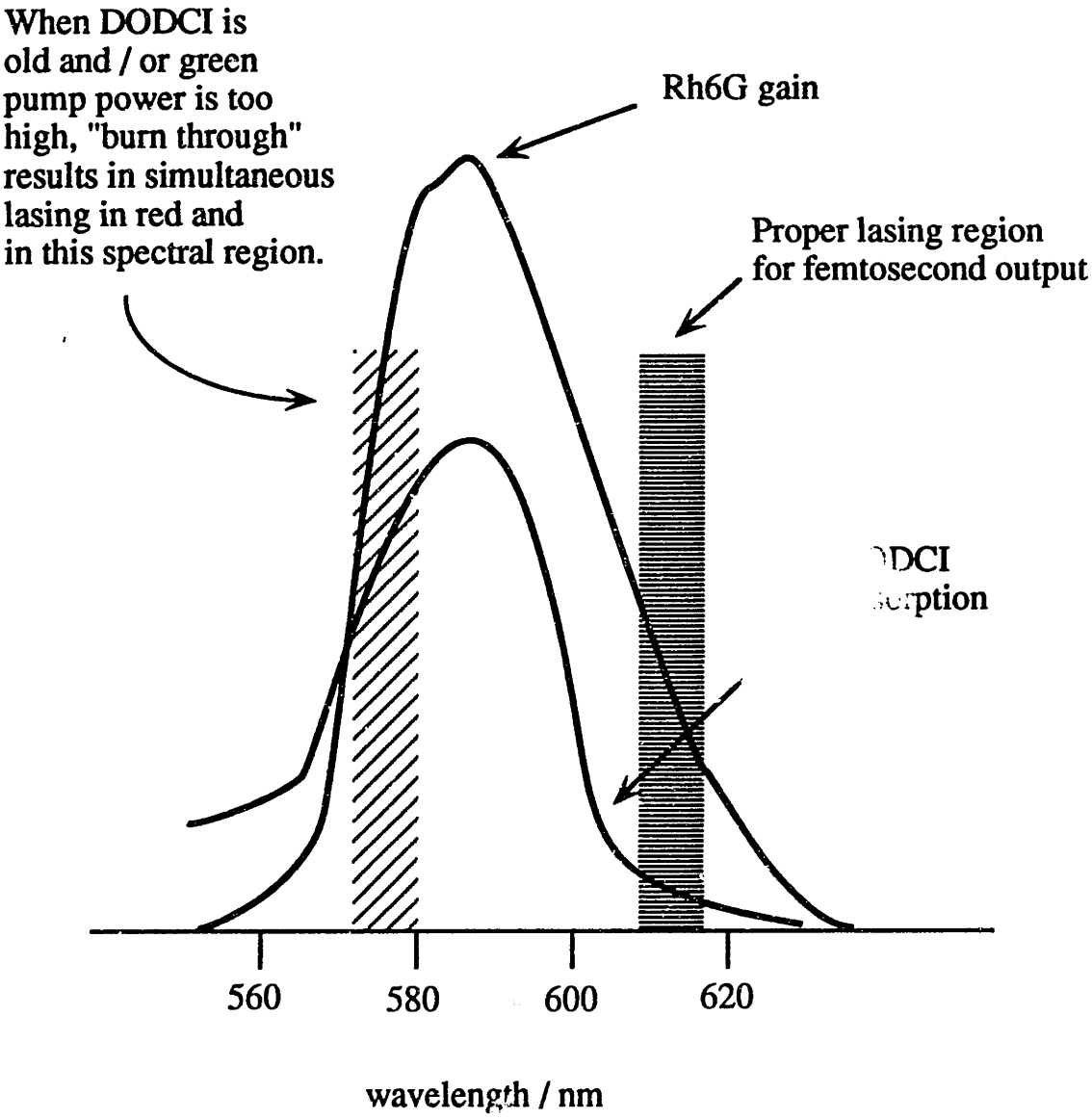

Figure 2.5 Absorption spectrum of DODCI saturable absorber dye and gain curve of rhodamine 6G, the laser gain dye.

present. When the SA jet is centered properly, pulses propagating in both directions around the ARR interfere so that the intensity in the jet is greatest. This has the effect of further saturating the DODCI absorption allowing the lasing to creep up towards the maximum of the Rh6G gain curve.

The spectrum is at its widest, indicating the shortest pulses, when the cavity length and the cavity dispersion are both optimally adjusted. Prism P1 is slowly translated either into or out of the optical mode, each time correcting the cavity length by translating the output coupler. The output of the dye laser once optimized consists of 60-80 fs pulses at an 82 MHz pulse repetition rate, centered about a central wavelength of 625 nm. A typical pulse spectrum is shown in figure 2.6. The pulse duration out of the dye laser is measured with a real-time autocorrelator using an interferometric design with the moving arm mirror mounted on a car stereo speaker driven by an inexpensive laboratory function generator.

A pump power of 1.0 - 1.5 W of green is satisfactory for producing the shortest pulses. For pump powers in this range, the concentration of the SA dye is adjusted until the the dye laser output is about 50 mW, corresponding to a per pulse energy of 0.5 nJ. Amplification is necessary to produce pulses with sufficient energy to generate an optical continuum and to perform most of the experiments described here.

2.4 Ultrafast amplification using a Nd:YAG regenerative amplifier

Typically a CPM laser is amplified by a flashlamp pumped Nd:YAG laser at a rate of 10-50 Hz [18]. Our synchronously amplified system uses a

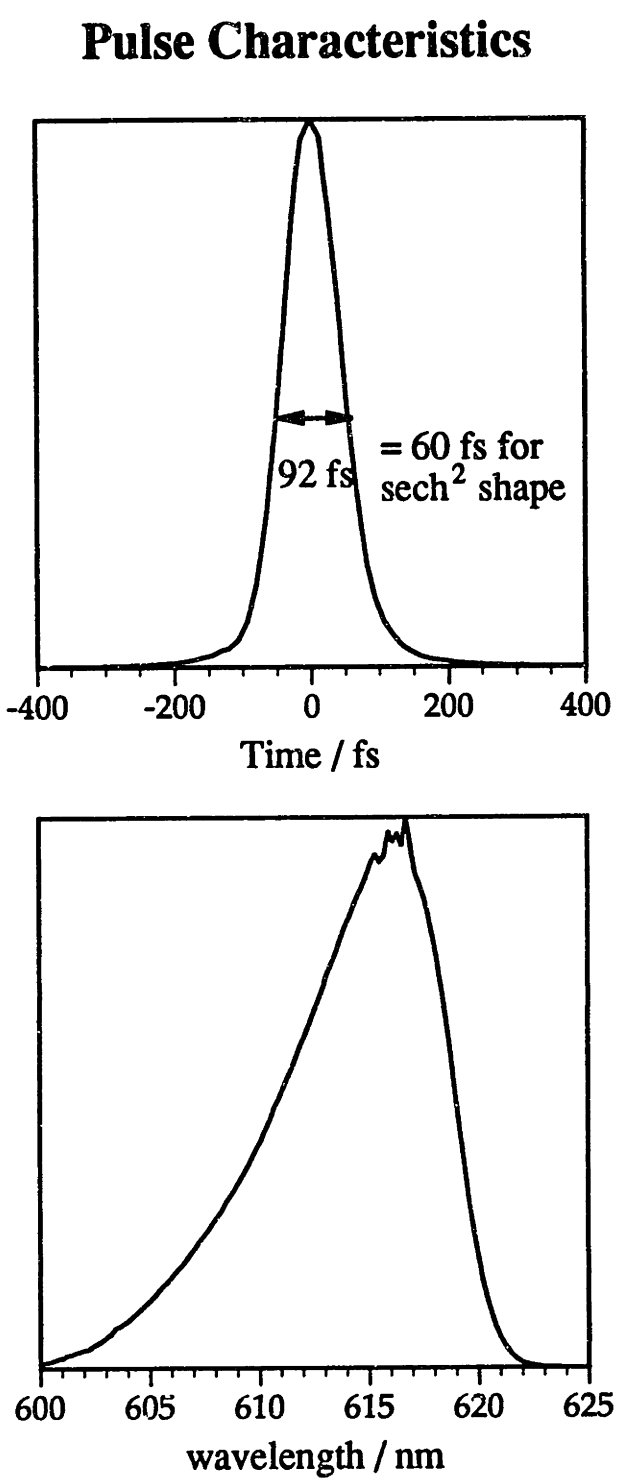

Figure 2.6 Autocorrelation showing pulse duration after amplification (top) and pulse spectrum (bottom).

second Nd:YAG laser operating as a regenerative amplifier at a PRR of 1-5 Khz. In order to achieve a similar PRR with a CPM system, one could use a copper vapor laser amplifier, but at considerably greater expense. Furthermore, the use of picosecond versus nanosecond pulses for amplification results in greater amplifier efficiency and better mode quality with a reduction in amplified spontaneous emission (ASE) [19].

The nanojoule energy pulses from the dye laser are amplified to energies of 10 microjoules in the three stage flowing dye cell amplifier shown in figure 2.1. The pump pulse for these amplifier stages is the doubled output of a second Nd:YAG laser configured as a regenerative amplifier (regen) [20,21]. Part of the RF which drives the A/O modulator in YAG 1 is sent into a custom-made circuit which produces a TTL output equal to the RF frequency divided by any integer N. This provides a master clock signal used to perform the important timing functions needed for synchronous amplification. Typically, N is chosen to yield a signal synchronous with a pulse in the modelocked Nd:YAG laser at a repetition rate of 1 kHz. This frequency determines the overall pulse repetition rate of the amplified output and is limited mostly by the speed with which the high voltage switching necessary for single pulse selection can be accomplished.

The TTL pulse triggers a high voltage driver to electrooptically switch a single pulse from part of the modelocked pulse train. This pulse is optically seeded into a second Q-switched Nd:YAG laser. The weak seed pulse completes 50 or so round trips inside the laser cavity to extract its stored gain, resulting in substantial amplification. The amplified seed pulse is cavity dumped to yield a 0.8 mJ pulse.

After frequency doubling in KTP, the resulting 400 microjoule pulse at 532 nm with a pulse duration of 80 ps is synchronous with a pulse from the dye laser. By fine-tuning an optical delay line, the two pulses copropagate through 3 flowing dye cells containing sulfarhodamine dye in methanol. The cells are pumped longitudinally with the pump and seed pulses made as collinear as possible. Two saturable absorber jets positioned between the dye cells use the saturable absorber dye malachite green to absorb the background of unamplified pulses. These jets also serve to reduce the ASE from the amplifier dye cells. Following amplification, a dispersive delay line is used to adjust the phases of the amplified pulses so that, after propagating through all remaining optical components, the shortest possible pulses arrive at the sample. The dispersive delay line consists of two 800 line / mm gratings (a pair of flint glass prisms [22] was also used successfully). The optimal spacing between the gratings (or prisms) is set by successively increasing or decreasing this distance while monitoring the pulse duration by autocorrelation in a thin crystal of KDP at the sample position where experiments are carried out.

Synchronous amplification has several advantages [19]. The use of a shorter pump pulse reduces the amount of ASE and results in higher efficiency. The fluorescence lifetime of most laser dyes is several hundred picoseconds. A pump pulse significantly longer than the dye lifetime results effectively in continuous pumping. Only a portion of a long pump pulse which arrives a few 100 ps before the seed pulse from the dye laser contributes to amplification. For a nanosecond pump pulse the efficiency is typically 1%. Pumping with nanosecond pulses increases the total amount of ASE. The careful synchronization between pump and seed pulse necessary for amplification with picosecond pulses is inherently achieved

with the optically seeded regenerative amplifier described here. Each stage of the amplifier is saturated enough to reduce output instability but not enough to cause saturation broadening of the femtosecond pulse. The amplitude stability of our amplified pulses is typically better than 5% peak to peak. A spectrum of the amplified pulse and a typical autocorrelation by noncollinear second harmonic generation in a 500 micron thick crystal of KTP are shown in figure 2.6.

2.5 Experimental setup

Figure 2.7 shows the optics used to form the three beams used to perform the transient grating experiment and the optical delays used to adjust the timing of the pulses. The configuration at the sample is shown in more detail in figure 2.8. Typically, a liquid contained in a quartz cuvette is placed at the intersection of three beams formed by splitting the beam after the amplifier. Two pulses, designated the excitation pulses, are overlapped in space and time within the sample to spatially modulate the sample's dielectric constant. The spatial modulation period is given by the wave vector difference between the crossed excitation pulses. The third or "probe" pulse is made incident on the sample at the Bragg diffraction angle. The polarizations of the incident pulses are set using half wave plates (if necessary to rotate the plane of polarization) and polarizers. A fourth polarizer is positioned in the diffracted signal beam behind the sample. Four polarizations are settable and can be used to discriminate between some of the different processes which give rise to a diffracted signal (see section 3.4).

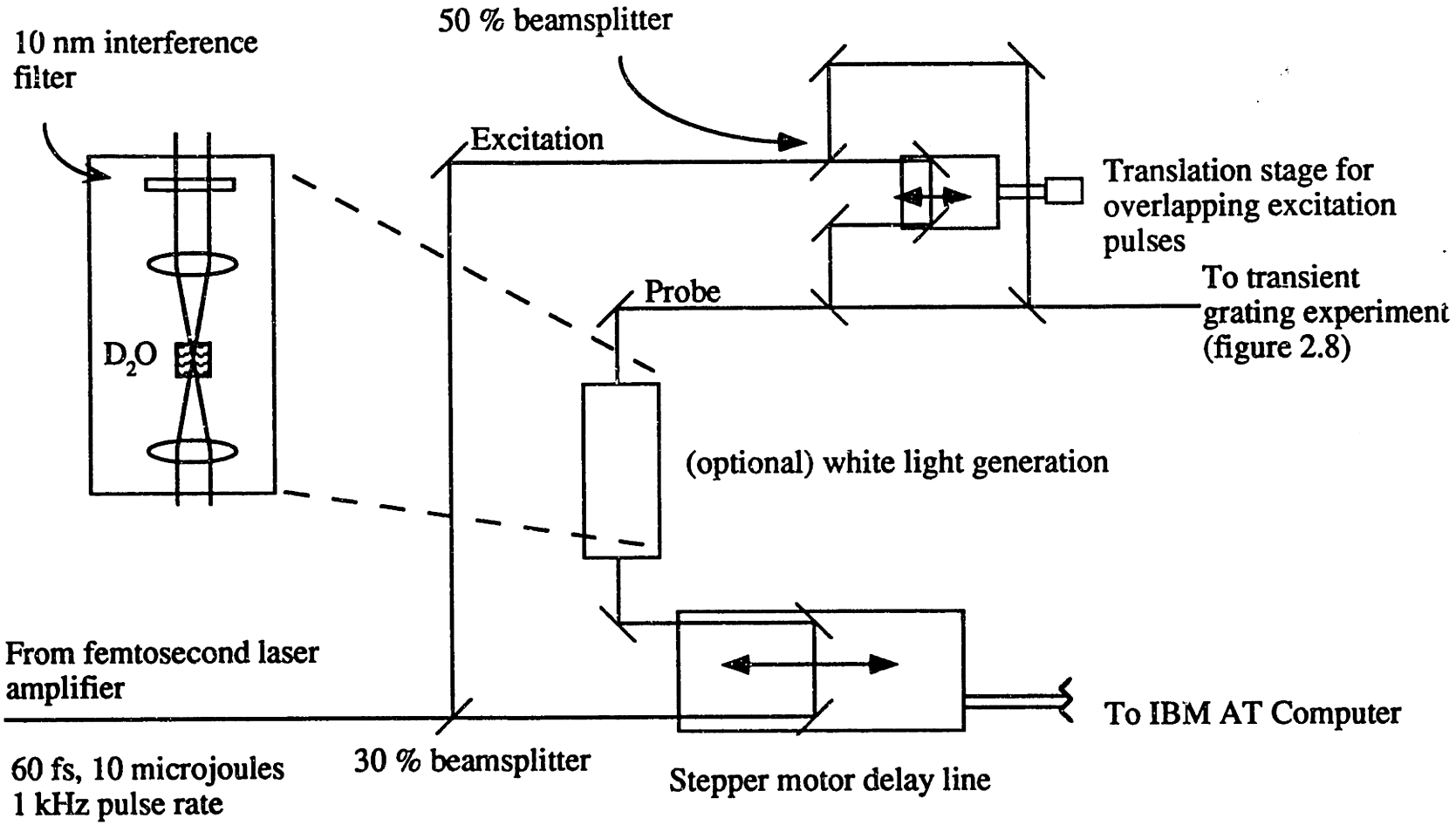

Figure 2.7 Transient grating experiment layout, showing the computer-controlled delay line for the probe pulse and the optics for temporally overlapping the excitation pulses. At upper left are the optics for selecting a 10 nm wide portion of the continuum light generated by focussing into a 1 cm long cell containing deuterated water.

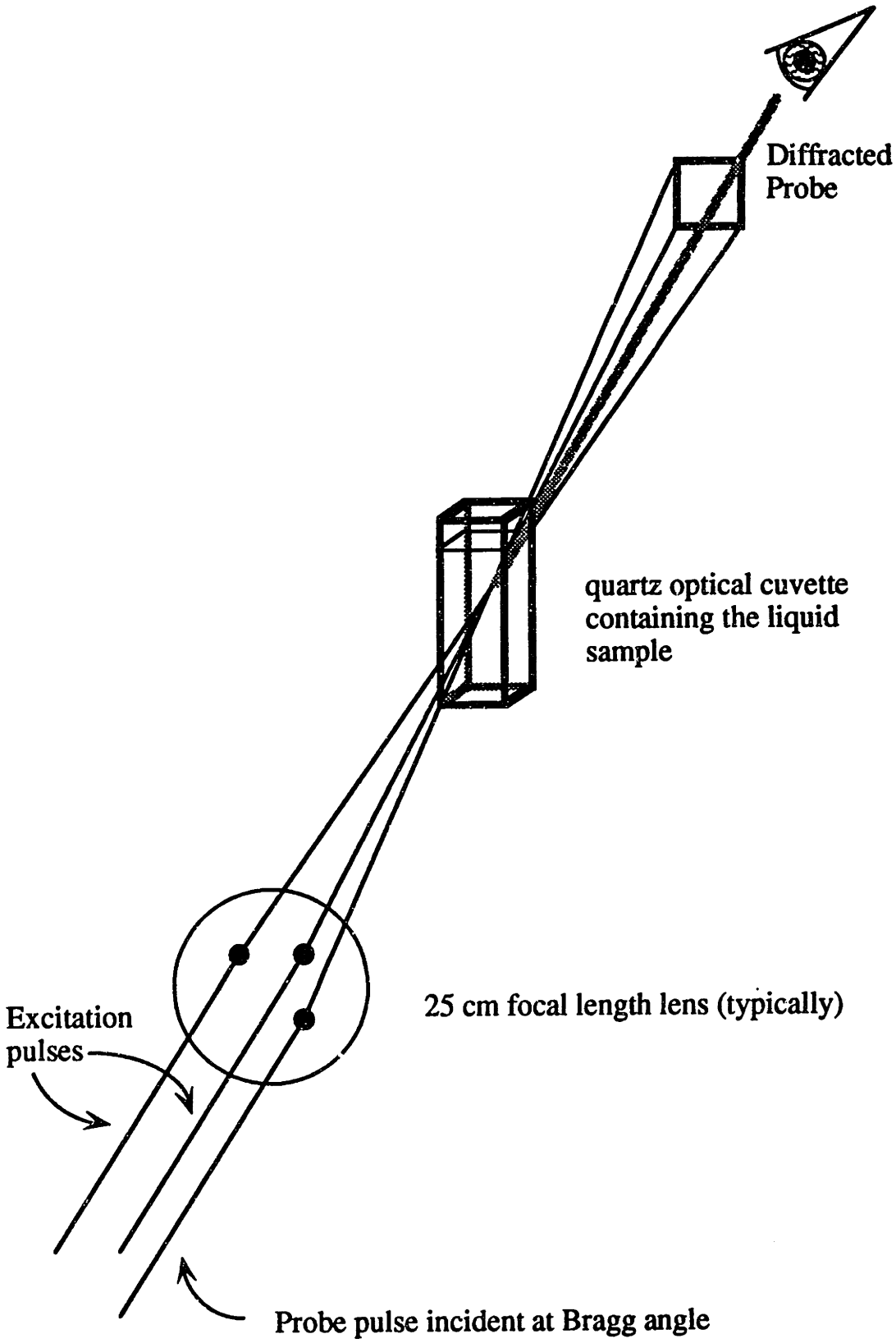

Figure 2.8 Closeup of transient grating experiment. The diffracted probe beam is shown by the thick gray line leaving the sample.

The peaks and nulls of the spatially modulated excitation form a transient grating which coherently diffracts the probe pulse. After the excitation pulses have left the liquid, the grating will relax over time and the diffracted signal will return to zero. The return to equilibrium of the transient excitation is monitored by measuring the intensity of the diffracted probe or "signal" beam as function of the time delay between the excitation pulses and the probe pulse. The time resolution of these experiments is limited not by the speed of the photodetector (limited to about 1 ps using a streak camera, and, in our setup, to about 2 ns using a photodiode) but by the pulse duration and spatial resolution of the stepping motor used to produce the probe pulse delay. Exactly how the diffraction efficiency of the probe pulse as a function of the delay time can be related to microscopic dynamical processes in liquids is the subject of chapter 3.

Occasionally it was desirable to obtain a probe pulse with a different color than the excitation pulses. This permits better rejection of scattered light from the excitation pulses through spectral filtering at the photodetector. A second-color probe pulse was produced by continuum ("white-light") generation by focussing an amplified pulse of high peak power into a 2 mm path length cell of D_2O [23]. This is illustrated in the upper left corner of figure 2.7. An interference filter with a bandwidth of 10 nm selects a particular region of the white-light spectrum. A two stage dye amplifier pumped by some of the green light from the regenerative amplifier was occasionally used to further amplify the white light pulse. Cross correlation with the pulses in the red proved that the white-light pulse was typically $\leq$ 100 fs in duration.

For the majority of experiments reported here the diffraction efficiencies are sufficient to yield a signal which is visible by eye. We use

an amplified photodiode (EG&G HUV 4000B) to measure the coherently diffracted probe signal intensity. The voltage from the photodiode is digitized by a 12-bit programmable gain A/D board (Data Translation DT2821) housed inside an IBM AT personal computer. The computer controls all aspects of the experiment including movement of the delay line stage, digitization of signal pulses, and pulse energy discrimination to improve the signal-to-noise ratio. All of the data acquisition software was designed and written by the author and is described in the next section.

2.6 Computer controlled data acquisition

The time of arrival of the probe pulse at the sample relative to the excitation pulses is controlled with an optical delay line as shown in figure 2.7. The position of a retroreflector mounted atop a translation stage (Klinger Scientific, Inc. model no. UT 100 CC) can be set in 1 micron steps with an integral stepper motor drive. In a double-passed delay line geometry, one micron of motion corresponds to a delay of 6.67 fs. This resolution is entirely adequate for our shortest pulse durations of 55 fs. The position of the delay line is programmed by the personal computer via an IEEE-488 interface in the stepper motor controller (Klinger Scientific Model CC-1).

After setting the delay position, the computer digitizes and stores a prescribed number of signal laser pulses with a 12-bit A/D board (Data Translation Model No. DT2821). This A/D board has a throughput rate of 50 kHz, making shot-by-shot data collection possible at our pulse repetition rate. A few percent of one of the excitation beams is picked off before the

sample with a glass microscope slide, and its intensity is measured by a second photodiode. The voltage output of this photodiode is also digitized by the computer and is used to provide a measure of the pulse energy incident on the sample. Since the intensity of every laser pulse is recorded, pulse energy discrimination is used to improve the signal-to-noise ratio. If the pulse energy is within a prescribed window of intensities, then the measured signal pulse is kept for further signal averaging; otherwise the signal pulse voltage is discarded. This discrimination or "windowing" technique reduces noise by suppressing laser intensity fluctuations at the expense of a lower effective pulse repetition rate.

An important design characteristic of data acquisition for any experiment is to achieve accurate measurements in a reasonable amount of time. We seek to optimize the signal-to-noise ratio per unit time of data collection. Windowing helps to achieve this goal. Since the ISS signal is quadratic in the excitation pulse intensity, signal fluctuations are reduced. This compensates for the smaller number of signal pulses which can be averaged per unit time due to discrimination, resulting in a better signal-to-noise ratio per unit time of data acquisition for windowing versus no windowing.

In practice, this scheme is even better than outlined, due to deviations of the laser pulse energies from a normal distribution. When the laser system is running very well, a normal distribution of pulse energies is observed. But when the dye laser periodically destabilizes for short time intervals or when the timing in the amplifier is not optimal, laser "dropouts" occur, resulting in a long tail in the pulse energy distribution to the low energy side. Incomplete modelocking in the dye laser is a frequent cause of dropouts. When this happens the pulse duration can fluctuate,

leading to large fluctuations in the intensity of the amplified pulses. Discrimination eliminates the noise introduced by averaging such pulses, since they fall outside the window and are rejected.

To avoid the additional coding complexity of real-time data acquisition, the data input is buffered. At each delay line position a specified number of laser pulses are collected into a buffer. Next, the buffer is scanned and diffracted probe pulses which fall within the discrimination window are averaged and stored. In this way, laser pulses incident during buffer servicing are lost. But for a PRR of 1 kHz the time between pulses is 1 ms, and since the time to service a buffer is on the order of a few milliseconds over 95+% of the incident laser pulses are digitized, justifying the simpler, buffered approach.

Scans are recorded by averaging several hundred good pulses at each delay line position. By repeatedly scanning the delay line, scans may be averaged together. Typically 100-5000 pulses were averaged at each point on the delay line (i.e. at each probe delay setting) to obtain the scans in this thesis. More averaging was required for liquids with weak signals or where substantial parasitically scattered light was present. The actual amount of averaging is a function, too, of the width of the discrimination window used. For the recording of very fast transients, steps of 1-2 microns were taken. Longer scans made to measure slower signals typically used a stepsize of 4-40 microns.

Chapter 3

Theory of Femtosecond Impulsive Stimulated Light Scattering From Molecular Liquids

3.1 Introduction

The experiments described in this thesis use femtosecond duration optical pulses to excite and probe elementary dynamical processes in nonassociated molecular liquids. The technique for observing these fast motions is impulsive stimulated light scattering (ISS), an entirely time-domain experimental technique used extensively by the Nelson research group. ISS results quite generally whenever sufficiently short optical pulses interact with matter. The name impulsive stimulated scattering emphasizes similarities with frequency-domain light scattering (described in section 3.5) and underlines the impulsive character of the optical excitation process. In this chapter, the discussion of ISS is limited to the study of dynamical processes in liquids. The ISS technique has been applied successfully in recent years in the Nelson research group to a wide range of topics, including phonon dynamics in molecular crystals [24], nonlinear optical properties of glasses [25], and, using picosecond pulses, to the viscoelastic behavior of glass-forming liquids [26].

Most ISS experiments described here were performed using a transient grating geometry, to be discussed in section 3.2. This is formally a four-wave mixing experiment and can be described using the methods of

nonlinear optics [27]. Indeed, the ISS experiment measures the time-dependent third-order nonlinear optical susceptibility of the material under study. This susceptibility gives the response (i.e. describes the polarization) of the material to excitation with ultrashort optical pulses. A convenient description of the ISS signal in terms of response functions is given in section 3.3. As a result of the Born-Oppenheimer approximation, contributions to the sample's response function can be divided into electronic and molecular processes. The different time-dependence of these two classes of effects is discussed in section 3.4. Ultimately, the molecular processes are the focus of this work since they contain information about the dynamics of molecular motion. Of course, frequency-domain light scattering is also sensitive to molecular motions and the connection between ISS and conventional light scattering is made in section 3.5. Section 3.6 discusses a microscopic theory of light scattering from neat molecular liquids in terms of time correlation functions. The goal of this section is to understand the different signal contributions to the ISS signal in terms of elementary molecular motions. Section 3.7 discusses interaction-induced light scattering from molecular liquids, and section 3.8 completes this chapter with a summary of the different contributions to the ISS signal.

3.2 The ISS transient grating experiment

Four-wave mixing (FWM) is a general description of the interaction of three optical fields inside a medium to produce a fourth [28]. In this thesis most of the experiments were carried out via degenerate FWM in the

transient grating geometry illustrated in figure 3.1. In the transient grating description of FWM, the excitation and probing processes are most readily described separately, as is done in the next section. Femtosecond transient optical Kerr effect (OKE) experiments have also been performed by this group and by others [29-32]. In this experiment a single excitation pulse induces a transient birefringence which can rotate the plane of polarization of a second, variably-delayed probe pulse as shown in figure 3.2. Formally, an OKE experiment can be described as a transient grating experiment in which the angle between the two excitation beams is reduced to zero.

The transient grating experiment is a useful technique for investigating material excitations in real time in condensed phase systems which interact with optical radiation [33]. The experiment was outlined briefly in section 2.5. In femtosecond ISS experiments, ultrashort optical pulses set up a transient holographic diffraction grating (simply called transient grating) in samples with light scattering active material modes. Two excitation pulses are crossed at a small angle of typically 5 degrees within the sample to set up a standing-wave excitation. The electric fields of the pulses set up an interference pattern or grating which periodically modulates the refractive index of the sample. Microscopically, modulation results from dynamical motions of intra- and intermolecular modes coherently excited through the interaction of the short pulses with molecular polarizabilities. This will be discussed in more detail in later sections of this chapter.

The manner in which these modes relax to their equilibrium or thermal values is monitored by measuring the time-dependent diffraction efficiency of a probe pulse scattered off the transient grating. Later

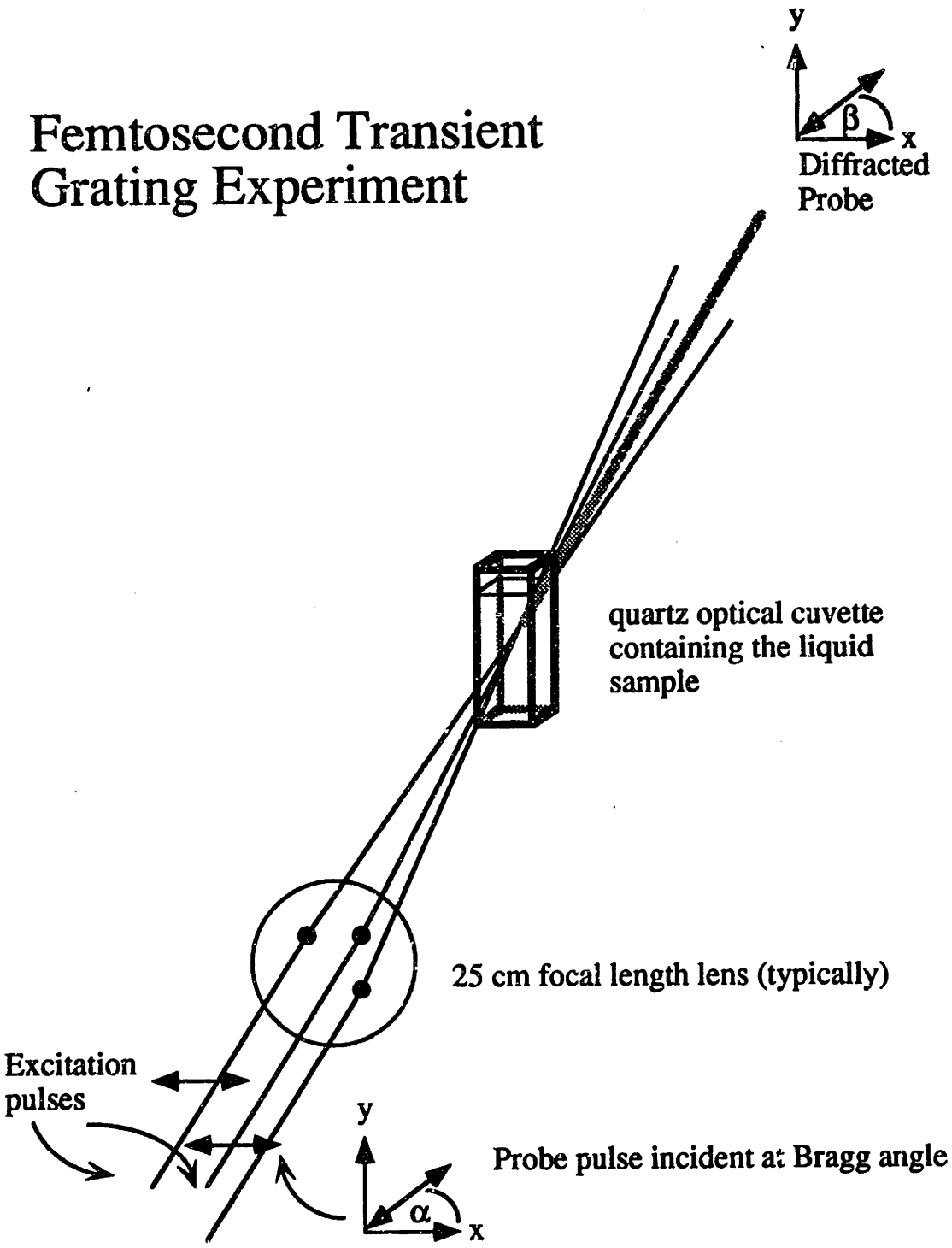

Figure 3.1 Transient grating experiment showing the polarizations of the linearly polarized pulses. Four polarizations are settable, corresponding to the input polarizations of the two excitation pulses, the probe pulses, and the detected polarization component of the diffracted probe pulse. The VHVH scattering experiment, for example, refers to vertically and horizontally polarized excitation pulses, vertically polarized probe pulse and a horizontally detected signal pulse.

Transient Optical Kerr Effect Experiment

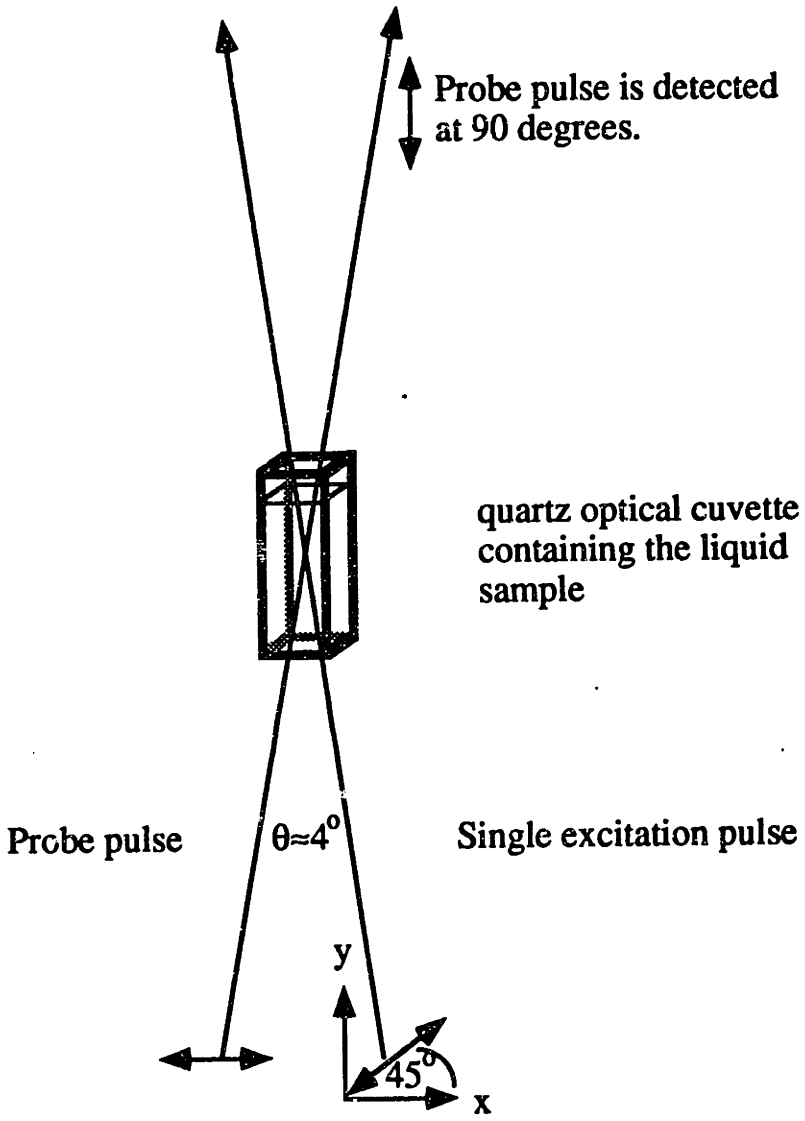

Figure 3.2 Femtosecond optical Kerr effect (OKE) experimental geometry. A probe pulse linearly polarized at 45 degrees to a linearly polarized excitation pulse is detected through a crossed polarizer. The transient birefringence induced by the excitation pulse rotates the plane of polarization of the probe pulse.

references in this thesis to "the signal beam" or to "the ISS signal" should be understood to refer to the probe light diffracted from the transient grating. Since the signal beam is spatially separated from the excitation and probe beams, the TG signal is a background-free, highly sensitive technique.

The transient grating technique was used by Nelson *et al.* with picosecond pulses to excite acoustic waves in materials [34]. In ISS the material modes are efficiently excited provided the pulse duration of the excitation pulses is short compared to the fundamental vibrational period of the mode [35-37]. Recast in the frequency domain, the pulse must have sufficient transform-limited bandwidth to excite a given mode through mixing of the Fourier components of the spectrally broad pulse.

The additional spectral bandwidth of 60 femtosecond pulses permits the efficient excitation of material modes out to several hundred wavenumbers. This makes the ISS technique complementary to frequency-domain light scattering for the study of microscopic dynamical motions in liquids.

3.2.1 Comparison with CARS

It is worth pointing out the differences between ISS and time-resolved coherent anti-Stokes Raman scattering (CARS) [38]. Both techniques probe material excitations by coherent scattering of a time-delayed probe pulse. But in CARS the vibrational frequency of the mode under study is determined by the difference between the two excitation laser frequencies. In ISS the different frequency components within a single spectrally broad pulse excite the mode under study. Additionally, since the probe pulse is

shorter than the oscillation period of the excited mode, it is possible to time resolve single vibrational cycles (see, for example, the ISS data in chapter 4). CARS is better suited for the study of high-frequency modes whose oscillation frequency cannot be resolved. ISS is better suited for studying intermolecular modes in liquids. Such modes are characterized by lifetimes given approximately by the inverse collision frequency of the liquid, and can often be more readily measured directly in the time-domain. Recently, time-resolved stimulated Raman scattering experiments performed with a 100 fs excitation pulse and 6 ps probe pulse from a dye laser were used to excite terahertz quantum beats between vibrational modes near 1000 cm^{-1} which are separated by less than 300 cm^{-1} by Leonhardt *et al.* [39].

3.3 Response function theory of ISS

Yan and Nelson have published a physically intuitive treatment of the ISS experiment [35,36]. The goal of their description is to derive an expression for the time-dependence of the intensity of a probe pulse coherently scattered from fluctuations in the sample's dielectric tensor which are driven by the excitation pulses. For excitation wavelengths far from any optical absorptions of the sample, the light-matter coupling can be expressed by the Hamiltonian,

$$\begin{aligned} H_2(t) &= -\frac{1}{8\pi}\int d^3r \sum_{ij} \delta\varepsilon_{ij}(r) E_i(r,t) E_j(r,t) \\ &= -\int d^3r \sum_{ij} \delta\varepsilon_{ij}(r) F_{ij}(t) \end{aligned} \tag{3.1}$$

where $\delta\varepsilon$ is the dielectric operator and **F** represents the force due to the excitation pulses on the material. Physically, the excitation pulses drive material modes which change the material dielectric constant.

Using linear response theory the time-dependence of the dielectric tensor can be written,

$$\varepsilon_{ij}(t) = \int_{-\infty}^{+\infty} dt' \sum_{kl} G^{\varepsilon\varepsilon}_{ijkl}(t-t') E_k(t') E_l(t') \tag{3.2}$$

where $G^{\varepsilon\varepsilon}$ is the impulse response function (Green's function) for the dielectric tensor. Causality requires that $G^{\varepsilon\varepsilon}(t\text{-}t') = 0$ for $t < t'$. In the limit of ultrashort pulses we can write the 'forcing function' as,

$$F_{kl}(t) = A_{kl}\delta(t) \tag{3.3}$$

where A_{kl} are constants related to pulse intensities, and we have neglected the optical-frequency components of **F**(t) which are of too high frequency to drive a significant material response. The dielectric response is then given simply by,

$$\varepsilon_{ij}(t) = \sum_{kl} A_{kl} G^{\varepsilon\varepsilon}_{ijkl}(t) \tag{3.4}$$

Thus, the dielectric tensor of the material changes according to the transient response of the excited material modes. These fast changes are time-resolved by detecting the intensity of a diffracted probe pulse.

3.3.1 ISS probing process

Let a third, ultrashort probe pulse with electric field, E^{probe}, be incident on the transient grating induced by the excitation pulses. In the presence of the driven fluctuations in the dielectric constant, this pulse will induce a nonlinear polarization, **P**, given by,

$$P_i(k,t) = \frac{1}{4\pi}\int \sum_j \frac{d^3k'}{(2\pi)^3} \epsilon_{ij}(k-k',t) E_j^{probe}(k',t). \qquad (3.5)$$

This polarization will give rise to a scattered field, E^s, which is the solution to the wave equation,

$$\sum_j (-k^2\delta_{ij} + k_i k_j - \frac{\varepsilon_{ij}^0}{c^2}\frac{\partial^2}{\partial t^2}) E_j^s(k,t) = \frac{4\pi}{c^2}\frac{\partial^2}{\partial t^2} P_i(k,t) \qquad (3.6)$$

where c is the speed of light and ε^0 is the unperturbed dielectric tensor.

If we approximate the time-dependence of an ultrashort, well-collimated probe pulse by a delta-function, then the scattered field is approximately proportional to the induced polarization,

$$\mathbf{E}^s(k,t) \propto \mathbf{P}(k,t) \qquad (3.7)$$

Inserting equations 3.4 and 3.5 into equation 3.7 we obtain an expression for the time-dependence of the diffracted probe pulse intensity,

$$I_i^{ISS}(t) \propto \left| \sum_{jkl} A_{kl} G_{ijkl}^{\varepsilon\varepsilon}(t) E^{probe} \right|^2 \tag{3.8}$$

In writing equation 3.8, factors relating to absolute intensities such as spot sizes, pulse durations, local field corrections, etc. have been neglected. This is justified since we are interested only in the time-dependence of the material excitations which cause coherent scattering of the probe pulse. As discussed in section 2.5, the polarizations of the excitation pulses, the probe pulse and the diffracted probe pulse are all set by polarizers. In this case, it is often possible to measure a single component of the tensor $G^{\varepsilon\varepsilon}$. More generally, if we understand $G^{\varepsilon\varepsilon}$ to represent the projection of the tensor relevant to a particular experimental geometry, then the time-dependence of the ISS experiment can be written,

$$I^{ISS}(t) \propto \left| G^{\varepsilon\varepsilon}(t) \right|^2. \tag{3.9}$$

This equation is the basic result of the theory of impulsive stimulated scattering. It states that the intensity of an ultrashort probe pulse diffracted from a transient grating induced in a sample will change with probe delay time according to the impulse response function of the underlying material modes.

Finally, for the investigation of very rapid material modes, it is sometimes necessary to account for the finite durations of excitation and probe pulses. The theory of how to incorporate finite pulse durations has been discussed extensively by Yan and Nelson [35]. These effects are given approximately by the expression,

$$I^{ISS}(t) = \int_{-\infty}^{+\infty} d\tau I^{probe}(t-\tau)\left[\int_{-\infty}^{\tau} dt' G^{ee}(\tau - t') I^{exc}(t')\right]^2 \qquad (3.10)$$

where I^{probe} and I^{exc} are the time-dependent intensity profiles of the probe and excitation pulses, respectively. This equation will be used in later chapters to simulate ISS data from liquids given an appropriate model for the response function.

3.4 Polarization selectivity

So far nothing has been said about the particular modes or physical processes which contribute to the response function, $G^{\varepsilon\varepsilon}(t)$. In this section we will see that processes divide into two classes according to the different time scales of electronic motion and the motions of the nuclei which constitute the molecules of the liquid under study. The impulse response function, $G^{\varepsilon\varepsilon}$, introduced above gives the response of the sample's dielectric tensor to a nonlinear optical field. $G^{\varepsilon\varepsilon}(t)$ is precisely the same quantity as the time-dependent nonlinear optical susceptibility, $\chi^{(3)}(t)$, familiar from the field of nonlinear optics. For many nonlinear optical effects, the assumption is often made that the characteristic response time of the susceptibility components is much faster than the rate of change of the field amplitudes of the optical pulses [40]. In this limit $\chi^{(3)}(t)$ can be written as a constant. With femtosecond pulses, however, the time-dependence of the fields is faster than part of the nonlinear polarization and it is necessary to include the full time-dependence of $\chi^{(3)}(t)$.

Hellwarth has presented a detailed theory of nonlinear optical susceptibilities for materials in the optically transparent regime [41]. In general, the susceptibility responsible for the nonlinear polarization in the material can be written as the sum of two terms,

$$\chi^{(3)} = \chi^{(3)}_{nuc} + \chi^{(3)}_{el}. \qquad (3.11)$$

The distortion of the electronic distribution around a fixed nuclear configuration gives rise to $\chi^{(3)}_{el}$, the "electronic only" contribution. The second term on the right hand side of equation 3.11, $\chi^{(3)}_{nuc}$, arises from electronic distortions which result from motion of the nuclei of molecules. In the ISS experiment these motions, electronic and nuclear, are coherently induced by the excitation pulses. For optical frequencies far from electronic absorptions the time of the electronic response is the electronic dephasing time and is given approximately by the inverse frequency of the UV absorption edge of the material. This corresponds to a process lasting approximately 10^{-15} seconds. For pulses of 60 fs duration this feature is effectively instantaneous.

The nuclear response, $\chi^{(3)}_{nuc}$, has the time dependence of molecular rotations, vibrations and translations and consequently extends over a range of time scales. It was recognized by several researchers that measurements of the time-dependence of this nuclear contribution could provide information about the influence of molecular interactions on rotations and vibrations in condensed phases [29,42].

$\chi^{(3)}$ (or, equivalently, $G^{\varepsilon\varepsilon}$) is a fourth-rank tensor relating the nonlinear optical response of the material to three electric fields, each of which is a vector quantity. Specific symmetries of the electronic processes

and nuclear processes of the material under study limit the number of independent components. Here our subject is liquids, and the isotropic symmetry of simple molecular liquids greatly reduces the number of independent tensor elements. Only 2 of the 81 total nuclear susceptibility tensor elements are independent, while only one component is independent for the electronic susceptibility tensor [41]. As a result of Kleinman symmetry, the nonlinear optical susceptibility tensor elements for nonresonant electronic processes satisfy the relation,

$$\chi^{(3)}_{1212} = \chi^{(3)}_{1221} = \chi^{(3)}_{1122} = \frac{1}{3}\chi^{(3)}_{1111} \tag{3.12}$$

while nuclear processes obey the relation,

$$\chi^{(3)}_{1212} = \chi^{(3)}_{1221} = -\frac{3}{2}\chi^{(3)}_{1122} = \frac{3}{4}\chi^{(3)}_{1111}. \tag{3.13}$$

Etchepare *et al.* have pointed out that the different underlying symmetries of the electronic and nuclear processes can be used to selectively measure only electronic processes, or only processes of molecular origin [43,44]. Four polarizations can be specified in the ISS experiment: The polarizations of the two excitation pulses, the probe pulse and the diffracted probe or signal pulse. In general, the signal will be given by a linear combination of various tensor elements of $\chi^{(3)}$ ($=G^{\varepsilon\varepsilon}$) for both electronic and molecular processes. We consider the case in which all beams are linearly polarized. If the two excitation pulses are polarized along the x direction of figure 3.1, and the probe beam makes an angle α to the x direction, and if the signal is detected along a direction which

makes an angle β with respect to x, then the resultant polarization induced in the sample is,

$$P = \sum_i (\chi^{(3)}_{1111,i} \cos\alpha\cos\beta + \chi^{(3)}_{2211,i} \sin\alpha\sin\beta) E^{exc} E^{exc} E^{probe} \qquad (3.14)$$

where index i sums over the different physical processes (nuclear and electronic) which can occur, and the exc and probe superscripts label the fields of the excitation and probe pulses, respectively. In practice, it is useful to select a polarization combination which completely eliminates the contribution of the electronic or nuclear processes. Two such combinations are listed in table 3.1. Note that the polarization of each linearly polarized pulse is specified by an angle made with respect to the positive x-direction of figure 3.1.

Table 3.1 Pulse polarizations in the transient grating experiment which permit discrimination between electronic and nuclear signal contributions. The leftmost column lists the process which is cancelled for the polarizations on the right (from reference 43).

	Polarizer angle relative to x-direction of figure 3.1			
Process	Excitation 1	Excitation 2	Probe	Diffracted Signal
Electronic	90	90	45	108
Nuclear	90	90	45	63

There are several advantages to using polarization selectivity. By eliminating the contribution of electronic processes, it is possible to study

unobscured the very short-time behavior of the molecular signal. Examples of this will be given in chapter 5. Measurement of the electronic-only signal precisely determines the zero delay time between the excitation and probe pulses, due to the instantaneous nature of this signal contribution on the time scale of these experiments. By inserting a delta function for the electronic response in equation 3.10, it is clear that the electronic-only ISS signal is a cross-correlation of the excitation and probe pulses, which can provide an accurate characterization of pulse shapes and durations. Many of the experiments described in this thesis were carried out with the above polarizations. In later chapters, I refer to the ISS signal recorded with polarizations set to the values of the first line of table 3.1 as the "nuclear" or "molecular-only" ISS signal to emphasize that this part of the signal contains dynamical information about the motions of molecules.

3.5 Comparison of ISS with spontaneous light scattering

Since the nonlinear optical response of a material contains a part which is modified by the motions of nuclei, it is not surprising that it can be related to the polarizability fluctuations measured by conventional frequency-domain light scattering (LS). A detailed, theoretical treatment of the comparison of ISS with spontaneous light scattering (LS) has been given by Yan and Nelson [36]. Hellwarth has shown how light scattering cross sections can be related to the third-order susceptibilities describing the nonlinear interaction of light with isotropic matter [41]. The argument in this section is similar, but we emphasize the dynamical information obtained from the two techniques. Chapter 4 illustrates these similarities

with data recorded from several molecular liquids using both Raman light scattering and femtosecond ISS.

In conventional light scattering, fluctuations of microscopic variables, due to molecular vibration and reorientation modify the collective polarizability of the sample and scatter light [1]. Because these motions are constantly excited by thermal energies this type of scattering is called spontaneous light scattering. The ISS signal, on the other hand, results from time-dependent nuclear (and electronic) motions which are coherently driven by ultrashort laser pulses. Ignoring certain factors relating to the geometry of the LS experiment, the intensity of the light scattered at frequency ω is conveniently expressed as the Fourier transform of a time correlation function of the liquids dielectric constant,

$$I(\omega) = \int_{-\infty}^{+\infty} e^{i\omega t} C^{\varepsilon\varepsilon}(t) dt \qquad (3.15)$$

where the correlation function of the liquids dielectric constant is given by,

$$C^{\varepsilon\varepsilon}(t) = \langle \delta\varepsilon(0)\delta\varepsilon(t) \rangle. \qquad (3.16)$$

The dielectric constant, a macroscopic quantity, is related to microscopic variables through molecular polarizabilities. This connection will be discussed further in the next section.

The fluctuation-dissipation theorem provides a link between the light scattering spectrum and the response function, $G^{\varepsilon\varepsilon}$,

$$I(\omega) = \frac{\hbar}{\pi}\left(\frac{1}{1-e^{-\hbar\omega/k_B T}}\right)\mathrm{Im}[G^{\alpha\alpha}(\omega)]$$
$$= \frac{\hbar}{\pi}\left(\frac{1}{1-e^{-\hbar\omega/k_B T}}\right)\int_0^{+\infty} G^{\alpha\alpha}(t)\sin(\omega t)dt \qquad (3.17)$$

where $G^{\varepsilon\varepsilon}(\omega)$ and $G^{\varepsilon\varepsilon}(t)$ are a Fourier transform pair.

Conversely, we may start with the light scattering intensity $I(\omega)$ and obtain the response function measured in the ISS experiment through the relation,

$$G^{\alpha\alpha}(t) = \int_0^{\infty}(1-e^{-\hbar\omega/k_B T})I(\omega)\sin(\omega t)dt. \qquad (3.18)$$

Finally, a useful relation exists between the response function, $G^{\varepsilon\varepsilon}$, and the correlation function, $C^{\varepsilon\varepsilon}(t)$,

$$G^{\alpha\alpha}(t) = -\frac{1}{kT}\frac{dC^{\alpha\alpha}(t)}{dt} \qquad (3.19)$$

Thus, the impulse response function of the ISS experiment measures the derivative of a correlation function of the dielectric tensor. Conversely, light scattering measures the Fourier transform of an integral of $G^{\varepsilon\varepsilon}(t)$. ISS is particularly sensitive to subtle changes of slope of the correlation function because of this relationship. Using equation 3.19, the extensive amount of work aimed at elucidating the microscopic contributions to $C^{\varepsilon\varepsilon}(t)$ can be used to interpret our experimental results. This is the subject of section 3.6.

Equations 3.17-3.19 show the equivalent information content of frequency-domain spontaneous light scattering and the ISS experiment.

There are situations where one technique is more advantageous than the other. High frequency molecular vibrations (e.g. > 1000 cm-1) are best characterized by LS since unrealistically high time resolution would be required to resolve the short vibrational periods. Detailed comparison of simulated ISS and LS data has shown the usefulness of the ISS technique for characterizing overdamped or weakly oscillatory modes [36]. In later chapters, data will be shown which illustrate the advantages of ISS for characterizing inhomogeneously broadened intermolecular vibrational modes. It will be seen that such modes play an important role in the reorientation of anisotropic molecules in dense liquids.

Whether we choose to study the behavior of the dielectric tensor of a liquid by observing the thermally induced fluctuations in the frequency domain, or by coherently driving changes using ISS, a way is needed to relate the changes in this quantity to microscopic variables in order to learn about liquid dynamics. The microscopic contributions to $C^{\varepsilon\varepsilon}(t)$ (or, equivalently, $G^{\varepsilon\varepsilon}(t)$) are discussed in the next section.

3.6 Microscopic theory of light scattering from neat liquids

The dynamical motions of molecules in liquids which contribute to light scattering through the correlation function $C^{\varepsilon\varepsilon}(t)$, or to impulsive stimulated scattering through the response function, $G^{\varepsilon\varepsilon}(t)$, are discussed here. In this section we focus on the time correlation function $C^{\varepsilon\varepsilon}(t)$. Of course, by using equation 3.19, the response function which gives the time dependence of the ISS signal intensity (equation 3.10) is easily determined.

Many treatments relating light scattering to molecular dynamics are available [1,45-47]. Fluctuating molecular polarizabilities modulate the dielectric constant of the liquid. Neglecting local field corrections, we write

$$C^{\alpha\alpha}(t) \approx \frac{1}{N} C^{\Pi}(t) = \langle \Pi(0)\Pi(t) \rangle \tag{3.20}$$

where $C^{\Pi}(t)$ is the time correlation function of the collective polarizability, Π, of the N molecules in the scattering volume. The collective polarizability can be written formally as the sum of two terms,

$$\Pi = \Pi^0 + \Pi^{I-I}. \tag{3.21}$$

Π^0 is the sum of single-molecule polarizabilities,

$$\Pi^0 = \sum_{i=1}^{N} \alpha_i \tag{3.22}$$

and Π^{I-I} is a term which accounts for polarizability contributions arising from interactions between molecules. This term embodies collective interactions which perturb the polarizability of the ensemble. This is called the interaction-induced (I-I) polarizability† and will be discussed in more detail in the next section.

For the remainder of this section we will neglect the interaction-induced polarizability contributions and discuss only the microscopic

† This polarizability is also called "collision-induced", but we prefer the term interaction-induced for induced polarizabilities in molecular liquids because it is more suggestive of the many-body nature of liquid state interactions.

contributions to the first term of equation 3.21. In the next section we will return to the I-I contributions. For liquids composed of anisotropic molecules the single-molecule polarizability, α, is a tensor quantity and can be expressed as the sum of an isotropic and an anisotropic part. Likewise, the polarizability correlation function can be written as the sum of isotropic and anisotropic parts,

$$C^{\Pi}(t) = C_0(t) + C_2(t) \tag{3.23}$$

where $C_0(t)$ and $C_2(t)$ are the correlation functions for the isotropic and anisotropic parts, respectively. Both $C_0(t)$ and $C_2(t)$ contribute to polarized light scattering (VV polarizations), while only $C_2(t)$ is measured by depolarized light scattering (VH polarizations).

Next, we determine the time dependence of the single-molecule polarizability, α, due to molecular motions. We can expand the polarizability of each molecule in a Taylor series in powers of the coordinates of the molecular vibrational modes. In this case, the jk-th element of the polarizability tensor of a particular molecule can be written,

$$\alpha_{jk}(t) = \alpha^0_{jk}(t) + \sum_{\nu} \alpha^{\nu}_{jk}(t) q^{\nu}(t) \tag{3.24}$$

where ν indexes the vibrational normal modes and q^{ν} is the vibrational coordinate of the νth mode. The time-dependence of the expansion coefficients in equation 3.24 arise from the reorientation of anisotropic molecules upon transforming from a molecular frame to a laboratory coordinate system. The first term of equation 3.24 gives rise to Rayleigh light scattering. It gives the polarizability of a molecule with the nuclei

held in fixed positions ($q^{\nu} = 0$) and is modulated by reorientation and translation. The second term is responsible for the narrow peaks due to intramolecular vibrational modes measured in Raman light scattering. We can write the contributions to the isotropic and anisotropic parts of $C^{\Pi}(t)$ as,

$$C_{\ell}(t) = C_{\ell}^{RAY}(t) + C_{\ell}^{RAM}(t) \qquad \ell = 0,2. \tag{3.25}$$

This equation expresses the different contributions of the two terms of equation 3.24.

We give here expressions for $C_{\ell}^{RAY}(t)$ and for $C_{\ell}^{RAM}(t)$ for liquids composed of symmetric top molecules. These will be used later to interpret ISS data from several molecular liquids including carbon disulfide and benzene. Assuming vibrations on different molecules are independent, and neglecting coupling between vibrations and rotations of the same molecule, the Raman correlation functions can be written,

$$\begin{aligned} C_0^{RAM}(t) &\propto \sum_{i=1}^{N} \langle q_i^{\nu}(0) q_i^{\nu}(t) \rangle = N \langle q^{\nu}(0) q^{\nu}(t) \rangle \\ C_2^{RAM}(t) &\propto \sum_{i=1}^{N} \langle q_i^{\nu}(0) q_i^{\nu}(t) \rangle \langle P_2[\mathbf{u}_i(0) \cdot \mathbf{u}_i(t)] \rangle \\ &= N \langle q^{\nu}(0) q^{\nu}(t) \rangle \langle P_2[\mathbf{u}(0) \cdot \mathbf{u}(t)] \rangle \end{aligned} \tag{3.26}$$

where ν labels intramolecular vibrational modes and $P_2[x]$ is the second Legendre polynomial, $P_2[x] = 1/2(3x^2 - 1)$. Within the context of the above approximations, the Raman correlation functions measure dynamical properties of single molecules.

Again neglecting interaction-induced effects, the Rayleigh terms, $C_\ell^{RAY}(t)$, are modified solely by molecular reorientation. Since reorientation cannot alter the isotropic component (tensor trace) of the polarizability, $C_0^{RAY}=0$. The anisotropic correlation function is,

$$C_2^{RAY}(t) = \sum_{i,j}^{N} \left\langle P_2[\mathbf{u}_i(0)\cdot\mathbf{u}_j(t)] \right\rangle. \tag{3.27}$$

This can be written further as the sum of two terms,

$$C_2^{RAY}(t) = \sum_{i}^{N} \left\langle P_2[\mathbf{u}_i(0)\cdot\mathbf{u}_i(t)] \right\rangle + \sum_{i,j\neq i}^{N} \left\langle P_2[\mathbf{u}_i(0)\cdot\mathbf{u}_j(t)] \right\rangle. \tag{3.28}$$

The first term, as in Raman scattering, arises from reorientational motions of single molecules, and is sometimes referred to as the distinct term. The second, or pair term, arises from orientational correlations of pairs of molecules. This dependence on dynamical properties of pairs of molecules is why Rayleigh scattering is sometimes referred to as coherent, while Raman scattering is termed incoherent.

In summary, Raman scattering is sensitive to vibrational dephasing and reorientation of single molecules, while Rayleigh scattering measures orientational correlations of single as well as pairs of molecules, neglecting all I-I polarizabilities. Raman and Rayleigh scattering are often treated separately in LS due to the generally higher frequencies of intramolecular vibrational modes compared to the frequencies of reorientational motions. Provided that the Raman and Rayleigh modes lie within the bandwidth of the ultrashort excitation pulses, however, intramolecular vibrations and reorientational motions will be simultaneously excited in the sample.

Examples of this appear in chapter 4. Other molecules such as CS_2 (chapters 5 and 6) and benzene (chapter 7) do not have low-lying intramolecular vibrational modes which contribute to the ISS signal. In this case, only $C_2^{RAY}(t)$ contributes to the scattering.

3.7 Interaction-induced light scattering from molecular liquids

At liquid densities the collective polarizability of N molecules is no longer the sum of the isolated or gas-phase molecular polarizabilities. Indeed, the per molecule light scattering intensity is observed to fall as molecules go from the gas to the liquid phase [48]. Interactions result in coupling between electronic states of different molecules which depend in a complicated way upon the orientations and positions of a number of molecules, leading to changes in band shape. A natural way of expressing the induced polarizability is to write an expansion in molecular configurations,

$$\Pi^{I-I} = \sum_{i,j} \alpha_{i,j} + \sum_{i,j,k} \alpha_{i,j,k} + \cdots \qquad (3.29)$$

where the terms on the right explicitly express the dependence of the collective polarizability on interactions of pairs, triplets, etc. of molecules. We call these higher-order terms interaction-induced (I-I) polarizabilities since they depend on interactions between molecules. Usually, the interaction-induced polarizability is assumed to be pairwise additive, and the irreducible terms on the right hand side of equation 3.29 are assumed to be negligible.

There are two principal mechanisms behind these interaction-induced polarizabilities. Distortion of the electronic distribution of a pair of molecules can occur as the result of a collision. This binary collision theory is useful for the description of the depolarized light scattered from dense gases. The more important mechanism for molecular liquids is the dipole-induced-dipole (DID) mechanism. In simple terms, the dipole induced in a molecule depends not only on the external field incident on the sample, but also on the electric field due to the dipoles induced on neighboring molecules. On average a molecule is surrounded by a spherically symmetrical shell of neighbors, so that the sum of the reradiated fields from dipoles induced by the incident light will cancel. Instantaneously, though, the molecules are not arranged symmetrically and anisotropic fluctuations will scatter light [49]. Since small orientational and/or translational motions are involved in these symmetry-breaking fluctuations, the I-I polarizabilities are expected to change on a much faster timescale (several hundred femtoseconds) than the single molecule polarizabilities.

The dynamics of these interactions are complex and still poorly understood in the case of molecular liquids. An excellent compendium of the extensive literature of interaction-induced light scattering has recently been published [50]. Part of the dynamics of interaction-induced polarizabilities will arise from translational motions as in the case of liquid rare gases. The additional rotational degrees of freedom of molecular liquids result in a dependence of the I-I scattering on rotational motions as well. Because of the fast decay of the I-I polarizability correlation function, these induced effects contribute mostly to the high frequency region of the Rayleigh light scattering spectrum. Consequently, they are

often of low amplitude and are frequently difficult to measure due to overlap with allowed Raman bands. There is also no satisfactory way to separate the interaction-induced spectrum from the allowed Rayleigh spectrum. The fast motions responsible for I-I scattering, however, will contribute to the short time part of the material's nonlinear susceptibility and are more readily measured in the ISS experiment [51]. Of course, in liquids of anisotropic molecules, there will still be a short-time signal contribution due to single molecule reorientation and orientational pair correlations.

3.8 Summary of signal contributions to the ISS signal

We summarize here the different contributions to the ISS signal arising from molecular dynamics in liquids. The response function, $G^{\varepsilon\varepsilon}(t)$, is given by the derivative of the time correlation function, $C^{\Pi}(t)$, of equation 3.20. The collective polarizability, Π, is written as a sum of allowed (single molecule) and induced (arising from interactions of pairs, triplets, etc. of molecules) contributions, as shown in equation 3.21. The correlation function of the collective polarizability can then be written as,

$$C^{\Pi}(t) = \langle \Pi(0)\Pi(t) \rangle = C^{0}(t) + C^{CR}(t) + C^{I-I}(t) \qquad (3.30)$$

where $C^{0}(t)$ is due to the allowed contributions of section 3.6, $C^{I-I}(t)$ is due to interaction-induced polarizabilities discussed in section 3.7, and $C^{CR}(t)$ gives the cross-correlation between these two contributions. We can

further write the allowed portion as a sum of Rayleigh and Raman processes,

$$C^{0}(t) = C^{RAY}(t) + C^{RAM}(t) \tag{3.31}$$

as described in section 3.6. Inserting equations 3.30 and 3.31 into equation 3.19, we write the response function symbolically as,

$$G(t) = \frac{d}{dt}\left\{C^{RAY}(t) + C^{RAM}(t) + C^{CR}(t) + C^{I-I}(t)\right\}. \tag{3.32}$$

Finally, according to equation 3.10, the ISS transient grating experiment measures the square of the response function, leading to additional cross terms. While the analysis of ISS data in light of equation 3.32 appears daunting at first, we will see in the chapters to come that, for many liquids of interest, reasonable assumptions about the various terms in equation 3.32 allow us to extract new information about molecular dynamics in liquids on the subpicosecond time scale.

Chapter 4

ISS Excitation of Coherent Intramolecular Vibrations

4.1 Introduction and experimental

This section presents ISS data from several molecular liquids which have vibrational modes of sufficiently low frequency that they can be efficiently excited by 60 femtosecond pulses. Thus, it is necessary to include the effects of intramolecular vibrations on the collective polarizability of the sample as discussed in the previous chapter. If the motion of vibrational coordinate, q, can be approximated as harmonic, then the relevant response function can be written as,

$$G^{\alpha}(t) \propto e^{-\gamma t} \sin \omega t \qquad (4.1)$$

where ω is the mode frequency, and γ describes the damping rate due to dissipative interactions with neighboring molecules. If a single, damped vibrational mode is excited and probed, then equation 3.9 shows that the ISS signal will oscillate at twice the vibrational frequency and decay at twice the vibrational dephasing rate. The data described next are the first to resolve individual cycles of coherently excited intramolecular vibrational modes. This ability to initiate phase-coherent microscopic

motion opens up prospects for carrying out time-resolved measurements on vibrationally distorted molecules [2,29].

Each liquid sample was placed in a quartz cuvette with a 1-2 mm optical path length. The 60 fs, amplified pulses with a central wavelength of 615 nm were crossed inside the sample in the transient grating geometry of figure 3.1. The intensity of the diffracted probe pulse was measured by an amplified photodiode as a function of delay time as described in section 2.5. The polarizations of the pulses appear in each figure.

4.2 Liquid Dibromomethane

Figure 4.1 shows ISS scattering data from liquid dibromomethane recorded with all-vertical polarizations, and the weaker depolarized scattering. The pronounced peak at zero time arises from the electronic polarizability discussed in section 3.4. This instantaneous feature is followed by distinct oscillations. The period of oscillation is 190 fs, which matches the 5.2 THz frequency (=173 cm^{-1}) of the Br-C-Br halogen bending mode of CH_2Br_2 [52]. This demonstrates that coherent vibrational motion is induced through impulsive stimulated scattering and monitored in the time domain. The approximately Lorentzian lineshape observed in the Raman spectrum of dibromomethane corresponds to an exponentially decaying oscillatory signal in the time domain. This is a general feature of ISS excitation of vibrational modes which will be seen in the examples below, and again in the results on liquid carbon disulfide in chapters 5 and 6. Vibrational dephasing of this mode can be accurately characterized by measuring the decay of the signal oscillations.

Liquid Dibromomethane

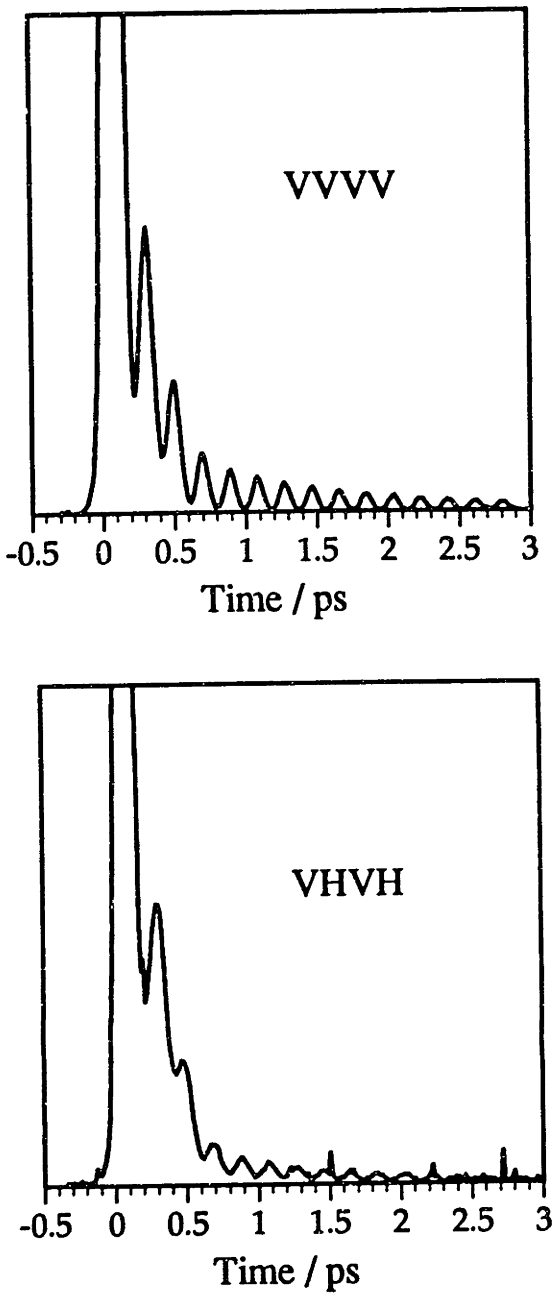

Figure 4.1 Impulsive stimulated scattering signal from liquid dibromomethane. The upper figure shows the polarized scattering. The lower figure shows the weaker, depolarized scattering. In both cases the oscillations in the signal correspond to coherent vibrational oscillations of the 173 cm-1 halogen bending mode. The first picosecond of data after zero time show very clearly the contribution of coherent Rayleigh scattering contributions.

Finally, the data show additional features beside the high-frequency oscillations. As discussed in section 3.6, orientational motions and intermolecular motions induced by the excitation pulses (i.e. the Rayleigh response) will also contribute to the signal. The correlation of these reorientational motions often decays exponentially, giving rise to the exponentially decaying baseline under the first few oscillations at short probe delay times. In VVVV ISS, for example, molecules in some orientations (relative to V) contribute more to the coherent scattering than ones with other orientations. The reorientational motions of these molecules will therefore reduce the coherent scattering intensity arising from vibrational motion.

4.3 Tetrahalide liquids

In figures 4.2 - 4.5 ISS data are shown for several tetrahalide liquids. These liquids possess two and in some cases three intramolecular vibrational modes which are of low enough frequency to be efficiently driven. Table 4.1 summarizes the frequencies of these compounds recorded in dilute solution in cyclohexane. The frequencies for the neat liquids are nearly identical. The scattering signal shows complicated beating patterns, resulting from the simultaneous excitation of several vibrational modes of different frequency. The electronic response of these liquids was found to be considerably larger than the nuclear one, and the peak of this signal component at zero delay time appears off-scale in the figures. Careful intensity filtering of the excitation beams was necessary to avoid white light generation and other parasitic nonlinear effects. High

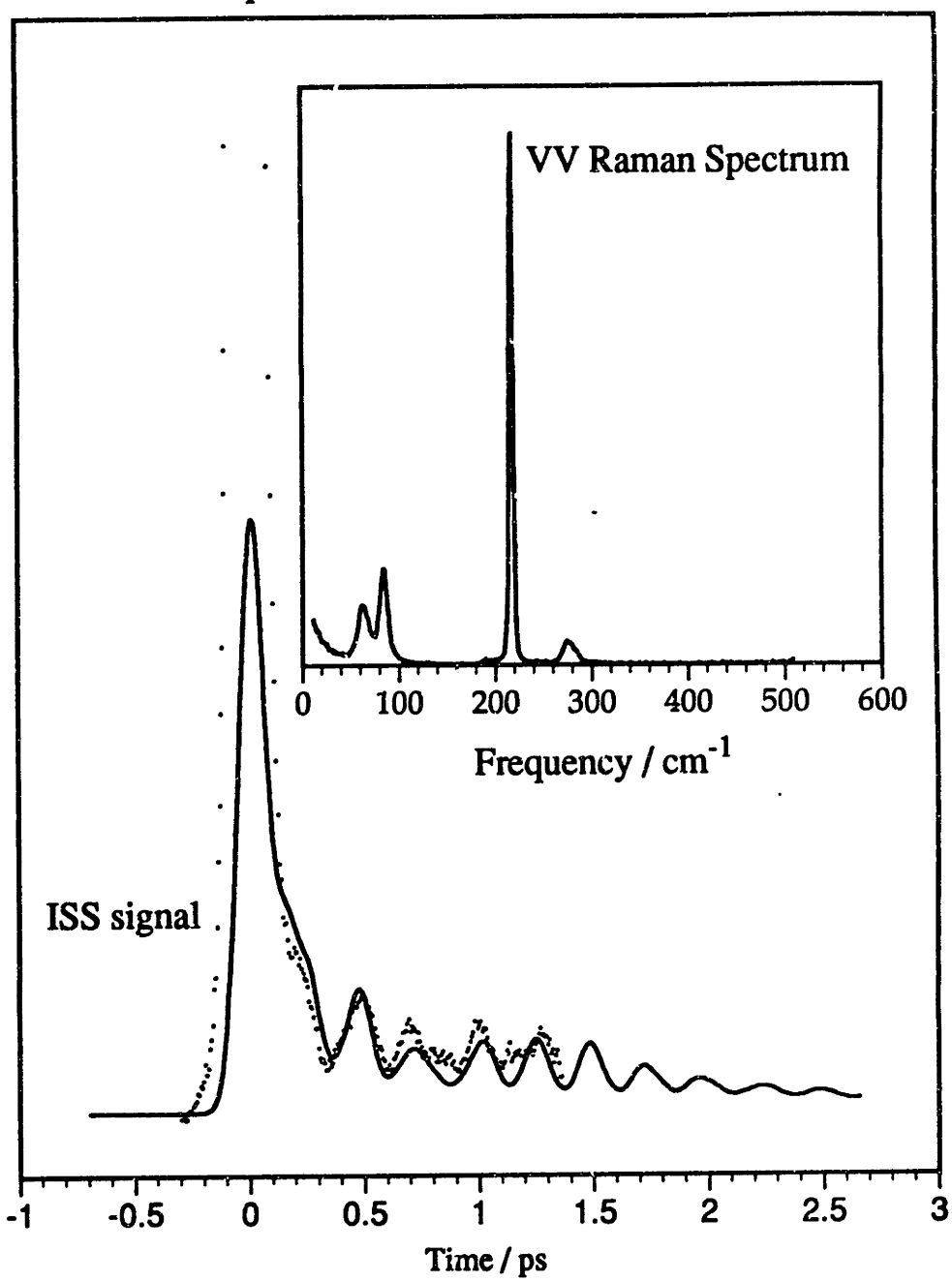

Figure 4.2 A comparison of frequency-domain light scattering with the ISS experiment. The figure inset shows the VV Raman spectrum of liquid tin tetrabromide recorded at 305 K. The main figure displays the VVVV ISS data (dots) recorded under the same conditions and the simulated ISS signal from the Raman spectrum (solid curve). Excitation and probe pulse durations of 110 fs were used in generating the ISS simulation from the Raman data.

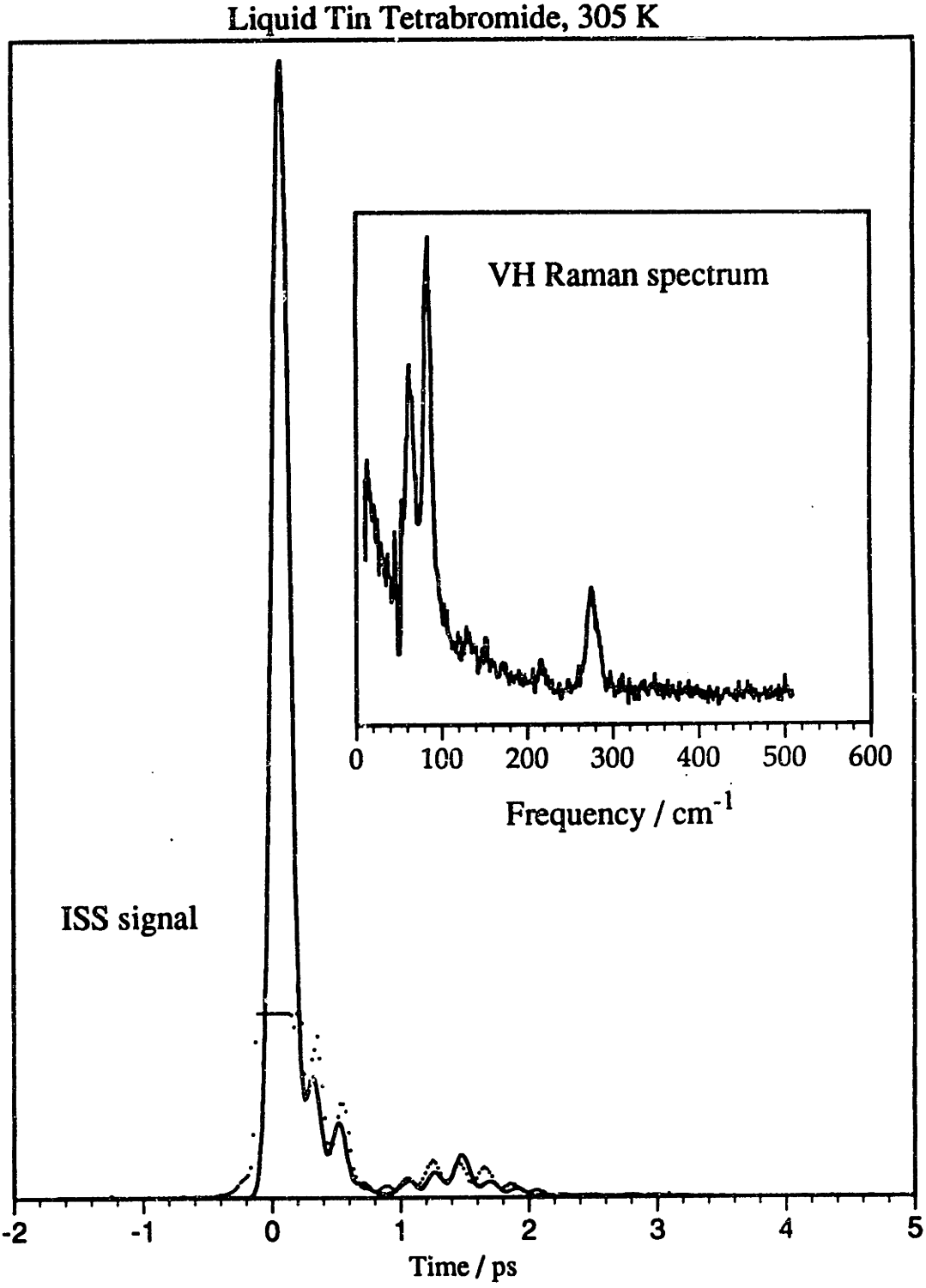

Figure 4.3 Comparison of VHVH ISS signal (dots) from liquid tin tetrabromide with ISS simulation from VH Raman spectrum (solid curve). Excitation and probe pulse durations used in equation 3.10 were 110 fs. The VH Raman spectrum is shown in the figure inset.

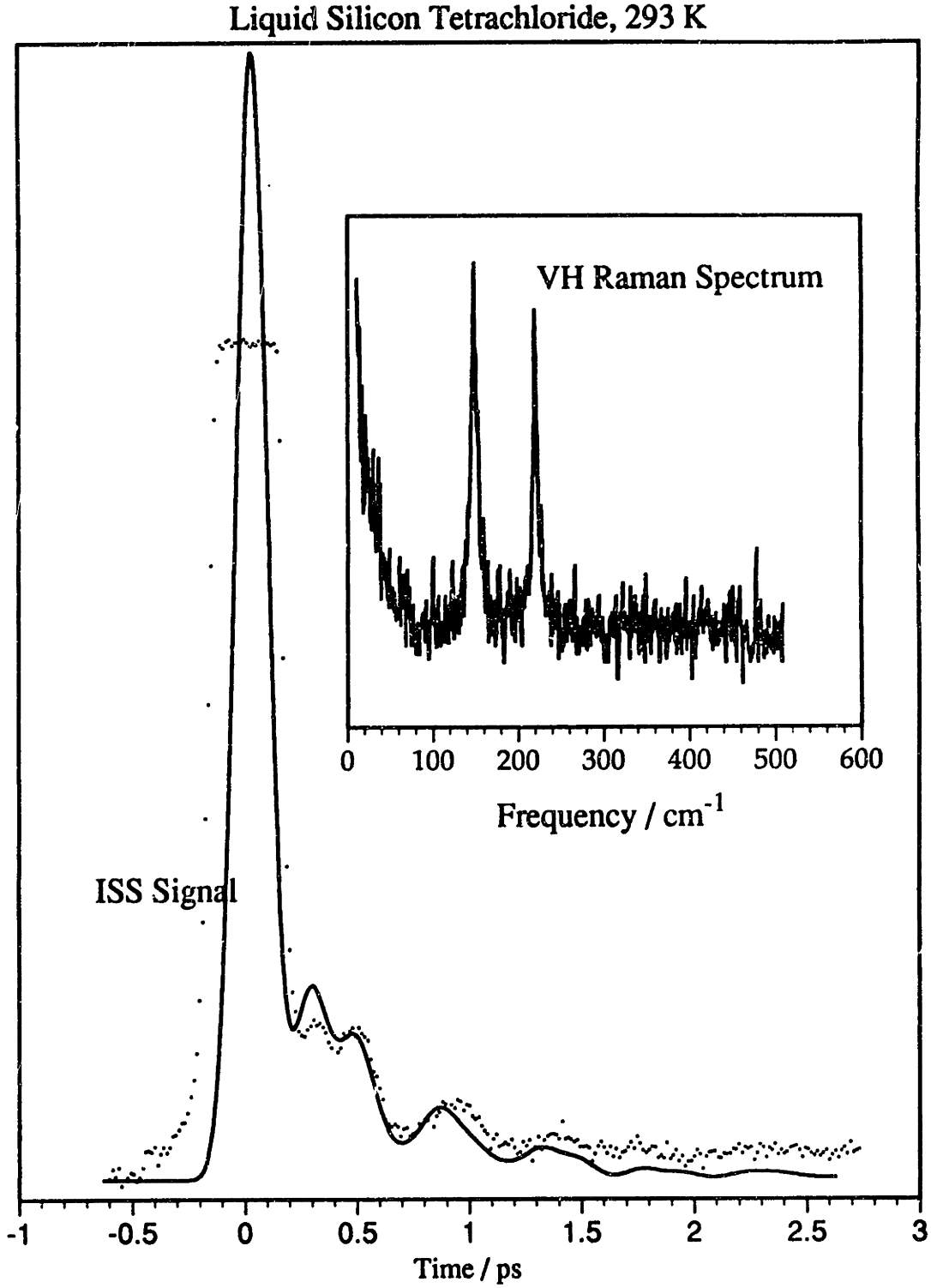

Figure 4.4 Comparison of VHVH ISS data (dots) with simulated ISS signal calculated from Raman spectrum of liquid silicon tetrachloride (solid curve). Excitation pulse duration was 100 fs. Amplified 580 nm probe pulse was 150 fs in duration.

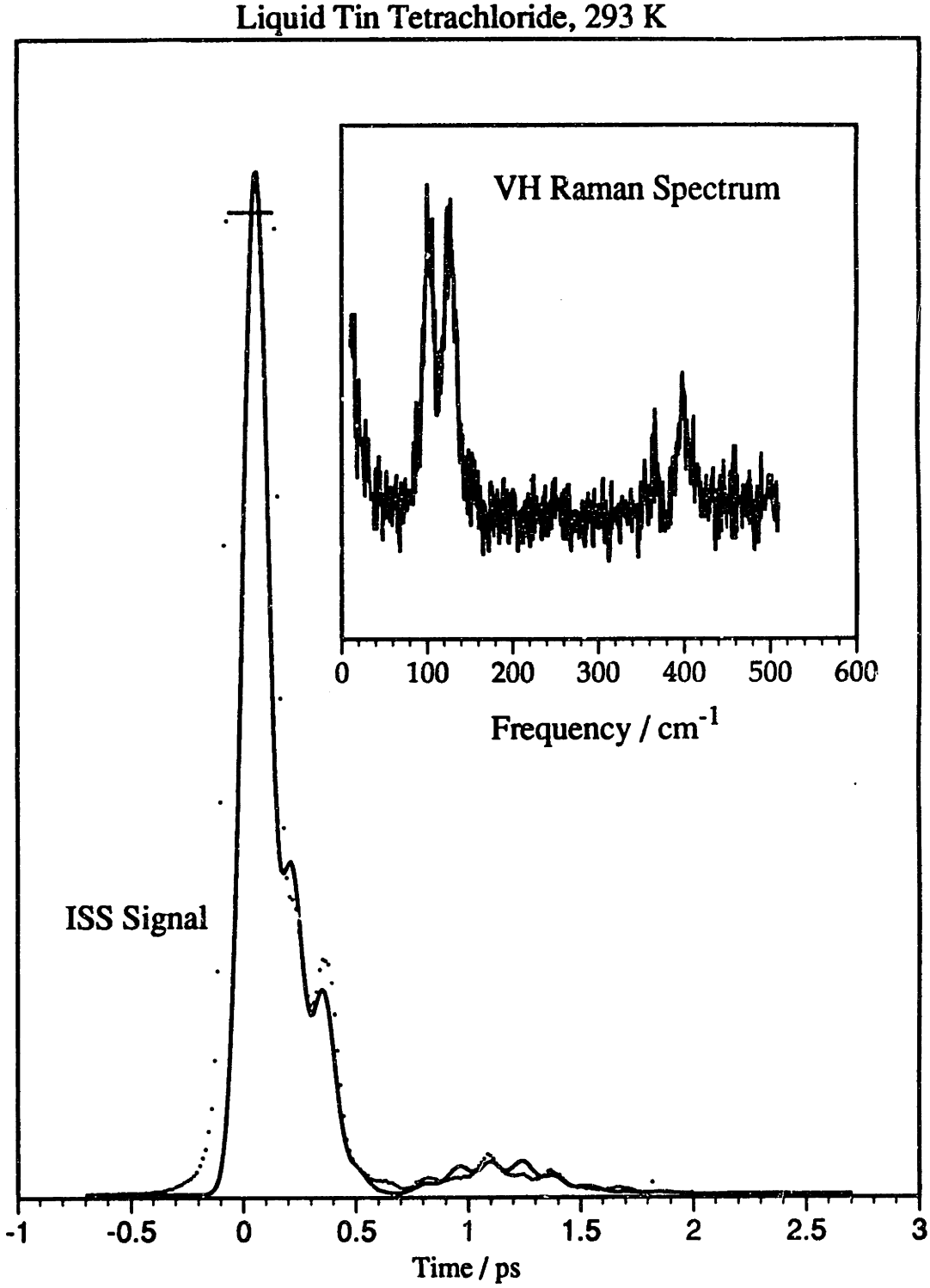

Figure 4.5 Comparison of VHVH ISS data (dots) with simulated ISS signal from VH Raman spectrum (solid curve) of liquid tin tetrachloride. Excitation and probe pulses were 100 fs in duration for the convolutions in equation 3.10.

sensitivity was necessary to observe the considerably weaker oscillations in the nuclear response. Some of the data shown in figure 4.2 - 4.5 were recorded with a continuum-generated probe pulse of 580 nm which was amplified to approximately 1 μJ in a two-stage dye amplifier. The use of a probe pulse of a different color allows spectral filtering at the photodetector which greatly improves the rejection of scattered excitation light.

Table 4.1 Fundamental frequencies (and symmetry group) of intramolecular vibrations of Group IV tetrahalides in cyclohexane solution [from ref. 53].

Compound	v1 (a1)	v2 (e)	v3 (t2)	v4 (t2)
CCl_4	459	219	763, 792	315
$SiCl_4$	424	151	610	222
$GeCl_4$	395	130	455	174
$SnCl_4$	368	106	402	130
CBr_4	268	124	671	185
$SiBr_4$	249	90	486	136
$GeBr_4$	235	79	330	112
$SnBr_4$	221	65	282	86

To illustrate the identical information content of spontaneous light scattering and ISS discussed in the previous chapter, Raman spectra were

recorded for each of these liquids and are shown as insets in figures 4.2 - 4.5. The spectra were measured with a standard Raman setup using 250 mW of the 514.5 nm line of an Argon ion laser and a half-meter monochromator. The spectral resolution was approximately 2 cm^{-1}. A photomultiplier with photon counting electronics recorded the light scattered at 90 degrees to the liquid contained in a 1 mm path length quartz cuvette. Raman lineshapes were measured from 10 cm^{-1} to 500 cm^{-1} at room temperature, except for the data from tin tetrabromide which were recorded at a temperature of 305 K.

For each liquid the Raman lineshape was transformed according to equation 3.18 to obtain the impulse response function, $G^{\epsilon\epsilon}(t)$. This response function was convoluted with pulse durations appropriate for the excitation and probe pulses using equation 3.10 to generate a simulated ISS signal. These simulations are shown as the solid curves in figures 4.2 - 4.5. In generating the ISS curves from the Raman data, no attempt was made to include the missing Rayleigh scattering below 10 cm^{-1}. To a first approximation, this signal contributes mostly to the ISS signal at long times. The omission of this feature together with the fact that the instrumental response of the monochromator was not removed account for the slight disagreement between the ISS and the Raman experimental data.

The excellent agreement shows that the information content of these two, very different experiments is identical. In practice, the frequency or the time domain offers specific advantages for different investigations as discussed in several places [36,37]. In particular, ISS is advantageous for the study of heavily damped vibrational modes. For the study of dynamical processes in liquids, the ISS technique has great promise for the study of the short-time aspects of reorientation and for the fast intermolecular

motions which give rise to interaction-induced scattering. Such fast motions are often difficult to measure with Rayleigh (or Raman) scattering due to the low signal amplitude at high frequency.

Finally, we note that the tetrahalide molecules discussed in this section have an isotropic polarizability on account of their tetrahedral symmetry. These molecules are a sort of molecular analog of the rare gas liquids. Consequently, depolarized Rayleigh scattering is symmetry-forbidden in these liquids and arises only from anisotropic interactions between molecules. In the depolarized Raman spectra shown in figures 4.3 - 4.5, this symmetry-forbidden wing is seen in the exponentially decaying lineshape below 100 cm^{-1}. In the spectrum of liquid tin tetrabromide (figure 4.3) a broad decay is seen out to 200 cm^{-1}. This is the reason the first few oscillations in the ISS data from this liquid do not go all the way to the zero intensity level. The dynamics of the intermolecular motions which give rise to interaction-induced scattering are of great interest in their own right. This topic is addressed further in chapters 5 and 6, where data from liquid carbon disulfide are presented. In the case of CS_2, the ISS signal is not complicated by the presence of intramolecular vibrations which are responsible for the distinctive oscillatory responses presented in this chapter.

Chapter 5

Femtosecond ISS from Liquid Carbon Disulfide: A Temperature-dependent Study†

5.1 Introduction

The highly polarizable nature and large optical nonlinearity of the carbon disulfide (CS_2) molecule make it a favorite of nonlinear laser spectroscopists. The strong femtosecond stimulated scattering signal led to a number of early time-domain studies [32,42]. We chose CS_2 as the initial liquid for studying short-time aspects of molecular reorientation. Liquid CS_2 is a good system for studying dynamics in anisotropic molecular liquids due to its linear symmetry and extended liquid range. Dynamical information has been obtained from a variety of techniques, including depolarized light scattering [54-59], NMR [60,61] and molecular dynamics simulation [62-70,84]. In this chapter and the following one, femtosecond impulsive stimulated scattering (ISS) experiments are described which measure the ultrafast nonlinear optical response of neat CS_2. Evidence is presented which demonstrates the nondiffusive character of the reorientation at short times. Furthermore, a temperature-dependent study of CS_2 is discussed in which weakly oscillatory signals are observed in the low-temperature liquid. These results indicate the importance of vibrational motions in dense liquids of anisotropic molecules, and they are

† Collaborators: Alan G. Joly and Sandy Ruhman.

discussed in terms of some "cage" models of molecular reorientation [7-12].

5.2 Room temperature ultrafast response of CS_2

Femtosecond transient grating experiments performed on spectroscopic grade carbon disulfide at ambient temperature and pressure are described in this section. The data were collected on the neat liquid contained in a 1 or 2 mm path length quartz cuvette. The experimental geometry and data collection method were described in detail in chapter 2. Most scans were performed with pulses taken directly from the amplified femtosecond laser, with a central wavelength of 615 nm. The pulse duration as determined by autocorrelation in a 500 micron thick single crystal of KDP was always found to be in the range 55-65 femtoseconds. The intensities of the probe and excitation pulses were carefully controlled with neutral density filters to avoid the generation of white light and thermal blooming in the liquid. In many cases signal was recorded at several different light intensities and comparison showed no significant intensity effects.

In CS_2, the lowest-lying allowed Raman-active mode, the ν_1 symmetric stretch, has a frequency of 655 cm^{-1} at 1 atm pressure and room temperature [58]. The $\nu 2$ mode (393 cm^{-1}) is lower in frequency, but contributes to Raman scattering solely through interaction-induced mechanisms. The 60 fs pulses used in these experiments are unable to efficiently excite such high frequency modes. Thus, in contrast to the ISS scans from molecular liquids presented in chapter 4, the intramolecular vibrations of carbon disulfide do not contribute to the ISS signal. This

separation of intramolecular from intermolecular frequencies is what makes CS_2 an excellent system for a time-domain study of molecular reorientation.

Figure 5.1 shows a typical ISS scan from liquid CS_2. The excitation pulses were polarized at 90° with respect to each other in VH fashion. The probe pulse was polarized vertically and the diffracted signal pulse was detected horizontally. We label this the VHVH scattering signal. Clearly visible in this scan are the different time signatures of the electronic and molecular signal contributions discussed in section 3.4. The signal arising from the electronic polarizability appears as a pulse duration limited spike at zero delay time. This feature is followed by a second, more intense peak near 180 fs separated by a dip in signal intensity. The second peak originates solely from the nuclear component of the nonlinear polarizability and, consequently, reflects dynamical motions of CS_2 molecules. This is one of the first measurements of the ultrafast nonlinear optical response of any material to resolve these two signal contributions. Greene and Farrow had observed the transient OKE signal from CS_2 [32], but their pulse duration (100 fs) was not short enough to resolve the subsequent rise in the nuclear signal. Kenney-Wallace et al. have also observed the noninstantaneous rise of the nuclear signal in CS_2 using 60 fs pulses in femtosecond optical Kerr effect (OKE) experiments [30].

In this chapter we will discuss the ISS signal in terms of reorientational motions, neglecting for the time being the motions induced in pairs and higher-order configurations of molecules. We will return to the issue of higher-order (interaction-induced) signal contributions in chapter 8. The nuclear motions which contribute to the signal are coherently driven by the

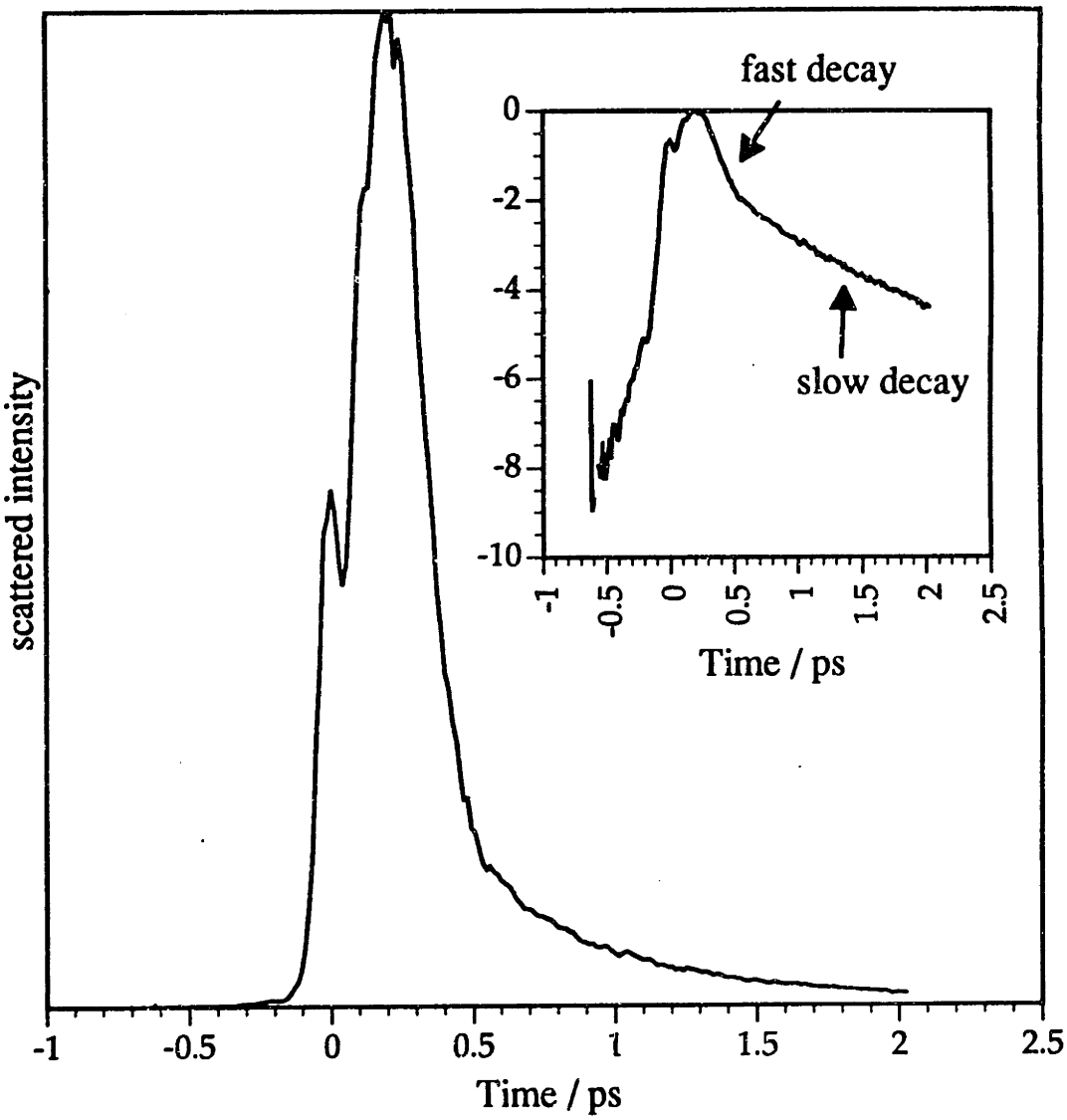

Figure 5.1 ISS signal from liquid carbon disulfide recorded at room temperature with VHVH polarizations. The electronic contribution to the response appears as the spike at zero time. The nuclear signal arising from molecular reorientation and higher-order motions continues to rise, reaching a maximum near 180 fs after the excitation pulses have left the sample. The log plot in the figure inset shows the different time signatures of the fast and the slow decays.

excitation pulses as discussed in chapter 3. The molecules experience impulsive torques through dipoles induced by the electric field of the ultrashort excitation pulses. These torques act to partially align molecules in the direction of the electric field polarization vector. The initial rise in signal from 75 to 180 fs is evidence, we believe, of the inertial character of the reorientational motion at short times. This represents the first time-domain evidence of nondiffusional aspects of reorientational motion.

Following the signal maximum near 180 fs, the transient orientational anisotropy decays to zero as molecules relax to their equilibrium (thermal) motions. At first the ISS signal intensity decays rapidly to delay times of 500 fs. If this part of the signal is fit to an exponential a decay time of roughly 200 fs is measured. After 500 fs the signal decays considerably more slowly and is fit reasonably well by a single exponential. The log plot in figure 5.1 confirms the different time dependence of the two decays. Following the partial orientational alignment induced by the excitation pulses, the molecules reorient in such a way to return the liquid to a state of orientational isotropy. The slow decay reflects the long-time diffusive reorientation of the heavy CS_2 molecules. The decay time measured from this portion of the data is 1.60 ps and is in good agreement with earlier femtosecond measurements [30,33]. The long time decay of the signal is discussed in more detail in section 5.4.

Figure 5.2 displays signal recorded from CS_2 at room temperature for several different polarization combinations of the four pulses involved in the transient grating experiment. The scan labelled "nuclear only" (figure 2.5c) was recorded with the polarizations from line 1 of table 3.1. This combination of polarizations cancels the electronic signal processes to reveal the signal arising from molecular motions [43]. In the VVVV scan

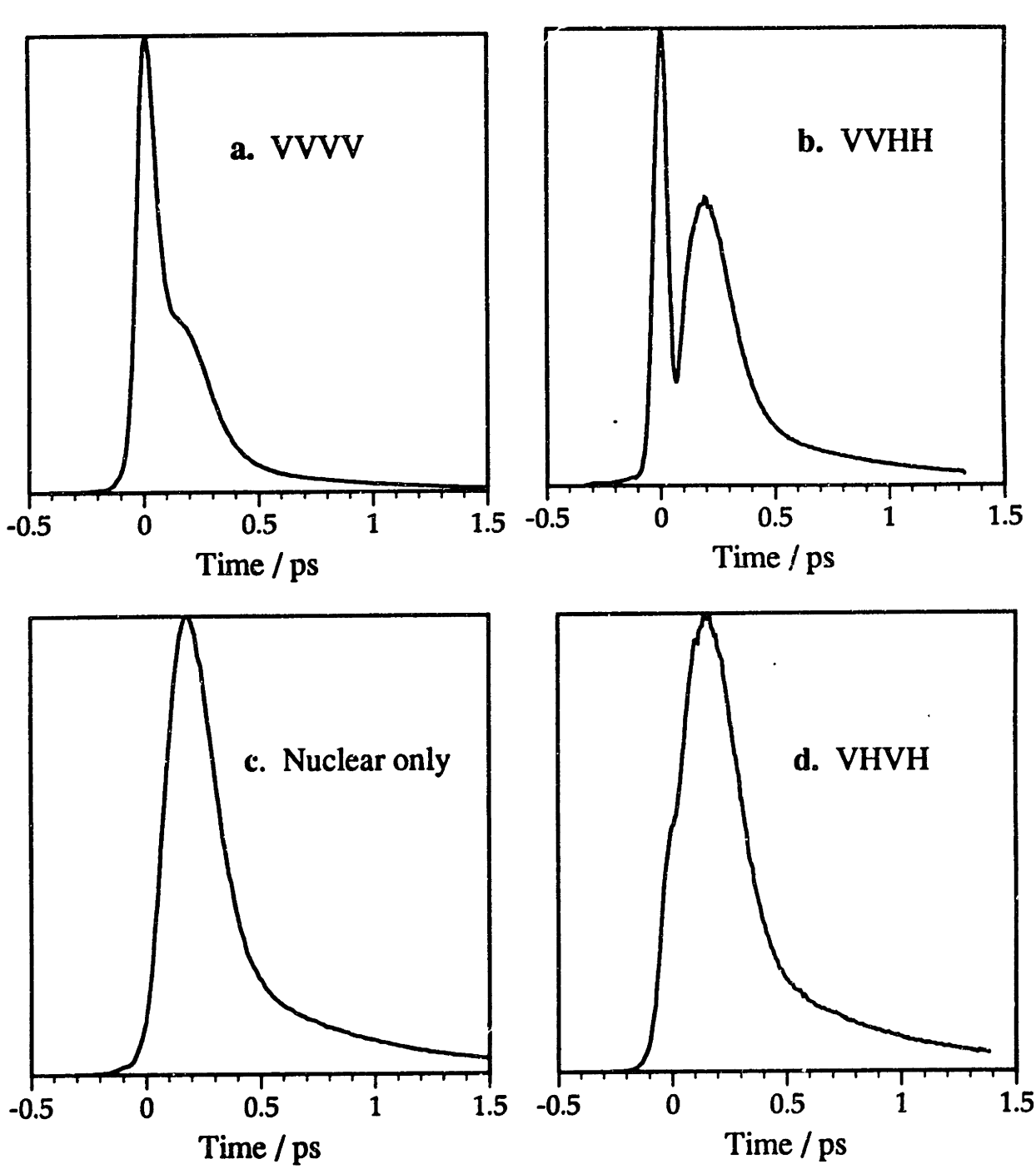

Figure 5.2 a-d ISS data from liquid carbon disulfide showing the effects of different polarization combinations. While the ratio of the nuclear to the electronic peak changes, the signal after the electronic feature is identical for all polarization combinations.

in figure 5.2a, the electronic signal contribution is larger than the nuclear component. In the depolarized scan recorded with VHVH polarizations in figure 5.2d, the nuclear signal rises to a higher level than the electronic peak. Hence, electronic processes are not as effective at depolarizing light as molecular ones for this polarization combination. For VVHH polarizations, the electronic and nuclear polarizations are of opposite sign and result in the pronounced dip in the ISS signal intensity near 100 fs. All curves in figure 5.2 show identical nuclear signal dynamics at times after the electronic response, when present, is over. This is illustrated in figure 5.3 where the curves of figure 5.1b and 5.1c have been replotted, scaling the nuclear signal at long times to equal values. We conclude that the same molecular dynamical processes are being sampled by the different polarization combinations. This is often true in Rayleigh light scattering where similar lineshapes (apart from intensity factors) are observed for VH (depolarized) and VV (polarized) scattering. This is a general result when the dominant signal contribution is due to reorientation of molecules. It would be interesting to see whether the additional polarization selectivity of the ISS experiment could be used to separate the allowed signal contributions of single molecule reorientation and pair correlation from the interaction-induced signal. Whether or not this is feasible depends on the symmetry properties of the complicated n-body dynamics which give rise to the interaction-induced polarizability.

The initial rise and decay of the short time signal dynamics of the room temperature CS_2 signal are suggestive of an overdamped vibrational response. Short-time vibrations and torsional oscillations have been suggested to be important in a variety of liquids composed of anisotropic molecules [71,72]. For such liquids molecular reorientation is expected to

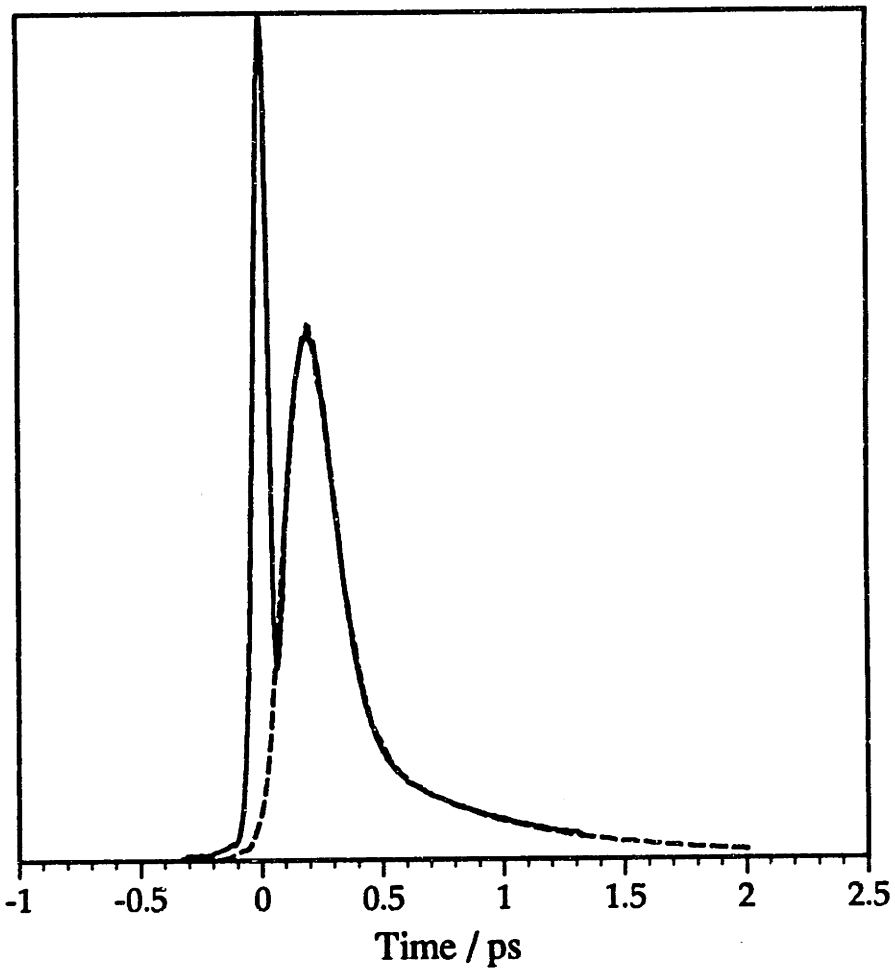

Figure 5.3 A comparison of VVHH (solid curve) and "nuclear only" (dashed curve) ISS data showing the identical response at times > 100 fs. The intensities of the two curves have been adjusted for best overlap.

show a librational character. In the next section, a temperature-dependent study is described which clearly demonstrates the vibrational character of the intermolecular motions probed by the ISS experiment. We interpret this signal in terms of reorientation which is modulated by molecular libration.

5.3 Temperature-dependent study

By varying the thermodynamic state of a liquid it is possible to vary the average energy available to each molecule and to change the average intermolecular separation. Any theory of the liquid state must be able to explain changes in experimental observables with changes in these properties. In the remainder of this chapter and in chapter 6, a systematic study of the femtosecond response of liquid carbon disulfide at a range of thermodynamic states is presented and discussed in terms of the underlying microscopic dynamics.

5.3.1 Experimental

Femtosecond ISS scans were recorded at a series of temperatures between 163 and 300 K. Liquid CS_2 was contained in a cuvette placed inside the cold head of a closed-cycle refrigerative cooler. The temperature was controlled to +/- 1 K with a P-I-D temperature controller (Lakeshore model no. DRC 82C). At each temperature the liquid was equilibrated for at least 15 minutes before the signal was recorded. The temperature-dependent data were recorded with VHVH polarizations to study the

anisotropic response function. Data recorded with other polarization combinations yielded identical nuclear signal dynamics, as seen from room temperature results.

At each temperature a scan was made out to 1.5 ps to measure the short time dynamics, stepping the optical delay by 2 microns (=6.67 fs). These scans appear in figure 5.4. Using longer optical delay steps of 5 microns (=33.33 fs) scans were made out to 7 ps to record the long-time decay of the ISS signal. These scans are shown in figure 5.5. For each scan the discrimination level was set to 2-3% peak to peak fluctuations. At each delay line position a total of 150 discriminated laser pulses were averaged. The pulse duration was determined on the same day by noncollinear autocorrelation in KDP to be 65 fs. The autocorrelation trace is shown underneath the 300 K data in figure 5.4 to illustrate the time resolution of the experiment.

5.3.2 Short-time dynamics

As the temperature is decreased, the rapid decay becomes faster and the long-time decay becomes slower. This is seen clearly in figure 5.6 where the short time part of the ISS data from another set of temperature-dependent scans are plotted. At temperatures below 240 K the transition between these two regions becomes considerably more complex with the appearance of a weak oscillation near 700 fs. This oscillation is most pronounced in the data recorded near the freezing temperature of CS_2. Representative data recorded at a temperature of 165 K are shown in a larger format in figure 5.7. The inset of this figure shows the oscillational

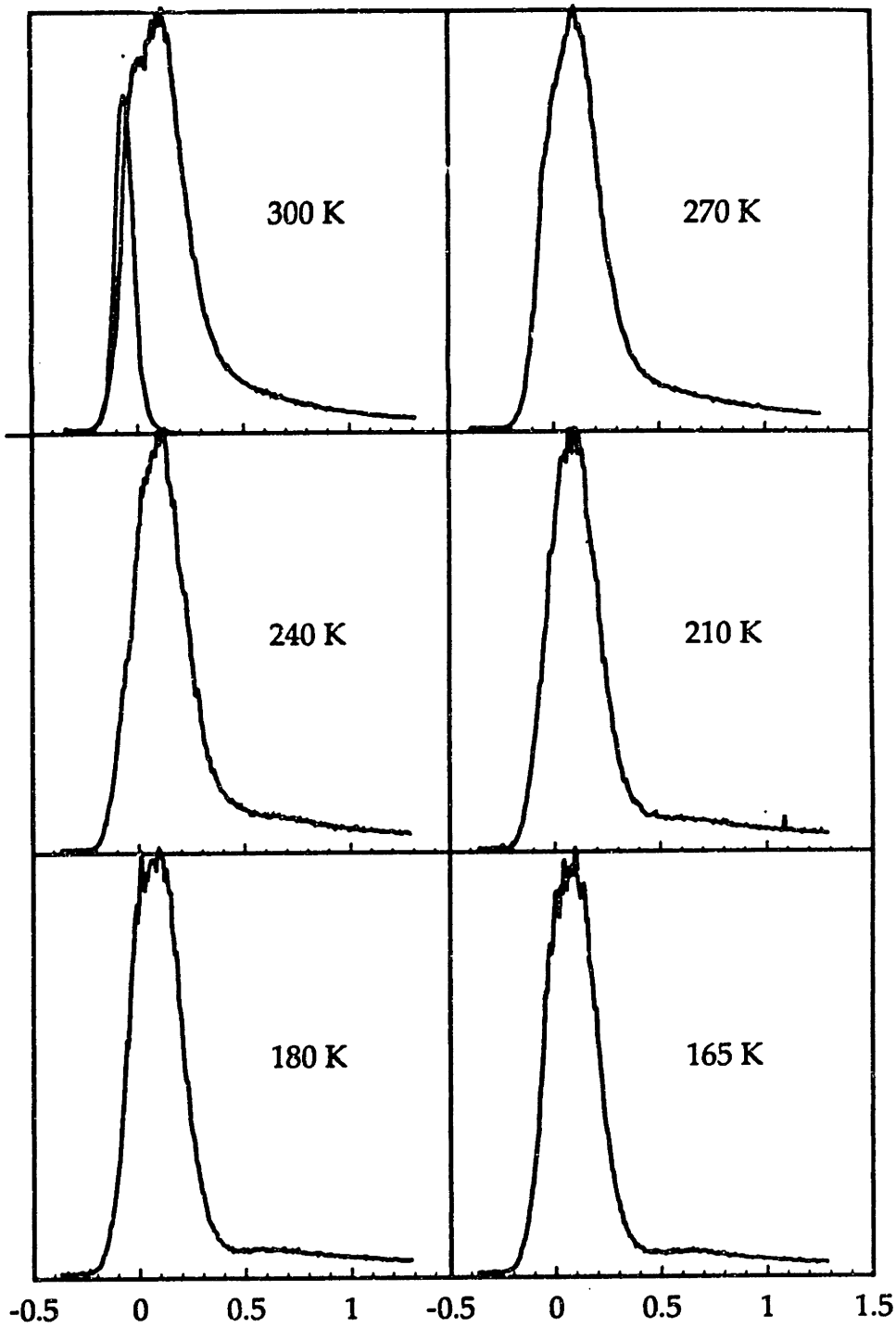

Figure 5.4 Temperature-dependent ISS data from liquid carbon disulfide showing the short-time response. All scans were recorded with VHVH polarizations using 60 fs pulses. As the temperature is lowered, a weak oscillation is observed near 700 fs probe delay time. The trace near zero time under the 300 K data is the pulse autocorrelation for comparison.

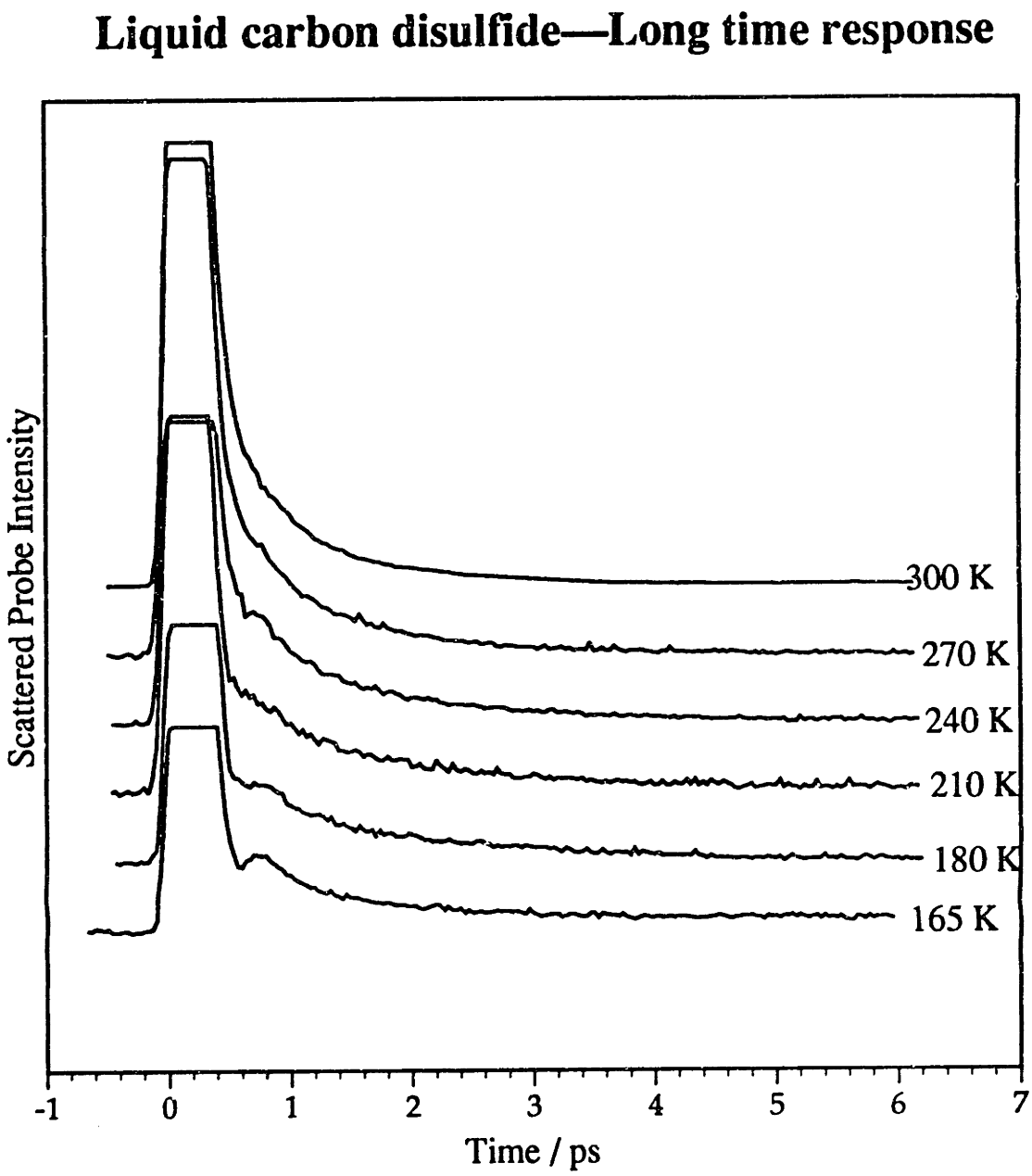

Figure 5.5 Long time decay of VHVH ISS signal from carbon disulfide as a function of temperature. The scans have been displaced vertically for greater clarity. The electronic peak at zero-time has been arbitrarily truncated.

Carbon disulfide—Temperature-dependent study

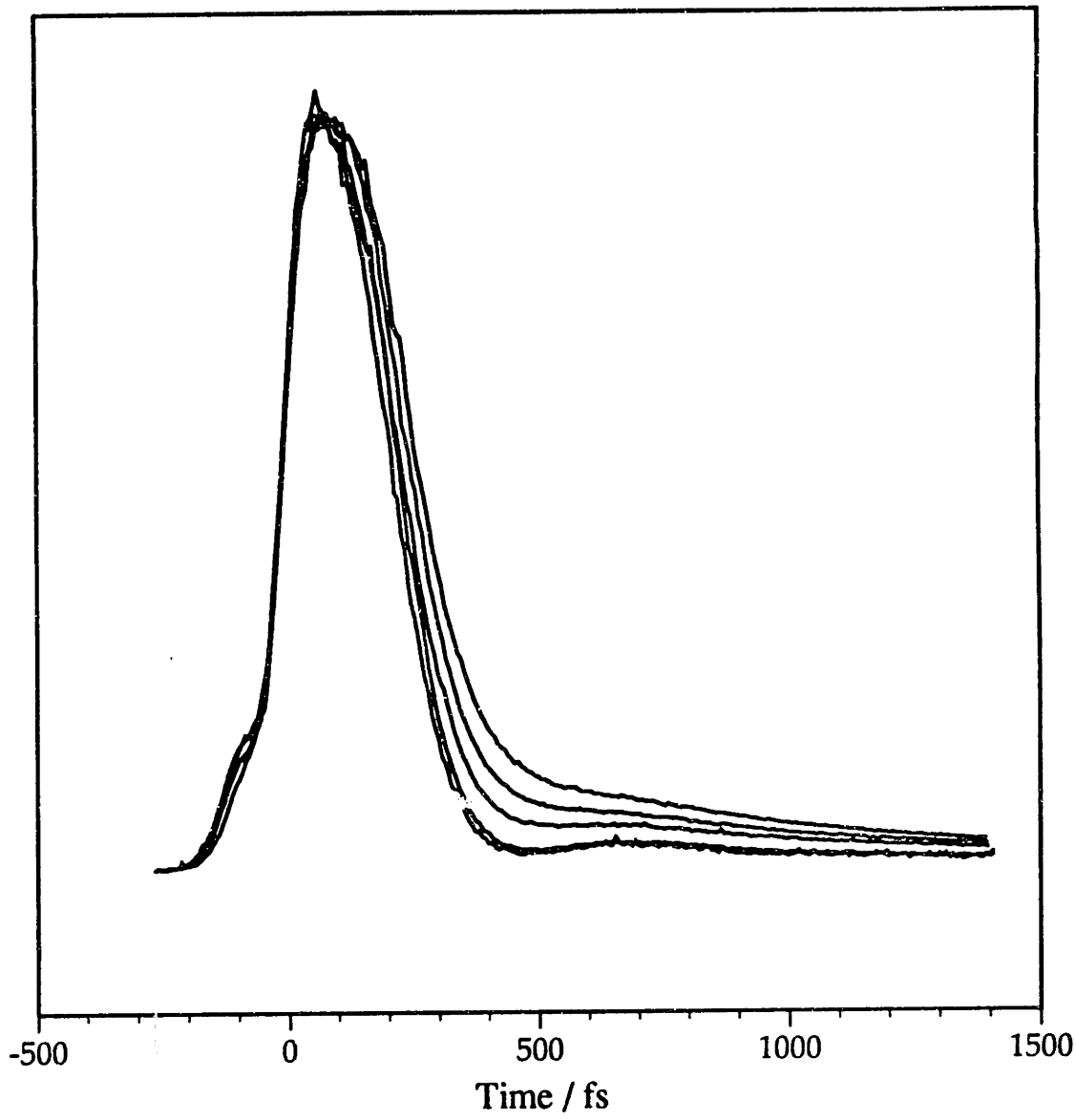

Figure 5.6 VHVH scattering data from liquid carbon disulfide as a function of temperature. From top to bottom at 500 fs delay the curves correspond to temperatures of 262, 232, 202, 168 and 162 Kelvin, respectively.

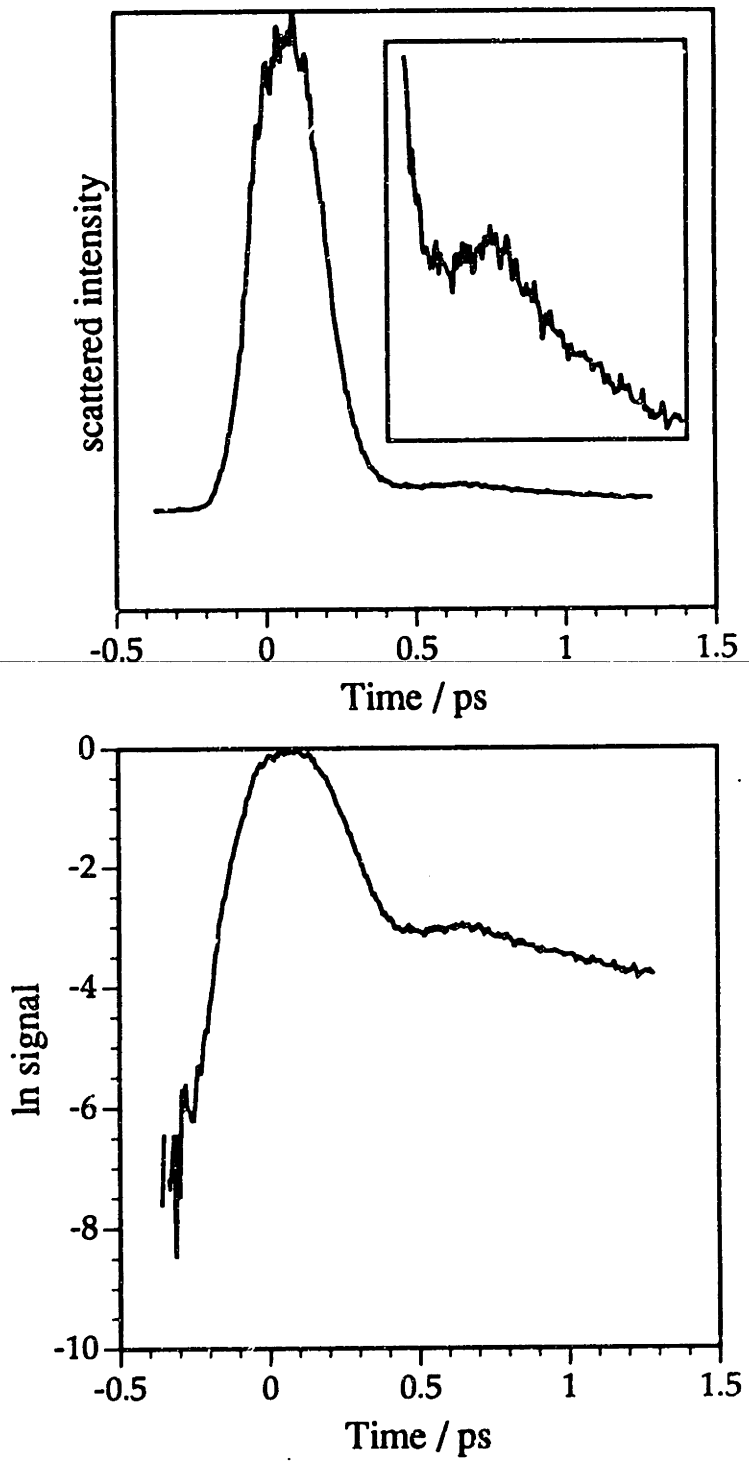

Figure 5.7 T = 165 K VHVH ISS data on a linear scale (top) and logarithmic scale (bottom). The inset in the top figure is a blowup of the weak oscillation near 700 fs.

feature more clearly on an expanded vertical scale. Note that the freezing temperature of CS_2 at atmospheric pressure is 163 K.

5.3.3 Models of reorientation in liquids

It has been pointed out by a number of researchers that the Debye model of rotational diffusion [73] fails to correctly describe reorientation at short times in dense liquids [8,9,12,74-77]. In physical terms, the diffusional model fails because it assumes that collisions are completely uncorrelated and of infinitesimal duration. This neglects interactions between molecules which occur in finite time. It also neglects the fact that in dense liquids cooperative motions of molecules are necessary for reorientation to occur. This description precludes the gas-like quasi-free rotation which is known to be important at very short times.

Starting with Gordon [74], and later extended by others [75-77], modifications to the Debye theory have been proposed. In these so-called extended diffusion models molecules are permitted to rotate through larger angles before experiencing reorienting collisions with neighboring molecules. This idea incorporates periods of free or inertial rotation into the description of reorientation. In these models molecules experience Poisson-distributed collisions which instantaneously randomize the direction or the direction and the magnitude of the molecular angular momentum of a reorienting molecule. Such a picture, however, still does not take into account correlation of angular momenta of different molecules. Evidence from light-scattering measurements [71,72,78] and from molecular dynamics simulation [79], indicate that substantial

correlation exists for dense, high-torque liquids composed of optically anisotropic molecules.

Another very different class of models of reorientation envision a more solid-like local environment for molecules. These models assume that the short-time dynamics are given by the motion of molecules in local potential wells or "cages" of near neighbors. For sufficiently short times these wells will appear harmonic and the molecules will execute torsional oscillations or librations. Of course, the oscillatory motion must be very heavily damped, otherwise liquids would show narrow peaks in the Raman spectra corresponding to librational modes. Such modes do occur in solids where diffusion does not occur and the cage structures about each molecule have infinite lifetimes.

A variety of ways have been developed to account for the damping of librational motions. In some librational models dephasing is achieved by postulating a broad distribution of oscillator frequencies [9]. In others the cage or potential well which a molecule occupies is assumed to instantaneously breakup after a time t, causing an instantaneous change in oscillator frequency [10-12].

The librational models of molecular reorientation are an appealing link between free rotation (the initial rise in the ISS signal) at very short times and diffusional reorientation at long times for dense liquids of anisotropic molecules. As a first step towards understanding our data, we have formulated a very simple model of librational reorientation to fit our data at short times. Implicit in our description is the assumption that the signal arises primarily from the reorientation of single molecules. Interaction-induced effects will, of course, contribute as well, but are likely to be a small component of the signal after 700 fs. Further discussion of our

neglect of higher-order signal contributions is given in section 5.5 below and in chapter 8. Here it is our hope that fitting the data to a simple functional form with a small number of parameters will permit a critical test of different models for short time reorientation in liquid CS_2.

5.3.4 Librational response functions

Let x represent the generalized coordinate which describes the motion of a carbon disulfide molecule in an approximately harmonic potential well at short times. Then the equation of motion, neglecting rearrangement of the potential well, can be written,

$$\ddot{x} + 2\gamma\dot{x} + \omega_0^2 = 0 \tag{5.1}$$

where γ is the damping constant and ω_0 is the natural (undamped) frequency of the oscillator. Several cases are possible depending on the amount of damping. The damping rate in the liquid is expected to be great in the sense that molecules experience frequent dissipative collisions with their neighbors. The motion can be overdamped in which case the time evolution, x(t), is given by

$$x(t) = A(e^{-\gamma_1 t} - e^{-\gamma_2 t}) \tag{5.2}$$

The constants γ_1 and γ_2 are related to the damping γ and the natural frequency ω_0,

$$\gamma_{2,1} = \gamma \pm (\gamma^2 - \omega_0^2)^{1/2} \tag{5.3}$$

For less damping the oscillators execute underdamped motion and the response is

$$x(t) = Ae^{-\gamma t} \sin \omega_1 t \tag{5.4}$$

where ω_1, the frequency of the damped oscillator, is given by,

$$\omega_1 = \sqrt{\omega_0^2 - \gamma^2}. \tag{5.5}$$

From these descriptions of motion in a harmonic well, we construct the following models of short-time reorientation. In the "homogeneous dephasing model" we envision each CS_2 molecules in a transient potential wells created by near neighbors. The molecules execute librational motion at a frequency ω. Dissipative interactions with neighbors, perhaps reflecting the break-up of cages, are incorporated in this model by the damping rate, γ. These phase-changing collisions result in homogeneous loss of vibrational (in this case, librational) phase coherence.

A more realistic model recognizes that a very broad range of local environments exists in the liquid state, resulting in a broad distribution of oscillator frequencies [9]. Neglecting the homogeneous damping completely, we consider the response of an ensemble of oscillators with frequencies given by a simple distribution function.

$$P(\omega) = \omega e^{-(\omega-\omega_0)^2/2\Delta^2} \tag{5.6}$$

where the parameter Δ measure the width of the librational frequency distribution about an average frequency ω_0. The lack of oscillatory structure in the room temperature data suggest that the inhomogeneity may be quite large, implying a broad distribution of frequencies. In order to avoid negative (unphysical) frequencies, and because the occurrence of very low frequencies is improbable, we have multiplied a Gaussian

frequency distribution by ω. We call this model the "inhomogeneous dephasing" model.

Due to the simplicity of the above descriptions, none of the above models for reorientation result in diffusional reorientation in the limit of long times. Consideration of cage relaxation leads to an additional relaxational term, $\exp(-\Gamma t)$, which we add here in an ad hoc manner to account for the long-time decay of the ISS signal. The functions which were used to model the impulse response function of the liquid are summarized below:

Overdamped oscillator:

$$G(t) = A(e^{-\gamma_1 t} - e^{-\gamma_2 t}) + Be^{-\Gamma t} \tag{5.7}$$

Homogeneous dephasing:

$$G(t) = Ae^{-\gamma t}\sin\omega t + Be^{-\Gamma t} \tag{5.8}$$

Inhomogeneous dephasing:

$$G(t) = Ae^{-\Delta^2 t^2/2}\sin\omega t + Be^{-\Gamma t} \tag{5.9}$$

The response functions of equations 5.7 - 5.9 were used as input to equation 3.10 to generate a simulated ISS signal. Gaussian pulses of 80 fs FWHM were used, and the convolutions in equation 3.10 were carried out numerically. Best fits were made in the least-squares sense using a Marquardt-Levenberg nonlinear optimization program. Each data point was weighted by a proportional error estimate of 3-5% of the recorded value.

At first, the overdamped oscillator model of equation 5.7 was used to fit the room temperature CS_2 data collected originally [80]. This model cannot reproduce the oscillatory structure of the low temperature data collected later and will not be considered further.

The homogeneous dephasing model was able to fit the high temperature data well, but was unable to accurately follow the shape of the weak oscillation at 700 fs. This is illustrated by fits to the 165K and 180K data shown in figures 5.8 and 5.9. The fit residuals show a systematic variation at probe delay times around the oscillatory feature.

In figures 5.10 and 5.11 fits made with the inhomogeneously broadened oscillator model (equation 5.9) are shown for two low temperature scans. This model yields a better fit at all temperatures than the homogeneous dephasing model as evidenced by residuals which scatter fairly evenly about zero. The modest disagreement near zero delay time where the electronic polarizability is greatest could be due to the deviation of the pulse intensity profiles from the idealized Gaussian profile used in the numerical convolution or to interaction-induced signal contributions which are likely to have a different time-dependence. In general, femtosecond pulses have a $\mathrm{sech}^2(t)$ shape and the use of this pulse function might yield a better fit to the zero time data.

The additional temporal structure of the data permits us to compare the fits from the two models. The fits with the inhomogeneously broadened oscillator models are substantially better and it is the only model which is able to reproduce the weak second oscillation at temperatures < 240K. The values of the parameters from the fits are given in table 5.1 for fits with the response function of equation 5.8 and in table 5.2 for equation 5.9. The mean librational frequency, ω, and the damping, γ, are of greatest

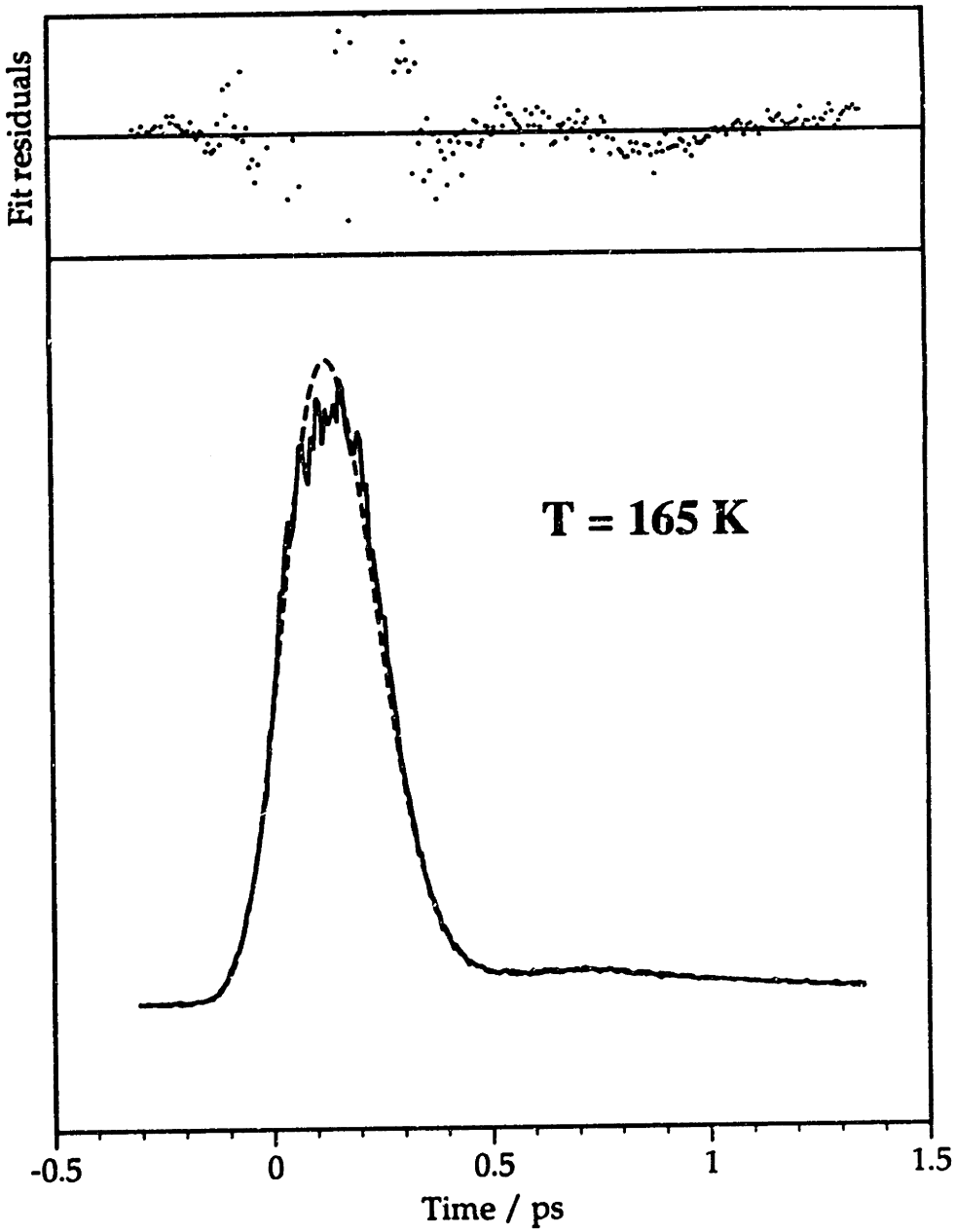

Figure 5.8 Fit to T = 165 K data with homogeneous dephasing model (equation 5.8). The systematic trends in the fit residuals at the top illustrate the failure of this model to accurately fit the weakly oscillatory ISS response.

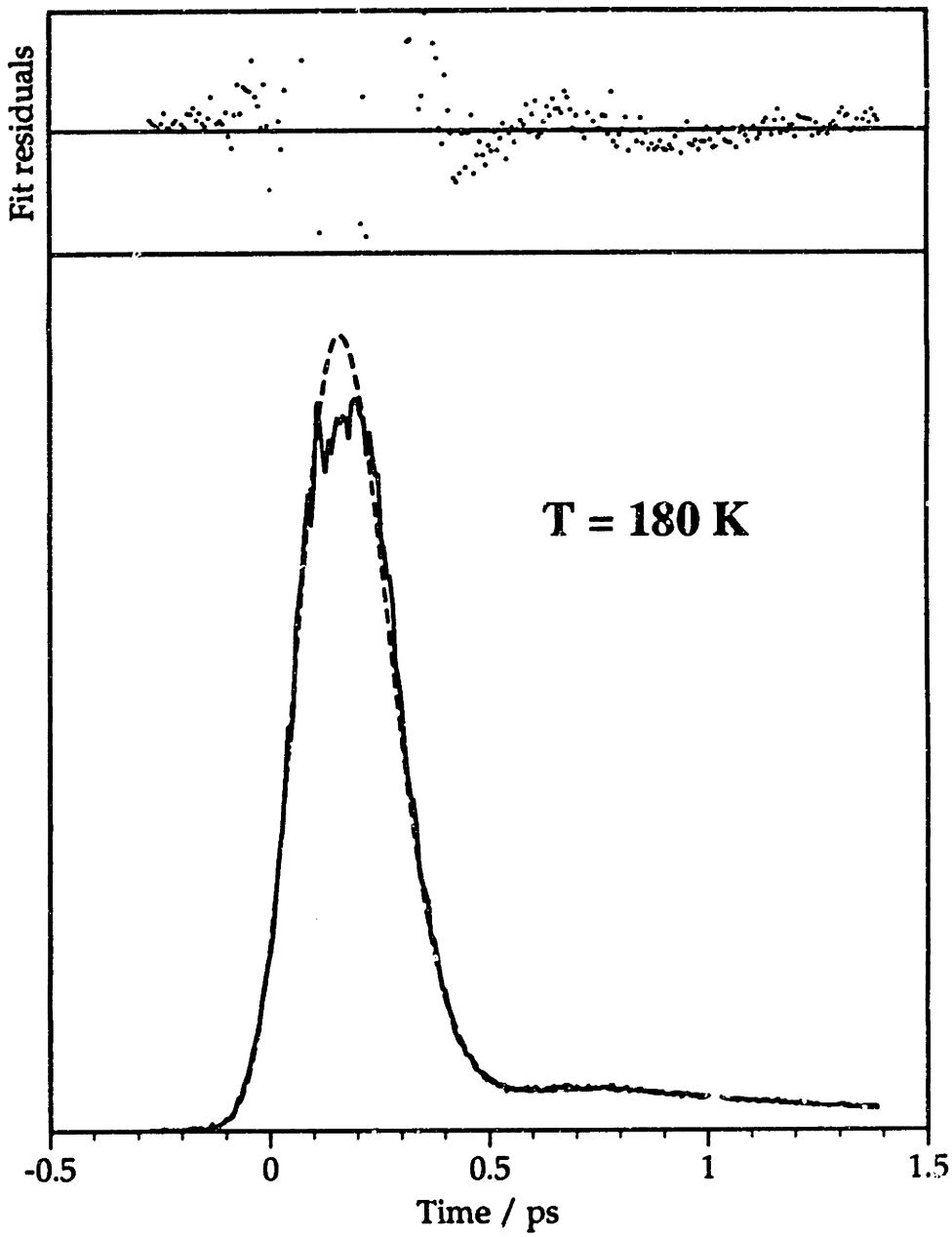

Figure 5.9 Fit to T = 180 K data with homogeneous dephasing model (equation 5.8). The residuals above show the failure of the functional form to accurately reproduce the data in the region of the weak oscillation.

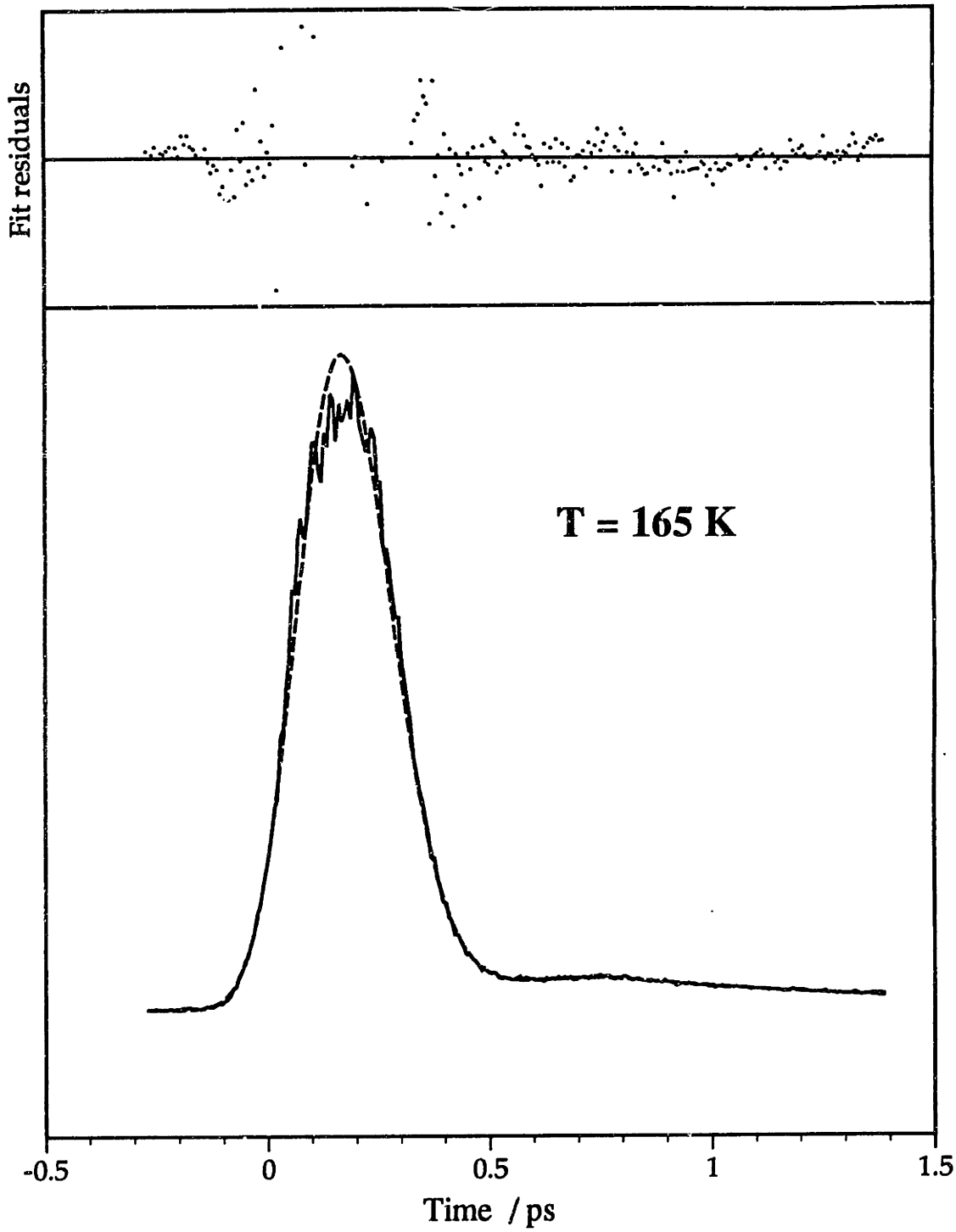

Figure 5.10 Fit to T = 165 K data with the inhomogeneous dephasing model (equation 5.9).

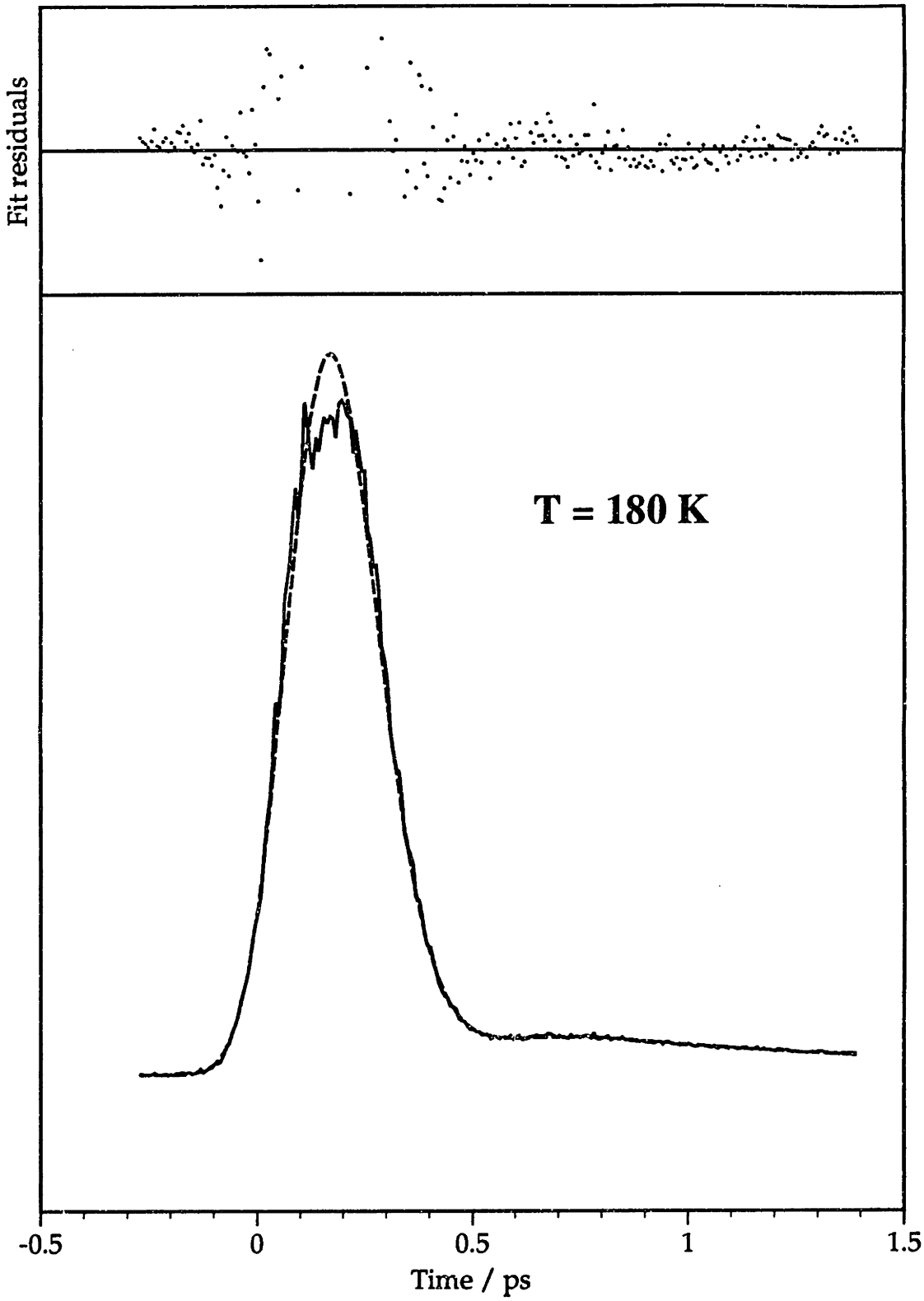

Figure 5.11 Fit to T = 180 K data with inhomogeneous dephasing model (equation 5.9).

interest for the homogeneous dephasing model. The frequency increases as the temperature is lowered, while the damping decreases. For the inhomogeneous model, the frequency is again found to increase with decreasing temperature and the parameter Δ, a measure of the distribution of librational frequencies, decreases. The trends in these parameters are physically plausible. Since the frequency is likely determined by intermolecular repulsions, reduction in the size of a cavity around a molecule as a result of higher density at low temperature should lead to higher frequencies. At low temperatures fewer local configurations are present which leads to a reduction in the inhomogeneity of oscillator frequency. The inhomogeneity is reduced as the local liquid environments become increasingly solid-like on the approach to the freezing point.

Table 5.1 Best-fit parameters from fits to CS_2 temperature-dependent ISS data using the librator response function with homogeneous dephasing (equation 5.8). Pulse shapes were assumed to be Gaussian with a FWHM of 80 fs. The third column gives the librational frequency, ν, in cm^{-1}, corresponding to the radial frequency, ω.

T / K	ω / ps^{-1}	ν / cm^{-1}	γ / ps^{-1}	Γ / ps^{-1}	A	B
300	5.10	27.1	9.42	0.823	3.58	0.489
270	5.79	30.7	9.08	0.699	3.40	0.457
240	6.54	34.7	9.53	0.604	2.95	0.418
210	8.03	42.6	7.18	0.671	2.26	0.434
180	8.86	47.0	7.66	0.581	2.43	0.361
165	9.09	48.2	6.75	0.774	2.08	0.389

Table 5.2 Parameters from best fits to temperature-dependent data using the inhomogeneously broadened librator response function (equation 5.9). Pulse shapes were taken to be Gaussian with a FWHM of 80 fs. The third column gives the librational frequency, ν, in cm^{-1}, corresponding to the radial frequency, ω.

T / K	ω / ps^{-1}	ν / cm^{-1}	Δ / ps^{-1}	Γ / ps^{-1}	A	B
300	4.64	24.6	6.05	0.855	1.65	0.522
270	4.99	26.5	5.46	0.738	1.50	0.492
240	6.74	35.8	5.04	0.643	1.16	0.451
210	7.27	38.6	4.63	0.597	1.15	0.414
180	7.55	40.1	4.41	0.578	1.22	0.376
165	7.79	41.3	4.26	0.737	1.14	0.396

In summary, a simple model in which CS_2 molecules librate in transient potential wells created by close-packing of neighboring molecules allows us to write simple, analytical expressions for the response of the liquid to ultrafast optical excitation. The rapid decay of the ISS signal and the weakness of the oscillatory response indicate that the dephasing of librational coherence is very rapid. Two dephasing models were considered. In the homogeneous dephasing model a damping term is associated with each local potential well. The damping rate reflects the breakup of cages. The second model achieves dephasing through a broad distribution of librational frequencies which accounts for the wide range of local environments. While both models yield satisfactory fits to the data,

the weak oscillation in the low temperature data was fit somewhat more accurately by the model which incorporated inhomogeneous dephasing. In reality, we expect both dephasing mechanisms to be important. A broad distribution of librational frequencies accounting for the wide variety of local configurations and local damping due to cage breakup will both be present. A number of more realistic descriptions of libration in liquids [10-12] point the way towards extensions of the analysis of this chapter. Unfortunately, most of these models suffer from the drawback that they do not yield simple, closed-form expressions.

5.4 Long-time behavior

In figure 5.12 a persistent tail in the femtosecond ISS data is seen which lasts for tens of picoseconds. This signal embodies all of the slow decay routes by which the transient orientational alignment induced at zero-time relaxes. The scattering signal after 2 picoseconds is weak and requires careful signal detection and precise estimation of zero-signal levels to characterize accurately. As this long-time signal was not the main focus of this work, extensive measures were not taken. Nonetheless, this section discusses some of the trends of the long-time ($t > 2$ ps) ISS data.

A diffusional model of reorientation, whether the small step model of Debye [73] or any of the extended diffusion models [74-77], predicts exponential decay of the correlation functions governing the reorientation of single molecules. This exponential decay is responsible for the often narrow, Lorentzian-shaped line observed in Rayleigh light scattering. In the ISS experiment, the response function measured is proportional to the

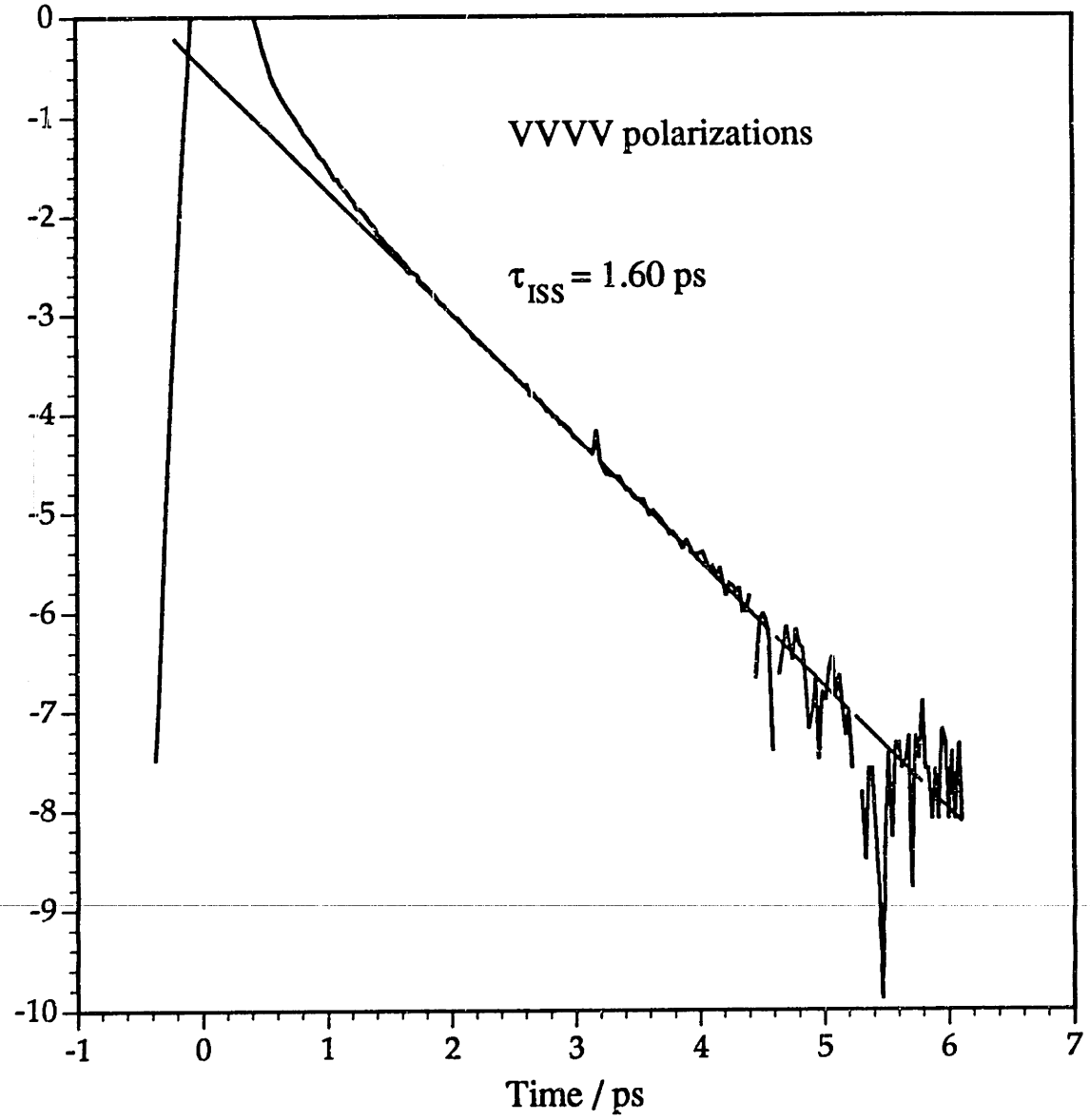

Figure 5.12 VVVV ISS data from room temperature carbon disulfide. A fit was made to a single exponential response function at times greater than 2 ps, yielding a decay time of 1.60 ps.

derivative of the light scattering correlation function as shown in equation 3.19. Consequently, diffusional reorientation predicts an exponentially decaying ISS signal. Figure 5.12 displays the natural logarithm of a VVVV ISS scan recorded from carbon disulfide at room temperature. The decay is indeed linear at times > 1.5 ps and is fit well by an exponential response function with a decay time of 1.60 ps.

The logarithm of the long time ISS signal of CS_2 is displayed as a function of temperature in figure 5.13. As the temperature is lowered, the decay becomes slower, consistent with more hindered reorientation in the increasingly viscous liquid. From the figure the decay at long times is seen to be approximately exponential after 2.0 picoseconds, except at 165 K. Three separate scans recorded sequentially over a time period of about twenty minutes at this temperature changed unreproducibly from scan to scan at long probe delay times, probably as a result of scattering from microcrystals of CS_2. Note that the appearance of a non-Lorentzian feature at low frequency in the Rayleigh spectrum would result in a nonexponential decay at long times. One final observation of the long-time data is that as the temperature is lowered, longer and longer times are required for the decay to become single-exponential. At room temperature after only about 1.5 ps the decay is exponential, but at 170 K (figure 5.14) the signal is clearly not single-exponential for times at least as great as 4.0 ps. This represents a further departure from a diffusional description in this time range and additional experimental work with improved sensitivity is needed.

A mode whose impulse response is given by a single exponential produces an exponentially decaying ISS signal with twice the decay rate. This is readily seen from equation 3.9, where the ISS signal is proportional

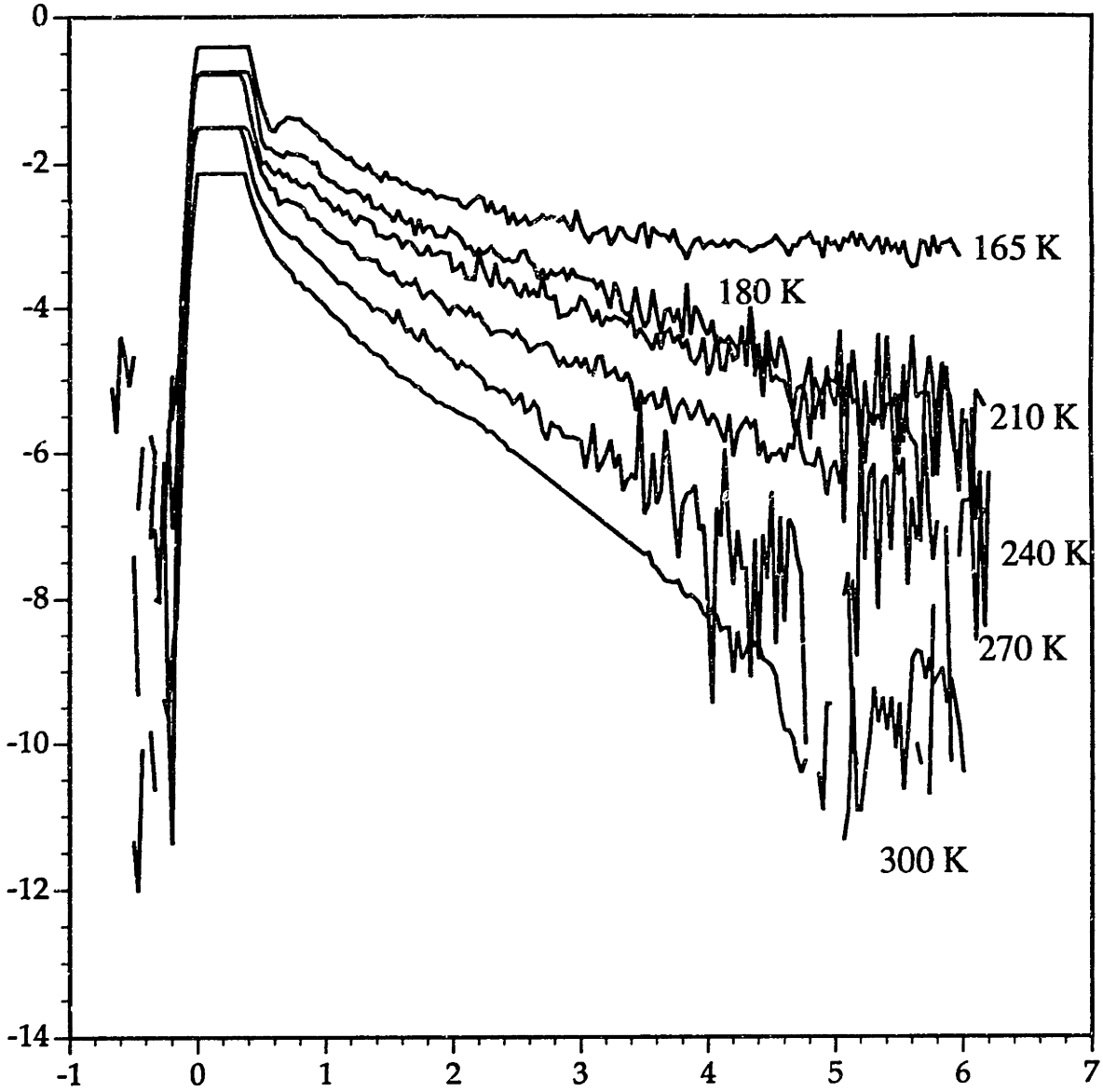

Figure 5.13 Logarithmic plot of long-time VHVH ISS scans as a function of temperature. The curves have been displaced vertically for clarity.

to the square of the impulse response function of the relevant material mode in the limit of perfect time resolution. Finite pump and probe pulse durations will not affect the decay time, since the convolution of an exponential with any symmetric function always yields an exponentially decaying function with the same decay rate. This means it is not necessary to fit the data using the convolutions over pump and probe pulse durations in equation 3.10. The response function can be written,

$$G(t) = A\exp(-t/\tau_{iss}) \tag{5.9}$$

where τ_{ISS} is the time constant for the decay and A is a constant giving the mode coupling strength to the driving force of the optical pulses. At each temperature τ_{ISS} was determined by fitting the functional form $A'\exp(-2t/\tau_{ISS})$ to the data at times $t > 2$ ps.

Several well-known pitfalls complicate the determination of an exponential decay time from the data. One difficulty is the relatively small number of lifetimes represented by the data in figure 5.13. This problem is particularly severe at low temperature where the reorientation is more hindered and the decay times are even longer. To accurately determine the decay at long times, effort should be made to improve the sensitivity of the detection to allow the recording of signal out to longer times. This would require recording the signal at several different sensitivities and then piecing the curves together. Careful spatial and, perhaps, spectral filtering of the diffracted probe pulse would be necessary to measure the small diffraction efficiencies at long times.

A more serious problem arises when the zero signal value or baseline is not extremely well determined. As is well known, even minute shifts in

this quantity lead to changes in the decay constant of 10-30%. The data at 210 K were fit with two different baseline corrections which differ by less than 0.5 % of the difference between the largest and smallest signal values in the scan. The best-fit decay times differed by 25 %. The main sources of error in determining the base line arise from not scanning the probe delay long enough prior to zero delay time. If the region before t=0 is too short, than the slowly rising wing of the electronic peak can make determination of the baseline difficult.

These problems make the accurate determination of decay times difficult from the current data. With this disclaimer, values for τ_{ISS} are given in table 5.3. In light of the sources of error, the values are likely accurate to no more than 20% with the largest errors at low temperature where the changeover to exponential decay occurs at later times and the total number of lifetimes is small. The room temperature decay value of 1.60 ps agrees extremely well with the results of recent femtosecond optical Kerr effect experiments on CS_2. G. Kenney-Wallace et al. report a decay time of 1.61 ± 0.05 ps [30], while Greene and Farrow reported a value of 1.56 ± 0.05 ps [32].

Table 5.3 Experimentally measured relaxation times for liquid carbon disulfide. τ_{ISS} was determined by fitting the expression $Aexp(-2t/\tau_{ISS})$ to the data at times $t > 2$ ps. The column at right gives the reorientational correlation time determined from Rayleigh scattering.

Temperature / K	τ_{ISS} / ps	τ_{RAY} / ps [ref. 57]
300	1.4	
293	1.6	1.86
270	1.8	
262	2.6	
240	2.6	2.73 (@ 248 K)
232	3.2	
210	3.6	4.82
202	5.0	
180	4.0	8.5
168	7.2	13.9 (@ 164 K)

The last column of table 5.1 gives the orientational decay time, τ_{RAY}, determined from the Rayleigh light scattering results of Madden *et al.* [57]. This quantity is determined from the half-width of a Lorentzian fit to the low frequency part of the Rayleigh band shape. It gives the decay time of the reorientational correlation function at long times. Since the response function of the ISS experiment is the derivative of the time correlation function measured in spontaneous light scattering, the definition in equation 5.9 above implies that τ_{ISS} should be equal to τ_{RAY}. But we find that at all temperatures $\tau_{ISS} < \tau_{RAY}$, with the biggest disagreement at low

temperature. At low temperature the Lorentzian measured by Rayleigh light scattering becomes narrower, and it may be more difficult to accurately determine linewidths. We would expect, however, for the light scattering measurements to *underestimate* the reorientational correlation time by overestimating the narrow width of the low temperature Lorentzian.

It is interesting to note that a similar disagreement was noted in the mid-1970s in picosecond optical Kerr effect experiments on nitrobenzene and m-nitrotoluene by Ho, Yu and Alfano [81]. For these molecules the relaxation of orientational correlations takes several tens of picoseconds and could be measured with the several-ps laser technology of the day. These authors found relaxation times which were 10-40% shorter than ones measured by Rayleigh light scattering. They suggested that the lower relaxation time is due to coupling of the reorientational motion to the shear mode relaxation. This shear mode-coupling has been observed in the depolarized Rayleigh spectra of some molecules where a narrow, inverted Lorentzian feature or dip is observed very near zero frequency [82]. Such a shear-dip (Rytov doublet) has been observed in the low-temperature depolarized Rayleigh scattering from liquid CS_2 [83]. Since the maximum width of the dip observed in CS_2 is 260 MHz, we believe the coupling of molecular rotation to shear modes will have no substantial effect on the dynamics observed on our experimental time scale.

As these investigations continue to be extended to a wider variety of liquids under a range of thermodynamics conditions, it should be possible to gain additional insight into the discrepancy between the long-time decay of the femtosecond light scattering experiments and the reorientational times determined from frequency-domain studies.

5.5 Dilution study†

By diluting one liquid in another it may be possible to learn about the importance of pair interactions [55]. Since the ISS signal is proportional to the square of the Raman cross section [36], signal from weakly scattering solvent molecules may be negligible at all concentrations. At sufficient dilution solute molecules will be surrounded by solvent molecules and can therefore be expected to show negligible orientational correlation with other solute molecules. Thus it may be possible by studying the ISS signal of a strongly scattering molecule in a variety of weakly scattering solvents to learn more about single molecule reorientation. This knowledge, in turn, will further help estimate the dynamical information content of interaction-induced scattering to the ultrafast response of simple, molecular liquids.

An initial dilution study of carbon disulfide was performed in cyclohexane. This solvent was chosen because carbon disulfide is readily miscible with it and because of its weak femtosecond stimulated scattering signal. Figure 5.14 displays the VHVH scattering data recorded from CS_2 at various concentrations in cyclohexane. The pulse durations were measured on the same day to be 60 fs. The data from neat cyclohexane are plotted with the data recorded at 80% CS_2 volume fraction at the upper left of figure 5.14. The electronic peak of cyclohexane is very strong relative to the nuclear signal and is off scale in this figure. As the concentration of

† Many thanks to Alan G. Joly who recorded the scans in this section.

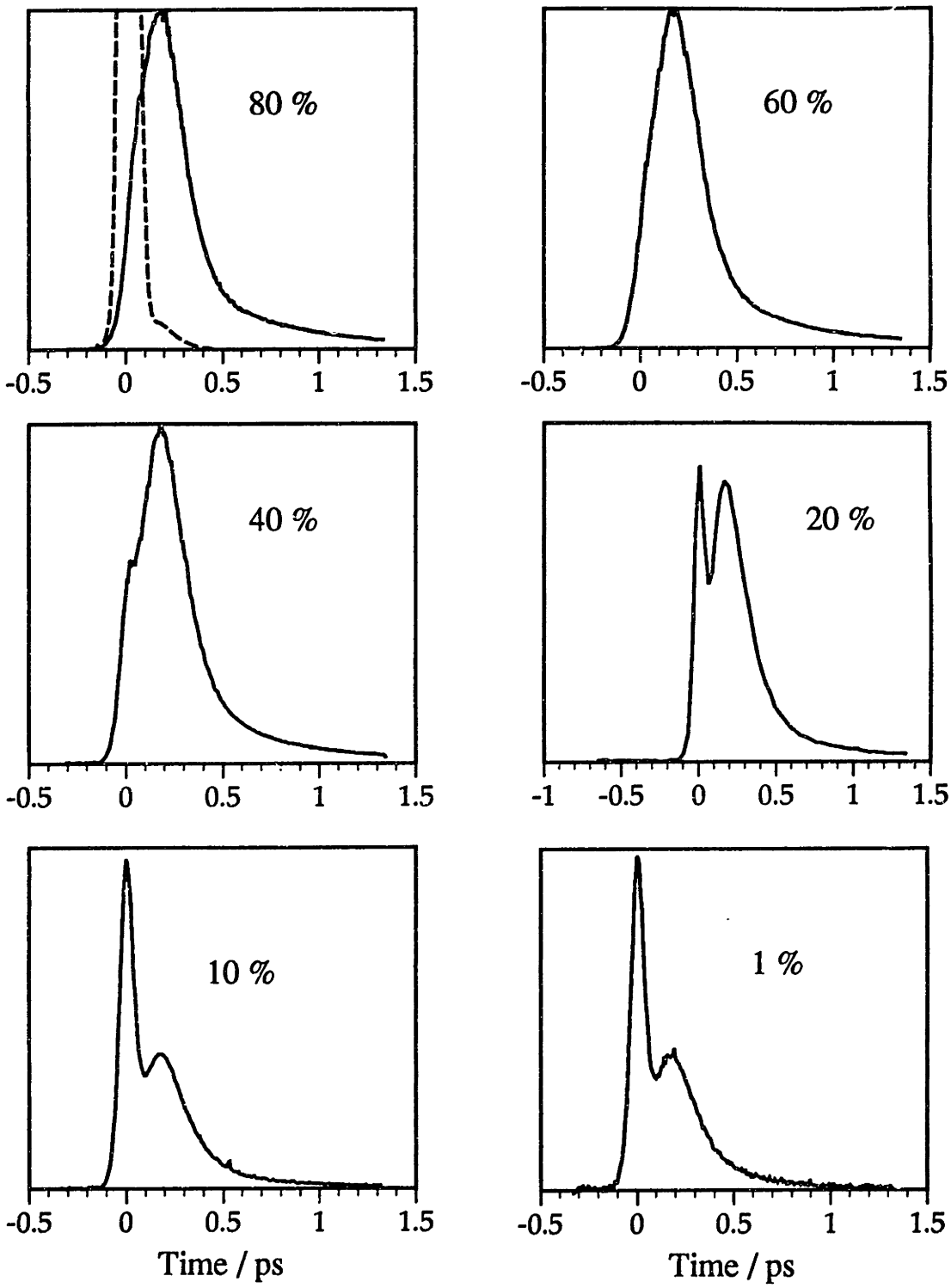

Figure 5.14 VHVH ISS signal recorded from CS_2 in cyclohexane at various concentrations. The volume fraction of CS_2 is given in each figure. The vertical axes are arbitrary and the vertical scales are not the same for all scans. The dashed curve at upper left is the ISS signal from pure cyclohexane on an expanded vertical scale.

CS_2 is reduced, the electronic signal peak becomes larger in proportion to the nuclear signal at later times. This is because the signal at zero times arises from both CS_2 and cyclohexane molecules, whereas the signal at later times is predominantly due to CS_2 molecules. Even at 1% volume fraction the signal from CS_2 is still strong and easily measured.

A striking aspect of the data is the similarity of the nuclear signal at all volume fractions. By simply adjusting the scaling, the scans can be made to superpose almost perfectly. This is shown in the top half of figure 5.15. Only on a log scale (bottom half of figure 5.15) do slight differences become evident. As the concentration of CS_2 is decreased, the signal near 1 ps is seen to decay somewhat more quickly. The relaxation becomes faster despite the fact that the viscosity of the liquid mixture becomes greater, in disagreement with the prediction of rotational diffusion. This observation of relaxation times which decrease despite increasing viscosity has been seen before in picosecond Kerr studies of nitrobenzene and m-nitrotoluene [81]. Van Konyenburg and Steele found that the reorientational correlation functions from iodomethane decay more rapidly upon dilution in CCl_4, despite the 1.7 times increase in the viscosity [78]. The more rapid decay is presumably because reorientation becomes less hindered in a solvent of spherical molecules despite the increase in shear viscosity. Of course, the decreased relaxation time may be attributable to the decreased importance of orientational correlations of pairs of molecules (these correlations contribute through the second term of equation 3.28) which are predicted by some investigators to lead to slower decay of the Rayleigh correlation function [84].

The short-time ($t < 1.0$ ps) signal dynamics, however, are surprisingly insensitive to dilution. This is in contrast to the pronounced changes

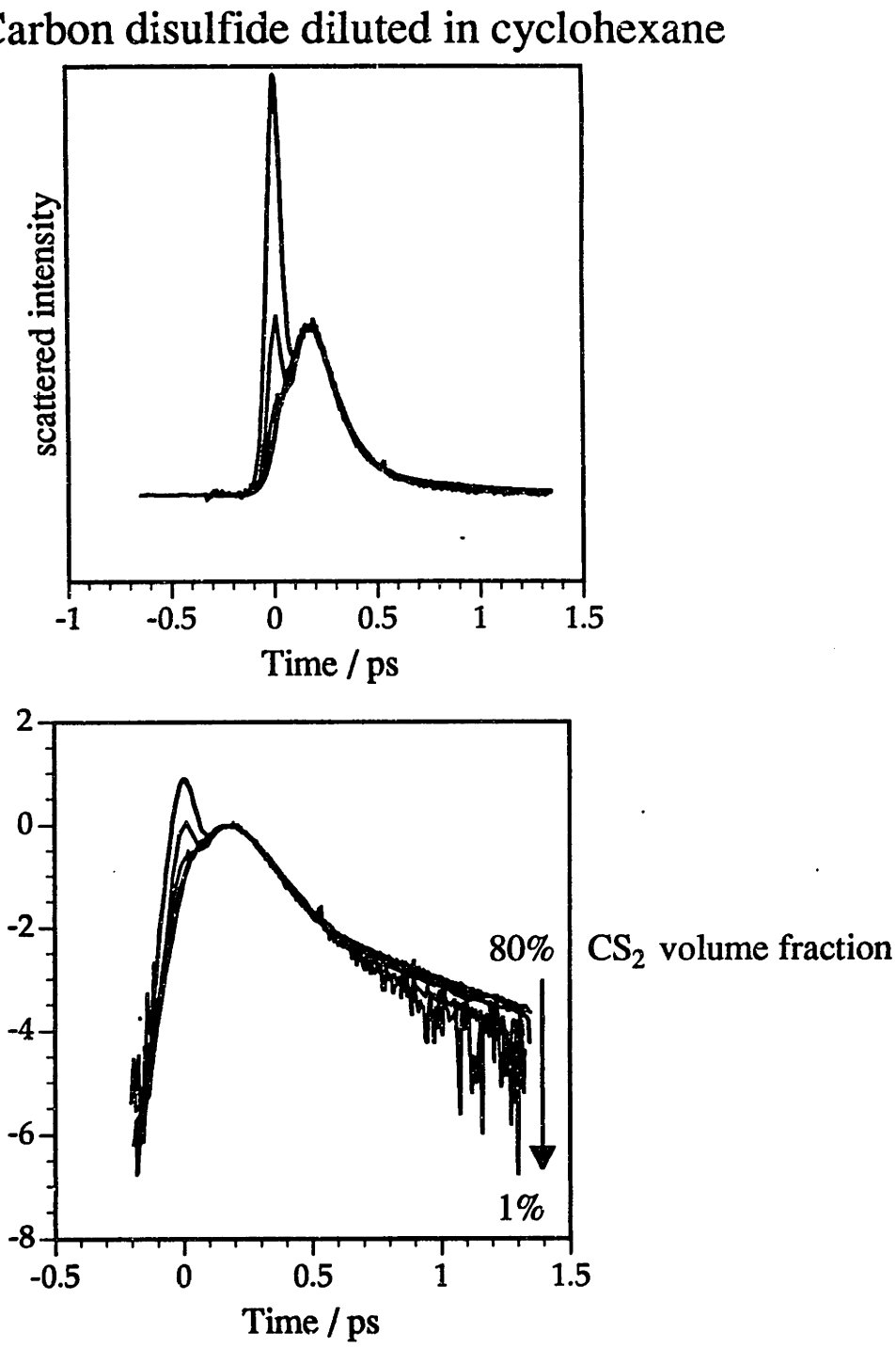

Figure 5.15 VHVH ISS data from carbon disulfide diluted in cyclohexane. In the top figure, the same scans from figure 5.14 are plotted together with the peak in the nuclear signal scaled to the same value. A logarithmic plot of these scans in the lower figure reveals identical short time dynamics, but a faster decay at long times as the volume fraction of carbon disulfide is reduced.

observed in the temperature-dependent study. If the nuclear signal from cyclohexane molecules can be neglected, then as the CS_2 concentration is decreased the average distance between scattering centers increases. The density of CS_2 molecules is effectively lowered and the interaction-induced signal, if it is significant, should change markedly with concentration. This suggests that the short-time signal from CS_2 arises primarily from the reorientation of single molecules. Of course each CS_2 molecule is still present in a cage of solvent molecules and the reorientation at short times may be similar to the reorientation of single molecules surrounded by a cage of CS_2 molecules. A next step would be to undertake dilution studies at a variety of thermodynamic state points. Another useful study would be the investigation of the ISS signal from CS_2 dissolved in a weakly scattering solvent of small, isotropic molecules. Some results along these lines have been reported by Kenney-Wallace's research group [31]. Systematic study of the fast signal dynamics should elucidate the importance of interaction-induced scattering and the sensitivity of reorientation of solute molecules to different intermolecular potentials.

Chapter 6

Femtosecond ISS Experiments on Liquid Carbon Disulfide at High Pressure

6.1 The importance of pressure

Under applied pressure the density of a liquid increases and average intermolecular distances in a molecular fluid decrease. Systematically varying pressure discloses different regions of the intermolecular potential to study [85]. While the orientations of molecules of simple liquids are isotropic when macroscopic volumes are considered, these liquids can show substantial orientational ordering over distances of a few molecular diameters. Steric effects in liquids of anisotropic molecules are one of the factors leading to enhanced local ordering of molecules. Particularly at high densities, the strong angular forces resulting from preferred arrangements of nonspherical molecules can lead to the caging of molecules by neighbors [79]. Not only will cages have a strong influence on single molecule dynamics, but the average lifetime of cages is expected to increase at high density, because the orientational and translational motions necessary for the breakup of cages become more hindered. This could result in an increased tendency for libration. In this section, initial experiments are described in which femtosecond impulsive stimulated light scattering (ISS) was performed on liquid carbon disulfide at a range of pressures at room temperature in a diamond anvil cell. While various

researchers have used diamond anvil cells in time-resolved experiments with picosecond pulses [86,87], the experiments reported here, represent, to our knowledge, the first use of femtosecond optical pulses in a high pressure study in a diamond anvil cell.

6.2 Diamond anvil cell technology

Diamond anvil cells have revolutionized optical high pressure studies of condensed phases since their introduction in the 1960s [88]. The principal of operation is simple: Two diamonds cut in the shape of anvils (a brilliant cut with an opened culet is adequate) compress a fluid or solid sample contained in a small hole drilled in a gasket material (usually made of steel). The pressure is generated as a result of force amplification by the diamond anvils. A load applied to the diamond tables is applied to a smaller area of the anvil tip resulting in a greater force per unit area, i.e. a greater pressure. The great strength of diamond makes it the ultimate anvil material.

The pressure is most commonly determined by measuring the pressure-induced shift of a doublet in the luminescense spectrum of a small chip of ruby contained with the liquid inside the cell. The review article by D.J. Dunstan and I. L. Spain provides useful information about the design and loading of diamond anvil high pressure cells [89].

Diamond anvil cells are most famous for their use at ultrahigh pressures. Recently, pressures up to 250 GPa† were used to study the

† 1 Gigapascal (GPa) = 10 kilobar

possible metalization of hydrogen [90]. At ambient temperature the typical freezing pressure of many molecular substances which are liquid at atmospheric pressure lies between 0.1 to 1 GPa (1 - 10 kbar). This is a low pressure range for the customary diamond anvil cell designs, and many high pressure studies of liquids have used conventional high pressure cells. These cells typically use a pressurizing fluid to drive a piston in a cell carefully machined from very high strength steel [91]. Nonetheless, the simplicity, compact size and lower cost of a diamond anvil cell are compelling. We found that a few simple modifications described next resulted in a practical high pressure cell for femtosecond impulsive stimulated light scattering.

6.2.1 Modified diamond anvil cell for pressures < 1 GPa.

The modified diamond anvil cell used in the high pressure experiments described here is illustrated in figure 6.1. The ratio of the areas of the diamond table (load bearing surface) to the diamond culet (the diamond surface next to the sample volume) was reduced by enlarging the culet diameter to 1.2 mm. For attaining pressures in excess of 10 GPa it is imperative that the diamonds be free of mechanical flaws which could lead to failure under high load. The lower pressures studied with this cell greatly reduce the requirements usually placed on the selection of diamonds for anvils. Due to the large stimulated scattering signal detected in the ISS experiment and our use of 615 nm pulses, it was unnecessary to select diamonds with special optical requirements such as low fluorescence or enhanced UV transmission. A pair of approximately 1/3 carat brilliant cut

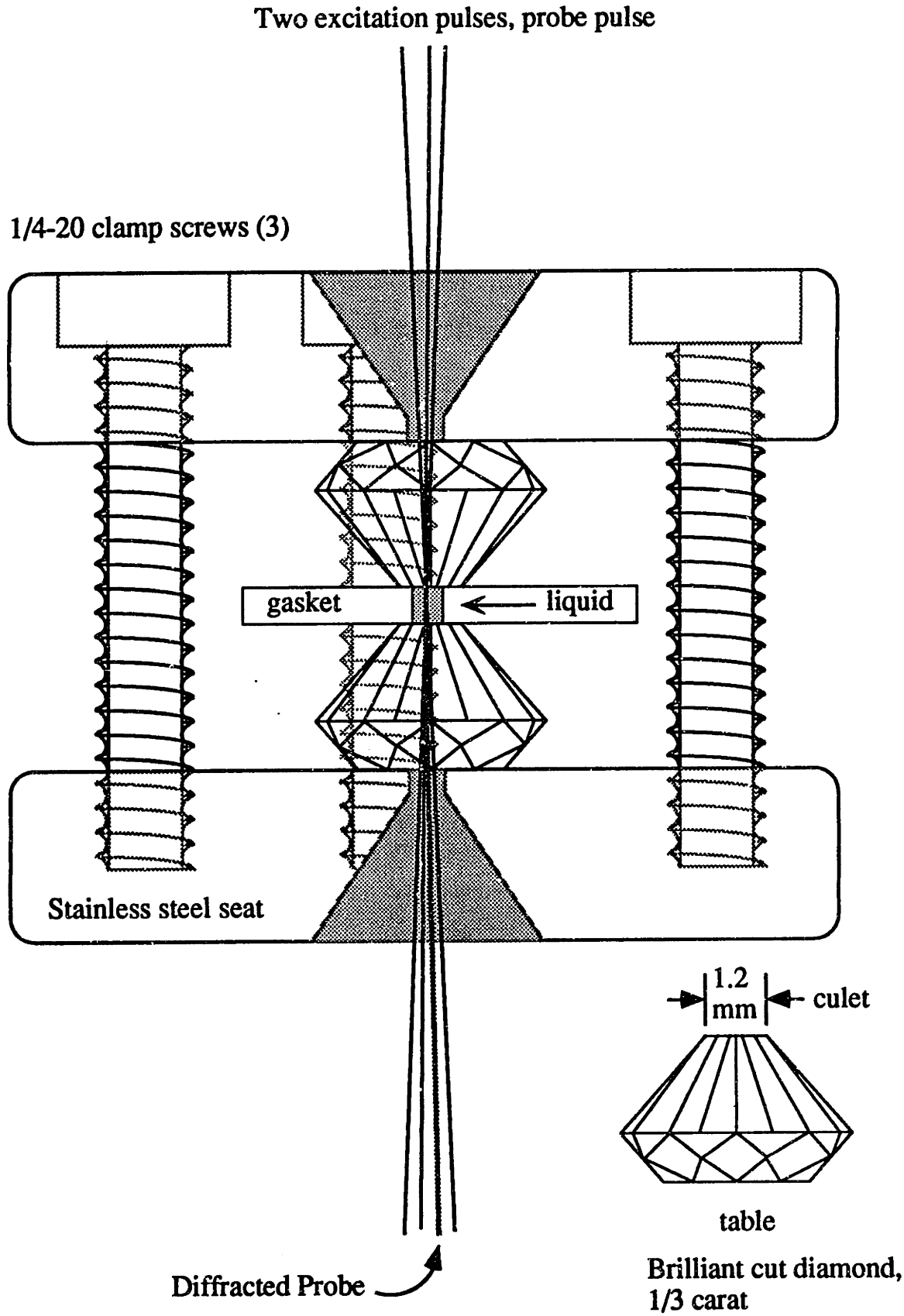

Figure 6.1 Diamond anvil cell design, side view.

diamonds purchased from a Boston jeweler for $600 were entirely adequate.

The maximum pressure which can be generated with a diamond anvil cell is limited by breakage of the diamond culets. Dunstan and Spain [89] suggest that the maximum pressure, P_{max}, is given by,

$$P_{max}(GPa) = \frac{12.5}{(d(mm))^2} \qquad (6.1)$$

where d is the diameter of the culet surface. The maximum pressure is lower when the diamonds are not optimally aligned with the culets as parallel as possible. These authors recommend a culet diameter of 750 microns for working at pressures up to 10 - 20 GPa, and a culet diameter of 500 microns for pressures up to to 30 GPa. The culets of our diamond anvils were cut by Lazare Kaplan Inc. (New York, NY) to a diameter of 1.2 mm. This considerably larger culet surface diminishes the pressure transmitted to the liquid for a given load and, according to equation 6.1, renders the cell incapable of achieving pressures greater than 8.7 GPa. This number is probably high and we estimate that the maximum pressure attainable with our cell is less than 3 GPa.

The advantages of larger culets for the present study are twofold. First, a given change in load results in a smaller incremental change in pressure. This is important for liquid studies where it is desirable to set a number of pressures for a given run. With our cell the load is increased by tightening the three screws which clamp the seats together shown in figure 6.1. Secondly, larger culets allow the use of a larger diameter gasket hole. Empirically, for a given culet diameter and gasket material,

the gasket thickness limits the highest attainable pressure. We used gaskets made from ordinary stainless steel shim stock 1/32" thick (800 microns). The hole diameter was 750 microns. Compare these numbers with a 100 micron thick gasket with a hole diameter of 200 microns used with 600 micron culets recommended for pressures to 10 GPa [89]. Our dimensions provide a larger sample volume which simplifies the crossing of the three optical beams necessary for a transient grating experiment. Pressures of 1 GPa were easily obtained as indicated by pressure-induced freezing of CS_2 in our cell which is known to occur at a pressure of 1.3 GPa.

6.3 Diamond anvil cell loading

Here we summarize the technique used to load liquids into our diamond anvil cell. The diamond anvils are secured to the stainless steel seats with ordinary epoxy. No special effort was made to insure parallel alignment of the culets. In practice, however, it was possible to routinely mount them parallel to within a few optical fringes with a minimum of effort. The cell is loaded by placing a finished gasket atop one of the diamonds. The diamond faces must be superbly clean to minimize parasitic light scattered in the direction of the ISS signal beam. Lens paper with a drop of methanol works well. Gaskets are made from 1/32" stainless steel (the particular steel is not so important) cut into 1/4" by 1/2" rectangles. A #69 drill held in a precision drill chuck was used to drill the hole. After drilling, the surfaces around the hole should be sanded smooth with emery paper to remove drill burrs. A gasket is precompressed to aid cell assembly. With the gasket hole centered over one diamond the anvil cell is

assembled by loosely bringing the diamonds together. Once the gasket is properly centered the screws which press the diamonds together are slowly tightened a little at a time. The gasket should be compressed enough that imprints from the diamond facets are visible but not so much that the hole diameter is reduced by more than ten percent. While the cell is closed the gasket is secured to one of the seats with a drop of superglue where the gasket contacts a steel ring placed around one of the diamond anvils to support the gasket. This prevents the gasket from slipping off when the two cell halves are clamped together.

The cell is opened and a drop of the liquid under study is placed in the gasket hole. A small chip of ruby should be added next, if used for pressure calibration. If the ruby chip is added first, the liquid often washes it out. A few air bubbles trapped in the liquid upon first loading the cell are not a problem as they can be squeezed out. In fact, a small amount of air is often useful, since it permits control measurements to be made at essentially atmospheric pressure.

6.4 Experiments on liquid carbon disulfide

Upon loading the cell, data scans were recorded at a series of pressures by incrementally tightening the three screws which clamp the cell halves together. Scans were recorded at four or five different settings before pressure-induced freezing was observed, indicating the pressure in the cell had reached 12.6 kbar [92]. Femtosecond ISS scans from a single such run are shown in figure 6.2. Polarizations were set to the "nuclear only" values of section 3.4. This made it easier to find the CS_2 signal which can

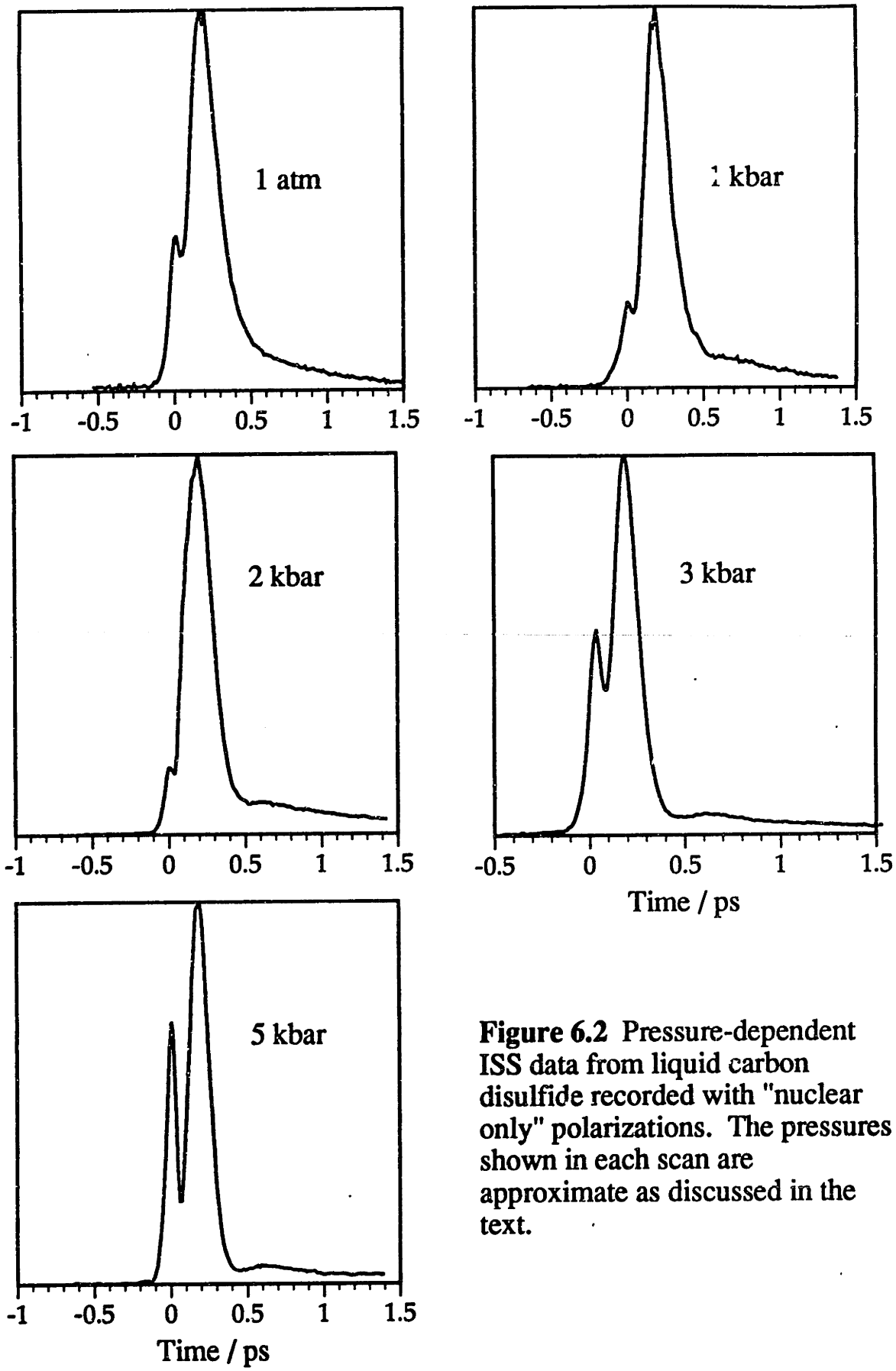

Figure 6.2 Pressure-dependent ISS data from liquid carbon disulfide recorded with "nuclear only" polarizations. The pressures shown in each scan are approximate as discussed in the text.

otherwise be obscured by the large electronic signal from the diamonds. We note that no noninstantaneous signal was observed from the diamond anvils. The scan in figure 6.3, recorded with all vertical pulse polarizations, shows only a pulse duration limited response in diamond, confirming the absence of any significant molecular signal component.

Each scan was obtained by averaging 500 laser pulses falling within a 20% peak-to-peak intensity discrimination window. At the highest pressures the carbon disulfide became a turbid, yellowish color and the scattered light increased tremendously, making it extremely difficult to record signal. Most likely the high-pressure liquid had corroded the stainless steel gasket. This problem might be avoided by using a gold-plated or teflon-coated gasket. Jonas and Hegemann reported that CS_2 becomes very corrosive at high pressure and they designed a special glass cell consisting of a glass piston in a glass cylinder for use with their conventional high pressure cell [58]. Baggen, van Exter and Lagendijk performed time-resolved stimulated Raman scattering experiments on CS_2 and found that it decomposed at 20 mW average power above 9.5 kbar [86].

In the experiments reported here, it proved impossible to determine the pressure in the usual way by measuring the pressure-induced shift of ruby fluorescence. The resolution provided by our 0.25 meter monochromator equipped with a diffraction grating run in first order was inadequate to resolve the small spectral shifts (0.365 nm GPa^{-1}) observed in this low pressure range. The only source we had available for exciting the ruby fluorescence was the doubled output from the Nd:YAG regenerative amplifier. The very high peak energies of these 70 ps pulses can cause damage in diamond via nonlinear absorption and a pair of

ISS signal from diamond

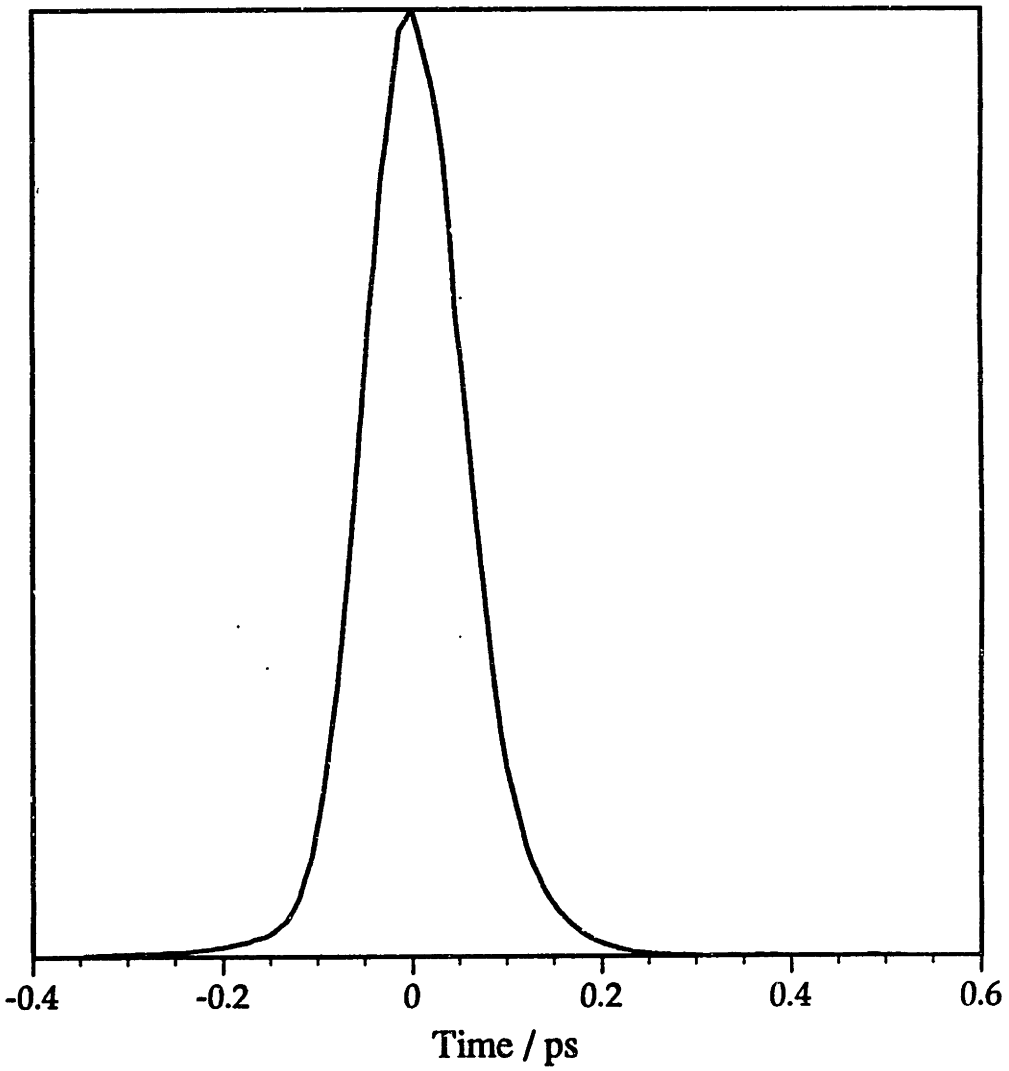

Figure 6.3 ISS signal from diamond used in diamond anvil cell. The scan shows that there is no measurable nuclear response from this material. All polarizations were vertical.

diamond anvils was actually destroyed trying to measure the ruby fluorescence. A low power CW laser source in the blue or green (helium cadmium or argon ion laser) and a higher resolution spectrometer should make such measurements simpler.

In principle, frequency-domain light scattering measurements of the reorientational correlation time of high pressure CS_2 could be used to estimate the pressure. S. Ikawa and E. Whalley measured the Raman reorientational correlation time, τ_{RAM}, of liquid CS_2 over most of the liquid range at room temperature up to a pressure of 10 kbar [59]. These authors report that the reorientation time is characterized well by a Debye-Stokes-Einstein law, increasing linearly with viscosity,

$$\tau_{RAM} \propto \frac{\eta}{k_B T} \tag{6.1}$$

Their best-fit expression for the reorientation time as a function of viscosity in units of the viscosity, η_0, at atmospheric pressure is,

$$\tau_{RAM} / \text{ps} = 0.555 + 0.780 \frac{\eta}{\eta_0} \tag{6.2}$$

As discussed in section 5.4, in the long-time limit, the ISS signal is expected to decay exponentially with the decay time given by the Rayleigh reorientational correlation time, τ_{RAY}. Of course, the Rayleigh reorientation time includes the effects of pair correlation and is known in the case of CS_2 to be longer than the Raman correlation time [57]. Ignoring the difficulties of correcting Raman correlation times for pair correlation, the major obstacle to using frequency-domain light scattering

estimates of the reorientation time vs. pressure as a means of pressure calibration is the disagreement between the ISS long-time decay times and the light scattering decay times discussed in section 5.4. Since the disagreement is greater at low temperature where the density of the liquid is higher, such a comparison was deemed too unreliable.

For this initial study, we had to settle for an approximate estimate of the pressure based on the following reasoning. Since the screws of the cell were turned through equal angles to increase the pressure between each scan, and because of the thick gasket used, it is reasonable to assume that the sample volume changed in an approximately linear fashion from scan to scan. From experience with several runs carried out on different days it was found that approximately six pressure steps could be made before pressure-induced freezing occurred. Using compressibility information for CS_2 at 293 K [92], we were able to estimate the density (and pressure) for each scan. These values appear in figure 6.2 and are likely accurate to no more than +/- 2 kbar. Certain, though, is the ordering of the magnitudes of the pressures, since the scans of figure 6.2 were made sequentially during the same day by incrementally increasing the load to the cell. In any event, the accuracy of the pressures is entirely adequate for elucidating the qualitative effects of pressure on the dynamics of CS_2 discussed in the next section.

6.5 Results and discussion

In figure 6.2 the ISS response of liquid CS_2 is shown at several pressures all recorded at room temperature. At zero delay time all scans show a

peak due to the effectively instantaneous electronic nonlinear polarizability of the liquid. The differing heights of this feature relative to the subsequent signal maximum of the nuclear nonlinear polarizability from scan to scan result from partial depolarization by the diamond anvils and are not significant. The scans have been scaled so that the maximum of the nuclear response of each scan has equal magnitude.

The same qualitative features of the data from the temperature-dependent scans of chapter 4 are evident in the scans in figure 6.2, suggesting a similar origin for the ISS signal of the two sets of experiments. Consequently, we have again chosen to analyze the signal by neglecting the scattering contribution from pairs of molecules and from interaction-induced effects. These assumptions will be critically discussed in chapter 8.

All scans show a rise in the signal after zero delay time which reaches a maximum after 180 fs, reflecting orientational inertial motion as discussed in section 5.2. The decay of the signal at later times reflects the return of the molecules to their isotropic orientations. At atmospheric pressure the decay shows two components, a rapid decay from the signal maximum out to approximately 500 fs followed by a much slower decay. As the pressure is increased, an oscillatory feature is observed near 0.5 ps probe delay time similar in appearance to the feature observed in the low temperature scans of chapter 5. The similarity is emphasized in figure 6.4 where data recorded at 170 K, 1 atm pressure is compared with the room temperature data recorded at 5 kbar pressure. Both scans were recorded with identical polarizations to suppress the contribution from the electronic material polarization. The orientational dynamics are similar whether density is increased by lowering the temperature at constant pressure or by

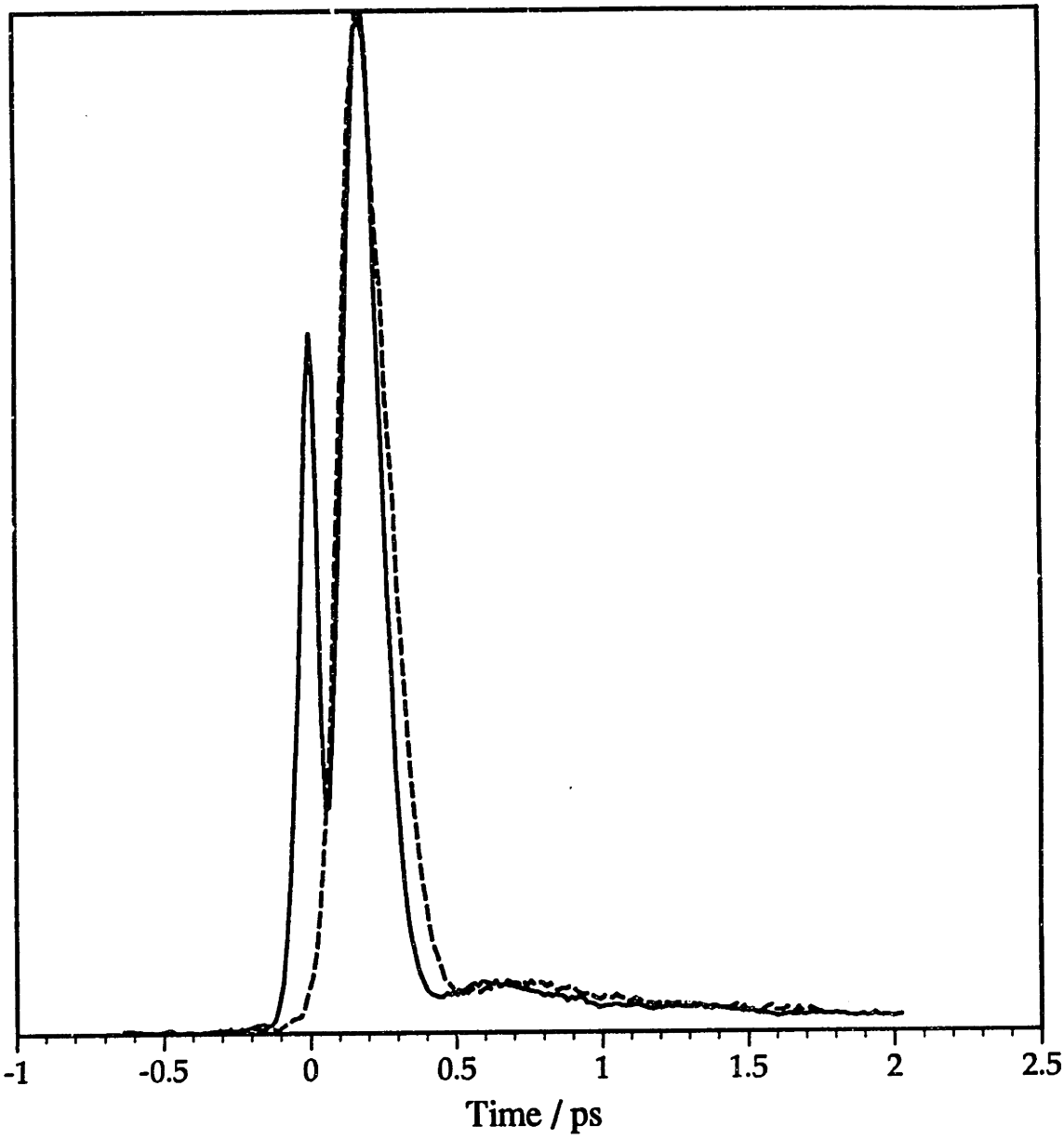

Figure 6.4 Comparison of 293K, 5 kbar ISS CS2 signal (solid curve) with signal recorded at 170 K, 1 atm (dashed curve) illustrating the similar response. Both signals were recorded with "nuclear only" polarizations.

increasing the pressure at constant temperature. Hegemann and Jonas found that the depolarized Rayleigh scattering from CS_2 in the spectral region corresponding to our oscillatory feature is strongly sensitive to density and insensitive to temperature changes at constant density [58]. Figure 6.5 compares scans from the temperature-dependent study of the previous chapter with scans from the high pressure study. Clearly, the ISS signal becomes weakly oscillatory in both cases.

One substantive difference between the scans recorded at high pressure and the scans recorded at low temperature is the time at which the maximum of the weak oscillation is observed. In all pressure-dependent scans in which the weak oscillation is apparent, the oscillation occurs at somewhat earlier times than in the temperature dependent data. Table 6.1 summarizes the results.

Table 6.1 Probe delay time, t_{MAX}, corresponding to the maximum of the weak oscillation for the ISS scans from the temperature- and pressure-dependent studies.

State point	t_{MAX} / fs	State point	t_{MAX} / fs
202 K	700	2 kbar	625
180 K	710	3 kbar	600
165 K	740	5 kbar	595
1 kbar	680		

If the oscillatory ISS signal arises from librational motions of CS_2 molecules, as discussed in the previous chapter, then this observation has a

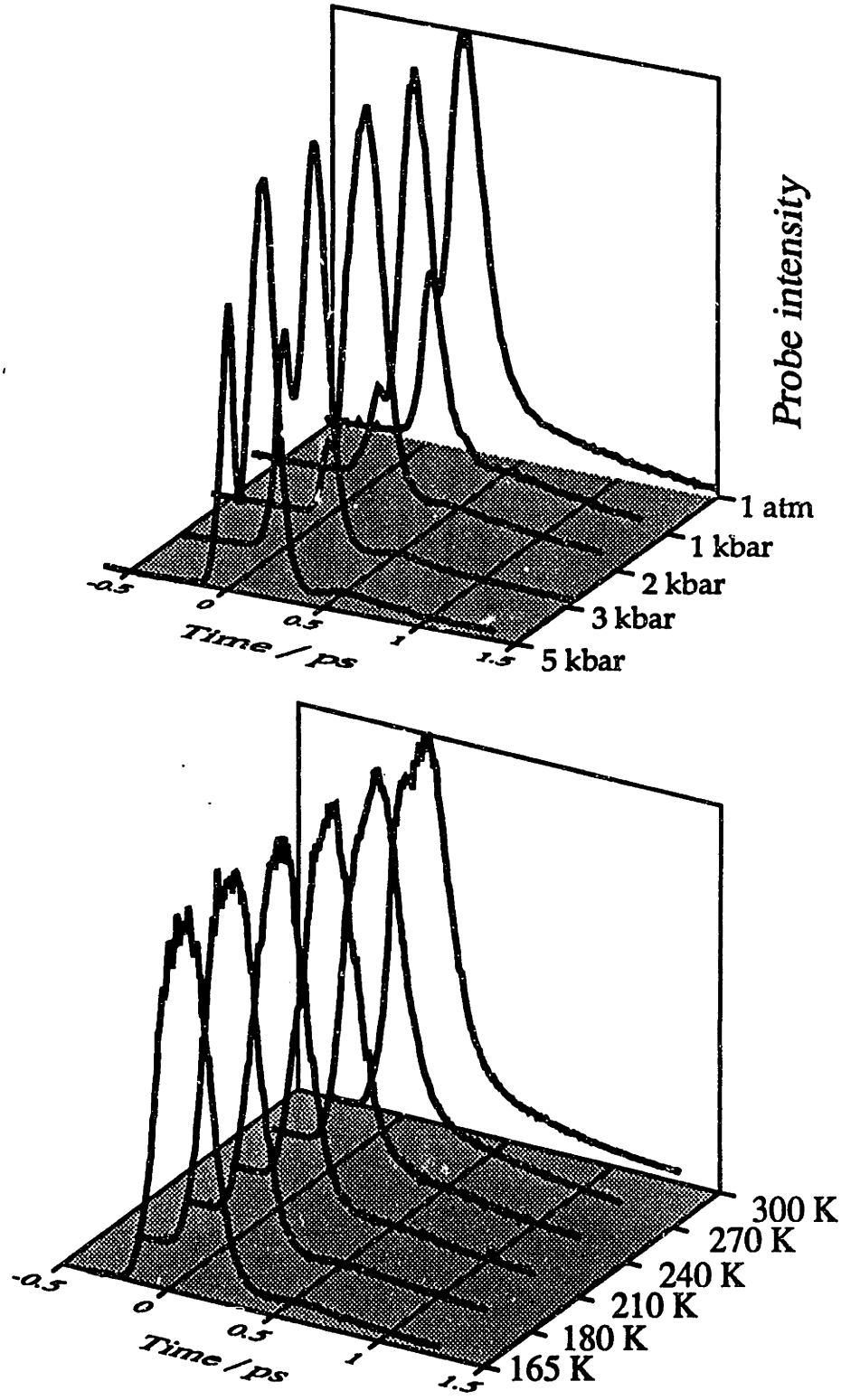

Figure 6.5 ISS data for CS_2 as a function of pressure and temperature.

simple interpretation. The mean frequency of libration is higher for the high pressure liquid at room temperature than for the low temperature liquid at atmospheric pressure. The kinetic energy per molecule is considerably greater in the case of the pressure-dependent scans than for the data recorded at low temperature. The greater mean angular velocity of each molecule will result in a rebound from the wall of a local cage at earlier times. Higher mean frequencies of libration are also found from fits to the data discussed next.

6.6 Fits to the short-time data

Fits were carried out using the same simple models of molecular libration with homogeneous and inhomogeneous dephasing discussed in chapter 5. As the signal / noise is not as good for these data, the fits were somewhat less well-determined than for the temperature-dependent data. Equally good fits were obtained using either equation 5.8 or equation 5.9. Some sample fits using the inhomogeneous dephasing model (equation 5.9) are shown in figures 6.6 and 6.7. The disagreement is greatest for the higher pressures at longer times, but in this region the signal / noise is worst. At these pressures considerable scattered light was observed to grow in over time due to the photochemical degradation of the liquid mentioned earlier. Since scans were recorded by sweeping the delay line from zero time towards longer times, there was usually significantly more scattered light at longer delay times.

The trends of the model parameters with increasing pressure are consistent with a librational model of reorientation. The best-fit parameter

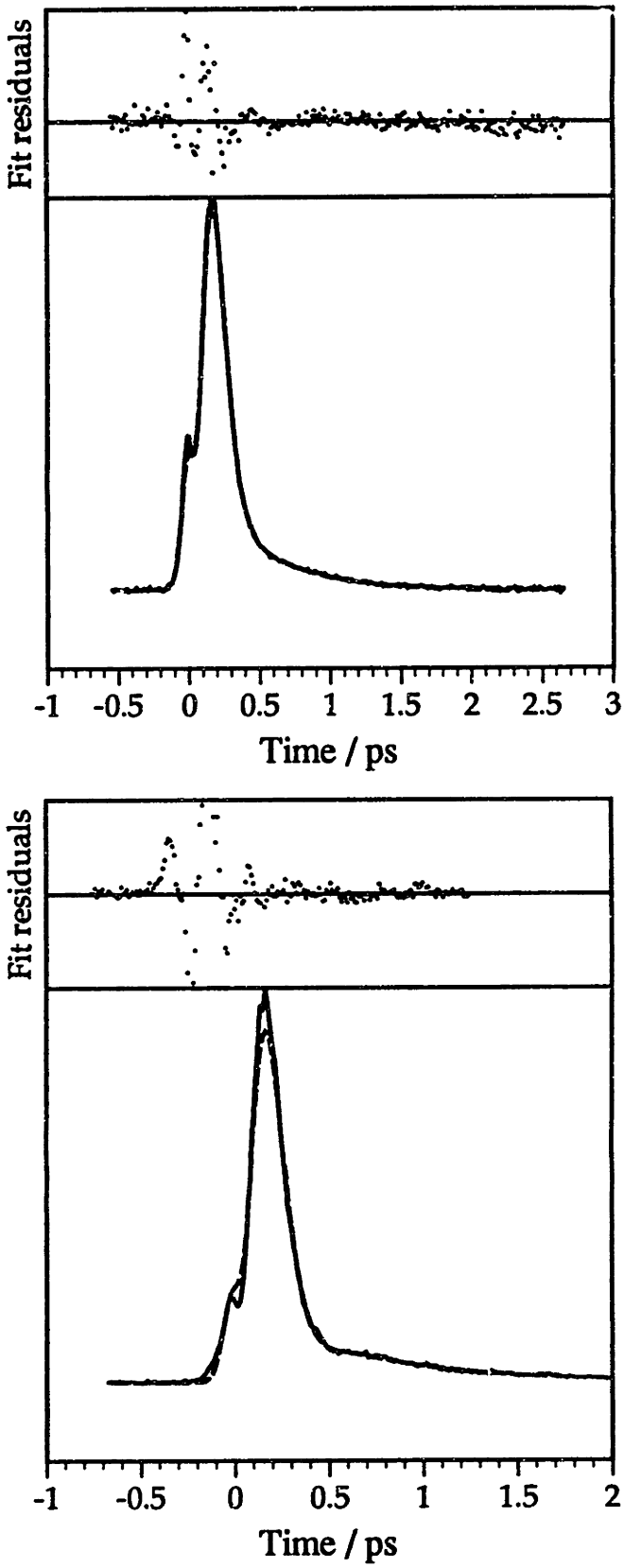

Figure 6.6 Fits to high pressure carbon disulfide ISS data using the inhomogeneously broadened librator model: 1 atm (top) and 1 kbar (bottom). Gaussian pulses with FWHM of 65 fs were assumed.

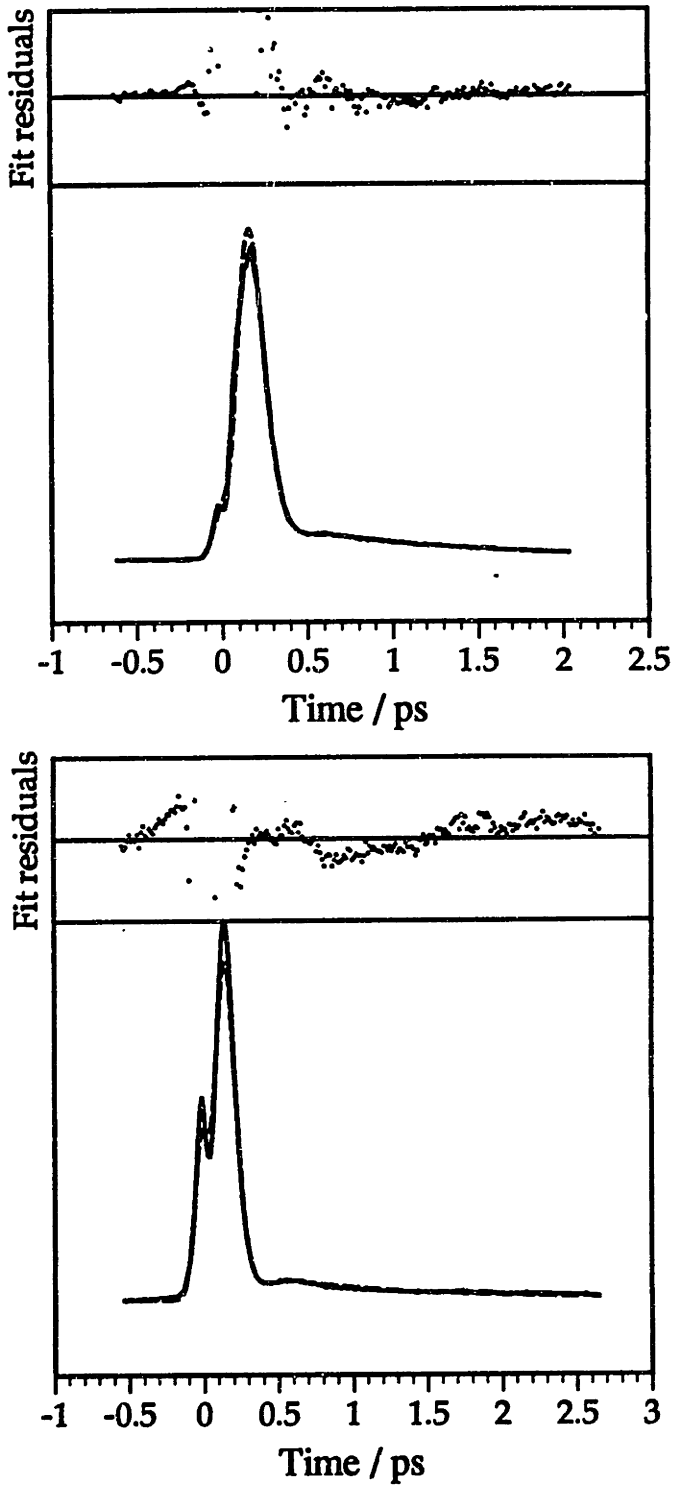

Figure 6.7 Fits to high pressure carbon disulfide data using inhomogeneously broadened librator model: 2 kbar (top), 3 kbar (bottom). The fit residuals are shown above each plot.

values are summarized in table 6.2 for fits made using the inhomogeneous libration response function of equation 5.9. Gaussian pulses with FWHM of 65 fs were used in numerical convolutions according to equation 3.10. Note that the values for the 1 atm scan given in the first line of the table agree reasonably well with the value for the 300 K data given in table 5.2. Just as in the case of the temperature-dependent study, the mean librational frequency, ω, is seen to increase with increasing liquid density. No definite trend in the parameter Δ characterizing the width of the frequency distribution is evident. This is in contrast to the results of the temperature-dependent study where the amount of inhomogeneity decreased as the oscillatory feature in the data became more pronounced. This suggests that the inhomogeneity, or the width of the distribution of librational frequencies, is affected most strongly by temperature.

Finally, the parameter characterizing the long-time decay of the data shows the proper trend with increasing pressure. The decay time is seen to increase with pressure, consistent with more hindered reorientation in the high density liquid. Note that the value obtained from the fits is considerably different than the value of an exponential fit to the long time part of the data. As discussed in chapter 5, this is due to the simplicity of the model underlying equation 5.9.

Table 6.2. Fitting parameters from fits to high pressure data with the inhomogeneously broadened librator model.

P / kbar	ω / ps^{-1}	ν / cm^{-1}	Δ / ps^{-1}	τ / ps
0.001	4.26	22.6	4.88	0.83
1	7.65	40.6	3.59	1.20
2	8.11	43.0	3.91	1.97
3	10.6	56.2	4.36	1.86
5	10.8	57.3	4.31	2.06

Chapter 7

ISS Experiments on Benzene and Substituted Benzenes

7.1 Introduction

We believe that short-time intermolecular vibrational motion is a general feature of the dynamics of many molecular liquids of anisotropic molecules. In this section ISS data is presented from benzene and from several benzene derivative compounds. The data again show an oscillatory response corresponding to a heavily damped vibrational process of low frequency. Comparison is made in this chapter to light scattering data which also provide evidence of librational reorientational dynamics.

7.2 Background

Liquid benzene has been studied extensively by Rayleigh light scattering. Depolarized Rayleigh scattering was performed as a function of temperature by Dardy, Volterra and Litovitz [71], and as a function of pressure by Dill, Litovitz and Bucaro [93]. In both studies, a pronounced shoulder is observed in the Rayleigh spectrum near 90 cm^{-1} which does not correspond to any of the intramolecular vibrations. The freezing temperature of benzene at atmospheric pressure is 283 K. Thus, benzene at

ambient temperatures has near-neighbor distances not too different from those in the solid and molecular reorientation ought to show a tendency for libration. This is the interpretation given by a variety of researchers to the short-time behavior of the reorientational correlation functions calculated from Rayleigh spectra [71,72,93]. The reorientational correlation functions determined by these authors show a "glitch" near 450 fs. Physically, they associate this behavior with the fact that molecular collisions do not completely randomize the angular velocity.

Danninger and Zundel point out that the reorientational motion in benzene is diffusional for times > 1.0 ps and is fit well by a free rotor expression at times < 0.1 ps [72]. At intermediate times, however, there is a complicated transition from free rotor to diffusional motion. Angular velocity correlation functions calculated from the data show several oscillations about zero, indicating librations of single molecules in potential wells caused by their neighbors which are damped by diffusion. The lack of significant differences in the signal from nonpolar molecules (benzene, mesitylene) and polar ones (benzonitrile) suggests that short-range forces are more significant for determining libration than long-range dipolar forces. This is further confirmed by the strong density dependence of these effects. Finally, there is a tendency for the librations to become more strongly damped as the temperature is increased. Danninger and Zundel do not believe that the collective orientations (pair correlations) will have much affect on the short-time part of the correlation functions.

7.3 ISS data and discussion

Impulsive stimulated scattering experiments were performed on benzene and several benzene derivatives using amplified 65 fs pulses all with a central wavelength of 615 nm. The data were recorded at ambient temperature and pressure in the transient grating experimental geometry already described at length in this thesis. A typical scan from liquid benzene is shown in figure 7.1. From this signal it is clear that benzene, like CS_2, shows a delayed rise, demonstrating the inertial character of the reorientational motion at short times. Noteworthy are the substantially different short time characteristics of the benzene signal compared to CS_2. This is evident in figure 7.2 where the benzene data from figure 7.1 are compared with the nuclear-only ISS data from CS_2 recorded at room temperature and pressure. The peak of the nuclear response occurs at 160 fs delay for benzene compared with 180 fs for carbon disulfide. After reaching a maximum the ISS signal from benzene also decays more rapidly than the CS_2 signal. In the framework of the short-time models discussed in chapter 4, this could be the result of a higher mean frequency of libration, or it may reflect greater damping. Increased damping (in the sense of equation 4.7) is plausible on the basis of the large steric hindrance of benzene molecules to rotation.

Following a rapid decay of the initial signal a broad hump is visible. This feature occurs at 450 fs probe delay time in excellent agreement with the time of the bump in the correlation functions calculated by Dill *et al.* [93]. The log plot at the bottom of figure 7.1 clearly reveals the vibrational character of the intermolecular motion in benzene.

Liquid benzene ISS response

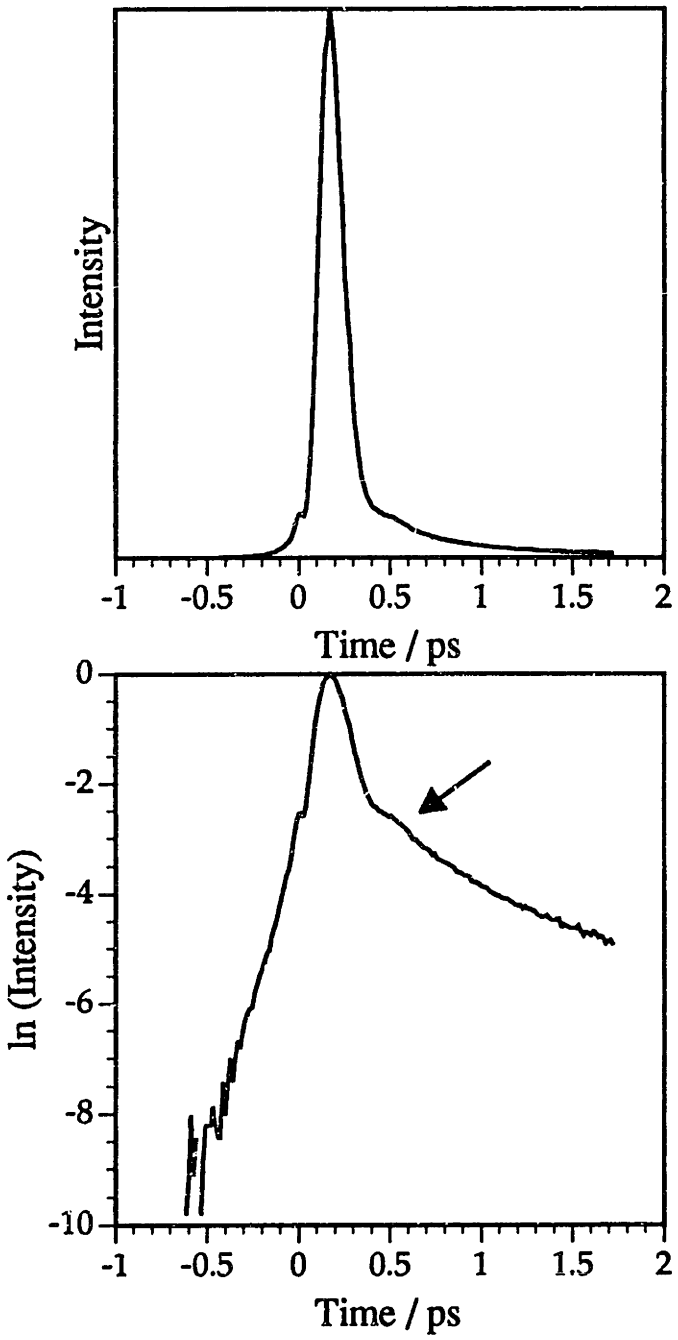

Figure 7.1 Impulsive stimulated scattering signal recorded from liquid benzene at 293 K on a linear (top) and logarithmic (bottom) plot. The polarizations were set to minimize the electronic signal contribution. The arrow in the log plot at bottom points to the heavily damped feature at 480 fs delay time.

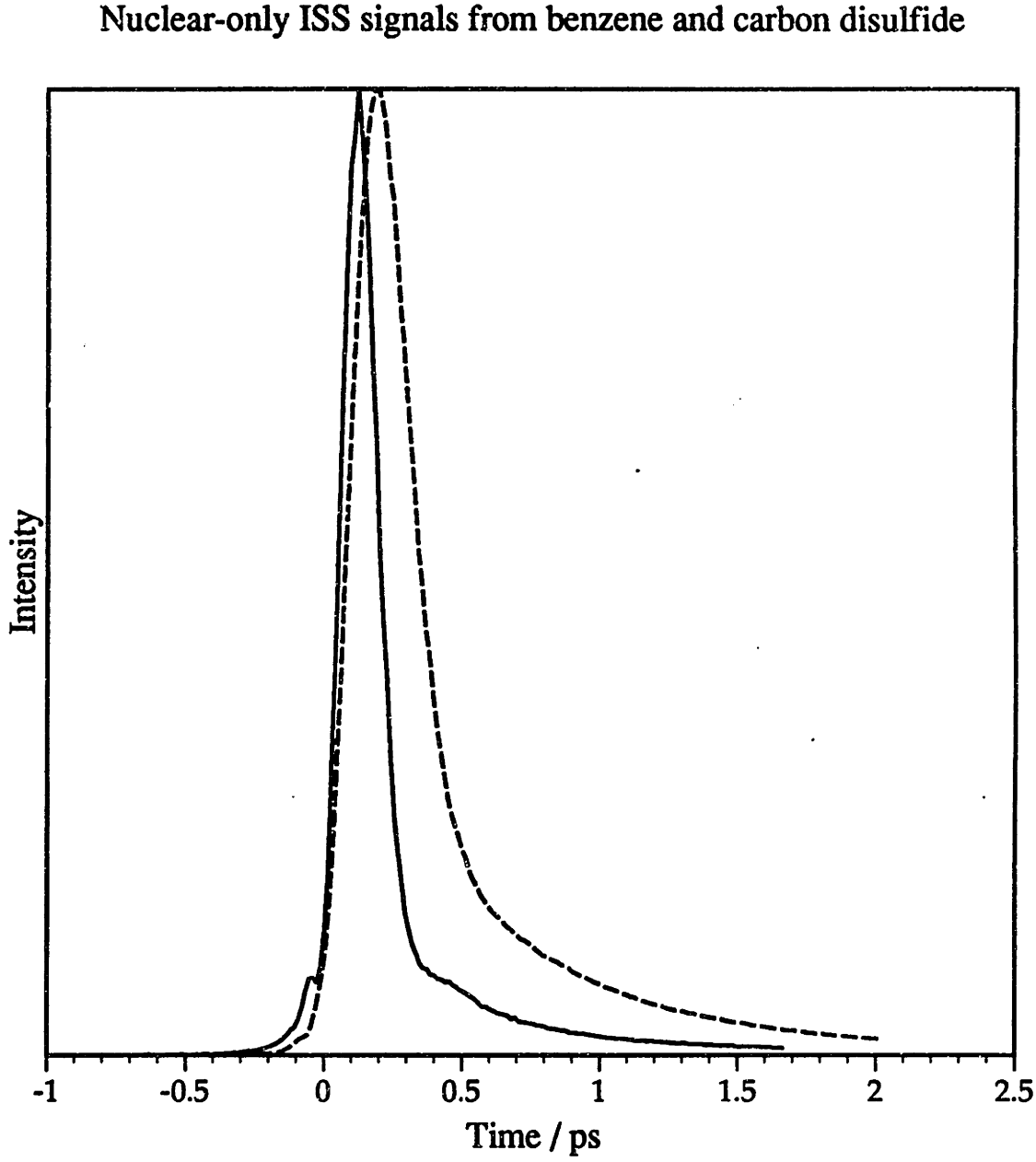

Figure 7.2 Comparison of nuclear-only signal for carbon disulfide (dashed curve) and benzene (solid curve). The benzene signal reaches a maximum at earlier times and then decays more rapidly than the CS2 signal.

We note that benzene was previously studied with 45 fs pulses in an optical Kerr effect experiment by Etchepare *et al.* [94]. While these authors did note the occurrence of several relaxation times for the molecular processes in the ultrafast response, they failed to observe the striking hump seen in our data. The explanation likely lies in our superior signal-to-noise ratio (compare figure 2 of reference 94 with the log plot in figure 7.1).

We expect an appreciable contribution to the collective polarizability of benzene from interaction-induced effects. Nonetheless, we feel that motions which contribute to I-I polarizabilities will decay rapidly enough that we are safe in assuming that the feature at 400-500 fs arises primarily from orientational dynamics. We believe, further, that the signal is primarily due to single molecule reorientation, since comparison of Rayleigh and Raman light scattering spectra suggest negligible pair correlation [72].

Data for a variety of related compounds are shown in figure 7.3. Each of these liquids also shows short-time inertial motion resulting in a rise in the scattering signal after t=0. Most of these liquids also show a librational response. This effect is somewhat obscured in the case of mesitylene where intramolecular oscillations are also visible. The persistence of nonoscillatory signal indicates the vibrational dephasing rate is more rapid than the orientational relaxation rate.

Extension of these experiments to pyridine, furane and thiophene should provide additional information on short-time librational motion as all of these liquids have been found to have significant librational features in frequency-domain light scattering spectra obtained by Versmold [56].

Figure 7.4 shows the long-time behavior of the VVVV ISS signal from benzene. The decay is more complex than single exponential.

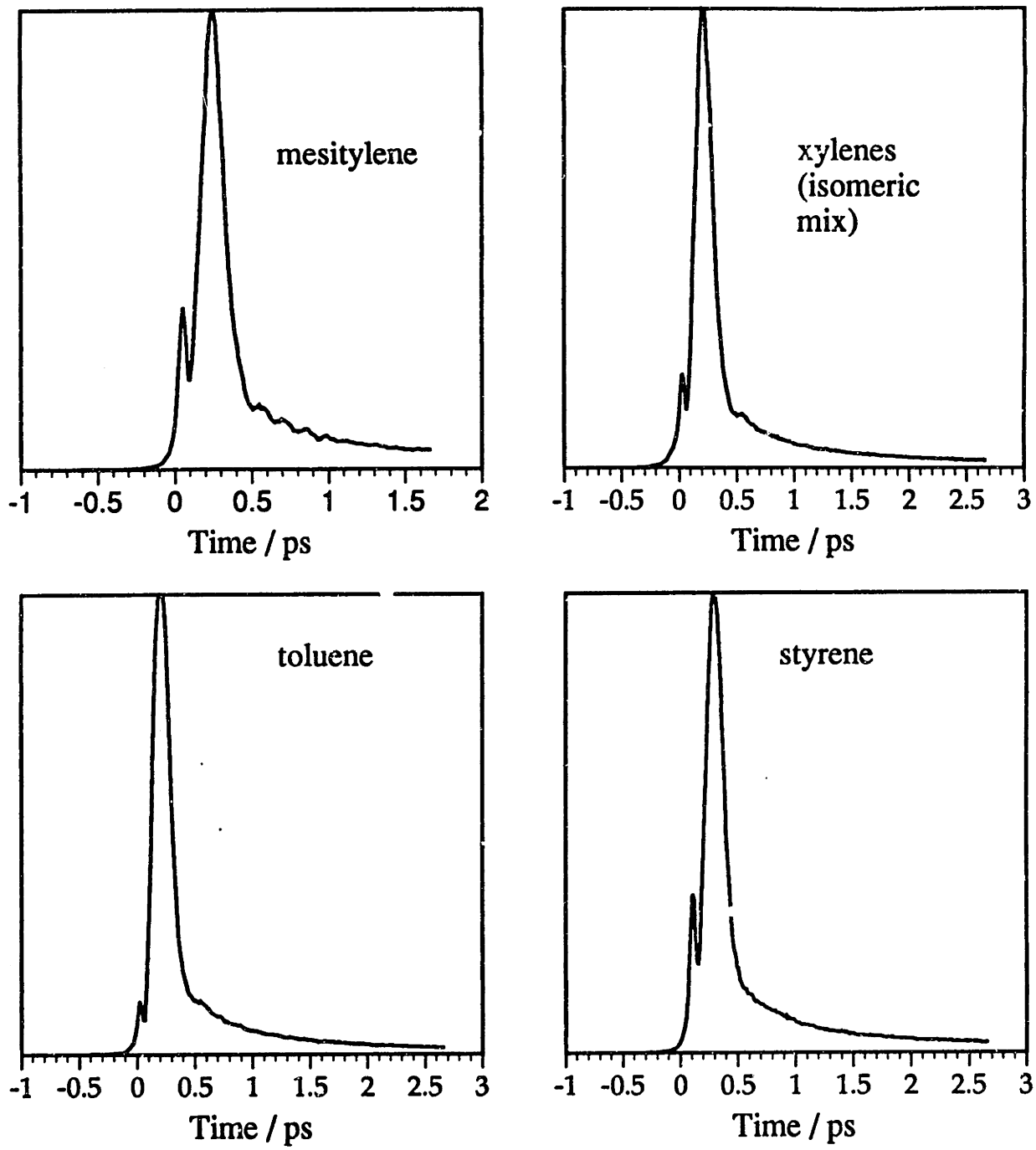

Figure 7.3 ISS data from several benzene related compounds showing short-time intermolecular vibrations.

Although data should be taken out to longer delay times in order to better characterize these decays, there is no doubt that the decay is not single exponential for the first 2 - 3 ps. Either pair correlations, interaction-induced motions or cross-terms involving both (see equation 3.29) may be responsible for this behavior. Keeping in mind that the data for these liquids is poorly characterized as exponential, the decay time, τ_{ISS}, of the long-time data was estimated by fitting the ISS data at times $t > 2.0$ ps to a single exponential. Table 7.1 summarizes the results. As was observed for carbon disulfide (section 5.4), the values are in poor agreement with the Rayleigh reorientational times, τ_{RAY}. This may be because of the difficulties of accurately measuring linewidths near zero-frequency from Rayleigh wing spectra, or it may be that ISS data recorded to longer times would eventually show a diffusional decay with the same decay time. The latter possibility is especially intriguing since, if true, it implies that the interaction-induced (and / or the Rayleigh pair contribution) to the signal decays very slowly in these liquids.

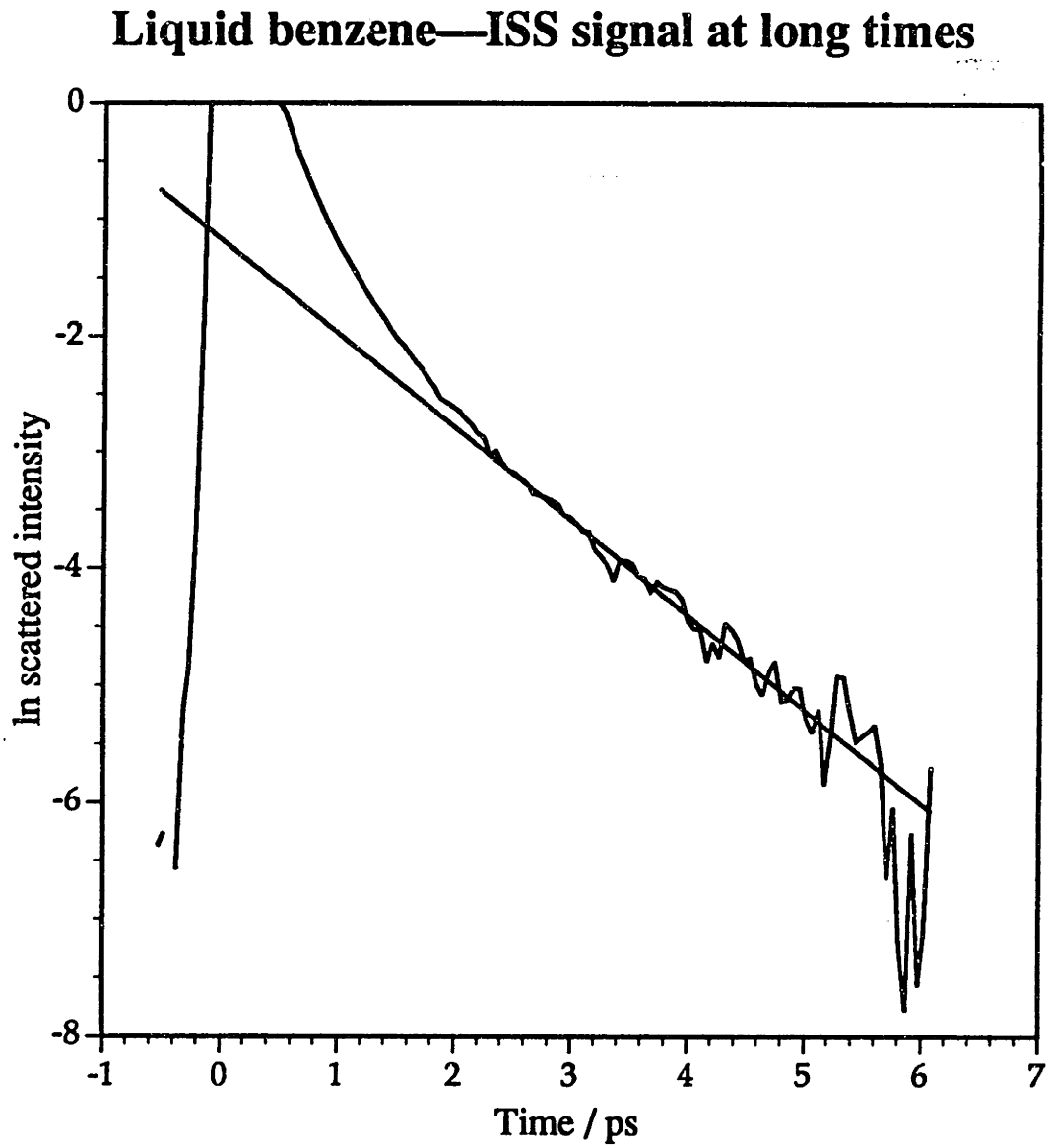

Figure 7.4 Logarithm of benzene data out to 6 picoseconds delay time. The straight line corresponds to a time constant of 2.4 ps, and shows that the ISS decay deviates significantly from single exponential, particularly in the first few picoseconds.

Table 7.1 Reorientational times from ISS data compared with data from Rayleigh light scattering of a few benzene compounds. τ_{ISS} was determined by fitting the ISS data to a single exponential at times t > 2.0 ps as described in section 5.4.

Substance	τ_{ISS} / ps	τ_{RAY} / ps (T / K) (ref. [72])
benzene	2.4	3.3 (283)
xylene	3.9	10.3 (293)
mesitylene	4.1	10.3 (293)
toluene	3.8	

In summary, the appearance of heavily damped, oscillatory structure in the ultrafast response measured by the ISS experiment appears to be a general feature of a variety of anisotropic molecular liquids. Extensions of this work to studies as a function of thermodynamic state are planned.

Chapter 8

Molecular Dynamics Study of Subpicosecond Reorientation in Liquid Carbon Disulfide

8.1 Introduction

The previous chapters described measurements of the subpicosecond nonlinear optical response of several molecular liquids of optically anisotropic molecules which indicate vibrational intermolecular dynamics. Since strong angular forces between molecules may lead to reorientational motion which is librational in character, it was suggested that the signal reflects mainly reorientational motions of single molecules. However, as discussed at length in chapter 3, the signal from the ISS experiment (as well as from frequency-domain spectral measurements) contains, in general, a complicated mix of contributions including single molecule reorientation, pair correlation, I-I terms as well as cross terms between all the different components. In this chapter computer simulations of CS_2 are described which were carried out to gain additional insight into the dynamics of the signal contribution arising from the short-time reorientation of single molecules.

Molecular dynamics (MD) simulation has been used for about thirty years to learn information which is often complementary to experiment. As discussed in chapter 3, there is still much work to be done to construct a theory of light scattering from molecular liquids which permits

unambiguous "inversion" of band shapes (from frequency-domain experiments) or transients (from time-domain experiments) to obtain microscopic dynamical information. In light of these difficulties computer simulation is invaluable. Since complete dynamical information is generated for a particular model of intermolecular interaction, MD simulation permits dynamical theories of liquids to be tested directly without having to first relate the light scattering observables to molecular dynamics.

8.1.1 Past MD studies of liquid carbon disulfide

Molecular dynamics studies of the structural and dynamic properties of liquid carbon disulfide have been reported by several researchers using a number of different intermolecular pair potentials. Steinhauser *et al.* performed the first MD simulations of the liquid using a Lennard Jones (LJ) atomic site potential [62]. They evaluated static pair correlation functions as well as time correlation functions for single molecule properties [63]. Tildesley and Madden used the same potential model with different LJ parameters to study both static [64] and dynamic properties [65]. They reported excellent thermodynamic agreement and excellent agreement of dynamical quantities with experiment for simulations using this potential model at several state points along the saturated vapor curve (also called the orthobaric curve). These authors also used this potential to study interaction-induced light scattering effects within the first-order dipole-induced-dipole polarizability model [66].

Ladanyi and Geiger used the Tildesley and Madden potential (hereafter called the TM potential) to study the Rayleigh and Raman line

shapes from CS_2 including dipole-induced dipole polarizability contributions to all orders [67]. These authors also compared their MD results for the collective polarizability of CS_2 with femtosecond experiments [69]. While many of the qualitative trends of the data were reproduced, their MD simulations failed to account for the oscillation at 600-700 fs seen in the dense liquid and discussed in chapters 5 and 6. The highest density simulated in all of the above studies is 1.42 g cm^{-3}, the experimental density for the liquid at 1 bar and 190 K. Since this density is at the low density edge of the range of densities for which our experimental data shows an oscillatory response, it is conceivable that still greater densities must be simulated before librational dynamics will be observed. This is the motivation of the present calculations.

This chapter describes MD simulations of CS_2 carried out over a very wide range of density with the goal of investigating whether molecular libration occurs in the computer model of the liquid. We have decided to focus on single molecule properties because the autocorrelation functions describing such processes can be accurately evaluated from computer simulations. In light of our experimental evidence, we believe the dominant mechanism for the oscillatory time-domain response arises from the reorientation of single molecules. This notion is further supported by the simulation results from Ladanyi and Geiger [67,69]. They found that modelling DID interactions to all orders increased the relative contribution of single molecule reorientation. Perhaps the most compelling reason for studying single molecule reorientation is that it can be exactly modelled with no approximations for a given interaction potential. We can thus avoid many of the assumptions which go into modelling interaction-induced polarizability fluctuations.

After briefly discussing the MD method, thermodynamic and structural results obtained from the TM potential are presented for some high density state points. Next, dynamic results are discussed with special emphasis on the orientational correlation functions necessary for the description of reorientation of linear molecules. Finally, comparison is made between the MD simulations and experiment.

8.2 Simulation of molecular liquids

The field of MD simulation has grown tremendously with increases in computational power and interest in simulating increasingly complex dynamical properties of condensed phase systems. In a typical MD simulation of a molecular liquid the equations of motion are solved as a function of time for N particles confined to a cubic box. Periodic boundary conditions are used to simulate an infinite liquid. Each time a molecule leaves the box, another reenters from the opposite side. The coupled set of second order differential equations governing the positions and orientations of the molecules in the system are solved by choosing a sufficiently small time interval, or timestep, during which the force on each molecule can be assumed constant. At each timestep the force on a molecule due to other molecules in the system is calculated. In practice, the intermolecular potential is sufficiently short-ranged that the potential between a pair of molecules is set to zero for distances greater than a specified cutoff radius. Once the total force on a molecule is known, its position at the next time step is predicted using a simple integration algorithm. The timestep is chosen such that the total energy of the system of N molecules is conserved to a specified level. In Appendix A additional

technical information is given about the design and implementation of the molecular dynamics code written by the author to perform these calculations. Appendix B provides a discussion of the minimization of run time in MD simulations.

8.3 MD simulation details

Molecular dynamics simulations were carried out at a variety of state points chosen to lie along two line segments drawn in the experimental phase diagram of liquid carbon disulfide, shown schematically in figure 8.1. Line segment AB corresponds to the 293 K isotherm, while line segment CD corresponds to the isobar at 1 atm pressure. These paths correspond to the experimental conditions of the temperature- and pressure-dependent femtosecond ISS studies described in chapters 5 and 6. The constant energy MD simulations described here do not, of course, constrain the temperature or the pressure. Nonetheless, we refer to the simulations as either isobaric or isothermal to emphasize the connection to experiment. The isobaric simulations were performed by setting the density to the experimental value at atmospheric pressure at a given temperature [95]. The desired temperature was set prior to each production run by velocity scaling. The isothermal runs used experimental densities [92] corresponding to a temperature of 293 K, and the temperature was likewise set by velocity scaling. All simulations were performed on a Sun Microsystems Sparcstation 1 computer configured with approximately 100 Mb of free disk space, 16 Mb of swap space and 8 Mb of RAM. The approximate CPU time for 1 timestep of a 108 molecule

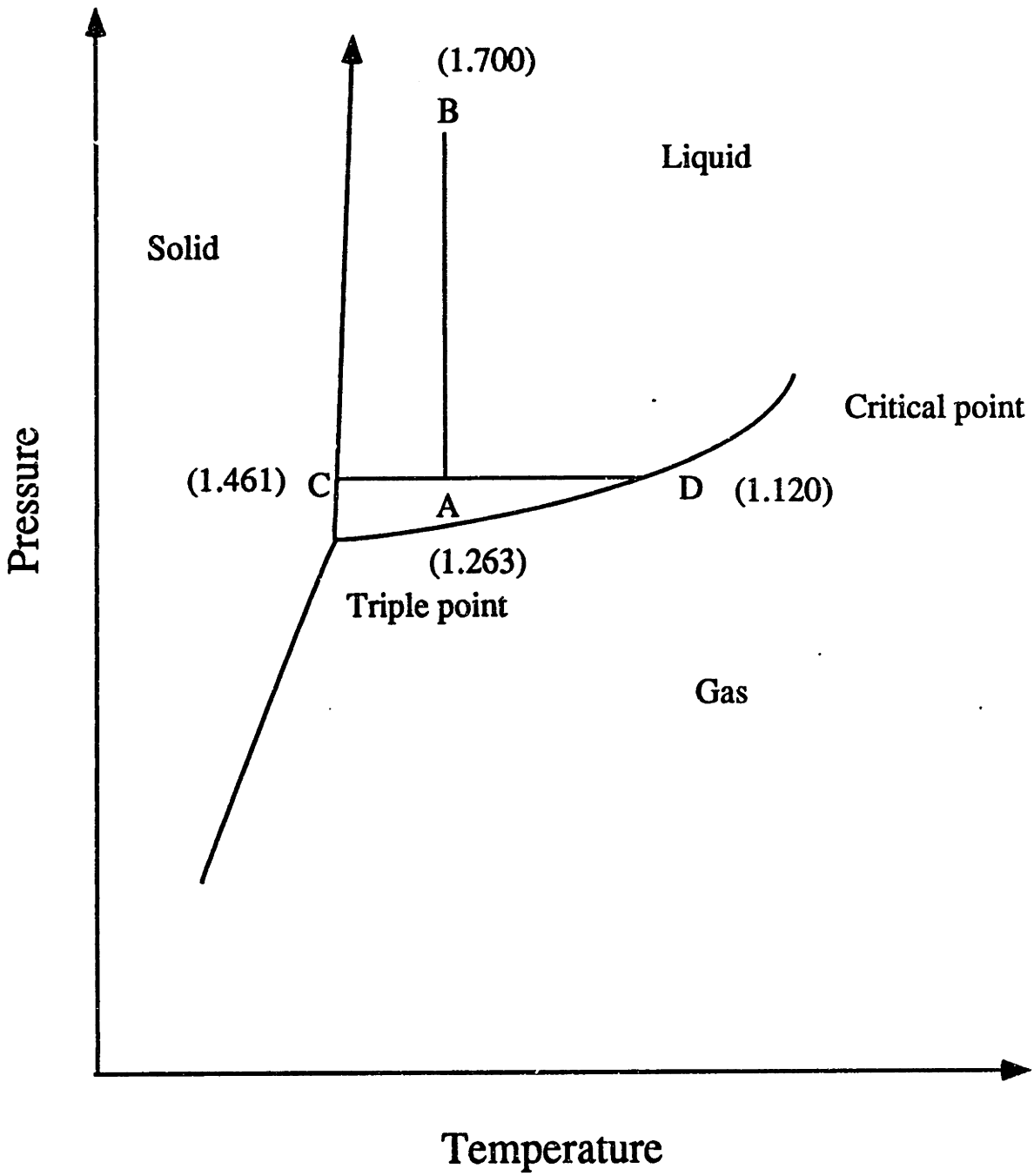

Figure 8.1 Schematic phase diagram of carbon disulfide. Line segment AB represents the 293 K isotherm, line segment CD represents the 1 atm pressure isobar from which state points for the MD runs were chosen. The end point of each path is labelled by the experimental density in grams per cubic centimeter.

simulation was 1 second. Thermodynamic properties, run lengths and other details are summarized in table 8.1 for all runs.

The TM intermolecular potential used in these simulations is a Lennard-Jones (LJ) site-site potential in which 3 interaction sites are positioned at the atomic positions of each CS_2 molecule. The potential parameters are given in table 8.2. LJ site-site potentials are the most common ones in use for the simulation of liquids of polyatomic molecules lacking long-range forces. Although the potential between two sites is spherically symmetric, the total potential between two molecules is anisotropic, since it is the sum of 9 site interactions (4 S-S, 4 C-S and 1 C-C) located at spatially distinct points. The molecules are modelled as rigid bodies with no internal degrees of freedom.

Table 8.2. Tildesley and Madden Lennard Jones interaction site potential parameters for CS_2 [from ref. 64].

sites, ab	ε_{ab} / k_B (K)	σ_{ab} (Å)
C-C	51.2	3.35
S-S	183.0	3.52
C-S	96.8	3.44
Bond lengths: $d_{CS} = d_{SS}/2 \simeq 1.57$ Å		

The translational equations of motion were solved using the Verlet leapfrog algorithm [96]. The rotational equations of motion were solved using the Singer algorithm generalized to n-site linear molecules [97]. The chosen

Table 8.1 Run statistics and thermodynamic variables from molecular dynamics simulations. Standard deviations are given with each thermodynamic variable X as σ_X. Key: ρ = mass density, T = temperature, U = configurational energy, E = total energy, P = pressure, Δt = timestep, nsteps = total number of steps in run, t_{tot} = total length in time of simulation.

ρ / g cm^{-3}	nmols	T / K	σ_T	U / kJ mol^{-1}.	σ_U	E / kJ mol^{-1}	σ_E	P / 10^8 Pa	σ_P	Δt / fs	nsteps	t_{tot} / ps
Constant temperature runs.												
1.263	108	293	11	-25.23	0.23	-19.13	0.020	0.194	0.28	4.0	37500	150
1.263	500	292	5	-25.27	0.097	-19.21	0.0058	0.135	0.12	3.0	5000	15
1.415	108	295	12	-27.80	0.25	-21.68	0.024	2.57	0.32	3.5	59700	209
1.415	108	296.5		-27.79	0.25	-21.62	0.04	2.60	0.31	3.5	288000	1008
1.415	1372	296.7	3.3	-27.81	0.069	-21.64	0.0046	2.58	0.086	3.5	18161	64
1.461	256	301	8	-28.29	0.17	-22.04	0.013	3.85	0.21	3.0	13800	41
1.500	108	293	12	-28.84	0.25	-22.75	0.03	4.83	0.32	3.0	50000	150
1.534	108	299	13	-28.93	0.28	-22.71	0.017	6.25	0.36	3.0	40000	120
1.593	108	294	13	-29.24	0.27	-23.13	0.015	8.65	0.37	2.5	44000	110
1.618	108	294	13	-29.40	0.3	-23.27	0.01	9.74	0.37	2.5	44000	110
1.663	108	291	13	-29.08	0.27	-23.03	0.016	12.5	0.38	2.25	44550	100
1.699	108	283	12	-28.96	0.25	-23.07	0.014	14.6	0.36	2.0	40000	80
1.900	256	307.4	8.4	-21.60	0.18	-15.21	0.0076	37.8	0.28	1.8	41581	75
1.618†	108	288	13	-27.30	0.3	-21.30	0.01	13.1	0.40	2.5	32000	80
Constant pressure runs.												
1.387	108	204	8	-28.80	0.18	-24.55	0.015	0.11	0.22	3.5	30000	105
1.433	108	183	8	-30.00	0.16	-26.20	0.016	0.34	0.22	3.5	20000	70
1.456	108	161	7	-30.86	0.14	-27.52	0.020	0.13	0.19	3	40000	120

Notes:

†This run used a potential suggested by Ladanyi (table 8.6). All other runs used the Tildesley and Madden potential (table 8.2).

Cutoff radius, r_{cut}, is 10 Angstroms for all runs.

density and number of molecules constrains the size of the simulation box. For all runs a cutoff radius of 10 Angstroms was used. Only molecules whose centers are separated by less than the cutoff radius interact, and in this case all site interactions are evaluated, regardless of site-site distances. As usual, the nearest image convention is used for determining the neighbors of a given molecule. At all simulated densities one-half the box side, $L_{box}/2$, was always greater than the cutoff distance.

The starting configuration for each run was obtained by adjusting the density (and, in some cases, temperature) of a configuration from another run at a nearby state point. In this manner it was necessary to generate an initial configuration from an overexpanded FCC lattice only once for a given N, where N is the number of molecules in the simulation. This procedure insured that each configuration was very well equilibrated with no net orientational alignment or angular or linear momentum. This procedure was critical for the high density simulations reported here. Some trial runs showed that it can require a very long time ($> 10^5$ timesteps) to reach translational and orientational equilibrium, if the molecules are started from an overexpanded FCC lattice at high number density. Appendix A discusses the equilibration procedure in greater depth.

Most MD runs were performed with 108 molecules. Simulations with larger systems produced orientational correlation functions which were identical within statistical noise (see figure 8.7a-c), justifying the use of a smaller number of molecules. The last column in table 8.1 shows the total run time in picoseconds. The comparatively long simulation times reported here are necessary to decrease the statistical error of the correlation functions calculated, since the relaxation times of the

correlation functions of interest become longer at high density (see section 8.6.1). As the density is increased the timestep must be decreased in order to conserve energy to the same degree.

8.4 Thermodynamic properties

A goal of this work was to investigate single molecule reorientation in liquid CS_2 over the entire liquid range along the chosen isobar and isotherm. The limiting values of temperature and density are shown in figure 8.1 for the two thermodynamic paths chosen for these simulations. There is no reason to expect the TM potential used here to exhibit phase transitions at the same state points. In order to determine whether the liquid range of this potential has been exhaustively studied, it is important to identify the conditions at which the behavior of the computer liquid ceases to be liquid-like. The phenomena of melting, freezing and glass formation in MD simulation have been reviewed by Frenkel and McTague [98]. Nucleation in LJ atomic liquids was first observed in 3D atomic LJ liquids by Rahman, Mandell and McTague [99]. Crystallization has been reported to occur more readily by isothermal compression than by isobaric cooling [100]. Still very little is known about nucleation in MD simulations of molecular liquids, and the liquid-solid phase transition in a computer simulation of a molecular liquid has never been observed.

At the pressure-induced freezing point of the real liquid (at a pressure of 12.6 kbar) the density is approximately 1.70 g cm^{-3} [92]. A simulation performed at the considerably higher density of 1.90 g cm^{-3} showed no evidence of crystallization. Even assuming the pair potential

used in these simulations is appropriate for the crystal, the run length is probably not long enough for a nucleation event to have a reasonable probability of occurring. The value for the translational diffusion constant at this density (described in section 8.6.2 below) is over 200 x smaller than for the liquid at ambient temperature and pressure, a value characteristic of a glass. Structure in the pair correlation function at this density (see section 8.5) also suggests that a changeover to glass-like dynamics may occur near this density. In conclusion, it appears likely that the entire liquid range of the TM potential along the 293 K isotherm was studied.

Since the TM potential has been investigated here in new regions of the liquid phase diagram, it is useful to compare the thermodynamic data from the MD runs with experiment. Table 8.1 lists the average pressures calculated from the virial equation for each run. A long-range correction was used in which the pair distribution function, g(r), governing the distribution of molecular centers was assumed to be unity at distances r greater than the cutoff radius, r_{cut}. In figure 8.2 the MD values are plotted versus density together with the experimental pressures [92]. While the MD pressures are consistently 20% greater than the experimental ones, the agreement is nevertheless quite good even at high density and we believe this potential will be an adequate initial model of interactions in the dense liquid.

8.5 Structural properties

In this section the static orientational structure of liquid CS_2 is discussed from the results of the isothermal MD runs. Information about the time-

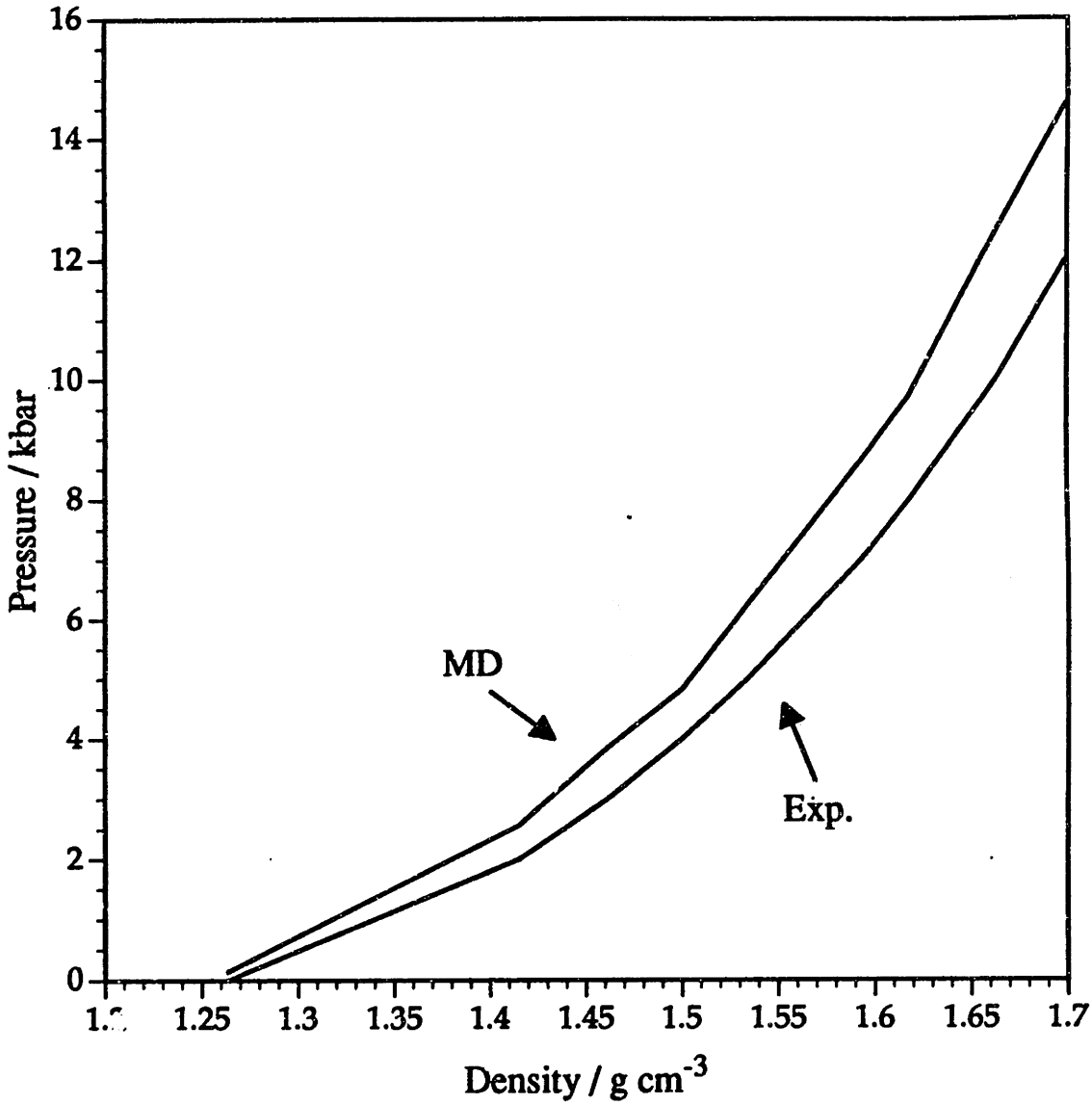

Figure 8.2 Comparison of pressures calculated from MD runs using the virial equation with experimental values from reference 92.

averaged structure of the liquid can be obtained from the site-site correlation functions,

$$g_{AB}(r) = \frac{V}{N^2}\left\langle \sum_{i \neq j} \frac{\delta(r - |r_{iA} - r_{jB}|}{4\pi r^2} \right\rangle. \qquad (8.1)$$

This quantity is proportional to the probability of finding the B-site of one molecule a distance r from the A-site of a different molecule, regardless of the orientation of the two molecules. These quantities are related to the intermolecular structure factor measured by x-ray and neutron scattering [62].

The site-site correlation function for carbon atoms is simply the radial distribution function, giving the distribution of molecular centers. In figure 8.3 the carbon-carbon site-site distribution function, $g_{CC}(r)$, is shown at several densities along the 293 K isotherm. As the density of the liquid changes, this function provides a measure of structural changes. At lowest density, figure 8.3a, the first peak near 4 angstroms appears as a soft shoulder on the rising edge of a much stronger second peak near 5 angstroms. As density increases towards the pressure-induced freezing point the two peaks become increasingly better resolved, until at a density of 1.90 g cm^{-3} the first peak is actually more intense than the second one. At this density an additional peak is also seen to grown in near 6.5 Å, indicating an increasingly structured liquid.

While $g_{CC}(r)$ is obtained by averaging over all relative orientations of pairs of molecules, its structure does implicitly reflect preferred orientational alignments. Tildesley and Madden observed that the first peak is associated with parallel alignments of molecules which become

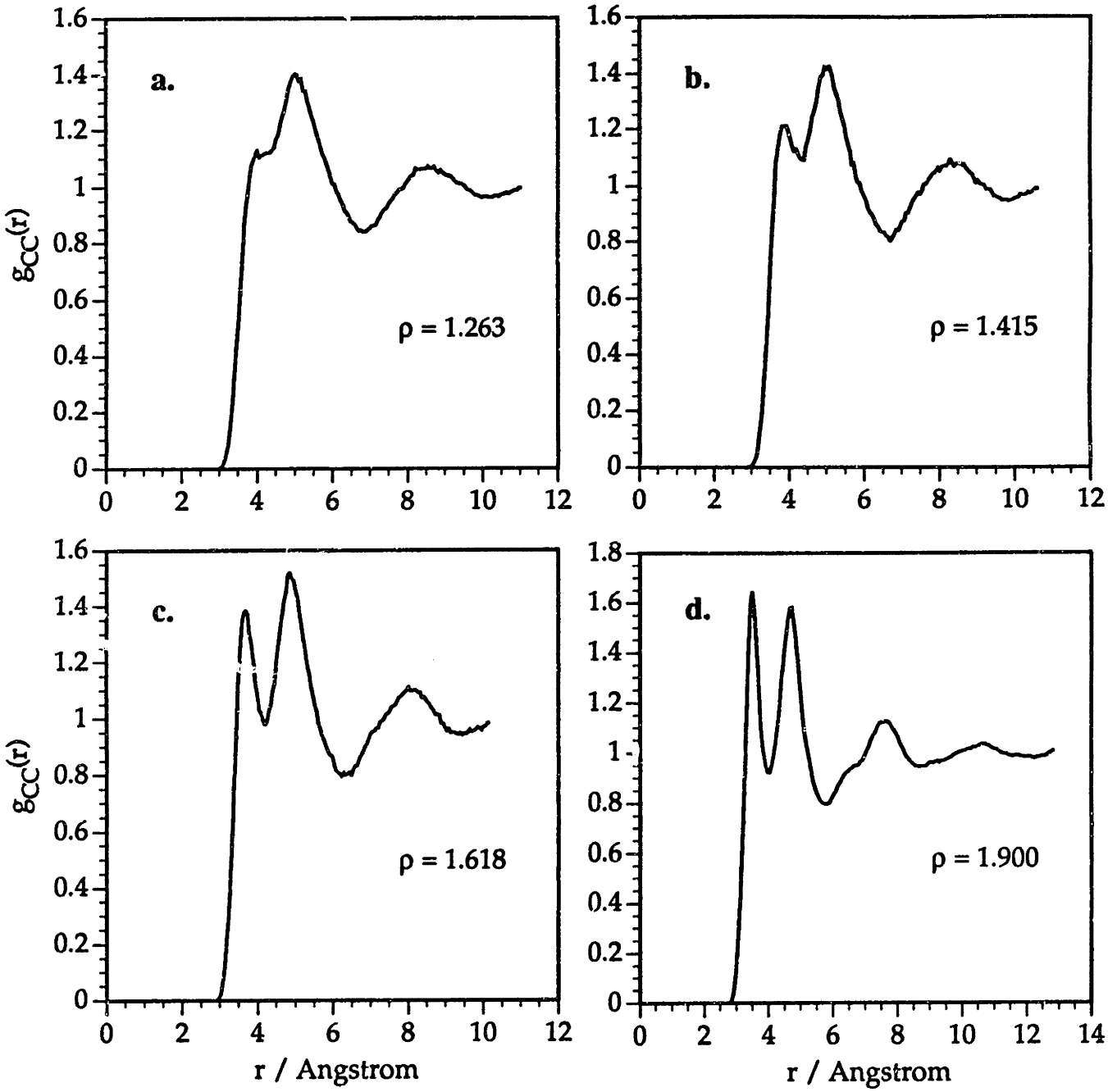

Figure 8.3a-d Carbon-carbon radial site-site distribution functions from MD liquid along 293 K isotherm. The upperleft curve corresponds to carbon disulfide under ambient conditions. The density of the curve at lower right corresponds to the solid phase of the real liquid.

increasingly dominant at high density [64]. The greater liquid densities of the present simulations show there is a greater preference for parallel alignments at short distances. The second peak in $g_{CC}(r)$ is due primarily to molecules which are oriented at right angles.

More complete information about the angular structure occurring in the computer liquid comes from the full molecular pair correlation function, $g(r, \omega 1, \omega 2)$. This function contains a complete description of the static correlation between a pair of molecules separated by a distance r, with mutual orientations symbolized by $\omega 1$ and $\omega 2$. For linear molecules this is a multidimensional function of distance and three angles and is usually impractical to evaluate [101]. We choose instead to evaluate certain partial pair correlation functions. These functions describe pair correlations in terms of a smaller number of variables taken as an unweighted average over the remaining variables. Figures 8.4 and 8.5 describe two particular partial correlation functions which were calculated for the lowest and highest density simulations. The function g1 is a measure of the probability that the vector between the two centers of mass of a pair of molecules a distance r away makes an angle, α, with the first molecule, independent of the orientation of the second. The function g2 is a measure of the probability that a pair of molecules a distance r away have an angle, θ, between their symmetry axes, independent of the value of the other two angles describing their relative orientation. These two particular partial pair correlation functions were first calculated for an MD simulation of liquid nitrogen at triple-point conditions by Quentrec and Brot [102]. In figures 8.6 and 8.7, these functions are plotted for low and high density states of the computer liquid. Both figures indicate a highly structured liquid. Unlike the case of liquid nitrogen [102], g2 is highly

Full pair correlation function:

$g(r, \omega 1, \omega 2) = g(r, \alpha, \theta, \varphi)$

Partial pair correlation functions:

$$g1(r,\alpha) = \frac{1}{4\pi}\int_0^{2\pi} d\varphi \int_0^{\pi} g(r,\alpha,\theta,\varphi)\sin\theta d\theta$$

$$g2(r,\theta) = \frac{1}{4\pi}\int_0^{2\pi} d\varphi \int_0^{\pi} g(r,\alpha,\theta,\varphi)\sin\alpha d\alpha$$

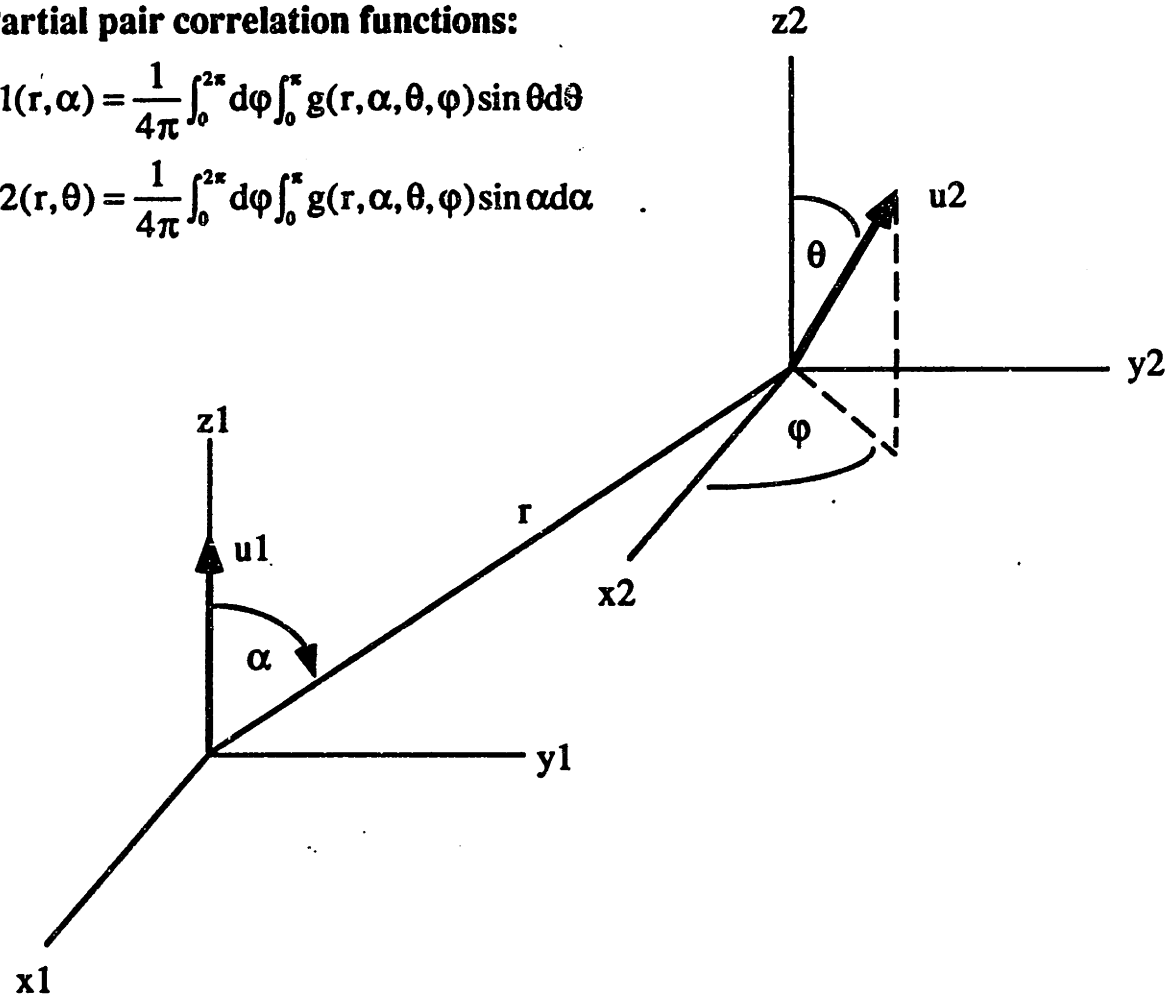

Figure 8.4 Frame of reference showing the four variables necessary to completely define the position of two linear molecules whose orientations are given by the unit vectors, **u1** and **u2**. The two axes systems are parallel, the vector **r**, giving the distance between molecules 1 and 2, lies in the y1, z1 plane.

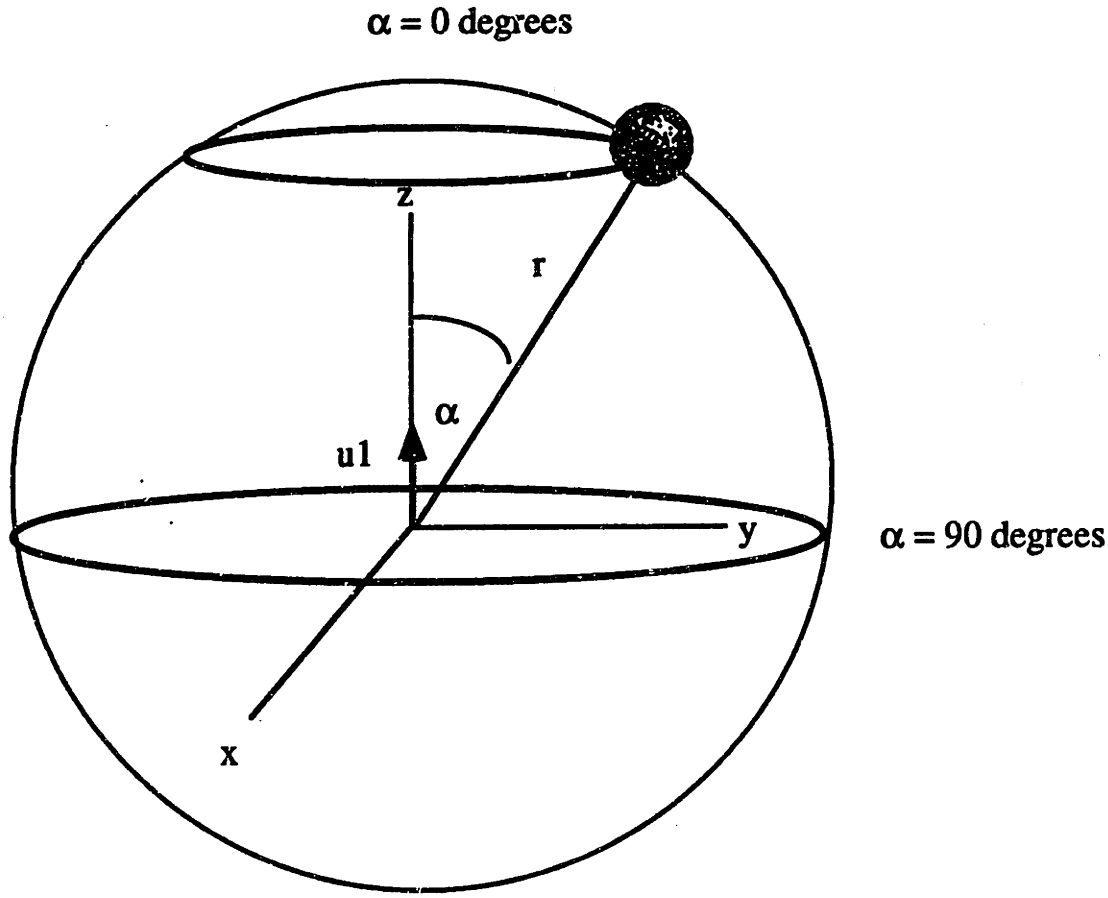

Figure 8.5 Illustration of the distribution function, g1(r, α). This function gives the normalized probability of finding the center of a molecule 2 a distance r away from the center of molecule 1, inclined at an angle α to the symmetry axis of molecule 1. All orientations of the second molecule are averaged over, indicated by the shaded sphere above.

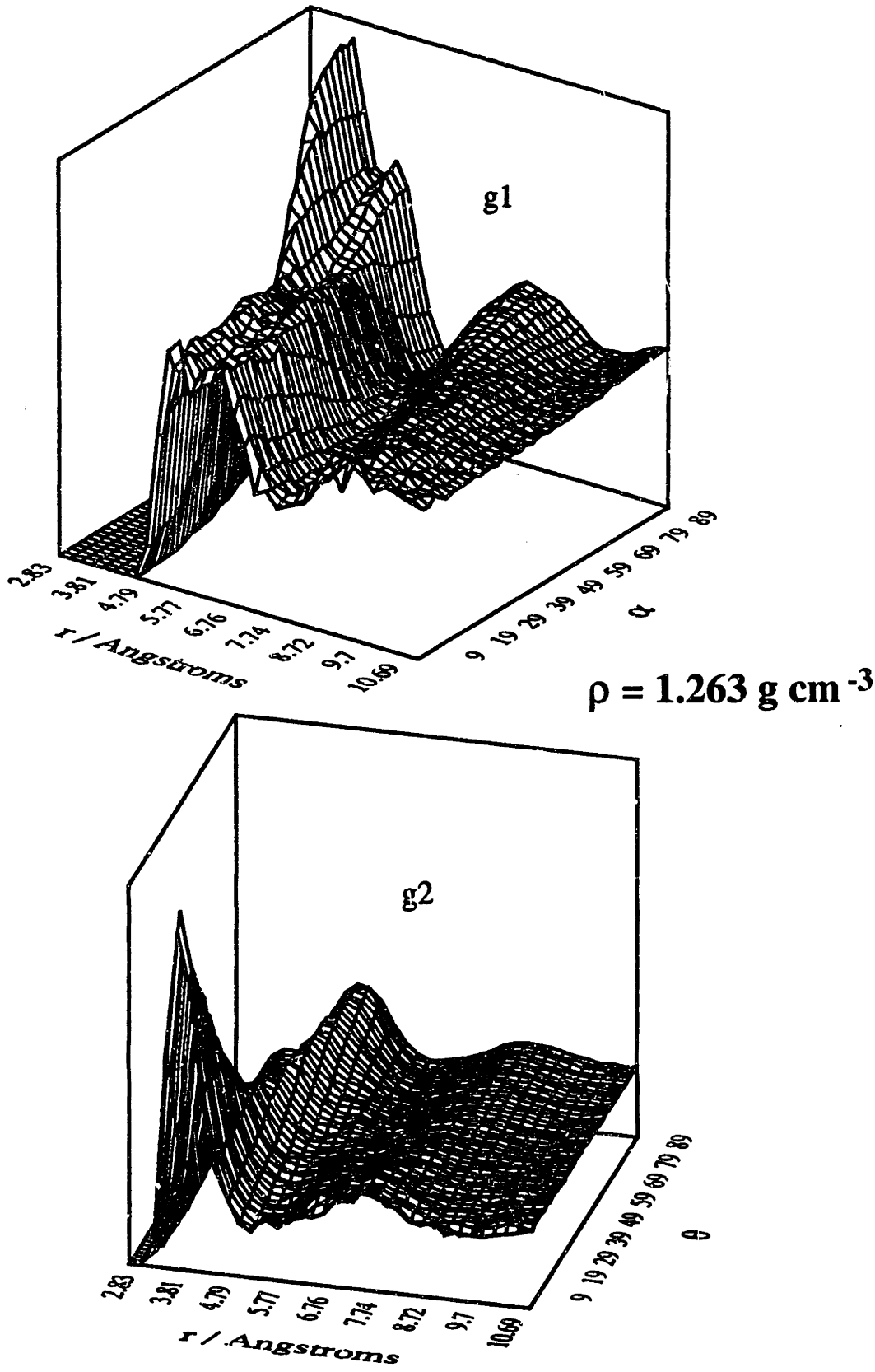

Figure 8.6 g1 and g2 (defined in figures 8.4 and 8.5) for 1 bar, 293 K simulation of liquid carbon disulfide.

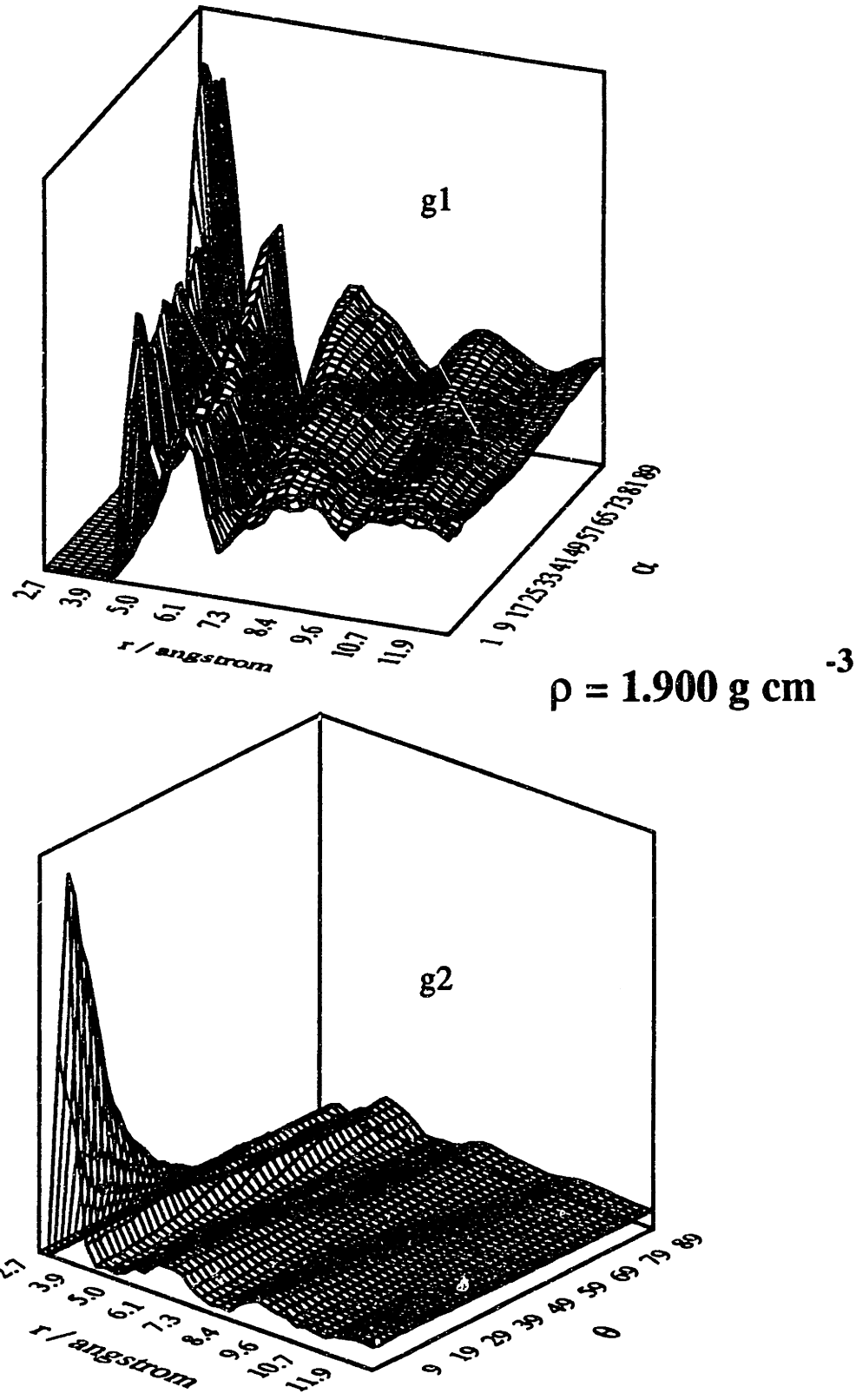

Figure 8.7 Partial pair correlation functions, g1 and g2, for ρ = 1.900 g cm-3 simulation of CS2. This density corresponds to the solid.

structured, indicating that the relative orientation of two molecules irrespective of the position of their centers of mass is important in determining the liquid structure. From the g1 surfaces we note the peaks near $\alpha = 90^{\circ}$. These indicate the increased likelihood of encountering neighbor molecules in directions perpendicular to the symmetry axis of a given molecule. This is consistent with the greater translational mobility of molecules in directions parallel to their initial orientations than in perpendicular directions [63]. The g2 surfaces indicate a tendency for the angle between a pair of molecules to be an oscillatory function of their mutual separation, r. Careful comparison of the surfaces in figure 8.6 and 8.7 with figure 8.3 reveals that the peaks of the center of mass correlation function are associated with predominantly parallel and perpendicular alignments of molecules. Finally, in figure 8.8, we show g1 for the ρ = 1.415 g cm^{-3} (corresponding to an experimental pressure of 2 kbar) simulation of 1372 molecules. This figure illustrates that orientational correlations in the high density liquid persist for several neighbor shells. Of course, the orientational structure discussed in this section is purely static, but we expect it to play a role in determining reorientational dynamics. In particular, it is reasonable to assume that static, local structure is a necessary condition for molecular libration.

8.6 Time correlation functions

This section describes the time correlation functions calculated from the MD runs. For the most part, autocorrelation functions of dynamic variables were computed since these quantities are more accurately

$\rho = 1.415$, 1372 molecules

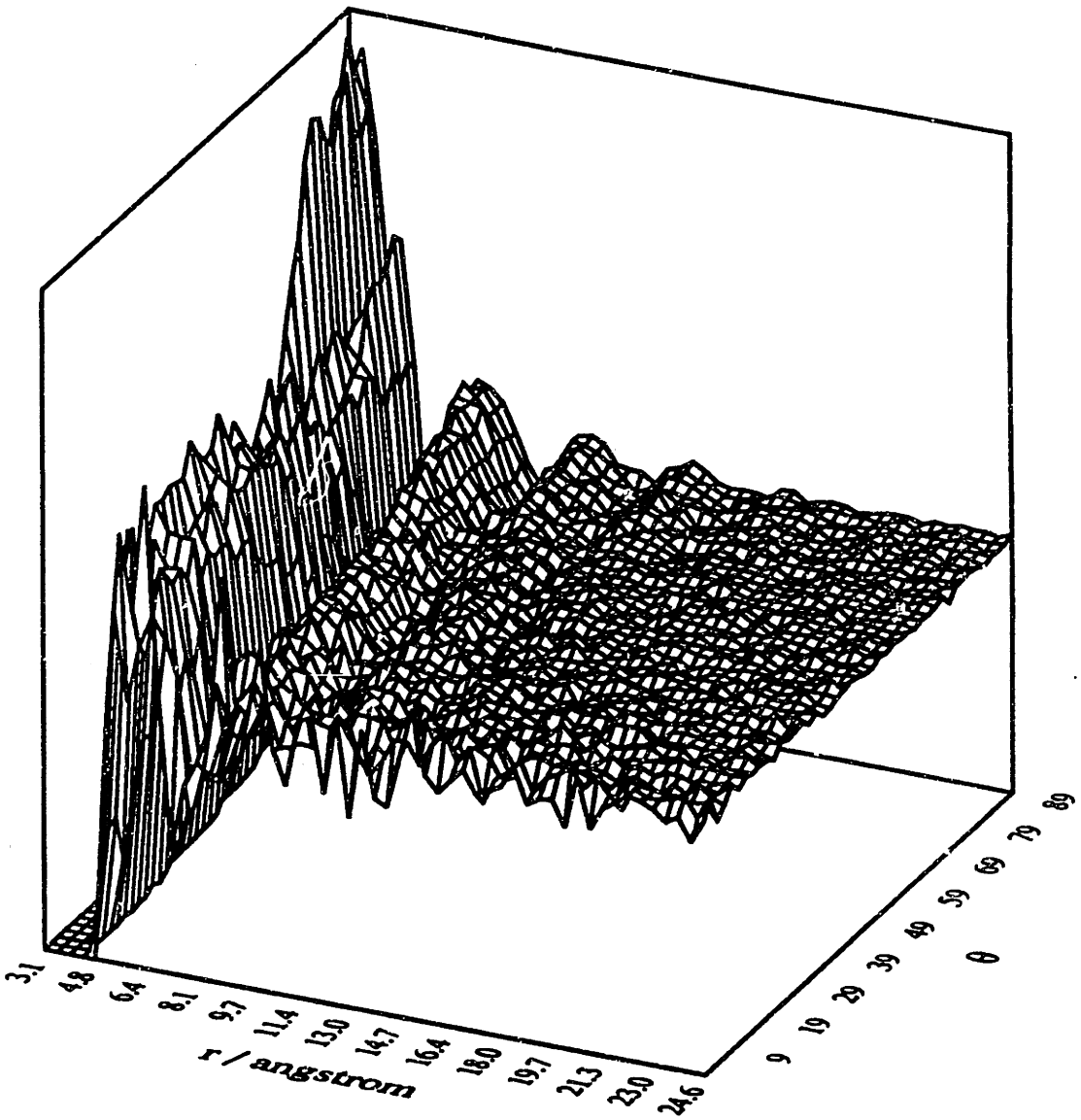

Figure 8.8 Partial pair correlation function, g1, for $\rho = 1.415$ g cm-3 MD simulation of CS_2. This figure shows that pair correlations persist out to distances as great as 15 angstroms at this density.

evaluated than collective properties. In the next section, the statistical error associated with the evaluation of time correlation functions from MD simulations is discussed in some detail, since it is important for the comparison of the MD results with the scans from the femtosecond ISS experiments.

During each MD run dynamic variables are saved to disk at fixed intervals. Variables were divided into two sets, "slow" variables and "fast" variables, according to the expected relaxation time of their autocorrelation functions. The slow variables are the center of mass positions and the unit vectors giving the orientation of the symmetry axis of each molecule. The fast variables are the center of mass force, torque, center of mass velocity and angular velocity. Typically the fast variables were saved at intervals of 8-12 fs. Slow variables were usually saved at intervals of approximately 60 fs. For the simulations of the ISS signal described in section 8.7, it was advantageous to save the slow variables at more frequent intervals of every 15-20 fs. In this way it was possible to attain better sampling of the first several picoseconds of the orientational correlation functions which are used to simulate the femtosecond scattering data. As the density is increased, the fast autocorrelation functions relax more quickly and the slow autocorrelation functions relax more slowly, requiring some adjustment of the sampling intervals given above.

8.6.1 Statistical error in MD time correlation functions

Time correlation functions were calculated after each run from the dynamic variables sampled as described in the previous section. The time autocorrelation function of a dynamic variable X is given by,

$$C_x(t) = \langle X(s)X(s+t) \rangle \tag{8.3}$$

where the angular brackets imply ensemble averaging. Because time correlation functions are stationary in time, $C_X(t)$ is independent of the arbitrary time s. Ergodicity permits the replacement of an ensemble average by an infinite time average for a single trajectory through phase space,

$$C_x(t) = \lim_{t \to \infty} \frac{1}{T} \int_0^T ds X(s)X(s+t) \tag{8.4}$$

In a computer experiment it is, of course, only possible to average for a finite time T. An autocorrelation function (acf) of dynamic variable X is calculated from MD trajectory data at a series of discrete values of time, t_k, from the expression,

$$C_x(t_k) = \frac{1}{N \cdot M} \sum_{i=1}^{N} \sum_{j=1}^{M} X^i(t_j)X^i(t_{j+k}) \tag{8.5}$$

where N is the number of molecules, and M is the number of time steps chosen as time origins. Zwanzig and Ailawadi have analyzed the statistical error associated with finite time averaging in detail [103]. The estimated standard deviation of the quantity evaluated in equation 8.5 from the true value of the autocorrelation function represented by equation 8.4, is given by,

$$\sigma_x = \sqrt{\frac{2\tau}{NT}} \tag{8.6}$$

where τ is the relaxation time of the acf and T is the total length in time of the MD data from which the M time origins are chosen. For the case of the orientational correlation functions described below, τ becomes considerably longer at high density, requiring longer simulations to attain the same accuracy. For all of the time autocorrelation functions reported in this chapter, the relative error estimated by equation 8.6 is always < 4%.

8.6.2 Translational diffusion coefficients

The mean square displacement, given by equation 8.7, was calculated at each density and is shown in figure 8.9. This function measures the squared distance molecular centers have travelled on average after a time t.

$$R^2(t) = \left\langle |\mathbf{R}(t) - \mathbf{R}(0)|^2 \right\rangle \tag{8.7}$$

If the translation of molecules is diffusional, then the long time limit of this function is given by the Einstein relation,

$$\lim_{t\to\infty} R^2(t) = 6D_t t \tag{8.8}$$

where D_t is the translational diffusion coefficient. Figure 8.9 shows the mean square displacement for the isothermal MD runs at 293 K. At very short times (t < 100-200 fs) $R^2(t)$ grows quadratically with time consistent with gas-like free translation. Between 100 fs and 2.5 ps the displacement

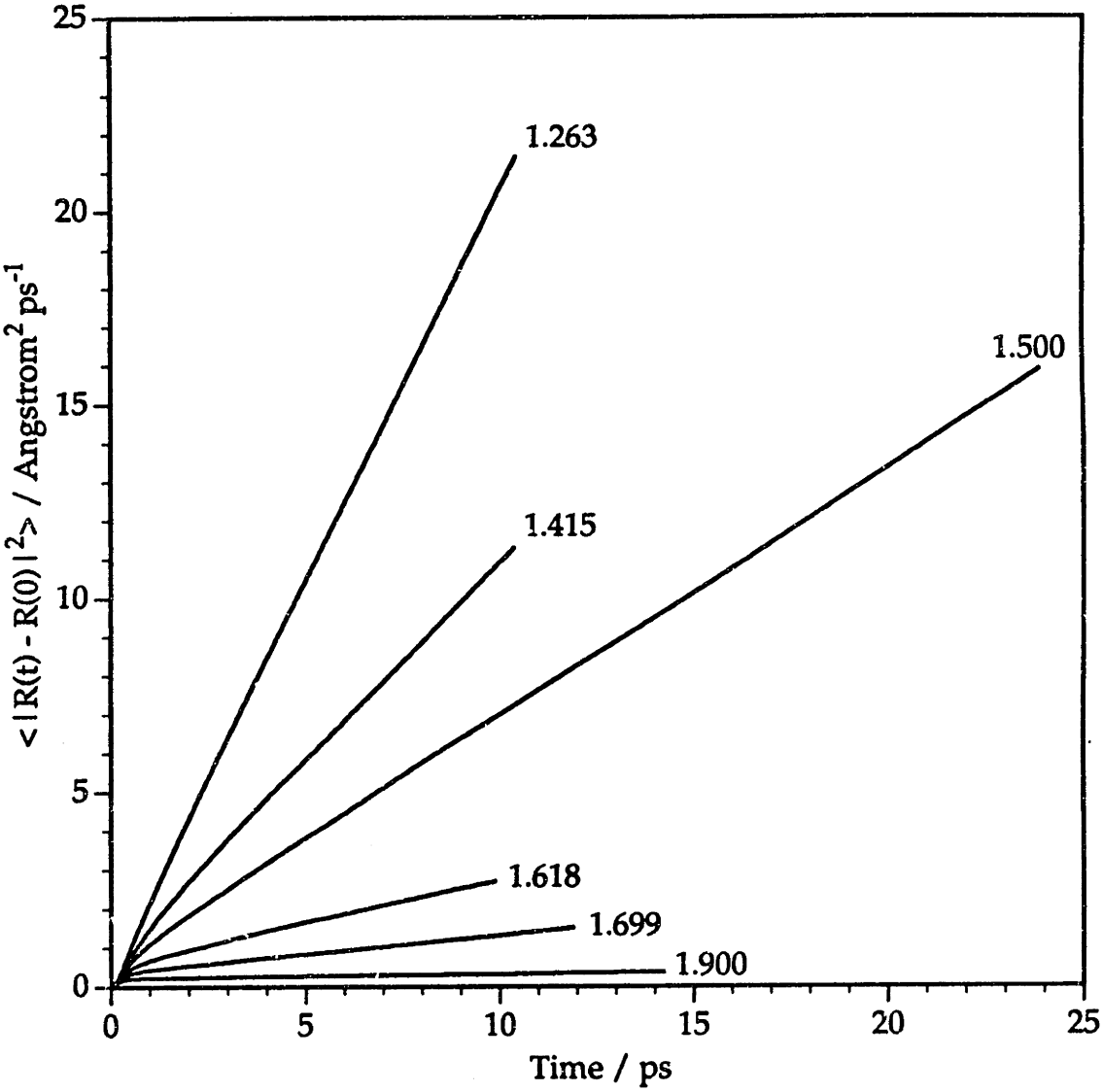

Figure 8.9 Mean square displacement for liquid carbon disulfide from isothermal MD runs. Each curve is labelled by the mass density in g cm-3.

changes in a more complicated fashion. At long times, $R^2(t)$ increases linearly with time at all densities, consistent with translational diffusion. By fitting a straight line to each curve at times $t > 2.5$ ps, D_t was determined at different state points and the results appear in table 8.3. Our value at ambient conditions is in fair agreement with the value of Tildesley and Madden, who reported $D_t = 3.9 \times 10^{-5}$ cm^2 s^{-1} at 294 K, 1.26 g cm^{-3} [65]. Finally, as already pointed out in section 8.4, the diffusion coefficient at ρ=1.900 g cm^{-3} is 200 times smaller than at ambient temperature and pressure, indicating glass-like dynamics, although the nonzero value for the translational diffusion constant suggests that we can not properly label the computer liquid a glass.

Table 8.3 Translational Diffusion constant, D_t, determined from long time behavior of the mean squared displacement.

Density / g cm^{-3}	$D_t \times 10^5$ / cm^2 s^{-1}
1.263	3.4
1.415	1.7
1.500	1.1
1.618	0.37
1.699	0.16
1.900	0.017

8.6.3 Autocorrelation functions of "fast" variables

The center of mass velocity autocorrelation function, $C_v(t)$, and the angular velocity autocorrelation function, $C_\omega(t)$, provide additional information about translation and reorientation in molecular liquids. Lynden-Bell has noted that most MD simulations of anisotropic molecular liquids show pronounced negative portions in these functions [104]. The origin of this effect is due to backscattering or rattling of molecules at short times in cages of near neighbors. For example, a negative value for the center of mass velocity autocorrelation function, $C_v(t)$, means that, on average, a molecule has acquired a component to its velocity oriented opposite to its direction at zero time.

The behavior of $C_\omega(t)$ can be appreciated by considering the limiting cases of a dilute gas and a solid of linear molecules. In a dilute gas, molecules will undergo essentially free rotation and the correlation function will be unity for all times, since the angular momentum (and, hence, the angular velocity for a fluid of linear molecules) is a constant of the motion. In a solid, an individual molecule librates about its mean position giving rise to oscillations in $C_\omega(t)$ which are eventually damped due to intermolecular interactions. The behavior of liquids fall somewhere in between these two cases. Gas-like decays are observed only in low torque fluids which are often characterized by conditions of low density and high temperature, or by a less strongly anisotropic interaction potential. For most molecular liquids at densities which are closer to the triple point than to the critical point, $C_\omega(t)$ typically shows a single minimum and a significant negative portion. A negative dip in $C_\omega(t)$ indicates that, on average, a molecule has acquired a component to its

angular velocity oriented opposite to the initial direction of this quantity. Random, uncorrelated collisions cannot give rise to such a reversal, but motion in a potential well will lead to such changes. Negative portions of $C_\omega(t)$ are a necessary condition for molecular libration.

In figures 8.10 and 8.11 $C_v(t)$ and $C_\omega(t)$ are displayed for two thermodynamic state points together with autocorrelation functions of the force, $C_F(t)$, and torque, $C_N(t)$. At all state points simulated, the center of mass velocity and angular velocity acfs show one or more negative minima. As seen in both figures, these minima become more pronounced at high density. From the figures it is also apparent that, while the minimum in $C_\omega(t)$ at high density is deeper than the minimum in $C_v(t)$, $C_v(t)$ shows a much more well-defined second minimum than $C_\omega(t)$. This is also true of the MD runs calculated as a function of temperature at constant pressure both from this study and from Tildesley and Madden's results [65]. It appears that caging has more of an effect on the translational degrees of freedom than on the rotational ones. Even at very high density, the angular velocity autocorrelation function, $C_\omega(t)$, never becomes positive at later times after the initial negative-valued minimum, but shows instead a long relatively flat tail. This would suggest that libration, if it does occur, is very heavily damped. Note that greater oscillatory structure is seen in the torque autocorrelation function, $C_N(t)$, at high density. Madden and Tildesley state that the similar decay times for both $C_\omega(t)$ and $C_N(t)$ are why many analytical theories of reorientation fail to predict $C_\omega(t)$ [65].

Finally, additional information about microscopic dynamics can be obtained by calculating correlation functions resolved along particular spatial directions or by calculating correlation functions for specially selected groups of molecules. The former approach was used by

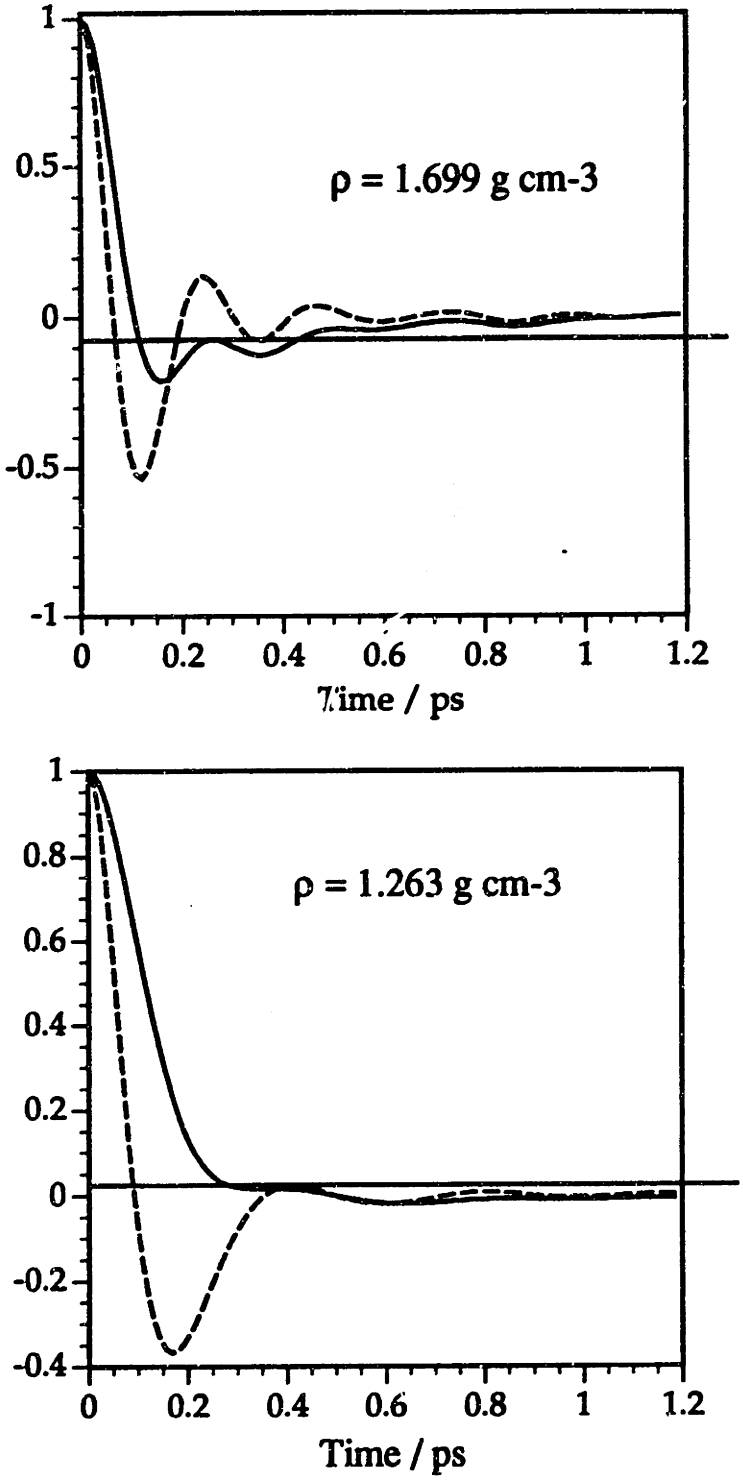

Figure 8.10 Center of mass force (dashed) and velocity (solid) autocorrelation functions for two MD runs at 293K. The lower panel is for the liquid at ambient conditions, while the density in the upper panel corresponds to an experimental pressure of 12 kbar.

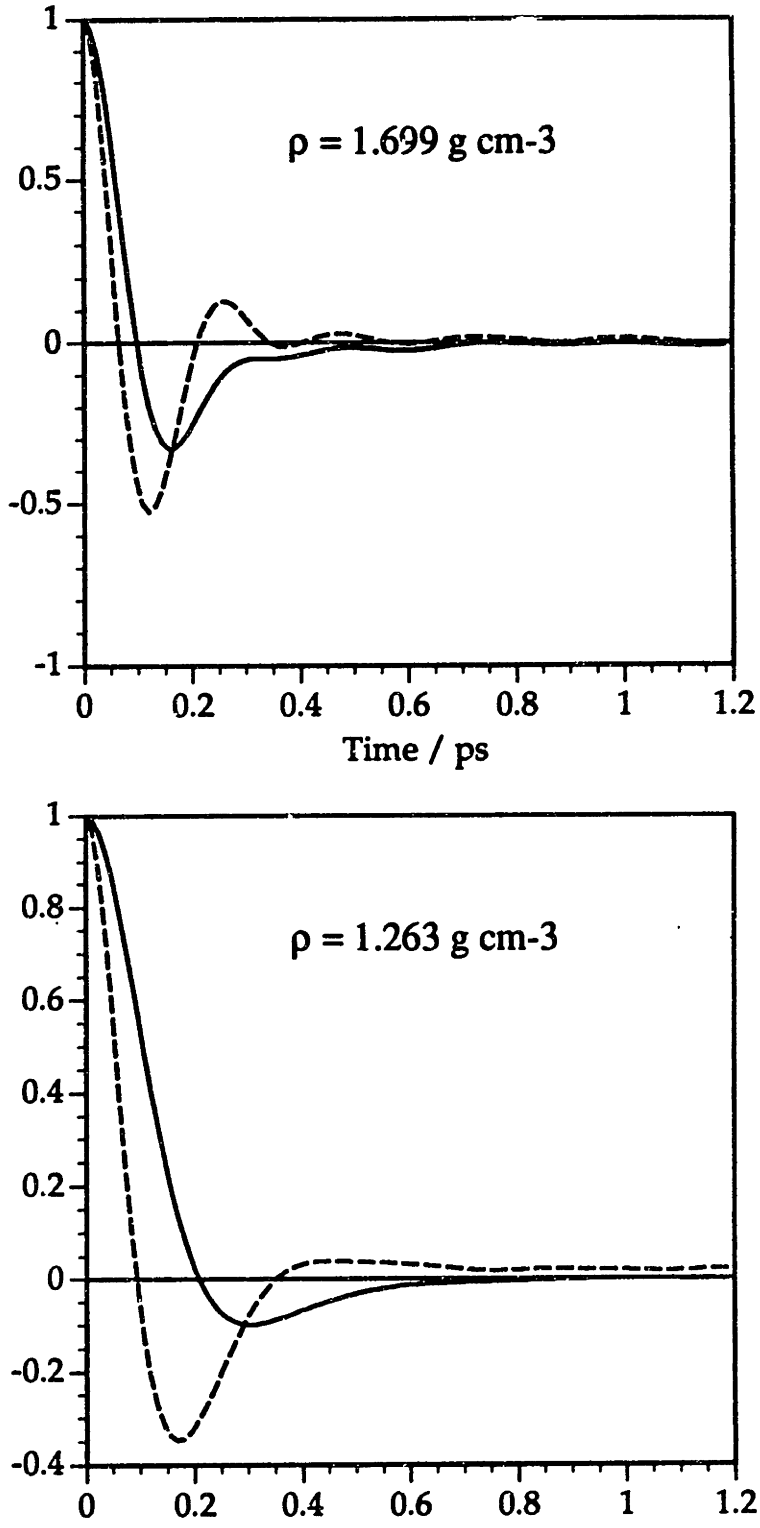

Figure 8.11 Torque (dashed) and angular velocity (solid) autocorrelation functions for the same two MD runs of figure 8.10.

Steinhauser, who resolved $C_V(t)$ along directions perpendicular and parallel to the initial orientation of the molecular symmetry axis [63]. Strong oscillations appear in the perpendicular component of $C_V(t)$, but not in the parallel component of this function, indicating greater hindrance to motion in directions perpendicular to the CS_2 symmetry axis. An example of the second approach is Lynden-Bell's study of caging effects [104]. This study shows that molecules with high translational kinetic energy rattle (i.e. show oscillatory velocity correlations) more than molecules with lower energy.

8.6.4 Orientational correlation functions

In this section the orientational correlation functions (ocfs) for liquid carbon disulfide are described as a function of thermodynamic state. The reorientation of linear molecules is conveniently described by correlation functions involving the following Legendre polynomials [105],

$$C_\ell(t) = \langle P_\ell(\cos\theta(t)) \rangle = \langle P_\ell(\mathbf{u}(0)\cdot\mathbf{u}(t)) \rangle \qquad (8.9)$$

where P_ℓ is the ℓth-order Legendre polynomial (i.e., $P_1(x) = x$, $P_2(x) = 1/2(3x^2 - 1)$) and $\mathbf{u}(t)$ is a unit vector giving the orientation of the molecular symmetry axis at time t. The ℓ=1 and ℓ=2 ocfs were calculated for all runs. As shown in chapter 3, the derivative of $C_2(t)$ contributes to the ISS signal.

$C_2(t)$ is plotted at different densities at approximately isothermal conditions in figure 8.12. Figure 8.13 shows $C_2(t)$ as a function of temperature at atmospheric pressure. At high density and low temperature reorientation becomes strongly hindered, resulting in the slow decay of this

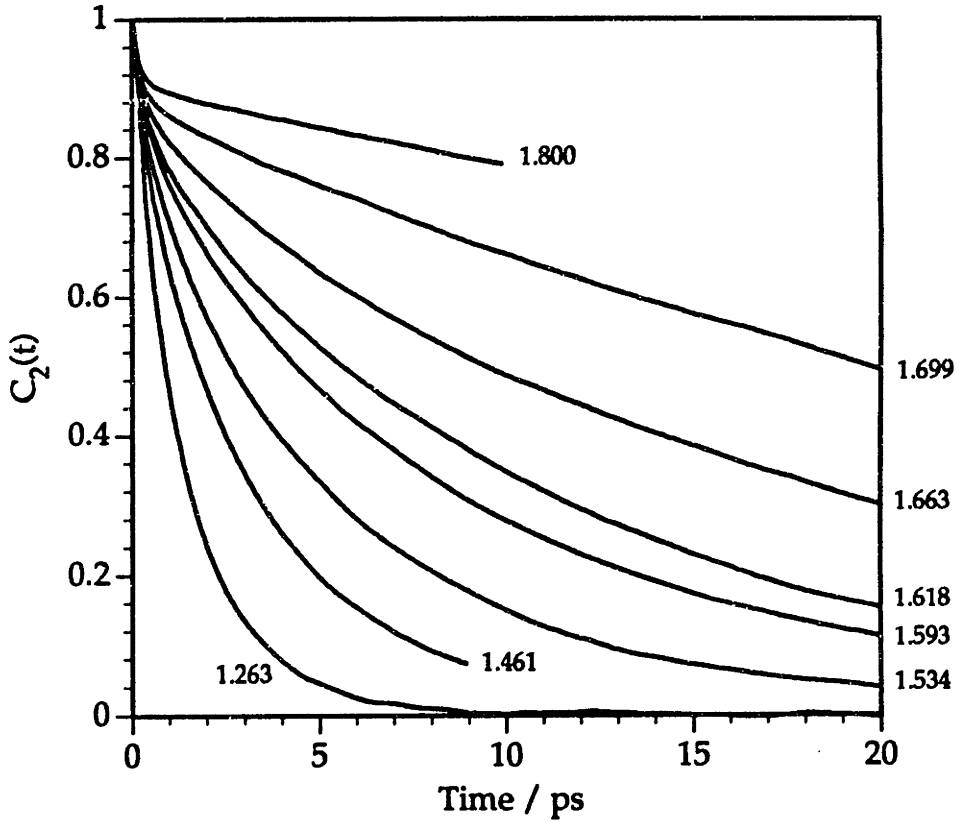

Figure 8.12 $C_2(t)$ orientational autocorrelation functions calculated from room temperature MD runs as a function of density (g cm-3). The density of the uppermost curve corresponds to the real solid.

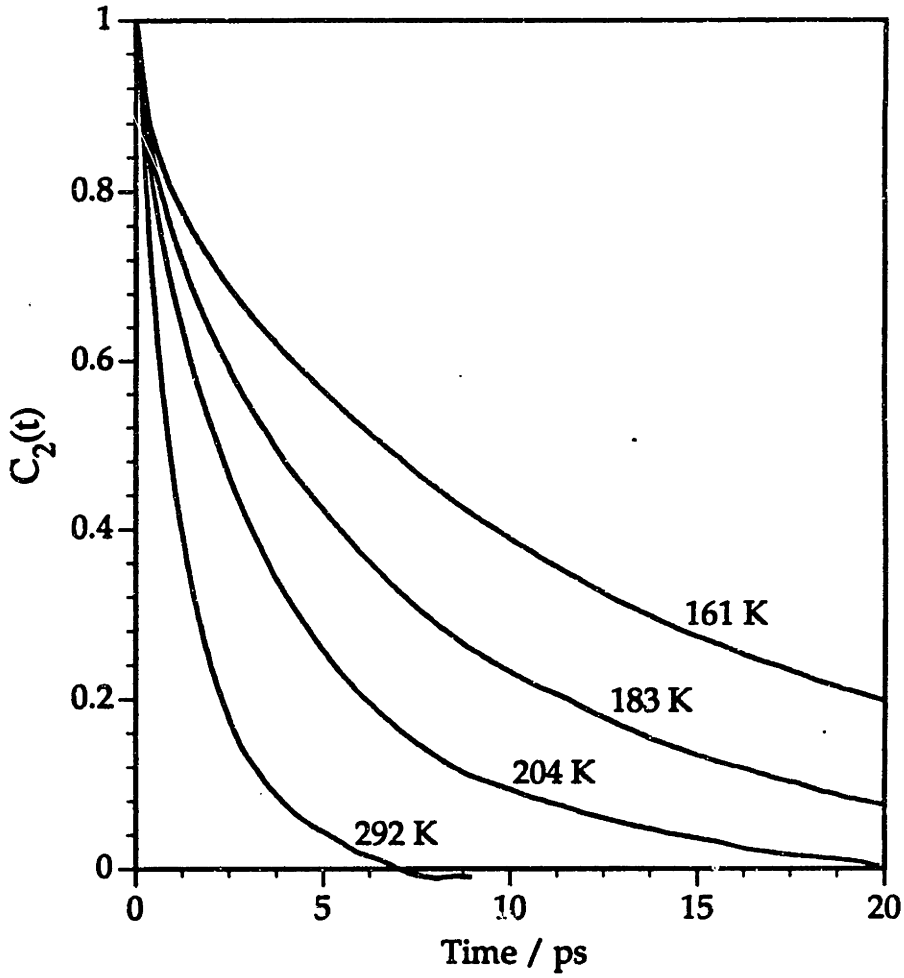

Figure 8.13 $C_2(t)$ orientational correlation functions from isobaric MD runs as a function of temperature.

function. The natural logarithm of the curves of figure 8.12 are displayed in figure 8.14. The linear behavior of these curves at long times is consistent with rotational diffusion. The long time decay of these functions is fit very well by a single exponential. The decay time, τ_2, is a measure of the reorientational correlation time for single molecules and is measured by Raman scattering as discussed in chapter 3. Table 8.4 lists values of τ_2 determined by fitting a single exponential to $C_2(t)$ for times greater than 4 ps along with the experimental values measured by Raman scattering. In agreement with Madden and Tildesley, we find that the reorientation times from the simulations are consistently longer than the experimental times, indicating that reorientation in the computer liquid is somewhat too strongly hindered.

For several MD runs $C_2(t)$ was calculated to high accuracy for the first 2.5 ps. Since the response function measured in the ISS experiment is proportional to the derivative of $C_2(t)$, it is necessary to minimize the noise in the calculated ocfs. These ocfs depict the short-time behavior of single molecule reorientation and are plotted on a logarithmic vertical scale in figure 8.15. The concave-down portion of $C_2(t)$ at very short times clearly shows the free-rotor behavior [105]. This is the inertial part of the motion when reorientation proceeds in an essentially free or gas-like manner. After approximately 1 ps, the logarithm of $C_2(t)$ decays linearly, consistent with small step rotational diffusion. The transition from gas-like to diffusional motion occurs smoothly, without the wiggles and bumps which are characteristic of librational reorientation. In fact, the shape of $C_2(t)$ is surprisingly similar at all densities, indicating the absence of significant, density-dependent changes to the dynamics of single molecule

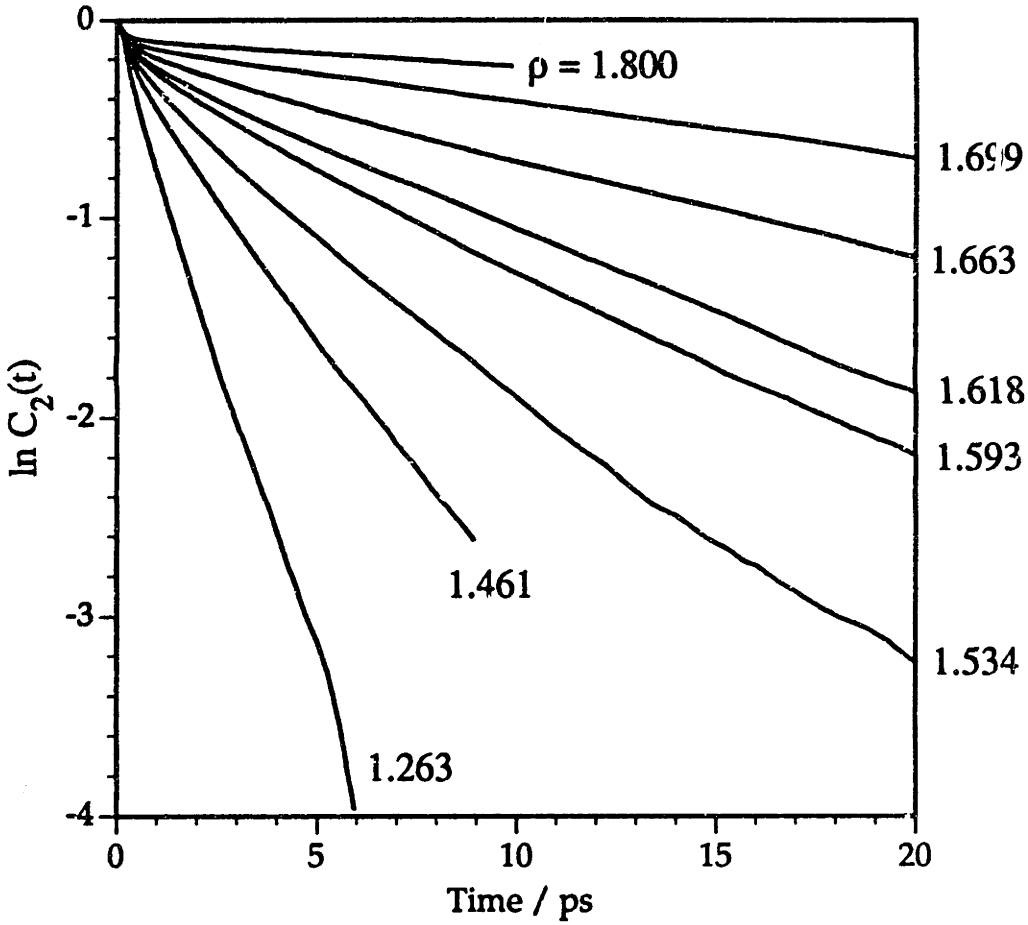

Figure 8.14 Semilogarithmic plot of $C_2(t)$ for the isothermal MD runs showing the linearity at long times. Each curve is labelled by the density in units of g cm-3.

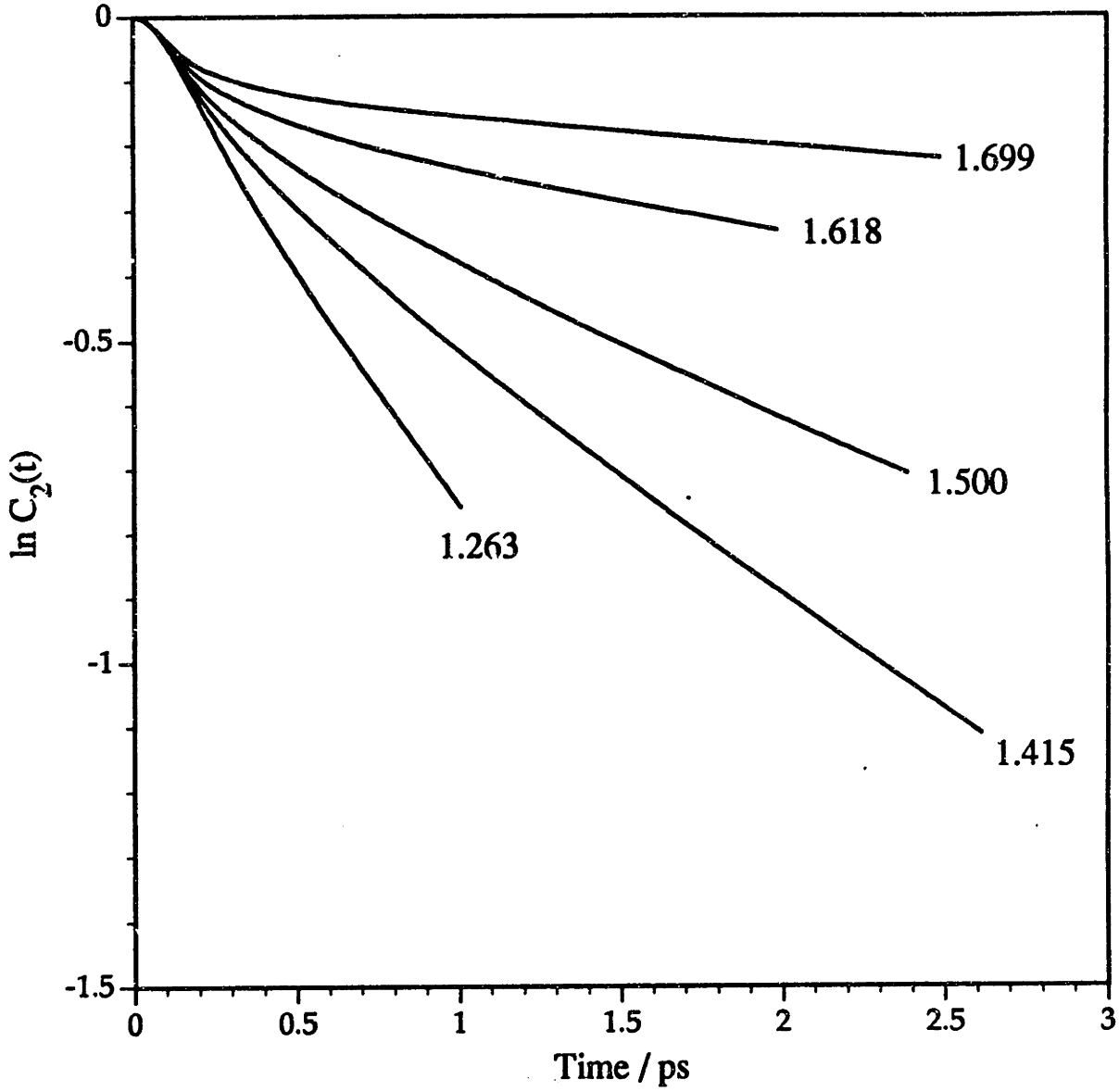

Figure 8.15 Natural logarithm of $C_2(t)$ orientational correlation functions showing inertial behavior at short times and single exponential decay at later times. Even at the highest densities simulated, there is no evidence of libration in the single molecule ocfs. Each curve is labelled by the density in units of g cm-3.

reorientation. It appears that over the entire liquid range of this computer liquid, molecules never appear to undergo significant periods of libration.

Table 8.4 Orientational relaxation time, τ_2, from MD isothermal runs (T ≈ 293 K) compared with experiment.

Density / g cm^{-3}	τ_2 / ps	τ_{RAM} / ps [ref. 57]
1.534	6.5	3.6
1.593	10.2	5.1
1.618	12.0	6.2
1.663	20.0	9.6
1.699	35.6	—

Table 8.5 Orientational relaxation time, τ_2, from MD isobaric runs compared with experiment.

Temperature / K	Density / g cm^{-3}	τ_2 / ps	τ_{RAM} / ps [ref. 57]
293	1.263	1.8	1.5
210	1.387	4.9	3.9
180	1.433	8.7	6.5
165	1.456	14.0	9.5

Figures 8.16 - 8.18 display reorientational trajectories for three different densities at isothermal conditions. Each figure displays 10 ps of reorientational motion for a chosen molecule in two ways. At the top of

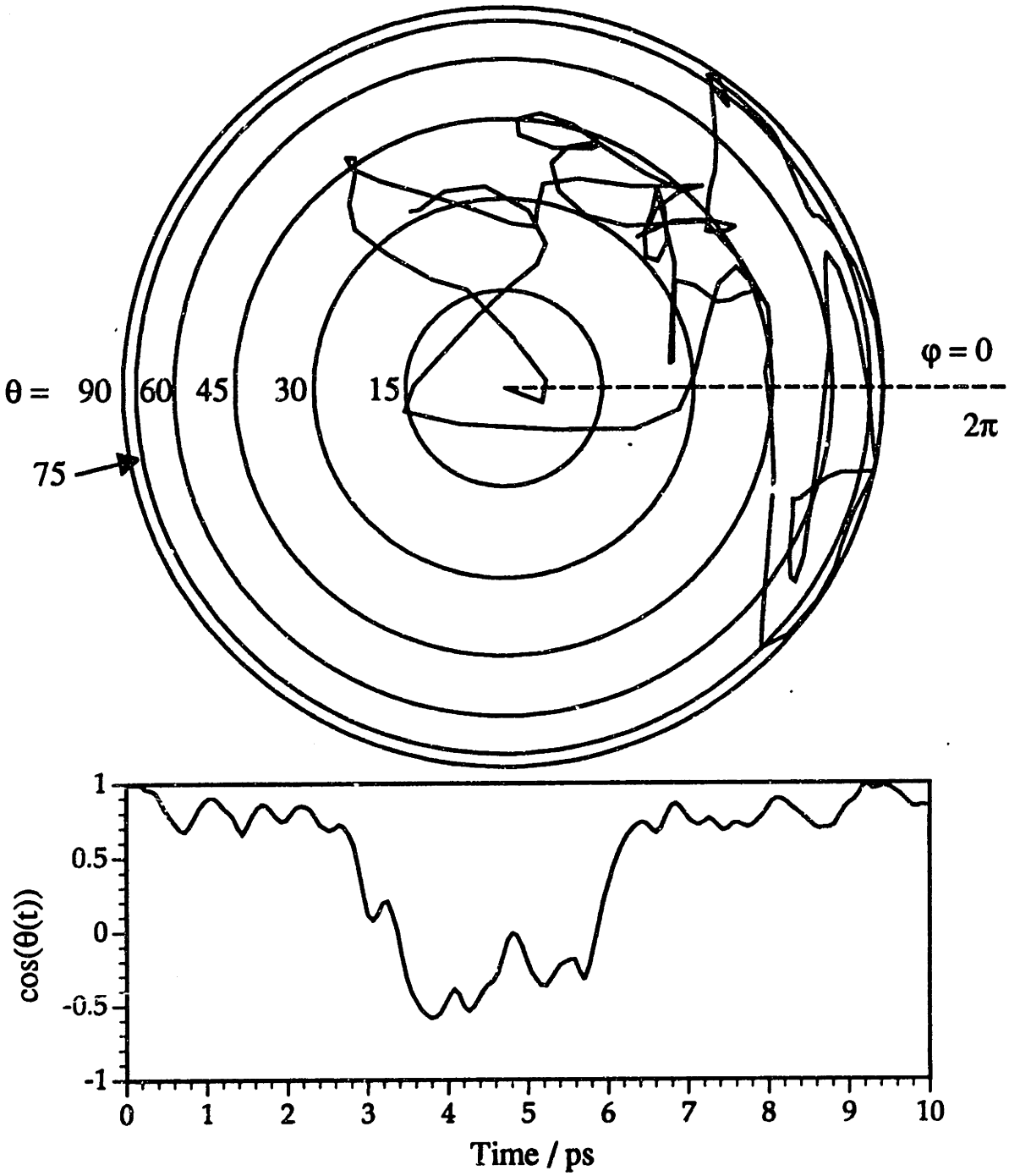

Figure 8.16 Typical reorientational trajectory for a single molecule from ρ = 1.263 g cm-3 MD run. At top is shown a polar plot of the path the symmetry axis of the molecule makes as a function of time. Each circle corresponds to 15 degrees. The total path length is 10 ps. The plot at the bottom gives cos(θ(t)) where θ(t) is the angle the molecule makes at time t with its initial orientation.

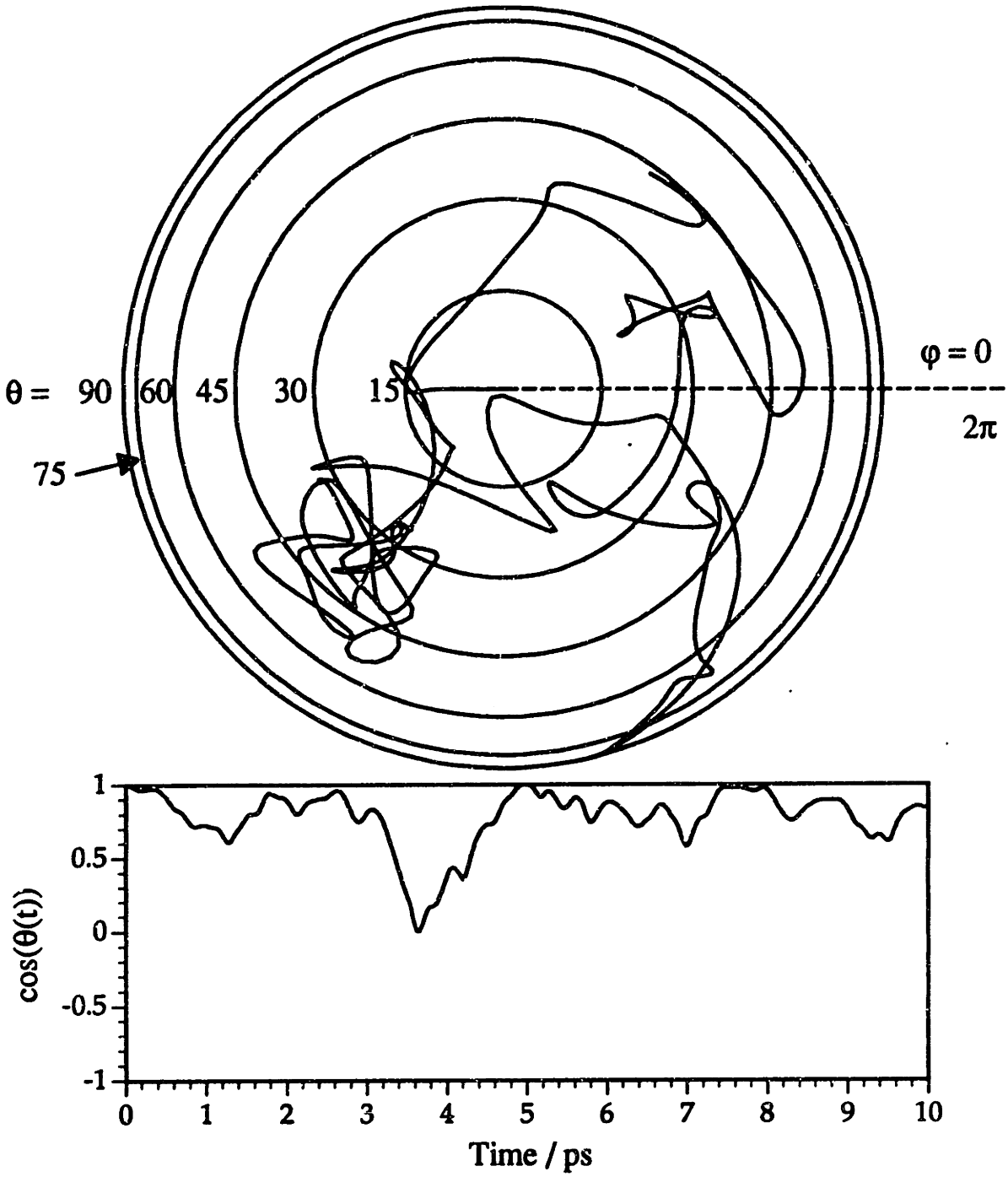

Figure 8.17 Same as figure 8.16, showing typical reorientation of a single molecule from $\rho = 1.500$ MD run.. The reorientation shows periods of free rotation and periods of trapping.

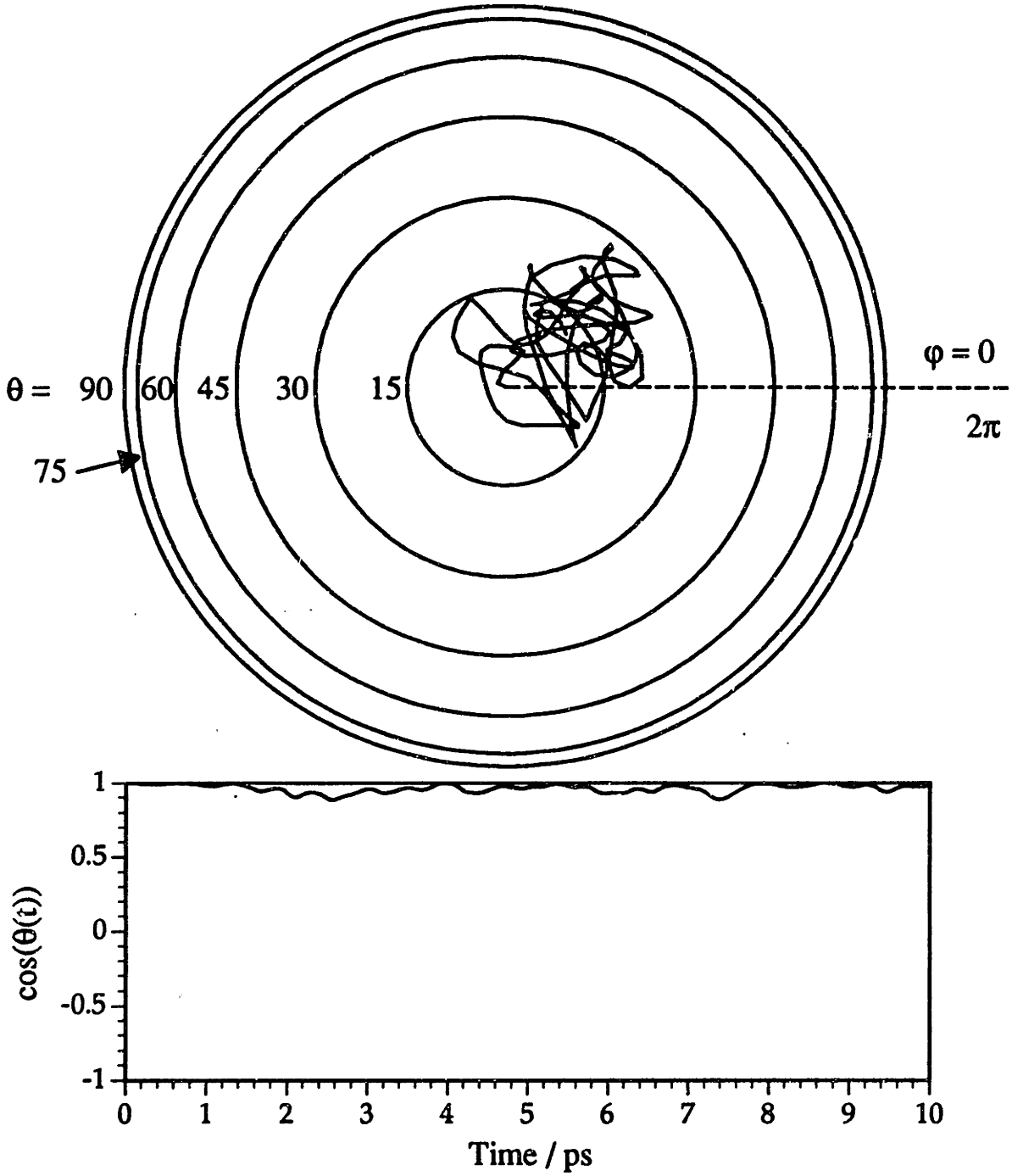

Figure 8.18 Same as figure 8.17, showing typical reorientation of a single molecule from $\rho = 1.900$ MD run.. The molecule shown here is essentially trapped.

each figure, the variables θ and φ, describing the orientation of the molecular axis relative to its initial orientation, are plotted as a function of time. The lower figure displays the cosine of the polar angle θ for the same 10 ps of trajectory data. At all densities reversals of angular velocity occur from time to time as seen by the sharp cusps in the polar maps at the top of the figures. As the density of the liquid increases, the orientational trajectory lasting 10 ps becomes limited to a smaller region of angular space, but shows similar characteristics to the low density trajectories. Libration in a plane with more than one oscillation is not seen at any density.

8.7 Comparison of simulation results with ISS data

The different contributions to the impulsive stimulated scattering signal were discussed in chapter 3. It was shown that the scattering is proportional to the derivative of a correlation function of the collective polarizability of the liquid (equation 3.30). Even when intramolecular vibrational modes need not be considered (i.e., we can set $C^{RAM}(t) = 0$), the collective polarizability correlation function still involves a complex sum of contributions from different molecular processes. There is a part due to the reorientation of single molecules, a part due to orientational correlations between pairs of molecules, an interaction-induced (I-I) part which reflects the dynamics of higher configurations of molecules and cross terms. With frequency-domain light scattering results and our own femtosecond results as guidelines, we have argued that in dense liquids like benzene and CS_2, the reorientation of single molecules will likely be the

largest contribution to the *dynamics* of the oscillatory signal we have observed.

Neglecting all I-I and pair terms, we approximate the correlation function for the collective polarizability by the $\ell = 2$ orientational correlation function,

$$C^{\Pi}(t) \approx C_2(t) \tag{8.10}$$

We then use equation 3.19 to write the response function for the liquid's dielectric tensor to the nonlinear optical fields as,

$$G^{\alpha} \propto -\frac{1}{kT}\frac{dC^{\Pi}(t)}{dt} \approx -\frac{1}{kT}\frac{dC_2(t)}{dt}. \tag{8.11}$$

This response function was calculated by numerically differentiating the $C_2(t)$ functions from the different MD simulations. Numerical differentiation greatly amplifies small noise present in $C_2(t)$. Thus, great effort was made to reduce noise in $C_2(t)$ as much as possible. According to the results of section 8.6.1 the statistical noise in an autocorrelation function can be decreased by increasing the number, N, of molecules in the simulation and by increasing the total time of the simulation. Both of these measures were tried independently by simulating a 108 molecule system for 1 ns and by simulating a 1372 molecules system for 64 ps. Figure 8.19 compares the effects of system size and run length on the $C_2(t)$ correlation functions. Increasing the system size at constant run length, and increasing the run length at constant system size both lead to improved statistics. It can also be seen from the figure that $C_2(t)$ calculated from the 1372

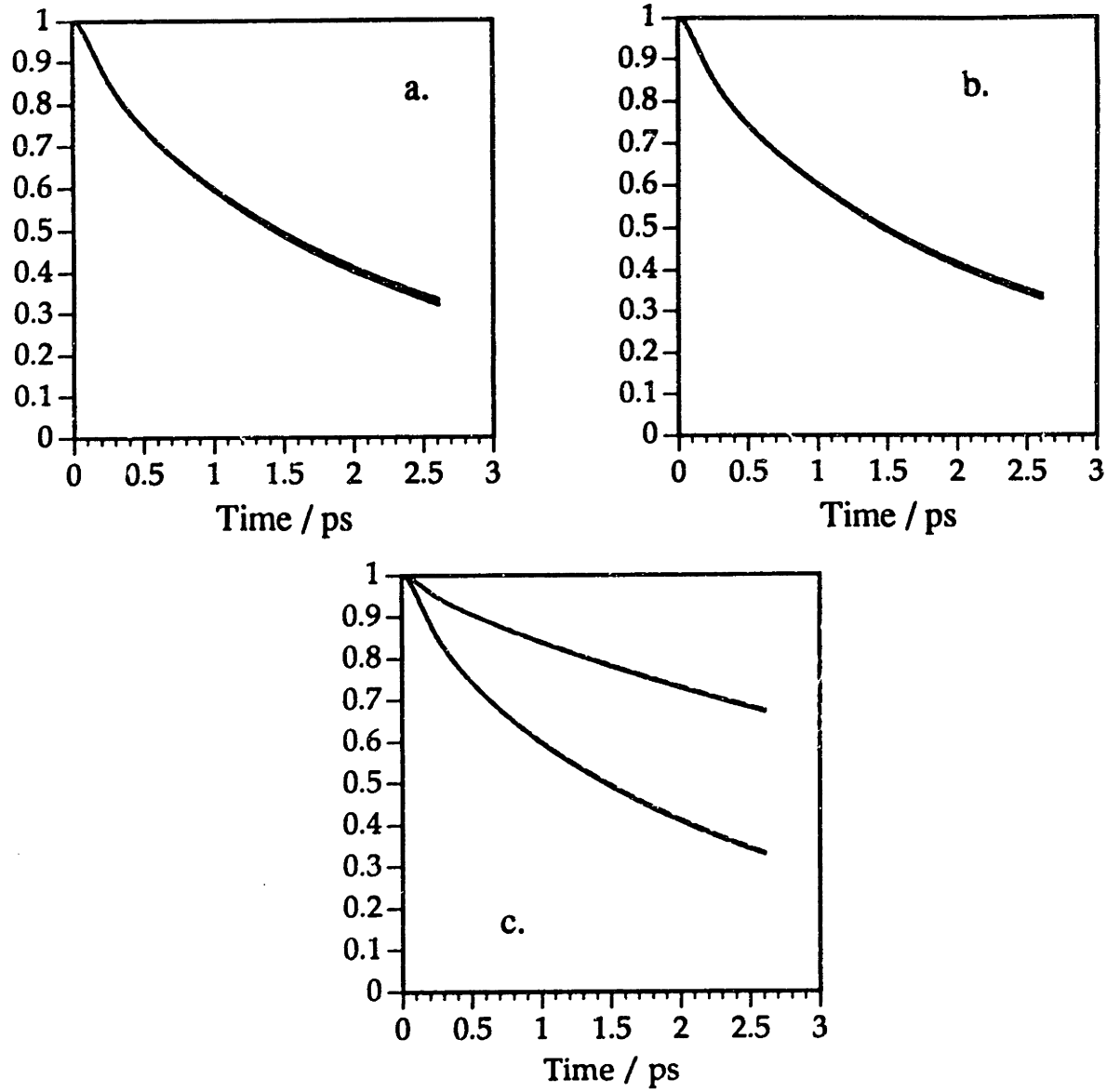

Figure 8.19a-c Effects of system size and simulation time on orientational autocorrelation functions. Two MD runs of 108 and1372 molecules at the same density (1.415 g cm-3) and temperature (293 K) provided the trajectory data for all curves. Figure a: C2(t) for two sets of 686 molecules calculated from 5000 timesteps (=53 ps) of the 1372 molecule simulation. Figure b: Comparison of C2(t) calculated from two different 38000 timestep sections (400 ps) of 108 molecule run. Figure c: C1(t) and C2(t) from 78000 timesteps (=819 ps) of the 108 molecule simulation (dashed curves) compared with the same quantities from the 1372 molecule run time calculated from 6000 timesteps (=63 ps). This demonstrates that these orientational correlation functions do not depend on the size of the simulation.

molecule run agrees nearly perfectly with this function evaluated from the 108 molecule simulation. This is the justification for our simulation of only 108 molecules at most state points. The single molecule reorientational dynamics simply do not depend on the size of the simulation. We also note that more computer time is required to simulate a larger system for a long enough time interval to attain the same level of statistical accuracy obtained by simulating a smaller number of molecules for longer times. Excellent results were obtained by saving orientational variables every 10-15 fs and running 108 molecule systems for at least 100 ps.

The response function from equation 8.11 was convoluted with Gaussian excitation and probe pulses of 65 fs FWHM according to equation 3.10 to obtain simulated femtosecond ISS data. The results for the isothermal MD runs are displayed for various densities in figure 8.20. The results from the constant pressure MD runs are similar.

The change in curvature during the inertial decay of $C_2(t)$ at very short times gives rise to a signal maximum at delayed times, as seen experimentally. The time of the signal peak agrees reasonably well with experiment. This is shown in figure 8.21 where the MD ISS signal at 293 K, 1 atm is plotted with the experimental data at the same conditions. While this does not prove the molecular processes observed in the ISS experiment are dominated by single molecule reorientation, it does prove the existence of a fast component (subpicosecond) to the correlation function describing the reorientation of single molecules. The simulations also reproduce the two decay times (a faster one, followed by a slower one) seen in the data. But even at the highest densities, the simulated ISS

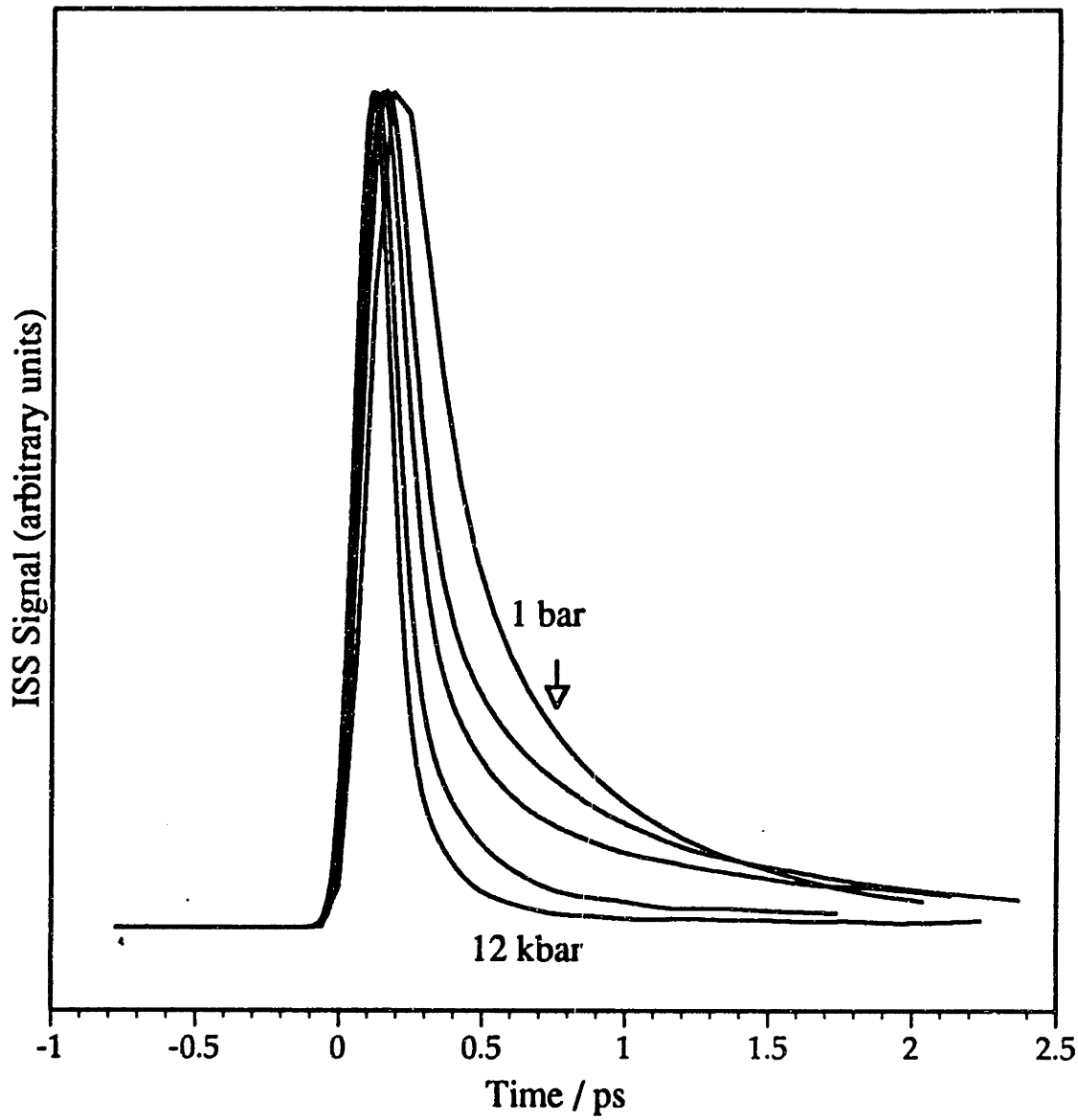

Figure 8.20 Simulated ISS signal calculated from isothermal MD runs. Excitation and probe pulse durations were assumed to be 80 fs. From top to bottom the experimental pressures corresponding to the liquid density used in the MD runs are: 1 bar, 2 kbar, 4 kbar, 8 kbar and 12 kbar, respectively.

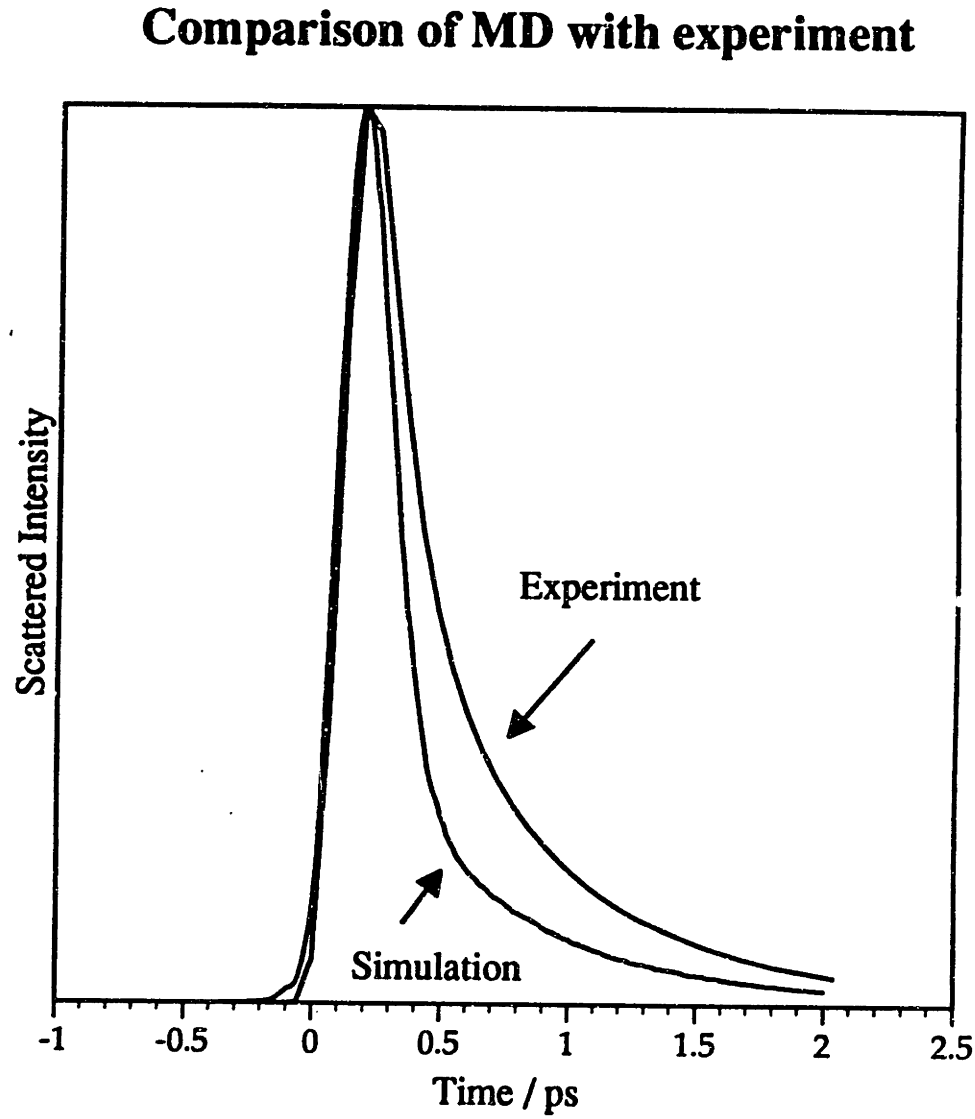

Figure 8.21 Comparison of nuclear-only ISS data from CS2 (solid curve) with simulated ISS response from molecular dynamics simulation (dashed curve). Both curves are for the 1 atm, 293 K state point.

response fails to reproduce the weak oscillation which is observed experimentally in the high density liquid.

For this particular intermolecular potential we conclude that molecular libration does not occur in the computer liquid at room temperature even at very high densities. In view of this surprising result, a different intermolecular potential was tried. Ladanyi suggested two LJ site-site potentials for CS_2, one with a quadrupolar term and one without [68]. We performed one simulation at ρ = 1.618 g cm^{-3} (corresponding to an experimental pressure of 8 kbar) using the potential without the quadrupolar interaction term. The parameters for this potential are given in table 8.3.

Table 8.6 Alternate LJ site-site potential for CS_2 from reference 68.

sites, ab	ε_{ab} / k_B (K)	σ_{ab} (Å)
C-C	51.2	3.35
S-S	172.02	3.59
C-S	93.85	3.47
Bond lengths: $d_{CS} = d_{SS}/2$ = 1.57 Å		

In table 8.1 the thermodynamic values obtained from this run are given. The pressure is considerably higher than that obtained with the TM potential due to the greater value of σ_{SS}. Just as Ladanyi *et al.* reported in their simulations, we observe no dynamical differences with this potential.

At a given density the ocfs decay more slowly than with the TM potential, but do not show any new dynamical structure.

In view of the failure of the MD simulation of single molecule reorientation to account for the oscillatory optical response, we must reconsider the interaction-induced (I-I) signal contributions discussed in chapter 3. As has been pointed out [106], pure reorientational scattering can never be observed, but purely interaction-induced scattering can be studied in monoatomic liquids and liquids of molecules of spherical symmetry. While the dynamics of reorientation in such liquids will be different than for liquids of anisotropic molecules, the I-I scattering may, to a first approximation, be similar. Little femtosecond scattering data exists on liquids which only have signal from I-I mechanisms. The ISS data in chapter 4 from several tetrahalide liquids do not have an allowed signal contribution from single molecule reorientation, but the presence of strong intramolecular vibrations makes the analysis of the signal difficult. The only other femtosecond light scattering of purely I-I scattering was done in 1984 with 180 fs pulses by Greene et al [107]. These authors measured the optical Kerr effect signal from liquid argon and liquid xenon. In the case of xenon, the authors observed only a single component to the nuclear signal, corresponding to a single exponential decay with a time constant of 450 fs. It would be invaluable to study the rare gas liquids once again, particularly as a function of density. Using polarization selectivity and the shorter pulse durations of the present time, more detailed conclusions could be made about the dynamics of the nuclear-only signal arising from I-I polarizabilities.

Finally, we ask the question, whether libration is ever observed in MD simulation of molecular liquids. A search of the literature suggests

that the answer, at least for nonassociated liquids, is no. As discussed in chapter 7 some of the strongest evidence for libration comes from experiments on liquid benzene. Yet several careful MD simulations of benzene at ambient conditions of temperature and pressure produced featureless (i.e. non-librational) ocfs similar to the ones observed here.

Linse, Engström and Jönsson studied benzene by MD simulation using a 12-site LJ potential with a point quadrupole term determined by ab initio calculations of the quantum chemical pair potential [108]. While the MD results reproduce the observation that spinning motion is relatively free, while tumbling motions are strongly hindered, it does not appear from the figure in their paper that the ocf of the tumbling axis (the motion detected in light scattering) reproduces the librational feature. Another MD simulation of benzene in which reorientational dynamics were considered is due to Steinhauser [109]. A persistent inertial part was observed in $C_2(t)$ out to 2 ps, but no librational "wiggles" were observed.

MD simulation of water at ambient pressure and temperature does yield reorientational correlation functions which show a pronounced glitch at very short times (0.06 - 0.10 ps), corresponding to librational motion [110]. In this case, each water molecule sits in a long-lived cage of four tetrahedrally coordinated neighbors. This liquid is known to be highly associated and the potential used in the simulation reflects this.

8.8 Conclusions

A systematic molecular dynamics simulation study of single molecule reorientation in liquid carbon disulfide was carried out using an

intermolecular pair potential which has been shown to give good agreement with experimental thermodynamic and dynamical data. Simulations of femtosecond ISS data show two decay times, one fast and one slow, and an inertial rise in signal, but do not reproduce the oscillatory signal seen after 500 fs delay time. Careful analysis of the single molecule reorientational correlation function, $C_2(t)$, showed no evidence of librational dynamics. Apart from an inertial effect at very short times, the reorientational correlation functions were found to make the transition from free-rotor to diffusional behavior without the occurrence of molecular libration, even at high liquid densities. In light of this finding, it may be necessary to revise our initial conclusions about librational motion in CS_2. Of course, libration may still depend sensitively on the details of the local intermolecular potential used in the computer simulations. Recently, a simulation of CS_2 has been reported for an intermolecular potential which includes a quadrupolar electrostatic interaction and intramolecular degrees of freedom [70]. The authors report better agreement with experiment using this potential than has been reported for rigid molecule potentials. It would be interesting to use their potential to simulate higher density state points.

Finally, mention must be made of the neglect of pair correlations and I-I terms. The pair contribution to the Rayleigh correlation function (the second term on the right hand side of equation 3.28) has seldom been evaluated from MD simulation, and to our knowledge no detailed study of this quantity has been undertaken for any liquid. Orientational pair correlations are quite long-lived, especially in dense molecular liquids, and there are many difficulties in accurately evaluating this collective property [111]. This quantity was calculated by Cheung and Powles [112] and by

Levesque and Weis [113] for a site-site model of liquid nitrogen. Levesque and Weis found that the total orientational correlation function (distinct and pair terms of equation 3.28) and the one calculated just by considering single molecules have virtually identical time dependences within statistical noise. In the case of N_2, the pair correlation term, although weak, appears to require several picoseconds to decay to zero, resulting in a somewhat slower decay for the total reorientation correlation function than just the singe molecule function. More theoretical and simulation work is needed, since there are currently almost no guidelines for predicting the dynamics of pair correlations in molecular liquids.

Ladanyi and Geiger's simulations [67,69] have attempted to include interaction-induced terms as wells as the collective orientational term (pair term), yet they still fail to reproduce a temporally oscillatory time-domain response (or, equivalently, the high-frequency shoulder in the Rayleigh spectrum). We believe this is a significant shortcoming in light of the oscillatory dynamics reported in this thesis. Given the difficulties involved in evaluating orientational pair correlations [111], it seems to us that a systematic study of the sources of error in the "all-orders" MD simulations is warranted.

The MD simulations reported here do demonstrate the presence of a rapid component to the molecular reorientation, arising from non-diffusional motion of CS_2 molecules. But in light of the failure of the simulation results to show an oscillatory response at high density, we suspect there are still difficulties in predicting even the "simple" dynamical process of single molecule reorientation. We believe that agreement with the short-time dynamics measured by femtosecond impulsive stimulated

light scattering may be a particularly stringent test of the intermolecular potential used in MD simulation of molecular liquids.

Chapter 9

Summary

The use of femtosecond duration optical pulses to study elementary dynamical processes has been successfully demonstrated on a variety of molecular liquids. The laser technology to achieve the time resolution necessary to conduct these investigations is considerable, but notable advances have already occurred in the last five years. Such improvements promise to increase the number of studies of ultrafast molecular dynamics. While understanding the microscopic dynamics of molecules in molecular liquids is a complex problem, this thesis has demonstrated a novel time-domain method for gaining additional information. It was shown how measurement of the time-dependent nonlinear optical susceptibility of a liquid provides information about a variety of dynamical processes of interest, including intra- and intermolecular vibration and reorientation. Coherent excitation and the subsequent dephasing of intramolecular vibrations was observed for a number of liquids.

Measurement of the ultrafast optical response of liquid carbon disulfide reveal oscillatory signal dynamics at low temperature. Femtosecond light scattering experiments carried out in a diamond anvil cell also show an oscillatory response, indicating vibrational dynamics which are strongly dependent on density. The data were interpreted in terms of intermolecular vibration which is predicted by cage models of the

liquid state. The data are consistent with heavily damped molecular libration in dense CS_2 which has substantial inhomogeneous broadening due to a wide range of local environments in liquids. Data from benzene and related liquids support the idea that intermolecular vibrational motion is of general importance in liquids of anisotropic molecules.

The femtosecond light scattering experiments on CS_2 were paired with molecular dynamics simulations to study single molecule reorientation in the dense liquid. The collective polarizability of the liquid was evaluated by including only the contribution from the reorientation of single molecules, neglecting interaction-induced polarizabilities and pair polarizabilities (the pair term in Rayleigh scattering). We felt justified in neglecting these terms in this initial study because of the difficulties associated with evaluating them and because we chose to answer the question of whether single molecule reorientation in the dense computer liquid could account for the observed signal dynamics. Single molecule orientational correlation functions computed from the simulations do not indicate significant molecular libration, and do not reproduce the oscillatory time-domain response. It is therefore possible that either the MD simulations are not adequate for describing the short time interactions of the liquid or the dynamics which contribute to the oscillatory ISS light scattering signal are dominated by the neglected polarizability contributions arising from motions of pairs and higher numbers of molecules. The computer simulations do predict a significant nondiffusional component to single molecule reorientation which occurs on a subpicosecond time scale.

While there are still many difficulties in interpreting the ISS data, the ability to observe the vibrational character of short-time molecular motion in many liquids is a significant advantage of the femtosecond

spectroscopy described in this thesis. Further systematic study by femtosecond ISS of a variety of liquids, neat and in dilution with others, as a function of thermodynamic state should provide additional insight into intermolecular interactions in molecular liquids.

Appendix A

Molecular Dynamics Simulation Notes

A.1 Introduction

There are a number of excellent reviews of the molecular dynamics (MD) technique as well as some recent monographs [49,114,115]. Molecular dynamics simulation usually conjures up images of supercomputer class resources, but with the diminishing performance gap between personal workstation computers and supercomputers it is frequently more cost effective to perform calculations on smaller, dedicated machines. All of the calculations reported in this thesis were performed on a single Sun Sparcstation 1 computer costing less than $10000. While the programming is challenging, the resources necessary for performing molecular dynamics simulations can be had in most research laboratories. This appendix contains some technical details of interest of the molecular dynamics code I wrote to study liquid carbon disulfide. Anyone interested can request programs by sending internet mail to root@vanna.mit.edu.

The programs described here simulate molecular liquids of linear molecules in the microcanonical ensemble. The molecules interact pairwise through Lennard Jones interaction site potentials. It is straightforward to include other sorts of interactions such as a Coulomb potential. It is also possible to generalize this code to molecules of arbitrary symmetry by modifying the code used to solve the rotational equations of motion.

In the first section of this appendix, some background information is given about the molecular dynamics technique. Next, I describe the simulation of linear molecules and how the equations of motion are solved. I describe solutions to the practical implementation problems of storing results and computing correlation functions which are of particular relevance to simulations performed on small workstation class computers. In appendix B, methods for minimizing the run time of simulations of large systems (> 1000 molecules) are discussed.

A.2 The molecular dynamics technique

An extensive literature as well as a number of review articles testify to the breadth of applications of molecular dynamics (MD) simulations. In this appendix the discussion is limited to the use of MD techniques to study simple molecular liquids composed of linear molecules. The molecules are modelled as rigid bodies with no internal degrees of freedom. The classical equations of motion governing the translation and rotation of N molecules confined to a cubic box of constant volume, V, are solved as a function of time. This constitutes an MD simulation in the microcanonical ensemble, where the length of a side of the box, L, is chosen in such a way that the number density $\rho = N/L^3$ is equal to the liquid density to be simulated. By computing forces and torques about molecular centers of mass it is possible to solve the translational and rotational equations of motion separately. Newtons equations of motions form a set of N coupled second order differential equations. They are solved by assuming constant forces and torques during a sufficiently small interval of time Δt, called the

timestep. The timestep is deemed sufficiently small when the total energy of the N molecule ensemble is conserved to an acceptable level. The positions and orientations of all molecules at timestep t_i are used to determine the forces and torques acting on all molecules. The positions and orientations are solved for at timestep t_{i+1} using an algorithm for solving linear differential equations.

It is assumed that the potential energy of the whole system can be written as a sum of pair terms,

$$U = \sum_{i<j}^{N} U_{ij} \tag{A.1}$$

In the simulation of an atomic liquid such as liquid argon it is often assumed that the interatomic pair potential can be approximated by the Lennard Jones 6-12 potential,

$$U(r) = 4\varepsilon\left\{\left(\frac{\sigma}{r}\right)^{12} - \left(\frac{\sigma}{r}\right)^{6}\right\} \tag{A.2}$$

where r is the distance between a pair of atoms. Unlike atoms, molecules possess both translational and rotational degrees of freedom. Furthermore, the potential between two molecules need no longer be spherically symmetric. A simple method for modelling these anisotropic potentials while keeping the simplicity of the Lennard Jones potential is to use an interaction site potential. With each site is associated a spherically symmetric LJ potential. Interaction sites are typically placed at the atomic positions in a molecule (although the site positions need not coincide with the atomic ones). The sites within a given molecule do not interact, i.e. a

molecule interacts only with other molecules and not with itself. The total potential between two molecules is given by the sum of the potentials between all sites,

$$U_{ij} = \sum_{a,b=1}^{nsites} U_{ia,jb} = \sum_{a,b=1}^{nsites} 4\varepsilon_{ab}\left\{\left(\frac{\sigma_{ab}}{r_{ia,jb}}\right)^{12} - \left(\frac{\sigma_{ab}}{r_{ia,jb}}\right)^{6}\right\} \tag{A.3}$$

where $r_{ia,\,jb}$ is the distance between site a on molecule i and site b on molecule j,

$$r_{ia,jb} = r_{ia} - r_{jb} \tag{A.4}$$

In order to solve the rotational and translational equations of motion we need the force on the center of mass of each molecule as well as the torque about the center of mass for each molecule. Both of these quantities can be written as simple sums over the quantities F_{ia}, where F_{ia} is the force on site a of molecule i due to all other molecules,

$$F_{ia} = \sum_{j\neq i}^{N} \sum_{b}^{nsites} f_{ia,jb} \tag{A.5}$$

where $f_{ia,\,jb}$, the force on molecule i, site a due to molecule j, site b is,

$$f_{ia,jb} = -\nabla U(r_{ia,jb}) = -\frac{dU_{ia,jb}}{dr_{ia,jb}}\frac{r_{ia,jb}}{r_{ia,jb}} \tag{A.6}$$

In the program it is convenient to save only the center of mass position vectors, r_i^{CM}, and the units vectors giving the orientation of molecule i, u_i.

Then at each timestep the site-site distance vectors are readily computed from,

$\mathbf{r}_{ia,jb} = \mathbf{r}_i^{CM} + d_a\mathbf{u}_i - d_b\mathbf{u}_j$

where the scalar d_a specifies the signed distance from the center of mass along the symmetry axis to site a.

The force on the center of mass of molecule i is,

$$\mathbf{F}_i^{CM} = \sum_a^{nsites} \mathbf{F}_{ia} \qquad (A.7)$$

A.3 Verlet algorithm for translational equations of motion

The translational equations of motion are solved using the Verlet leapfrog algorithm [96]. To simplify the notation in this section, I write $\mathbf{r}(t)$ for $\mathbf{r}_i^{CM}$, the position vector of the center of mass of molecule i at time t. We write the Taylor series expansions,

$$\mathbf{r}(t+\Delta t) = \mathbf{r}(t) + \dot{\mathbf{r}}(t)\Delta t + \tfrac{1}{2}\ddot{\mathbf{r}}(t)\Delta t^2 + O(\Delta t^3) \qquad (A.8)$$

$$\mathbf{r}(t-\Delta t) = \mathbf{r}(t) - \dot{\mathbf{r}}(t)\Delta t + \tfrac{1}{2}\ddot{\mathbf{r}}(t)\Delta t^2 - O(\Delta t^3) \qquad (A.9)$$

By summing (A.8) and (A.9) we obtain

$$\mathbf{r}(t+\Delta t) = 2\mathbf{r}(t) - \mathbf{r}(t-\Delta t) + \mathbf{F}(t)\Delta t^2 / m \qquad (A.10)$$

where we have used Newtons equation of motion for $\mathbf{r}$, $\mathbf{F}$ (= $\mathbf{F}_i^{CM}$) is the force on the molecular center of mass, and m is the mass of a molecule. The position increment, $\delta\mathbf{r}(t)$, is defined by,

$$\delta \mathbf{r}(t) = \delta \mathbf{r}(t - \Delta t) + \mathbf{F}(t)\Delta t^2 / m \qquad (A.11)$$

This equation specifies an iterative method for obtaining $\delta \mathbf{r}(t)$ at each timestep from the value at the previous timestep, $\delta \mathbf{r}(t-\Delta t)$. Knowing $\delta \mathbf{r}(t)$ at each timestep we can advance $\mathbf{r}(t)$ since,

$$\mathbf{r}(t + \Delta t) = \mathbf{r}(t) + \delta \mathbf{r}(t) \qquad (A.12)$$

The pair of equations A.11 and A.12 constitute the Verlet algorithm. They specify how to solve for the center of mass position of each molecule at the next timestep given the position at the previous timestep. The Verlet algorithm is simple and compact: For each molecule it is only necessary to store a position, $\mathbf{r}$, and a position increment, $\delta \mathbf{r}$. This algorithm is usually a better choice than higher-order algorithms (such as the predictor-corrector method [116]), because of its simplicity and because it conserves energy well even with a large timestep [117].

A.4 Singer algorithm for rotational motion of linear molecules

Rotational equations of motion present some added difficulties. One problem involves the choice of coordinate system. The eulerian equations of motions possess a singularity in the polar angle θ. This means that a computer algorithm will be unstable whenever this angle approaches zero. This is clearly unacceptable, but fortunately a variety of techniques have been used which circumvent this problem. For the case of rigid bodies of arbitrary symmetry, Evan's quaternion method can be used [118]. This technique uses a 4-dimensional vector, a quaternion, which can be used to express singularity-free equations of motion. The SHAKE algorithm of

Ryckaert *et al.* has also been used successfully for molecules as complex as large proteins [119]. For the special case of linear molecules, simpler algorithms can be constructed which take into account the fewer rotational degrees of freedom. The algorithm by Singer *et al.* [97] is the one used in these programs and is described next.

The equation of motion of the unit vector, $\mathbf{u}_i$, giving the orientation of the axis of the ith molecule can be written,

$$I\ddot{\mathbf{u}}_i = \mathbf{G}_i = \sum_{a=1}^{nsites} d_a \mathbf{F}_{ia} \tag{A.13}$$

where I is the molecular moment of inertia. Vector $\mathbf{G}_i$ is related to the torque on molecule i, $\mathbf{N}_i$,

$$\mathbf{N}_i = \mathbf{u}_i \times \mathbf{G}_i \tag{A.14}$$

Equation A.13 must be solved subject to the constraint that the length of $\mathbf{u}$ remains equal to unity. This is done by subtracting off the component of the force, $\mathbf{G}_i$, directed along $\mathbf{u}_i$. Then the equation of motion can be written,

$$I\ddot{\mathbf{u}}_i = \mathbf{G}_i^{\perp} - I|\dot{\mathbf{u}}_i|^2 \tag{A.15}$$

The last term of this equation represents a centripetal force term which keeps $\mathbf{u}$ constant. This term is difficult to evaluate accurately so the Singer algorithm uses an equivalent kinematic constraint instead. At timestep t_n, we use the current orientation, $\mathbf{u}_n$, the orientation at the previous timestep,

$\mathbf{u}_{n-1}$, and the angle between these two orientations, θ_n to obtain the orientation at the next timestep, $\mathbf{u}_{n+1}$ according to the steps:

$$\begin{aligned} \mathbf{x} &= \frac{\tan\theta_n}{\theta_{n+1}}(\mathbf{u}_n - \mathbf{u}_{n-1}/\cos\theta_n) + \frac{\Delta t^2 \mathbf{G}^{\perp}}{I} \\ \theta_{n+1} &= |\mathbf{x}| \\ \mathbf{u}_{n+1}' &= \mathbf{u}_n + \frac{\tan\theta_{n+1}}{\theta_{n+1}}\mathbf{x} \\ \mathbf{u}_{n+1} &= \mathbf{u}_{n+1}'/\left|\mathbf{u}_{n+1}'\right| \end{aligned} \qquad \text{(A.16)}$$

The last step enforces the unit length of **u**. In the program it is necessary to allocate storage for the orientation at the previous timestep and for the angle reoriented through in the last step.

A.5 Format of MD run files

It is useful to generate production runs independently of the computation of correlation functions or other quantities of interest. This breaks the computer tasks into more manageable pieces and it permits further analysis at later times. Production runs were written as a series of files to a hard disk with a reasonable amount of free space (50 - 100 Mb). Each file is typically sized to be 1 Mb. The tremendous volume of data which can be generated from even a modest simulation of a small number of molecules.requires judicious consideration of what to save. In general, we wish to save as little information as needed to obtain statistically accurate

correlation functions. Fortunately, it is rarely necessary to save information at every timestep.

I find it useful to divide the variables into two sets: a fast set and a slow set. The fast set includes variables which change rapidly. These are the angular velocity, the center of mass velocity, the force and the torque. The slow variables include the positions and orientations. The slow variables were saved at less frequent intervals than the fast variables. This reduces the amount of information saved to a more reasonable amount. The total number of times to save the slow variables and the fast variables is specified at the start of the run. Since the autocorrelation functions of the fast variables decay rapidly to zero, it is not necessary to simulate as long as necessary for computing correlation functions of the slow variables. Slow variables are saved every ns timesteps, while the fast variables are saved every nf time steps, where ns > nf. Typically, ns was chosen so that ns*timestep = 80 fs when computing correlation functions at long times, whereas nf*timestep = 10-20 fs.

A.5.1 Compact storage of floating point numbers

Due to the large quantity of numbers generated in a molecular dynamics simulation it is desirable to store numbers in a compact manner which permits sufficient precise digits to be saved. There is also no sense in saving more digits than are accurate. A simple representation for floating point numbers was chosen for this program which achieves nearly optimal compression. Floating point numbers are converted to a normalized form, i.e. +1.32523e-02. Each floating point number consists of a mantissa, an exponent, a sign for the mantissa and a sign for the exponent. One bit is

needed for each sign and the exponent is binary encoded in 6 bits. This limits the maximum exponent to an integer < 64, but this is never a problem for an MD program which utilizes normalized box units (L_{box} = 1). In other words, the program can always be constructed so that numbers are scaled to always fall within this range.

NDIGIT total number of precise digits from the mantissa are BCD-encoded in NDIGIT/2 bytes. The total number of bytes needed to store a floating point number with NDIGIT precise digits is NDIGIT/2 + 1. This figure can be compared with optimal compression of 2+6+NDIGITS*(log210) bits. I save 8 precise digits, a number which is probably excessively conservative.

All variables are compressed before they are written to disk. The compression algorithm is simple, runs fast, and achieves nearly optimal compression. Another virtue of this scheme is that the data files generated are truly machine-independent and can be processed trivially on any computer. In this lab, files have been shared trivially by programs running on Cray supercomputers, IBM PCs and on Sun workstations.

A.6 Equilibration of liquid configurations

The usual technique for generating a liquid-like configuration is to place the molecular centers of mass at the lattice sites of an FCC lattice. The initial translational ordering is lost after several thousand timesteps. Avoiding orientational ordering poses a more serious problem. If the molecules are initially given random orientations, it can happen that two sites of molecules at adjacent lattice sites are positioned unphysically close

When sites are too close, the forces derived from the intermolecular potential are enormous, and the simulation is unstable. This is the case for the CS_2 potential used here and for many other molecular potentials used for simulations at typical liquid densities.

The problem can be avoided if all mclecules are given identical initial orientations. Unfortunately, such a net orientational alignment can persist for very long times, lasting longer than 100 ps for a CS_2 simulation at 1.500 g cm^{-3}. A better method is to start molecules at FCC lattice sites with random orientations, choosing the initial liquid density low enough that no two sites can ever be positioned unphysically close. Let d_a be the distance from the molecular center of mass to the furthest site, a, and σ_{aa} be the LJ sigma parameter for interactions between a sites. The initial number density ρ is chosen $\leq \rho_{max}$,

$$\rho_{max} = \frac{\sqrt{2}}{\left(2^{1/6}\sigma_{aa} + 2d_a\right)^3}. \qquad \text{(A.17)}$$

The distance of closest approach between randomly oriented sites is then $2^{1/6}\sigma_{aa}$, corresponding to the minimum of the LJ potential. For the TM CS_2 potential, this corresponds to a mass density of about 0.5 g cm^{-3}.

While the starting density given by equation (A.17) is overly conservative, a configuration at a different density is easily generated by gradually relaxing the density to the desired value. The walls of the simulation box are effectively shrunk in such a way that the density changes linearly from the initial value to the final value [117]. If the density is changed too rapidly, the temperature will rise in the same way that the temperature of a gas subjected to a sudden compression will increase. I

found the most effective technique is to linearly increase (or decrease) the density over 200-1000 timesteps (with a larger number of steps for larger density changes), while applying a constant temperature bath. In order to avoid perturbing the system too strongly the temperature bath was slowly "turned on" in the manner suggested by Ryckaert [117]. This method of temperature and density skewing can obviously be applied to any liquid-like configuration. In practice, then, it is only necessary to start N molecules once from the FCC lattice sites as described above. Later configurations were obtained from previous ones. This procedure allows efficient generation of even very high density configurations which were well equilibrated and showed no net orientation.

A.7 Computation of acfs

After a run is completed autocorrelation functions (acfs) of the variables are calculated. For an autocorrelation function, any point in time can be considered an origin of time. If a correlation function is to be evaluated at a total of m points starting from the beginning of the run, a buffer is loaded with the variable at the first m points. From this buffer the acf is calculated. The m+1st step overwrites the 1st step (the oldest data) and the acf is again calculated now with the next step as time origin. The memory requirements of this algorithm are,

nc*nmols*3*nf

where nc is the number of points at which the correlation function is evaluated, nmols is the number of molecules in the simulation, and nf is the number of bytes for the machine representation of a floating point number. This can become larger than available RAM, requiring frequent swapping If necessary, the correlation function can be calculated for subsets of the entire system of molecules and later averaged together to avoid excessive disk thrashing.

Appendix B

Minimization of Run Time for MD Simulation of Molecular Liquids

B.1 Introduction

This section presents methods for reducing the run time of MD simulations of molecular liquids performed on a single-processor computer. It is often necessary to simulate larger systems in order to check for system-size dependent effects. A number of properties of interest (pair correlation, shear viscosity, etc.) depend upon sufficiently long-ranged interactions that it is essential to simulate larger numbers of molecules. It is shown here that the run time can be kept approximately linear in N, where N is the number of molecules in the simulation.

Nearly all of the time required to perform a simulation is spent evaluating forces between molecules. Using the profiling option of the Unix C compiler, I determined that for a simulation of 1372 CS_2 molecules on a Sun Sparcstation 1 computer, over 98 % of the total run time is spent on the evaluation of forces. Consequently, it only pays to optimize this step. Of course, an obvious way of reducing run time is to increase the step size and / or run a smaller number of total steps. The multiple time step method of Street *et al.* describes a technique for increasing the step size [120].

As the number of molecules, N, in an MD simulation increases, the number of pairs of molecules grows as,

$$\frac{N(N-1)}{2} \approx \frac{N^2}{2}. \qquad \text{(B.1)}$$

Since the molecules interact pairwise, it appears at first sight that the run time is condemned to grow quadratically with N. Fortunately, the forces in liquids are frequently of sufficiently short range that the potential between two molecules separated by more than a given distance, r_{cut}, can be set to zero. Then only molecules contained in a sphere of radius r_{cut} interact with a given molecule. For the Lennard-Jones intermolecular potential used in simulations r_{cut} = 10 Angstroms. At typical liquid densities this means a molecule interacts with about 40 neighbor molecules instead of N-1 molecules. With no prior knowledge of pair distances, it is necessary to evaluate N(N-1)/2 pair distances. However, only a considerably smaller number of pairs ($\approx$ 40 N) will be sufficiently close that it is necessary to evaluate the forces between them. A number of researchers have pointed out that the run time can be improved by reducing the number of pairs which must be distanced.

The first way to reduce the number of unnecessary pair distance evaluations was suggested by Verlet [96]. Every n timesteps a list is formed for each molecule containing other molecules whose centers of mass are closer than a distance $r_{cut} + \Delta$. For the next n timesteps, possible pair interactions for a given molecule are looked for only among the entries of the molecules neighbor list. Clearly Δ must be chosen large enough so that after n timesteps, no molecules which are not on the list

have a chance of penetrating the interaction sphere of radius r_{cut} about the central molecule. There are two principal drawbacks to this approach. First of all, for large N, the storage required for maintaining neighbor lists becomes prohibitive. Secondly, since all N(N-1) pair distances must be calculated every n timesteps (n is typically 10), this algorithms retains a substantial N^2 behavior.

B.2 The cell algorithm

A superior method is the cell algorithm, suggested by several authors [121,122]. This approach recognizes that the coordinates of each molecule already contain implicit information about their mutual distances. The simulation box is divided into a total of K (where $K = m^3$, m integer) equal-volume, cubic cells. Since only certain cells will be near enough to (possibly) have molecules which interact with molecules in a given cell, the number of pair distances which must be considered can be reduced. This is illustrated for two dimensions in figure B.1. The expected run time is analyzed in greater detail below.

At each timestep all N molecules are sorted into cells. This step is very efficient, requiring only 3N multiplications. Next, all cells are visited in sequence and the interactions of the molecules contained in each cell are computed. Molecules within a given cell interact with other molecules in the same cell and with all molecules in the set of cells which are less than a distance r_{cut} away. Actually only one half of the cells comprising the interaction sphere are visited in order to avoid overcounting pairs. The number of molecules in each cell is, on average,

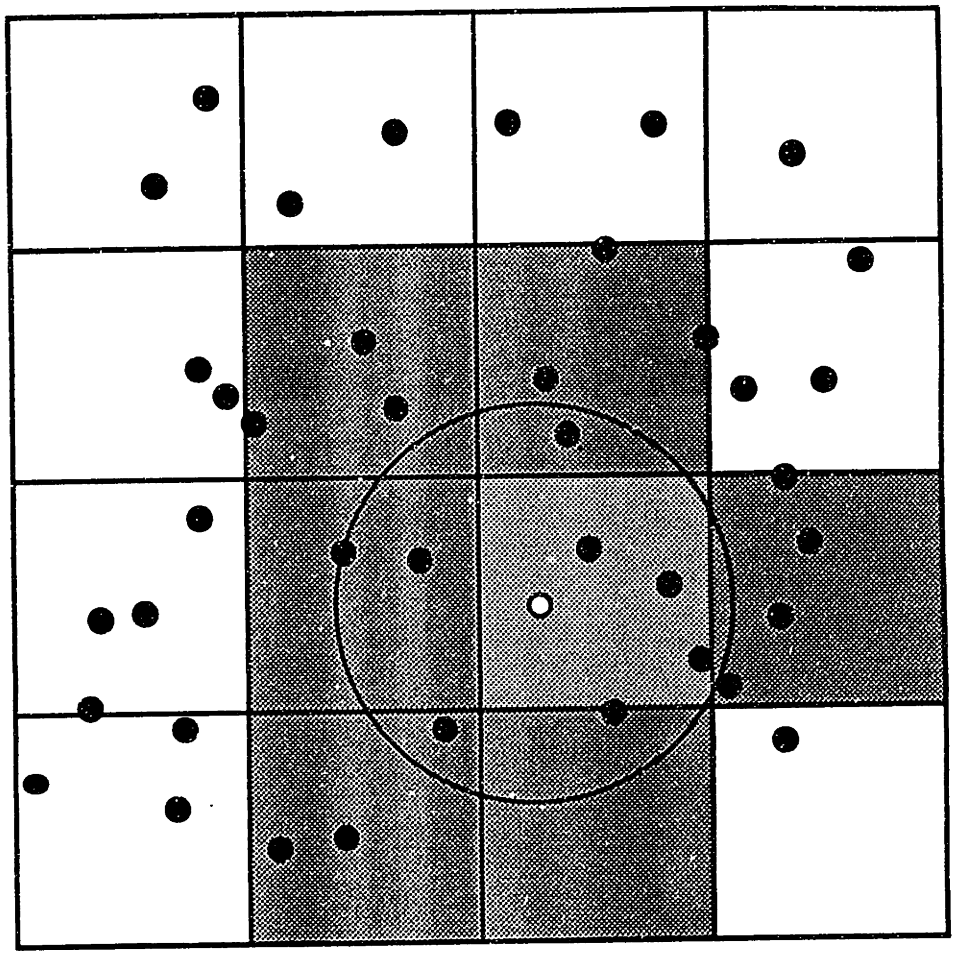

Figure B.1 Depiction of cell algorithm in two dimensions. The circle above represents the potential cutoff distance for the 'white' particle. The shaded boxes indicate neighbor cells which may contain particles which can interact with the white particle. The complete set of neighbor cells is determined by taking the intersection of the cells in the simulation box with the object formed by the intersection of cutoff circles drawn from every point within the lightly shaded cell. In this manner, all cells which can possibly contain particles closer than the cutoff distance to particles in the lightly shaded cell will be considered.

$$n = \frac{N}{K}. \tag{B.1}$$

For each cell in the box we must evaluate pair distances among molecules within the cell and all pair distances with molecules in the set of neighbor cells. If S is the number of cells which include one half of the cutoff sphere, the total number of pair distances computed for one cell is

$$n^2 S + n(n-1)/2 \tag{B.2}$$

Multiplying by K, the total number of cells, the expected number of evaluated pair interactions is obtained,

$$npairs = (S + \frac{1}{2})\frac{N^2}{K} - \frac{N}{2} \tag{B.3}$$

This expression has the proper limiting values. In the most unfavorable case, S = (K-1)/2. That is, a cell must interact with one half of all other cells in the box. Then,

$$npairs = \frac{N(N-1)}{2} \tag{B.4}$$

and no time savings is achieved. As K gets large at constant r_{cut}, N and ρ,

$$S = \frac{2}{3}\pi\rho r_{cut}^{\ 3}\frac{K}{N} \tag{B.5}$$

and the number of pairs is,

$$\text{npairs} = \frac{N}{2}(\frac{4}{3}\pi\rho r_{cut}^{\ 3} - 1). \qquad \text{(B.6)}$$

This is just the minimum number of pair interactions which must be evaluated for a potential cutoff distance of r_{cut}. This is because the interaction sphere about each molecule contains on average $\frac{4}{3}\pi\rho r_{cut}^{\ 3} - 1$ neighboring molecules.

From equation (B.3) the number of pairs which must be distanced will decrease as K, the number of cells, increases. There is, however, a limit to how big K can be made. This is because the quantity S, the number of neighbor cells, increases as K increases for constant N, r_{cut}. For each nonempty cell, S neighbor cells must be checked. Assuming there is about one molecule per cell, the number of integer operations goes as SK and can be shown to increase as the sixth power of m, where m is the number of cells along a box side. There will be then, in general, an optimal value of m. Further increasing the number of cells will actually increase the run time, as more and more time is spent on integer operations searching through cells. This is seen from the timing results in table B.1.

Finally, the cell algorithm is useful only when more time is spent evaluating pair distances than on the evaluation of forces. For small N not much optimization is achieved, since most of the time is spent evaluating forces anyway. The time spent evaluating pair interactions can be broken down into a sum of time evaluating the distance between pairs of molecules and time spent evaluating forces between pairs. Let t_d be the time to

evaluate the distance r between two molecules. Let t_i be the time to evaluate the forces between all sites of two molecules. The total time spent evaluating pair interactions is given by the sum,

$$\text{runtime} = T_d + T_f = N_d t_d + N_f t_f \tag{B.7}$$

In the worst case (no knowledge of positions of particles) this runtime is given by,

$$\text{runtime} = \frac{N(N-1)}{2} t_d + \frac{N}{2}(\frac{4}{3}\pi\rho r_{cut}^3 - 1)t_f \tag{B.8}$$

The times t_d and t_f are independent of N with $t_f > t_d$. At short times more time is spent evaluating forces than distancing pairs of molecules. At large N however the quadratic dependence of the first term is more important than the second term and most run time is spent evaluating all possible pair distances. This is illustrated in figure B.2, where T_d/T_{tot} and T_f/T_{tot} are plotted vs. N, andT_{tot} is the total run time. For small values of N more time is actually spent evaluating pair interactions, then is spent evaluating the full set of N(N-1)/2 possible pair distances. In generating this figure, I use the value t_f/t_d = 20, appropriate for simulating CS_2 on a Sun Sparcstation 1 computer. The curves cross near N=600. This means that for systems with more than 600 molecules more time is being spent evaluating pair distances than forces. Consequently, for this example, it is only reasonable to use the cell technique when the simulation system contains more than 600 molecules. More significant time savings are obtained as N increases.

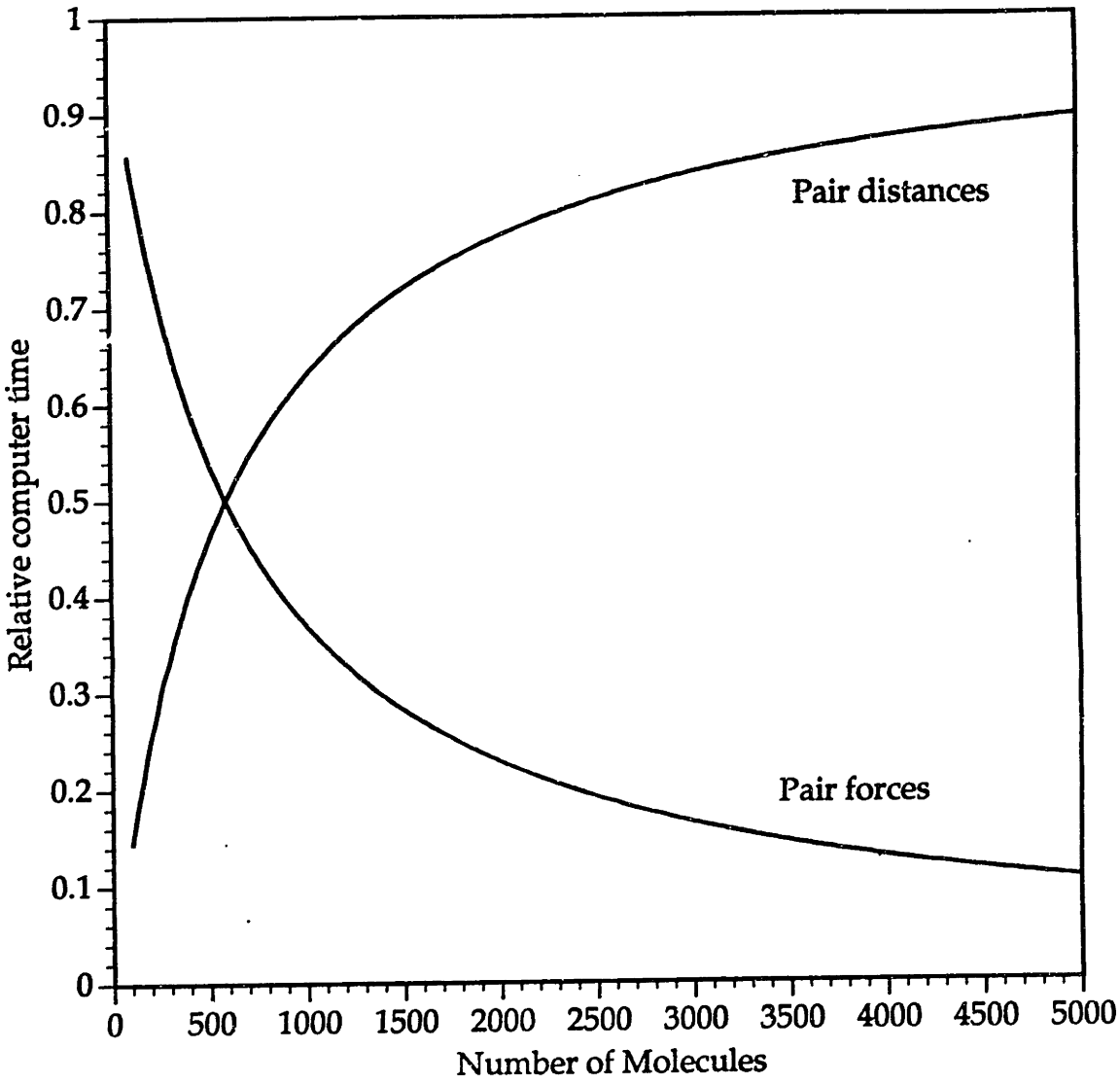

Figure B.2 Relative computer time spent evaluting pair distances and evaluating pair forces as a function of MD simulation size. Curves drawn are for a simulation of liquid carbon disulfide at a number density of 0.01 per cubic angstrom.

B.3 Timing results

In this section results are presented for the cell algorithm for various size simulations of liquid CS_2 performed on a Sun Microsystems Sparcstation 1 computer. The times below are for a liquid density of 1.263 g cm^{-3}. For a 1372 molecule system, profiling revealed that 61% of runtime was spent evaluating pair distances, 27% of time was spent actually evaluating pair forces. So the use of the cell algorithm is expected to significantly improve run times. The dependence of the time per timestep vs. m (number of cells per box side) is shown in table B.1. The cutoff radius was held constant at 9 Angstroms.

Table B.1 Run time as a function of m, the number of cells per box side, for a simulation of 1372 molecules. Columns 3-6 give the percentage run time spent on different parts of the simulation.

m	S	% pair dist	% pair inter	pair dist calls	% cell search	time / iteration
0	N.A.	61.1	26.6	941000	N.A.	20.6
8	40	14.9	55.9	148000	2.6	9.1
9	58	14.5	54.5	150000	3.7	9.4
10	62	11.7	56.1	117000	3.7	9.1
11	62	8.8	57.4	87700	3.6	8.8
17	155	5.5	50.9	58900	7.6	9.9

A factor of two improvement is obtained by using the cell algorithm. Note that m = 11 is optimal, with the run time increasing slowly as m increases. The response is relatively flat.

In conclusion, for the simulation of molecular liquids the number of particles for which the gains become appreciable is greater than in the case of simulating atomic liquids This is because of the greater percentage of time spent in the evaluation of forces between interacting pairs of molecules. I have analyzed in detail how the cell algorithm can result in significant time savings for single-processor simulations of systems containing several thousand molecules.

References

1. B.J. Berne and R. Pecora. *Dynamic light scattering*. Wiley-Interscience, New York, 1976.

2. K.A. Nelson and E.P. Ippen. Femtosecond coherent spectroscopy. *Adv. Chem. Phys.* **75** (1989) 1.

3. G.R. Fleming. Subpicosecond Spectroscopy. *Ann. Rev. Phys. Chem.* **37** (1986) 81.

4. W.G. Rothschild. *Dynamics of Molecular Liquids*. Wiley, New York, 1984.

5. W. Coffey, M. Evans and P. Grigolini. *Molecular Diffusion and Spectra*. Wiley, New York, 1984.

6. C.H. Wang. *Spectroscopy of Dense Media: Dynamics of Molecular Liquids* . Academic Press, New York, 1985.

7. C. Brot and I. Darmon. Statistical dynamics of a rotator in a potential of cubic symmetry. *Mol. Phys.* **21** (1971) 785.

8. W.T. Coffey. On the calculation of orientational autocorrelation functions for simple models of molecular reorientation. *Chem. Phys. Lett.* **52** (1977) 394.

9. J.N. Kushick. A librational model for molecular reorientation in condensed phases. *J. Chem. Phys.* **67** (1977) 2068.

10. V.I. Gaiduk and Y.P. Kalmykov. Application of the confined rotator model for microwave and far-infrared absorption of some polar liquids. *J. Chem. Soc. Faraday Trans. II* **77** (1981) 929.

11. K. Pasterny and A. Kocot. Application of the confined rotator model for the calculation of higher-order orientational correlation functions. *J. Chem. Soc. Faraday Trans. II* **82** (1986) 485.

12. S.K. Deb. Collision-interrupted librational model for molecular reorientation in liquids. *Chem. Phys.* **120** (1988) 225.

13. R.L. Fork, B.I. Greene and C.V. Shank. Generation of optical pulses shorter than 0.1 psec by colliding pulse mode locking. *Appl. Phys. Lett.* **38** (1981) 671.

14. T. Norris, T. Sizer II and G.A. Mourou. Generation of 85-fsec pulses by synchronous pumping of a colliding-pulse mode-locked dye laser. *J. Opt. Soc. Am. B* **2** (1985) 613.

15. J.A. Valdmanis and R.L. Fork. Design considerations for a femtosecond pulse laser balancing self phase modulation, group velocity dispersion, saturable absorption and saturable gain. *IEEE J. Quant. Electron.* **QE-22** (1986) 112.

16. R.L. Fork, O.E. Martinez and J.P. Gordon. Negative dispersion using pairs of prisms. *Opt. Lett.* **9** (1984) 150.

17. J.P. Zheng, U. Sen, D.M. Benenson and H.S. Kwok. Observation of periodicity multiplication in a synchronously pumped dye laser. *Optics Lett.* **11** (1986) 632.

18. R.L. Fork, C.V. Shank and R.T Yen. Amplification of 70-fs optical pulses to gigawatt powers. *Appl. Phys. Lett.* **41** (1982) 223.

19. I.N. Duling III, T. Norris, T. Sizer II, P. Bado and G.A. Mourou. Kilohertz synchronous amplification of 85-femtosecond optical pulses. *J Opt. Soc. Am. B.* **2** (1985) 616.

20. I.N. Duling, P. Bado, S. Williamson, G. Mourou and T. Baer, in *Digest of Conference on Lasers and Electro-Optics* (Optical Society of America, Washington, D.C., 1984), paper PD3.

21. J.C. Postlewaite, J.B. Miers, C.C. Reiner and D.D. Dlott. Picosecond Nd:YAG regenerative amplifier with acoustooptic injection and electrooptic VFET switchout. *IEEE J. Quant. Electron.* **QE-24** (1988) 411.

22. J.D. Kafka and T. Baer. Prism-pair dispersive delay lines in optical pulse compression. *Opt. Lett.* **12** (1987) 401.

23. R.L. Fork, C.V. Shank, R. Yen and C.A. Hirlimann. Femtosecond optical pulses. *IEEE J. Quant. Electron.* **QE-19** (1983) 500.

24. L.R. Williams and K.A. Nelson. Excimer formation in pyrene molecular crystal: Femtosecond dynamics of an oriented bimolecular reaction. *J. Chem. Phys.* **87** (1987) 7346.

25. B. Kohler and M. Banet, unpublished work.

26. Y.-X. Yan, L.-T. Cheng and K.A. Nelson. The temperature-dependent distribution of relaxation times in glycerol: Time-domain light scattering study of acoustic and Mountain-mode behavior in the 20 MHz -3 GHz frequency range. *J. Chem. Phys.* **88** (1988) 6477.

27. Y.R. Shen. *The Principles of Nonlinear Optics.* Wiley-Interscience, 1984.

28. Y.R. Shen. Basic considerations of four-wave mixing and dynamic gratings. *IEEE J of Quantum Electronics* **QE-22** (1986) 1196.

29. S. Ruhman, A.G. Joly, B. Kohler, L.R. Williams and K.A. Nelson. Intramolecular and intermolecular dynamics in molecular liquids through femtosecond time-resolved impulsive stimulated scattering. *Revue Phys. Appl.* **22** (1987) 1717.

30. C. Kalpouzos, W.T. Lotshaw, D. McMorrow and G.A. Kenney-Wallace. Femtosecond laser-induced Kerr responses in liquid CS_2. *J. Phys. Chem.* **91** (1987) 2028.

31. C. Kalpouzos, D. McMorrow, W.T. Lotshaw and G.A. Kenney-Wallace. Femtosecond laser-induced optical Kerr dynamics in CS_2 / alkane binary solutions. *Chem. Phys. Lett.* **150** (1988) 138.

Corrections appear in, *Chem. Phys. Lett.* **155** (1988) 240.

32. B.I. Greene and R.C. Farrow. The subpicosecond Kerr effect in CS_2. *Chem. Phys. Lett.* **98** (1983) 273.

33. M.D. Fayer. Dynamics of molecules in condensed phases: Picosecond holographic grating experiments. *Ann. Rev. Phys. Chem.* **33** (1982) 63.

34. Keith A. Nelson, R.J. Dwayne Miller, D.R. Lutz and M.D. Fayer. Optical generation of tunable ultrasonic waves. *J. Appl. Phys.* **53** (1982) 1144.

35. Y.-X. Yan and K.A. Nelson. Impulsive stimulated light scattering. I. General theory. *J. Chem. Phys.* **87** (1987) 6240.

36. Y.-X. Yan and K.A. Nelson. Impulsive stimulated light scattering. II. Comparison to frequency-domain light-scattering spectroscopy. *J. Chem. Phys.* **87** (1987) 6257.

37. Y.-X. Yan, L.-T. Cheng and K.A. Nelson. Impulsive stimulated light scattering. In *Advances in Non-linear Spectroscopy*, eds. R.J.H. Clark and R.E. Hester, Wiley, New York, 1987, p. 299.

38. For a review see: A. Laubereau and W. Kaiser. Vibrational dynamics of liquids and solids investigated by picosecond light pulses. *Rev. of Mod. Phys.* **50** (1978) 607.

39. R. Leonhardt, W. Holzapfel, W. Zinth and W. Kaiser. Terahertz quantum beats in molecular liquids. *Chem. Phys. Lett.* **133** (1987) 373.

40. J.F. Reintjes. *Nonlinear optical parametric processes in liquids and gases.* Academic Press, Orlando, 1984.

41. R.W. Hellwarth. Third-order optical susceptibilities of liquids and solids. *Prog. Quant. Electronics.* **5** (1977) 1.

42. J.-M. Halbout and C.L. Tang. Femtosecond interferometry for nonlinear optics. *Appl. Phys. Lett.* **40** (1982) 765.

43. J. Etchepare, G. Grillon, J.P. Chambaret, G. Hamoniaux and A. Orszag. Polarization selectivity in time-resolved transient phase grating. *Optics Comm.* **63** (1987) 329.

44. J. Etchepare, G. Grillon and J. Arabat. Polarization effects in femtosecond time-resolved coherent scattering from molecules in liquids. *Appl. Phys B* **49** (1989) 425.

45. M. Fixman. Molecular theory of light scattering. *J. Chem. Phys.* **23** (1955) 2074.

46. S. Kielich. A molecular theory of light scattering in gases and liquids. *Acta Phys. Polonica* **19** (1960) 149.

47. R. Pecora and W.A. Steele. Scattering from fluids of nonspherical molecules. II. Light. *J. Chem. Phys.* **42** (1965) 1872.

48. M. Thibeau, G.C. Tabisz, B. Oksengom and B. Vodar. Pressure-induced depolarization of the Rayleigh light scattered from a gas of optically isotropic molecules. *J. Quant. Spectrosc. Radiat. Transfer* **10** (1970) 839.

49. D. Frenkel in *Intermolecular Spectroscopy and Dynamical Properties of Dense Systems (Proceedings of the International School of Physics "Enrico Fermi" course 75)* ed. J. van Kranendonk, North-Holland, 1980, p. 506.

50. A. Borysow and L. Frommhold. Collision-induced light scattering: A bibliography. *Adv. in Chem. Phys.* **75** (1989) 439.

This excellent bibliography contains over 700 references to a broad variety of works covering experiment, theory and molecular dynamics simulation. Many are directly related to interaction-induced scattering from molecular liquids.

51. P.A. Madden. Interaction-induced, subpicosecond phenomena in liquids, in *Ultrafast Phenomena IV*, eds. D.H. Auston and K.B. Eisenthal, Springer-Verlay, Berlin, 1984.

52. DMS RAMAN / IR Atlas, eds. B. Schrader and W. Meier, Verlag Chemie GmbH, Weinheim, 1974.

53. R.J.H. Clark and C.J. Willis. Raman intensity measurements on group IV tetrahalides. *Inorganic Chemistry* **10** (1971) 1118.

54. S. Claesson and D.R. Jones. Depolarized Rayleigh light scattering and reorientation of molecular liquids under high pressure, *Chemica Scripta* **9** (1976) 103.

55. Y. Higashigaki, S.L. Whittenburg and C.H. Wang. Light scattering studies of orientational fluctuations of CS_2. *J. Chem. Phys.* **7** (1978) 3297.

56. H. Langer and H. Versmold. Depolarized Rayleigh scattering: Orientational correlation functions of acetonitrile and carbon disulfide, *Ber. Bunsenges. Phys. Chem.* **83** (1979) 510.

57. T.I. Cox, M.R. Battaglia and P.A. Madden. Properties of liquid CS_2 from the allowed light scattering spectra. *Mol. Phys.* **38** (1979) 1539.

58. B. Hegemann and J. Jonas. Separation of temperature and density effects on collision-induced Rayleigh and Raman line shapes of liquid carbon disulfide. *J. Chem. Phys.* **82** (1985) 2845.

59. S. Ikawa and E. Whalley. Polarized and depolarized Raman spectra of liquid carbon disulfide in the pressure range 0-10 kbar. II. Reorientational and vibrational relaxation. *J. Chem. Phys.* **86** (1987) 1836.

60. H.W. Spiess, D. Schweitzer, U. Haeberlein and K.H. Hausser. Spin-rotation interaction and anisotropic chemical shift in $^{13}CS_2$. *J. Magn. Reson.* **5** (1971) 101.

61. J.R. Lyerla, D.M. Grant and R.D. Bertrand. Field-dependent contributions to carbon-13 nuclear relaxation. *J. Phys. Chem.* **75** (1971) 3967.

62. O. Steinhauser and M. Neumann. Structure of liquid carbon disulphide: a molecular dynamics study. *Mol. Phys.* **37** (1979) 1921.

63. O. Steinhauser. Single particle dynamics of liquid carbon disulphide. *Chem. Phys. Lett.* **82** (1981) 153.

64. D.J. Tildesley and P.A. Madden. An effective pair potential for liquid carbon disulphide. *Mol. Phys.* **42** (1981) 1137.

65. D.J. Tildesley and P.A. Madden. Time correlation functions for a model of liquid carbon disulphide. *Mol. Phys.* **48** (1983) 129.

66. P.A. Madden and D.J. Tildesley. Interaction-induced contributions to Rayleigh and allowed Raman bands. A simulation study of CS_2. *Mol. Phys.* **55** (1985) 969.

67. L.C. Geiger and B.M. Ladanyi. Higher-order interaction-induced effects on Rayleigh light scattering in molecular liquids. *J. Chem. Phys.* **87** (1987) 191.

68. L.C. Geiger and B.M. Ladanyi. Higher-order interaction-induced effects on the allowed Raman spectra of liquid CS_2. *J. Chem. Phys.* **89** (1988) 6588.

69. L.C. Geiger and B.M. Ladanyi. Molecular dynamics simulation study of nonlinear optical response of fluids. *Chem. Phys. Lett.* **159** (1989) 413.

70. S.-B. Zhu, J. Lee and G.W. Robinson. Molecular dynamics simulation of liquid carbon disulphide with a harmonic intramolecular potential. *Mol. Phys.* **65** (1988) 65.

71. H.D. Dardy, V. Volterra and T.A. Litovitz, Rayleigh scattering: Orientational motion in highly anisotropic liquids, *J. Chem. Phys.* **59** (1973) 4491.

72. W. Danninger and G. Zundel, Reorientational motion and orientational correlation functions in weakly associated organic liquids by depolarized Rayleigh scattering. *Chem. Phys. Lett.* **90** (1982) 69.

73. P. Debye. *Polar molecules.* Dover Publications, New York, 1928.

74. R.G. Gordon. On the rotational diffusion of molecules. *J. Chem. Phys.* **44** (1966) 1830.

75. M. Fixman and K. Rider. Angular relaxation of the symmetric top. *J. Chem. Phys.* **51** (1969) 2425.

76. R.E.D. McClung. Rotational diffusion of symmetric top molecules in liquids. *J. Chem. Phys.* 57 (1972) 5478.

77. A.G. St. Pierre and W.A. Steele. Collisional effects upon rotational correlations of symmetric top molecules. *J. Chem. Phys.* **57** (1972) 4638.

78. P. van Konyenburg and W.A. Steele. Angular time-correlation functions from spectra for some molecular liquids. *J. Chem. Phys.* **56** (1972) 4776.

79. R.M. Lynden-Bell in *Molecular Liquids—Dynamics and Interactions* A.J. Barnes et al. (eds.) (1984) D. Reidel, p. 501.

80. S. Ruhman, L.R. Williams, A.G. Joly, B. Kohler and K.A. Nelson. Nonrelaxational inertial motion in CS_2 liquid observed by femtosecond time-resolved impulsive stimulated scattering. *J. Phys. Chem.* **91** (1987) 2237.

81. P.P. Ho, W. Yu and R.R. Alfano. Relaxation of the optical Kerr effect of anisotropic molecules in mixed liquids. *Chem. Phys. Lett.* **37** (1976) 91.

82. G.I.A. Stegeman and B.P. Stoicheff. Spectrum of light scattering from thermal shear waves in liquids. *Phys. Rev. A* **7** (1973) 1160.

83. G. Enright and B.P. Stoicheff. Depolarized Brillouin spectrum of liquid CS_2. *J. Chem. Phys.* **60** (1974) 2536.

84. H. Versmold. Depolarized Rayleigh scattering: Reorientational motion and orientational correlations in acetonitrile and carbon disulfide. *Ber. Bunsenges. Phys. Chem.* **82** (1978) 451.

85. Jiri Jonas. Pressure effects on the dynamic structure of liquids. *Acc. Chem. Res.* **17** (1984) 74.

86. M. Baggen, M. van Exter and A. Lagendijk. Time-resolved stimulated Raman scattering in a diamond anvil cell. *J. Chem. Phys.* **86** (1987) 2423.

87. D. Ben-Amotz, R. Jeanloz and C.B. Harris. Torsional dynamics of molecules on barrierless potentials in liquids. III. Pressure dependent picosecond studies of triphenyl-methane dye solutions in a diamond anvil cell. *J. Chem. Phys.* **86** (1987) 6119.

88. A. Jayaraman. Diamond anvil cell and high-pressure physical investigations. *Rev. Modern Physics* **55** (1983) 65.

89. D.J. Dunstan and I.L. Spain. The technology of diamond anvil high-pressure cells: I. Principles, design and operation, II. Operation and use. *J Phys E: Sci. Instrument.* **22** (1989) 913, 923.

90. H.K. Mao, R.J. Hemley. Optical studies of hyrodgen above 200 gigapascals: Evidence for metalization by band overlap. *Science* **244** (1989) 1462.

91. P.W. Bridgman. *The Physics of High Pressure.* G. Bell, London, 1949.

92. International Critical Tables, Vol III, ed. E.W. Washburn, McGraw-Hill, New York, 1928, p. 40.

93. J.F. Dill, T.A. Litovitz and J.A. Bucaro. Molecular reorientation in liquids by Rayleigh scattering: Pressure dependence of rotational correlation functions. *J. Chem. Phys.* **62** (1975) 3839.

94. J. Etchepare, G. Grillon, G. Hamoniaux, A. Antonetti and A. Orszag. Molecular dynamics of liquid benzene via femtosecond pulses laser excitation. *Revue Phys. Appl.* **22** (1987) 1749.

95. International Critical Tables, Vol III, ed. E.W. Washburn, McGraw-Hill, New York, 1928, p. 23.

96. L. Verlet. Computer "experiments" on classical fluids. I. Thermodynamical properties of Lennard-Jones molecules. *Phys. Rev.* **159** (1967) 98.

97. K. Singer, A. Taylor and J.V.L. Singer. Thermodynamic and structural properties of liquids modelled by '2-Lennard-Jones centres' pair potentials. *Mol. Phys.* **33** (1977) 1757.

98. D. Frenkel and J.P. McTague. Computer simulation of freezing and supercooled liquids. *Ann. Rev. Phys. Chem.* **31** (1980) 491.

99. A. Rahman, Mandell and J.P. McTague. Molecular dynamics study of an amorphous Lennard-Jones system at low temperature. *J. Chem. Phys.* **64** (1976) 1564.

100. J.H.R. Clark. Molecular dynamics studies of glass formation in the Lennard-Jones model of argon. *J. Chem. Soc. Faraday Trans. II* **75** (1979) 1371.

101. W.B. Street and K.E. Gubbins. Liquids of linear molecules: Computer simulation and theory. *Ann. Rev. Phys. Chem.* **28** (1977) 373.

102. B. Quentrec and C. Brot. Angular correlations and rotational motion in computer-simulated liquid nitrogen. *Phys. Rev. A* **12** (1975) 272.

103. R. Zwanzig and N.K. Aliwadi. Statistical error due to finite time averaging in computer experiments. *Phys. Rev.* **182** (196?) 280.

104. R.M. Lynden-Bell, D.J.C. Hutchinson and M.J. Doyle. Translational molecular motion and cages in computer molecular liquids. *Mol Phys.* **58** (1986) 307.

105. W.A. Steele. The rotation of molecules in dense phases. *Adv. Chem. Phys.* **34** (1976) 1.

107. B.I. Greene, P.A. Fleury, H.L. Carter, Jr. and R.C. Farrow. Microscopic dynamics in simple liquids by subpicosecond birefringences. *Phys. Rev. A* **29** (1984) 271.

108. P. Linse, S. Engström and B. Jönsson. Molecular dynamics simulation of liquid and solid benzene. *Chem. Phys. Lett.* **115** (1985) 95.

109. O. Steinhauser. On the structure and dynamics of liquid benzene. *Chem. Phys.* **73** (1982) 155.

110. R.W. Impey, P.A. Madden and I.R. McDonald. Spectroscopic and transport properties of water, model calculations and the interpretation of experimental results. *Mol. Phys.* **46** (1982) 513.

111. R.W. Impey, P.A. Madden and D.J. Tildesley. On the calculation of the orientational correlation paramter g_2. *Mol. Phys.* **44** (1981) 1319.

112. P.S.Y. Cheung and J.G. Powles. The properties of liquid nitrogen IV. A computer simulation. *Mol. Phys.* **30** (1975) 921.

113. D. Levesque and J.J. Weis. Collective motion and depolarized light scattering for diatomic fluids. *Phys. Rev. A* **12** (1975) 2584.

114. W.G. Hoover. *Molecular Dynamics Simulation.* Springer-Verlag, Berlin, 1986.

115. M.P. Allen. *Computer Simulation of Liquids.* Clarendon Press, New York, 1987.

116. C.W.Gear. Argonne National Laboratory Report No. ANL-7126.

117. See J.P. Ryckaert's article in reference 79.

118. D.J. Evans and S. Murad. Singularity free algorithm for molecular dynamics simulation of rigid polyatomics. *Mol. Phys.* **34** (1977) 327.

119. J.-P. Ryckaert, G. Ciccotti and H.J.C. Berendsen. Numerical integration of the cartesian equations of motion of a system with constraints: Molecular dynamics of n-alkanes. *J. Comp. Phys.* **23** (1977) 327.

120. W.B. Street, D.J. Tildesley and G. Saville. Multiple time-step methods in molecular dynamics. *Mol. Phys.* **35** (1978) 639.

121. B. Quentrec and C. Brot. New method for searching for neighbors in molecular dynamics computations. *J. Comp. Physics* **13** (1973) 430-432.

122. P. Schofield. Computer simulation studies of the liquid state. *Comp. Physics Comm.* **5** (1973) 17-23.